REFERENCE ONLY

UNIVERSITY OF LONDON THESIS

Degree	Year	Name of Author
PhD	2006	BUGIOLACCHI, R.

THE NUBIUM AND IMBRIUM REGIONS ON THE MOON: A HISTORY OF MARE FLOWS.

A thesis submitted to the University of London
for the degree of Doctor of Philosophy

by

Roberto Bugiolacchi

Department of Earth Sciences,
University College London,
Gower Street, London WC1E 6BT, United Kingdom

February 2006

ProQuest LLC
789 East Eisenhower Parkway
P.O. Box 1346
Ann Arbor, MI 48106-1346

ABSTRACT

The objective of my research is to identify, classify, measure, date, and place in a geological context distinctive lava flows within the Nubium and Imbrium regions of the Moon. I used multispectral filter data from the Clementine mission to create regional compositional maps based on the estimated abundance of iron and titanium in the regolith. In addition, by letting the 415 nm, 950 nm, and 750 nm wavebands respectively control the BRG channels, I produced a 'stretched' true colour image. A 'false colour' map was also derived by combining the 415/750, 750/1000, and 750/415 nm ratios; this type of image benefits from having albedo differences suppressed and colour differences considerably 'stretched'.

Most of the exposed maria unit flows were thus identified, outlined, and classified according to their FeO and TiO_2 weight percentage content.
I also estimated the basalts' ages by establishing their crater size frequency distribution using Lunar Orbiter and Apollo images.
A map produced from the filter ratio 750/950 nm helped identify late extrusive materials, fresh impact ejecta, and newly exposed regolith.
Iron content variations in the ejecta blankets of several craters were used to estimate the area's minimum maria thickness at the time of impact.

This work also focused on geological formations of outstanding interest related to the igneous history of regions.

Finally, most data and results were collected and employed to produce multi-layered geological maps of the Nubium and Imbrium regions.

ACKNOWLEDGMENTS

First I need to thank my adoptive country, Britain, for allowing me, through both financial and moral support, to undertake the ambition of my life and study planetary sciences this late in life. I will always be grateful to UCL and its phenomenal teaching staff for friendship and knowledge.

As an undergraduate, the 'planetary group' offered me all: from patience in putting up with my disputable jokes and mood swings, to gathering around me in moments of need, to showering me with friendship, laughs, and, dare I say, love... on the little me. You know who you are.
Above all, this work would have never being possible if not for the help, encouragement, and opportunities given to me by Prof John Guest.
Thanks to John I also had the pleasure in working along another luminary of lunar science, Dr Paul Spudis whose respect for my research betrays a great mind and... polite generosity. Is has been a pleasure and an honour to have worked alongside scientists of this calibre! Who would have believed that one day a paper by 'Bugiolacchi, Guest, Spudis', would have bothered the scientific world, amazing!

Thanks to Dr Tony Hurford for his offer of a place at UCL those many years ago; to Prof. David Price for offering me the opportunity of this PhD; to Richard Rabe and Danuta Kaminski for fixing my computers a million times; Brian Fessler for his, as yet, un-rewarded stunning Clementine images; and Terry, my colleague in all things 'maria', for his feedback and camaraderie. Oh, and my family for accepting another change of profession at 35 years of age!

Massive final thanks must go to my friend Dr Dominic Fortes, whose amazing humour, married with one of the finest brains in the human business, has produced endless hours of entertainment and cheap innuendos and vulgarity, all of which have kept me vaguely sane and happy throughout this journey. And his proofreading is from another world... In debt to you.

This work is dedicated to the people I love and those I have lost. Sorry to you both.

CONTENTS

LIST OF FIGURES

LIST OF TABLES

Part I

Introduction

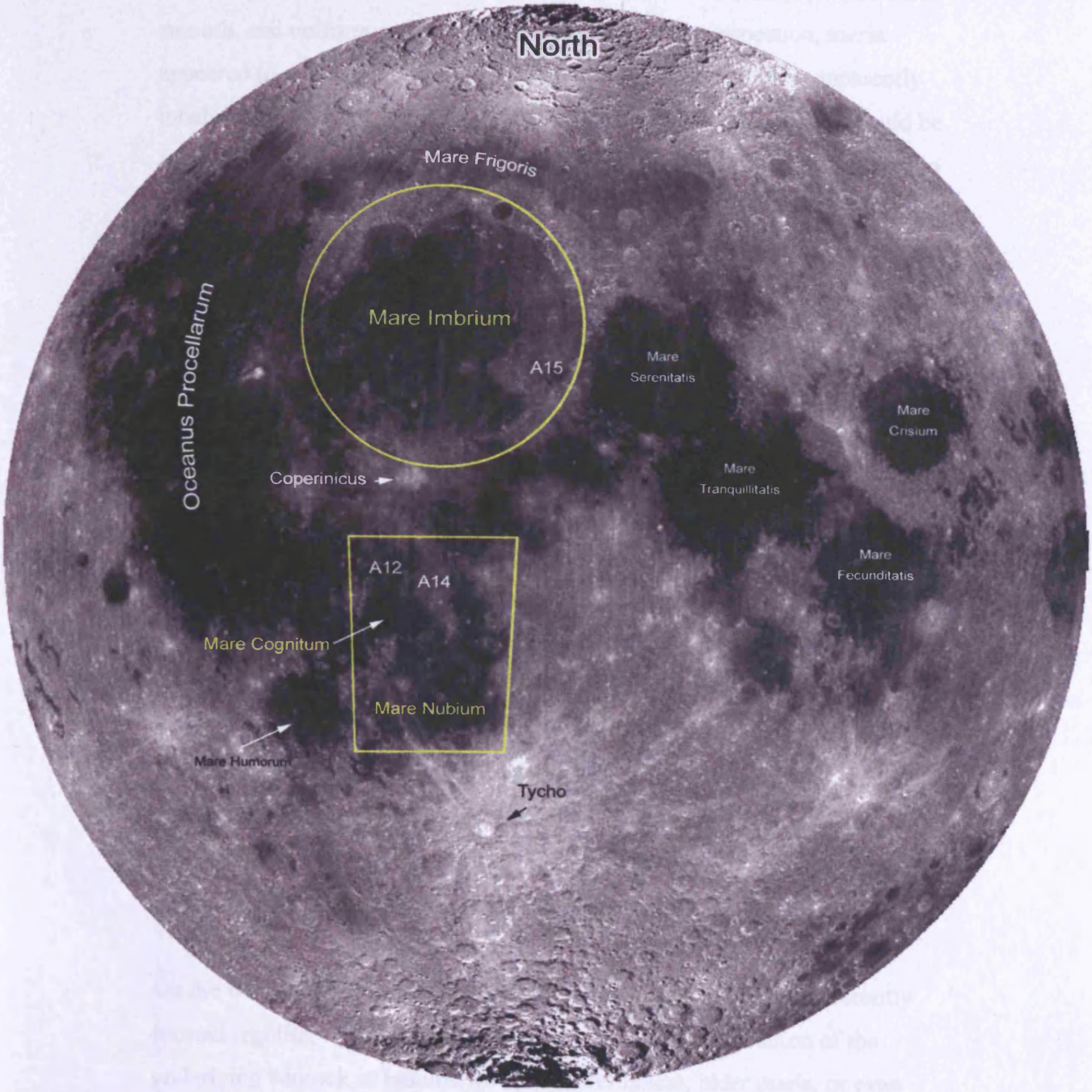

CHAPTER 1 INTRODUCTION

1.1 The Moon and its maria.

To the early telescopic observers, the lunar surface must have appeared alien, mysterious, and difficult to compare with known terrestrial landscapes. The bright rugged and elevated terrains were baptised Terræ (land), and the dark, smooth, and uniform surfaces Maria (seas). On closer inspection, maria appeared to possess characteristics similar to liquid bodies: they apparently inhabited low elevation basins; 'pools' or 'lakes' of similar material could be spotted around the lunar surface dotted around the terrae, and they seemed to have embayed and penetrated coastal landforms creating promontories and lagoons; 'islands' could also be identified. Further inspection even revealed the unmistakable outlines of massive 'sea waves'. The difference with our seas was that these ones did not move. The maria were very dark and static, like oceans frozen in time. They once must have moved and flowed, just like water or molten rock from a volcano. The more observers looked the more they found similarities with terrestrial igneous phenomena. They were observing solidified lava fields on a massive scale.

Since then, numerous manned and unmanned missions to the Moon, plus telescopic and remote observations, have answered many questions relating to the stratigraphy of the maria. We now know that the surface of the Moon is covered with two distinctive kinds of materials: one bright, the other dark. Remote sensing technology has allowed us to investigate subtler colour differences among lunar soils; in particular, regions where the maria appear uniform have been shown to exhibit a range of mineral compositions, differences large enough to suggest distinctive basalts flows.

On the whole, what we observe is the uppermost layer of the most recently formed regolith, which is taken to reflect mainly the composition of the underlying bedrock or basaltic flow(s). Nevertheless, older maria, or even bedrock samples, are often revealed in the ejecta of larger impacts through excavation, or exposed on steep slopes through gravitational wasting.

1.2 Aims and objectives of this work

A complex history of basalt petrogenesis and mare volcanism has shaped the present lunar maria. Establishing the relative abundances of mafic minerals such as olivine, pyroxene, and ilmenite is instrumental in establishing this history. Their presence can be ascertained by obtaining the bulk oxide content in the regolith, dominated by SiO_2, FeO, TiO_2, Al_2O_3, MgO, and CaO (Papike *et al.*, 1991). Mafic minerals' presence varies across the maria due to lateral differences in magma source regions and fractionation histories (Campbell *et al.*, 1997).
To summarise, three factors - soil maturity, mineralogy, and contamination - (from impact debris) control the spectral reflectance of the lunar surface.

Today, new compositional and maturity degree information on the regolith comes from spectrophotometric observations and orbital geochemistry data that have been calibrated using directly sampled materials collected at the Apollo and Luna landing sites (Campbell *et al.*, 1997). Remote sensing of the lunar maria has allowed us to investigate subtler colour differences among lunar soils; in particular, regions where the maria appear uniform have been shown to exhibit a range of mineral compositions, differences large enough to suggest distinctive basaltic flows.

The aim of this work is to investigate the stratigraphy and composition of Mare Nubium, Mare Cognitum and Mare Imbrium by combining data on the geographical distribution of the elements iron and titanium within the maria, relative and estimated dating of each potential unit, and estimates of emplacement volumes.
Moreover, the interpretative techniques for analysing multispectral surface data developed in this work will be, hopefully, refined and eventually applied to other remote sensing missions directed at comparable planetary bodies.

Ultimately, this work should help advance our understanding of lunar petrogenesis and maria emplacement.

1.3 Altering factors in surface geochemistry

Objects ranging in size from tens of kilometres to less than one micron have battered the lunar surface since its formation, some 4.5 Ga ago.
This has produced a layer of shattered rocks and fine debris called regolith (McKay *et al.*, 1991), which covers most of the lunar surface. The bulk of it consists of particles smaller than one centimetre in size, and it is referred to as (lunar) soil.
Regolith cover is 3-8 meters deep in the maria (Hoerz *et al.*, 1991; Moore *et al.*, 1980) but may be up to fifteen meters deep on older highland regions (McKay *et al.*, 1991). What we see of the lunar surface is the top layer of this mixed (or 'gardened'), pulverised, and reworked veneer of ancient crystalline rocks, breccias, glasses, minerals, and agglutinates. The topmost regolith (in the region of a few centimetres) is also matured and saturated by solar wind and solar flare particles.

Generally, differences in brightness of the lunar soil are due to the reflectance properties of those materials with higher plagioclase feldspar content (higher albedo) relative to those rich in mafic minerals (lower albedo). Concurrently, the continuous exposure to space weathering, mainly in the form of micrometeorite bombardment, solar wind particles, and galactic cosmic rays, modifies the reflectance property of the lunar soil with time (e.g. Pieters *et al.*, 1993a). Depositional processes such as accreted impact materials (spherules), sputter deposits, and impact-derived vapours (Keller *et al.*, 1999) combine in altering the lunar surface's optical characteristics.

Direct (Apollo and Luna missions, lunar meteorites) and indirect sampling (telescopic and remote sensing using lunar orbiting satellites) of the Moon's surface have helped us build, refine, and constrain models of the geophysical make up of the upper crust. Confidence on remote sensing as a reliable instrument employed to sample crustal materials of the lunar surface relies on the assumption that regolith is geo-chemically representative of the underlying bedrock. Much research has gone towards proving this connection since the first samples were brought back to Earth (Oberbeck et al., 1973). Further

investigation found that, on average, only about 5 % of the regolith at any one place comes from distances beyond a 100 km radius and 50 % from less than 3 km (Gault et al., 1974; Taylor, 1975).
The bulk of highlands debris in mare regolith comes directly from beneath relatively thin mare flows, derived dominantly by vertical mixing (Rhodes, 1977; Hoerz, 1978).

Since the depth of penetration for reflected VIS-NIR energy is only a few microns, the observed spectrum reflects the composition of the uppermost surface material. The optical properties of this layer are dominated by the finer fractions (<10 μm) (Pieters *et al.*, 1993b; Keller *et al.*, 1998b), which, while composing only about 10-20% of the regolith by weight, constitute about 2/3 of the surface area (Housley 1980).

In mature regolith, major contributors to reflectance variations in these fractions are the size and distribution of the nanophase metal iron (Fe^0) in the soil grains (Keller *et al.*, 1998b, 2000; Noble *et al.*, 2000). Agglutinates represent a major source of Fe^0; they form as micrometeoroid impacts melt and mix lunar soils that contains previously implanted solar-wind elements (mainly H and He). As the grains melt, forming glasses, they give up the hydrogen, which reacts with ferrous oxide (FeO) reducing it to Fe^0 and H_2O (which vaporises). Agglutinates are very important in remote lunar geology because both Fe^0 and glasses obscure and modify the soil's infrared reflectance and x-ray fluorescence. They are also ubiquitous (up to 60% of the soil composition) and their content is directly proportional to the soil's cumulative exposure age. According to Keller *et al.* (2000), nearly every grain in both the Apollo 17 mare soil and the Apollo 15 highland soil samples (both <20 μm sieve fraction) has nanophase Fe^0 within 100 nm of the particle surface.

This work has made extensive use of multispectral surface data acquired by the Clementine spacecraft mission[1] in 1994. The bulk of the mapping was based on observations taken from the approximate local zenith (Kresalvsky *et al.*, 2000). Among several other scientific instruments, Clementine carried ultraviolet-visible (UVVIS) and near-infrared (NIR) multispectral cameras. These allowed, by means of suitably chosen filters, the collection of reflected solar radiation in eleven discrete wavelength bands (see table 2.1). The spectral bands were focused on parts of the spectrum affected by both compositional variation and maturity of the regolith (Pieters *et al.*, 1994).

Table 2.1. Clementine UVVIS instrument parameters. Compiled using data from Nozette *et al.* (1994).

Filter	band centre ± 1σ
A	415 ± 20 nm
B	750 ± 5 nm
C	900 ± 15 nm
D	950 ± 15 nm
E	1,000 ± 15 nm

The Clementine raw data sets, traditionally called EDR (Engineering Data Records, Eliason *et al.*, 1995), were made available by the Planetary Data System (PDS)[2] in cooperation with the Naval Research Laboratory in the form of 88 CD-ROM[3] volumes. The UVVIS Digital Image Model (DIM) was imported into ISIS (Integrated Software for Imaging Spectrometers, see Torson and Becker 1997)[4] software running on a Unix/Sun workstation computer[5]. This produced an 'image cube' ('*.*.cub.'; see figure 2.1 for a full explanation of the format) which subsequently underwent a five-step processing routine (Stages 0

[1] For a full account on the mission, including history, chronology, details on the spacecraft and scientific payload, please refer to Nozette *et al.*, 1994; Regeon *et al.*, 1994; and McEwen *et al.*, (1997).
[2] Part of the U.S. Geological Survey's Astrogeology Program in Flagstaff, Arizona, USA.
[3] Images can be also downloaded from the NASA Planetary Data System Geosciences Node at Washington University (http://www-pdsimage.jpl.nasa.gov/PDS/public/clementine/frontpage.html).
[4] See http://wwwflag.wr.usgs.gov/USGSFlag/Data/Software/documentation.html
[5] Kindly supply by Paul Spudis, Applied Physics Laboratory, John Hopkins University, Laurel MD, USA.

to 4) designed to minimise inaccuracies, such as radiometric and geometric errors, and normalise the sun-viewing geometry (Eliason, 1997; Torson and Becker, 1997). The obtained DIM data were finally mosaicked to obtain an image cube in the chosen orthographic projection.

Since the software carried out most of these tasks automatically, please refer to Eliason *et al.* (1999), Isbell *et al.* (1999), Robinson *et al.* (1999) for a full account of the applied methodology.

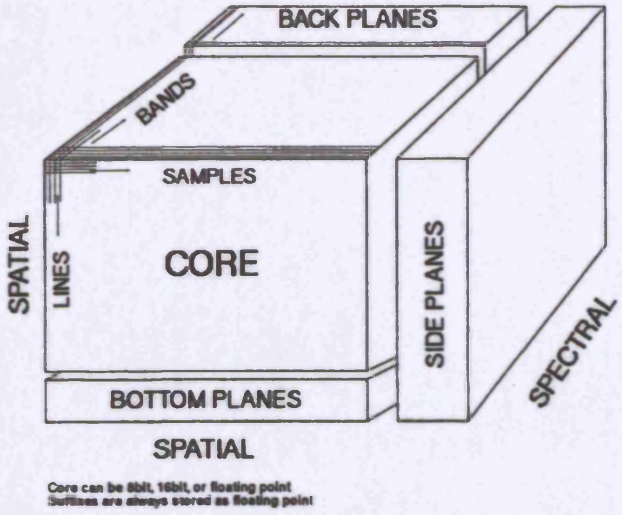

Figure 2.1. The main body of the image is called the core. The image has spatial dimension in the X (samples) and Y (lines) direction. By stacking images from different bands, the image now has three dimensions and is called a cube. The different planes (back, side and bottom) contain additional viewable information about the images in the cube. These three regions of the image cube are called suffixes. The bottom and side planes are seldom used but the back planes may contain information about the image emission, incidence and phase angle (Eliason *et al.*, 1999).

The program NASA View, a PDS software[6] display tool supplied by PDS/JPL, can show full resolution cube images with an average spatial resolution of around 200 meter per pixel. These can either be from a single filter (such as the 'albedo' 750 nm image) or multispectral (such as the Fe and Ti maps), combined and processed according to specific algorithms (see below for individual descriptions).

[6] NASA View can be freely downloaded from: http://pds.jpl.nasa.gov/

By making use of the multilevel data potential of cube images, a more basic version of NASA View software, called Quick View, was used to extract the absolute location of each interrogated pixel on the Moon (lat/long) along with the iron and titanium chemical abundance it represents.

Geographical distances were also determined by exploiting the given absolute location between two points (i.e. pixels), expressed as line and sample numbers.

Part II

Mare Nubium and Mare Cognitum

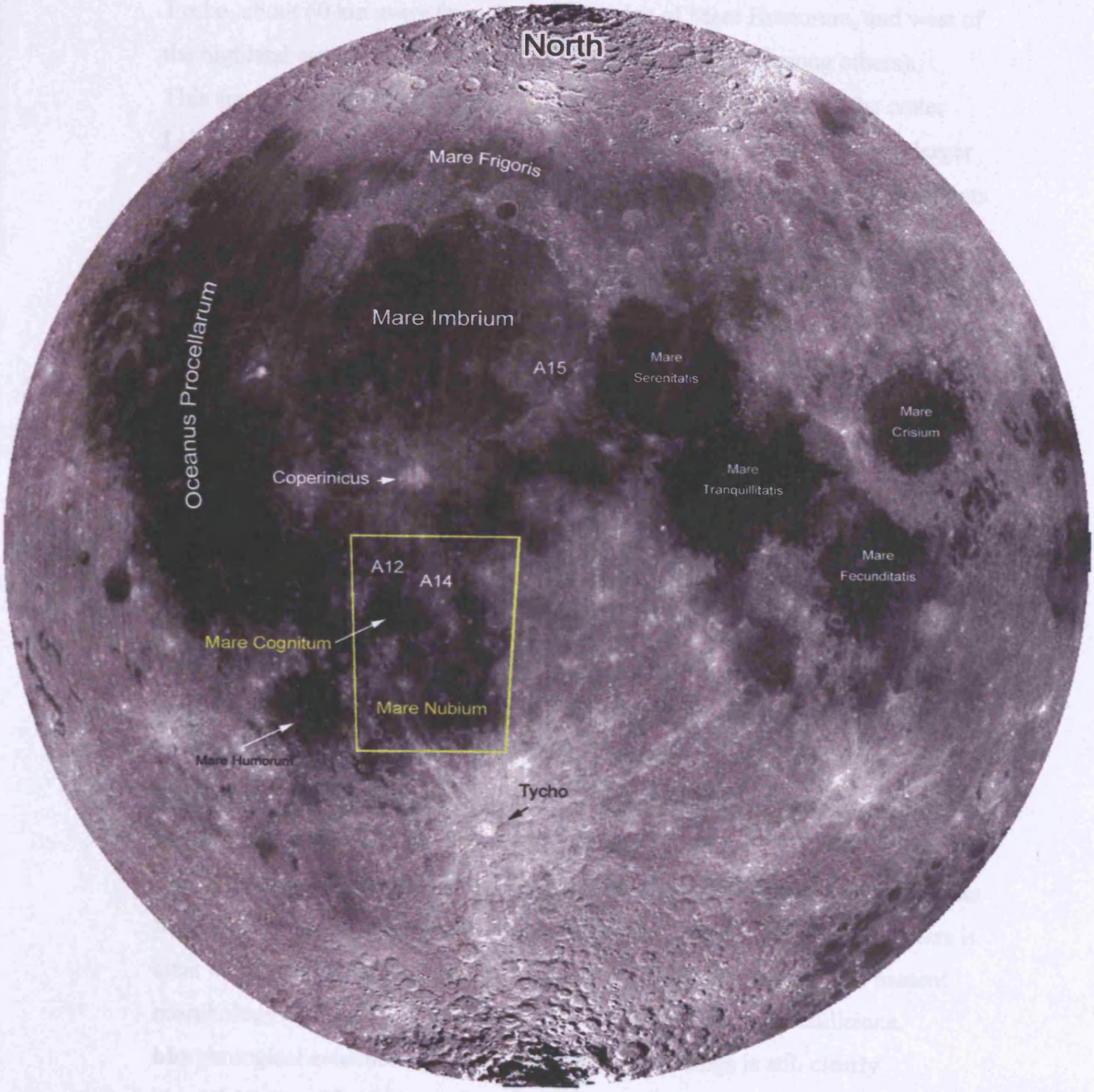

CHAPTER 3 GENERAL DESCRIPTION OF THE AREA
MARE NUBIUM AND MARE COGNITUM

3.1 Mapped area

The area covered by this study is a quadrangle with 908.6 km sides with coordinates 0 S 30.0 W and 30.0 S 32.0 W (Fig. #3.1) giving a total surface area of 825,554 km^2. It encompasses the region 10° south of Copernicus, 15° north of Tycho, about 60 km away from the eastern edge of Mare Humorum, and west of the highland craters Ptolemaeus, Alphonsus and Arzachel (among others).
This area represents the southern edge of Mare Insularum, south of the crater Lansberg, and Mare Cognitum in the NE and Mare Nubium in the South; larger craters within the mare are Bullialdus, König, and Birt, plus the surface remnants of, among others, craters Kies, Wolf, Opelt, Lubiniezky, and Lassel. This region is also characterised by a north-south aligned peninsula containing the Fra Mauro, Parry, Bonpland, and Guericke plains. Other noteworthy geological features are the Rima Hesiodus in the SW and Rima Flammarion in the NE. The Rupes Recta (also called Straight Wall) in the SE is a 120 km long scarp that averages 300 m in height (De Hon, 1977). Monte Riphaeus delineates Mare Cognitum on its northeasterly boundary.

3.2 Mare Nubium

The pre-Nectarian Mare Nubium covers geographically nearly two-thirds of the area under study, centred at 21.3 S 16.6 W. Its official name since 1935, Mare Nubium, or "Sea of Clouds", derives from early telescopic observations. The mare's numerous ghost features, and various higher-albedo crater ejecta criss-crossing the basin, conjured up the idea of lunar clouds.
Mare Nubium has a diameter of 750 km, and it is one of the most ancient circular basins on the Moon (Stuart-Alexander and Howard, 1970). Nevertheless, there is clear evidence that the basin did not form by a single large impact. Its present morphology appears to be a consequence of a number of major collisions. Morphological evidence of at least four major basin rings is still clearly identifiable (see Fig. 3.2, also De Hon, 1977).

3.3 Mare Cognitum

Mare Cognitum, "the sea that has become known", with a diameter of 376 km (10.0 S 23.1 W), is located in a basin that sits within the proposed second ring of the Procellarum basin. The mountain range Montes Riphaeus to the northwest of the region may represent part of the rim-crest of a large buried crater, containing the mare.

A number of missions visited this region: Apollo 12 landed close to Surveyor 3, and Apollo 14 landed on the hills at the edge of the Fra Mauro crater. Mare Cognitum is also the location where the Ranger 7 probe crash-landed.

Table 3.1. Main topographic features within the Nubium basin region.

RIMAE:

Rima Hesiodus.....from south Nubium to Palus Epidemiarum

Rupes Recta. Straight wall delimiting a difference in level of 300 m height x 120 km length.

MAIN CRATERS:

	Diameter - Depth
Fra Mauro	80 km - 720 m
Parry	82 km - 1450 m
Bonpland	58 km
Guericke	53 km - 670 m
Palisa	30 km - 900 m
Davy	32 km - 1350 m
Lassel	22 km - 930 m
Alpetragius	43 km - 4000 m
Alphonsus	110 km - 2000 m
Arzachel	104 km - 4000 m
Purbach	120 km - 2400 m
Regiomontanus	130 km - 2000 m
Ptolemaeus	140 km - 3000 m
Deslandres	200 km -
Pitatus	80 km - 870 m
Hesiodus	45 km - 1200 m
Kies	a buried crater - 44 km - 750 m
Konig	26 km - 1960 m
Bullialdus	61 km - 2400 m
Lubiniezky	38 km - 300 m
Darney	6 km - 1500 m
Opelt	a buried crater - 45 km -
Gould	a buried crater - 33 km -
Max Wolf	26 km - 700 m
Nicollet	15 km - 2000 m
Birt	17 km - 1800 m
Campanus	48 km - 2030 m
Mercator	40 km - 1300 m
Capuanus	58 km - 2450 m
Cichus	32 km - 3700 m

MARGINAL REGIONS:

Palus Epidemiarum.....SW of mare Nubium

Mare Cognitum.....north side of mare Nubium

NEIGHBOURING PLAINS:

Sinus Aestuum.....30,000 km^2 - North

Oceanus Procellarum .....4,000,000 km^2 - West

Mare Humorum.....80,000 km^2 - West

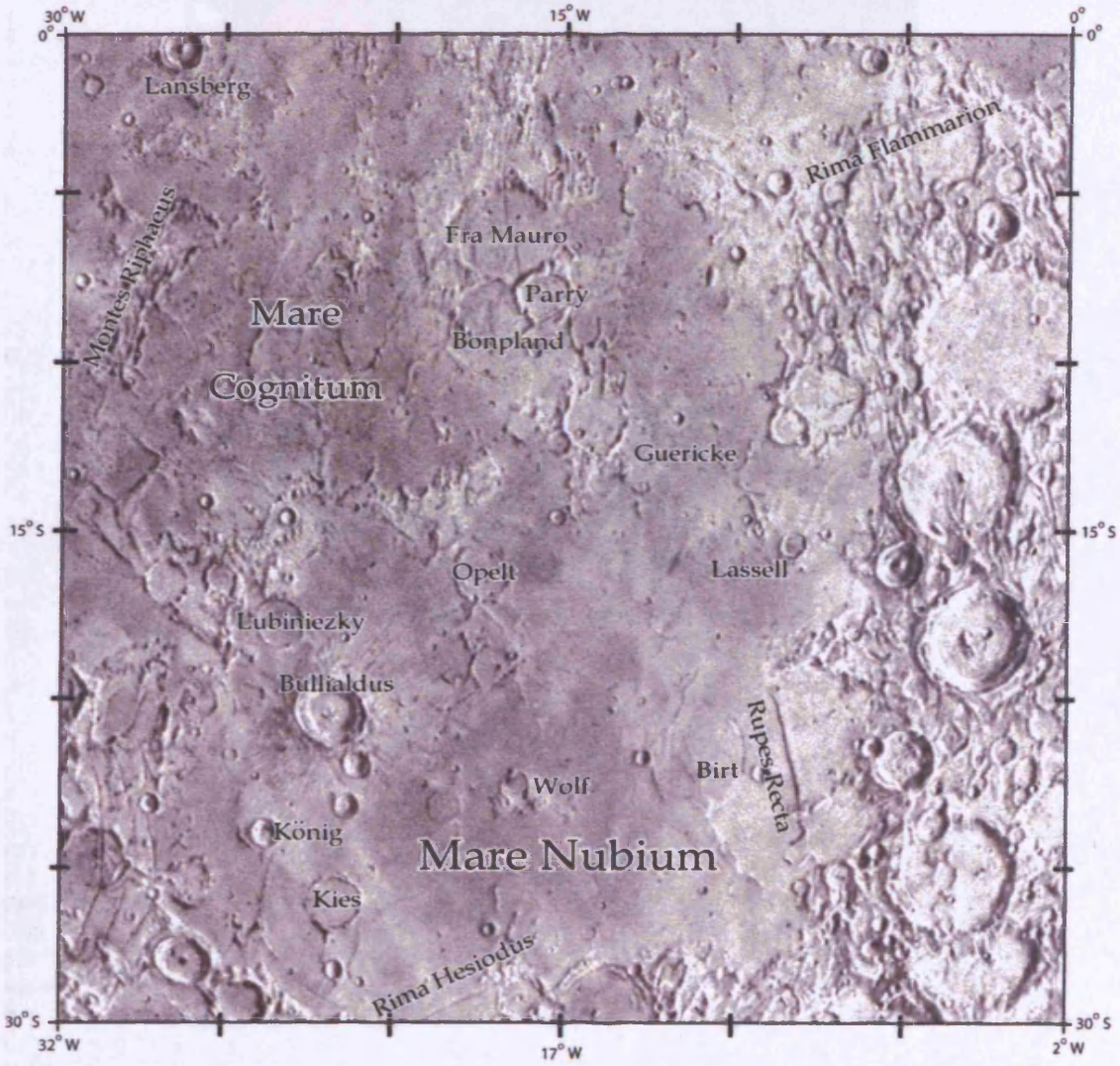

Figure 3.1. Shaded relief map of the areas studied (U.S. Department of the Interior)

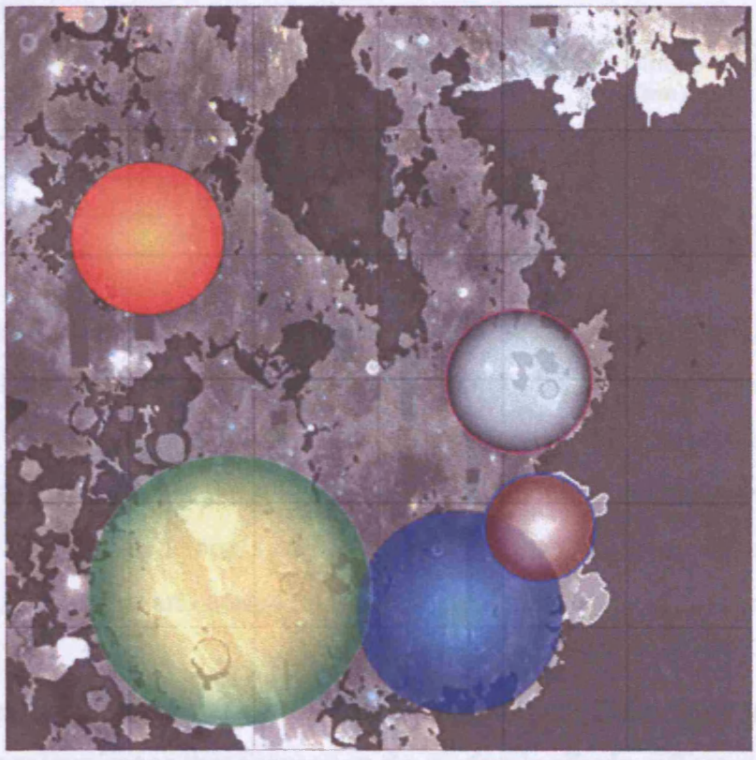

Figure 3.2. Topographically inferred ancient basin rings

4.1 Production of the albedo map (DBA)

The first image I produced was the region's "true colour" map, often called DBA (filters 'D, B, and A'). Data from three individual filters were assigned to the RGB display channels to produce a colour composite image (Table 4.1):

Table 4.1. Comparison between the visible spectrum values for the three fundamental colours and the assigned RGB colours.

Represented Primary Colour	Real approximate wavelength ranges (nm)	Assigned controlling bandpass filters (nm)
Red	740-620	**950** (NIR) filter D
Green	575-500	**750** (red) filter B
Blue	500-445	**415** (UV) filter A

The 'true' colour image effectively stretches the visible range from the NIR at one end to the violet at the other. The underlying red colour of the regolith, mostly due to oxidation, here displayed as green, contributes to the general greenish hue of this image. The result is a picture that subtly, but significantly, emphasises the visible colour range of the Moon's surface. It was also used as an excellent topographic source, alternative and complementary to available optical photographs (e.g. Orbiter IV).

Following appropriate brightness threshold filtering and emphasis, I produced an enhanced true colour image that focuses on the surface's albedo differences in the region (see Fig. 4.1).

4.2 Production of the compositional maps

Smith (1985), along with many other researchers in the field of remote sensing geology (e.g. Mustard *et al.*, 1989), laid down the theoretical foundations for the quantitative determination of mineral types and abundances from reflectance spectra using principal components analysis. Building on a number of methodologies that have been developed in the last three decades (Whitaker 1972a; Charette *et al.*, 1974; Pieters 1978; Jonhson *et al.*, 1991; Pieters *et al.*, 1993a; Melendrez *et al.*, 1994), Lucey *et al.* 1995, 1996, 1998, 2000a) I have utilised data from the

Clementine mission's 415, 750, and 950 nm filters to estimate FeO and TiO_2 abundances and mineral distribution.

4.3 Titanium map

One of the major parameters used in the classification of mare basalts is their TiO_2 content (reflecting the abundance of the mineral ilmenite $FeTiO_3$). Titanium is an important elemental indicator in mare basalt petrogenesis (e.g. Elphic *et al.*, 2001a, b). Moreover, lunar samples demonstrated that this mineral content is the major compositional variable among mare basalts (e.g. Lucey *et al.*, 2000b).

Charette *et al.* (1974) was among the first researchers to notice a correlation between UVVIS colour balance and TiO_2, a relationship further explored by Hapke *et al.* (1975). He found that opaque minerals, such as ilmenite (the major mineral carrier of Ti and the dominant opaque phase), have a strong influence on lunar reflectance. Opaques are by definition dark and their presence therefore decreases the reflectance of an iron-bearing regolith, its spectral contrast, and its spectral slope, in essence, making it less red (Lucey *et al.*, 2000b).

These findings allowed the development of the first titanium content maps based on early telescopic multispectral images of the Moon. In the following years many researchers worked on improving and refining the mathematical algorithms (Johnson *et al.*, 1985. Lucey *et al.*, 1998, 2000a). Others conducted parallel research on the photometric properties of the Moon's surface (for instance Kreslavsky *et al.*, 2000) by experimenting on various lunar samples, confirming and validating the work of the Hawaiian group (Lucey and coworkers).

The Ti map (Fig. 4.2) was produced using an updated version of the original algorithm presented by Lucey *et al.* (1996). It uses measurements of the 415 nm and 750 nm reflectance and, in a simplified way, can be expressed as[1]:

[1] For full description of the equation, please refer to Lucey *et al.*, (2000a).

$$TiO_2 wt\% = 3.708 \times \arctan\left\{\frac{[(R_{415}/R_{750}) - y_{0Ti}]}{[R_{750} - x_{0Ti}]}\right\}^{5.979};$$

where R_x is the reflectance at wavelength x (nm) and x_{0Ti} and y_{0Ti} represent the origin. Or, conceptually:

$$TiO_2 = \frac{415/750nm}{750nm}.$$

Experimental data have shown on ten direct trials that the relative average standard deviation of the test set data was 1.00 wt% TiO_2 (Lucey *et al.*, 2000a). This shows that titanium values are directly proportional to the 'blueness' of an area and inversely proportional to its reflectance in the red part of the spectrum.

The geological implications of this and all the other images will be discussed in detail in the next chapter.

4.4 Iron map

A reduction of ferrous iron (FeO) in glass and minerals to sub-micrometer particles of native iron (Fe, or I_s) occurs with exposure to the space environment (McKay *et al.*, 1991). Shultz (1974, page 436 for references) lists three principle factors: solar wind emplacement, proton bombardment, and impact-induced mixing and vitrification. Bleaching by ultraviolet irradiation and darkening of materials with high absorption coefficients by reduction in particle size also contribute to the darkening and reddening of the regolith with time (Fisher and Pieters 1994, 1996).

Lucey *et al.* (1995) proposed that a colour ratio involving 750 nm reflectance and the far end of the visible spectrum (NIR, 950 nm) would indicate the (ferrous) iron abundance percentage (see Fig. 4.3). According to Lucey *et al.*, (2000a):

$$FeOwt\% = \left\{17.427 \times \left[-\arctan\frac{[(R_{950}/R_{750}) - y_{0Fe}]}{[R_{750} - x_{0Fe}]}\right]\right\} - 7.565;$$

where R_x is the reflectance at wavelength x (nm) and x_{0Fe} and y_{0Fe} represent the origin. Or, conceptually:

$$FeO = \frac{950/750nm}{750nm} .$$

The average standard deviation of the test set data was 1.29 wt% FeO. Effectively, the Lucey method aims to measure the spectral effects of ferrous iron in major lunar minerals such as pyroxene and olivine (Blewett and Hawke 2001). Figure 4.3 represents the distribution map of iron content in the regolith.

4.5 'False Colour' (FC) map

Another type of map, a 'false colour' composite (see Fig. 4.4) was also derived from Clementine DIMs. The use of ratios is to compensate for albedo variations and exaggerate colour variations (Pieters *et al.*, 1994). The resulting multispectral composite mosaic is a much clearer representation of the reflectance characteristics in the region due to variations in regolith maturity and mineralogy. The ratio between images taken through filters 750 nm and 950 nm also helps identifying the presence of fresh mafic minerals in the lunar materials. This is due to the absorption band centred near 1.0 μm resulting from a combination of spectral absorption by Fe^{2+} in clinopyroxene and Fe^{2+} in olivine (Charette *et al.*, 1974, 1975; Walker *et al.*, 1975). Table 4.2 shows the ratios controlling the RGB values:

Table 4.2. Ratios controlling the RGB values

Colour	Ratios (nm)
Red	750/415
Green	750/950
Blue	415/750

Figure 4.1
The Nubium Basin

'True' Colour Image (DBA)

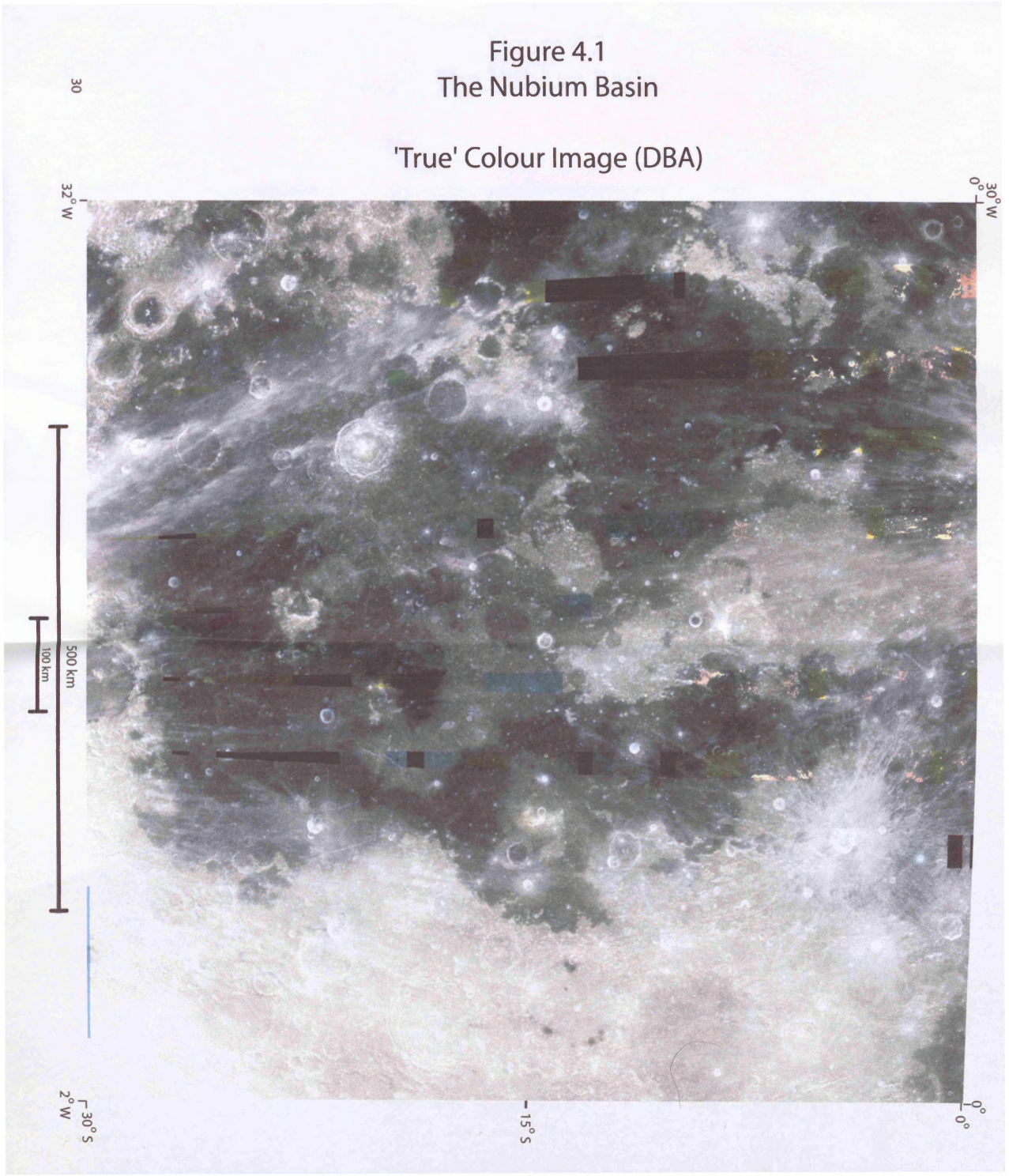

Figure 4.2
The Nubium Basin

Ti abundance (brighter = higher %)

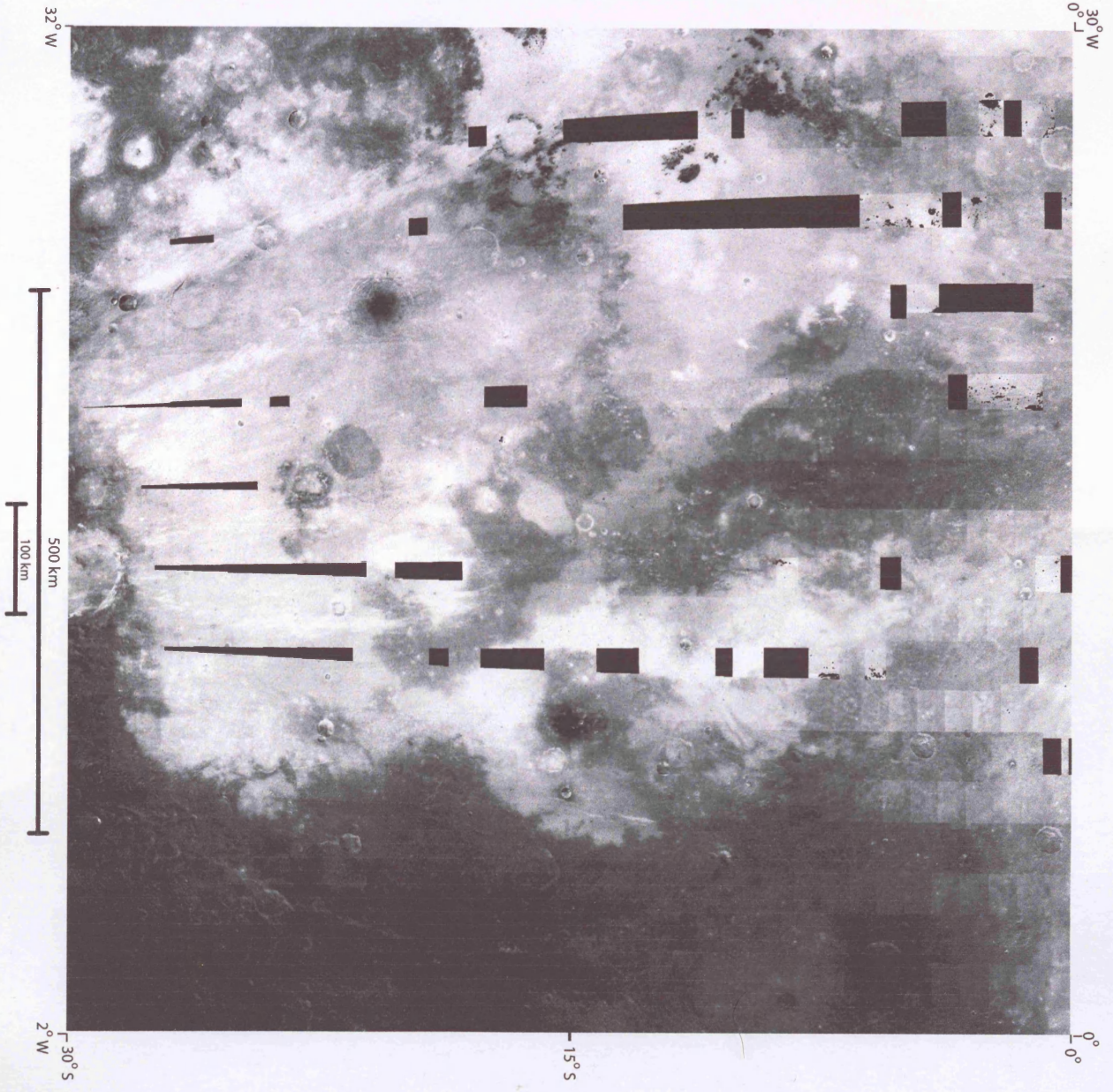

Figure 4.3
The Nubium Basin

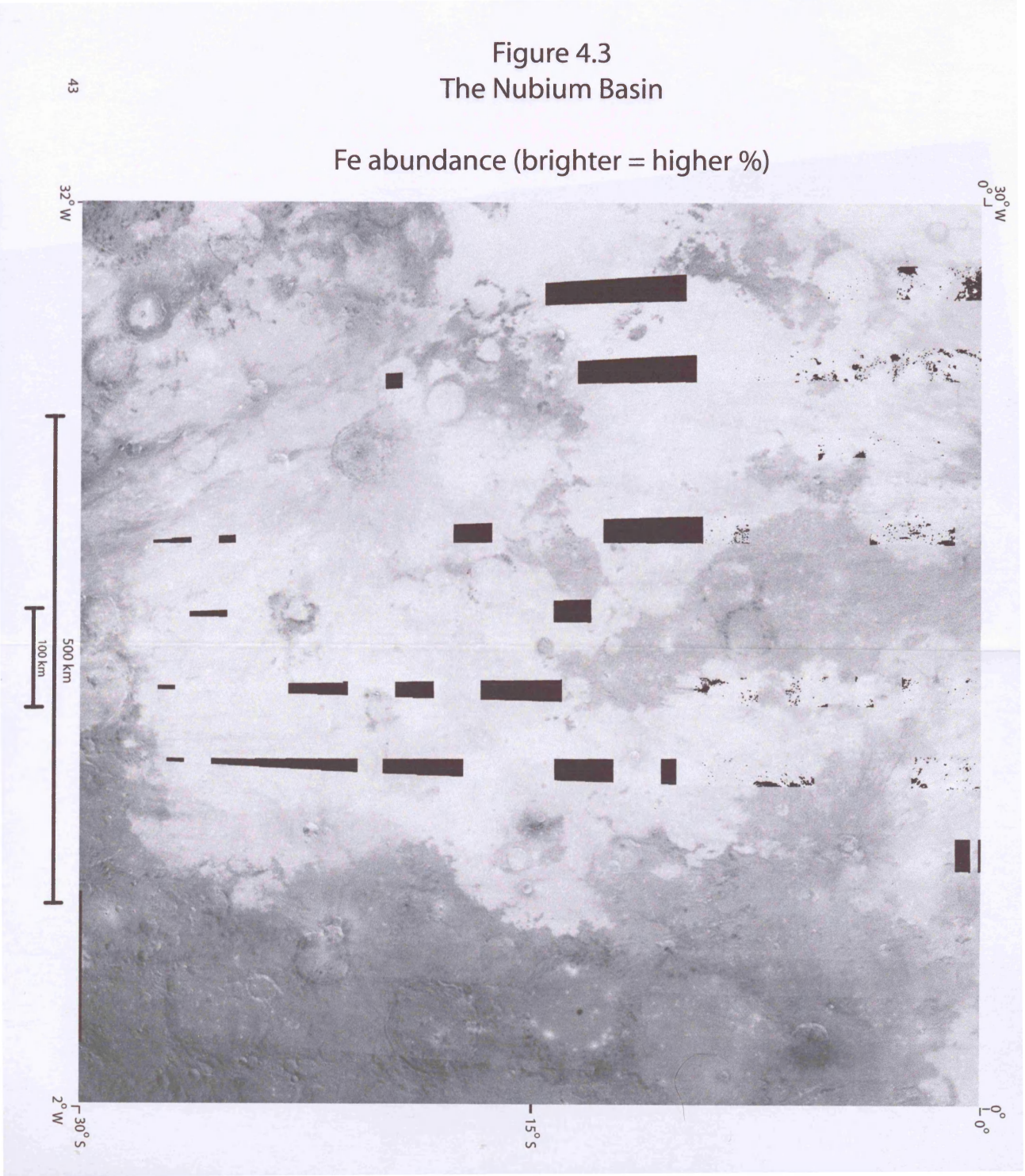

Figure 4.4
The Nubium Basin

Colour-ratio composite (FC)

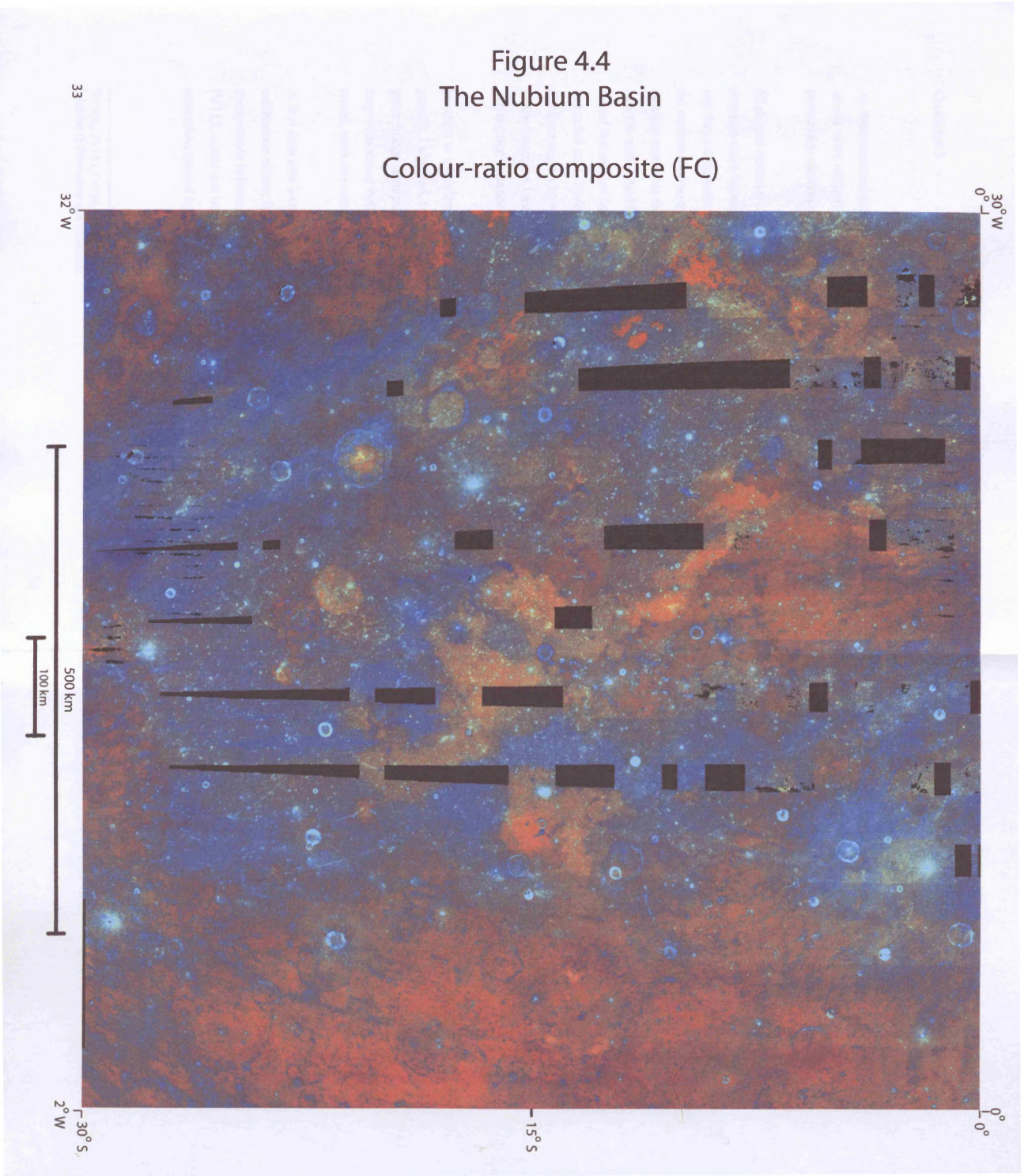

As demonstrated on Chapter 4, data from the Clementine multispectral instruments were utilised to produce a 'stretched' true colour image, titanium, and iron percentage distribution maps, and a false colour map.

Highland material is generally Fe and Ti poor and high albedo in comparison to average mare basalts. The task of delineating clear mare/highland boundaries using these diagnostic tools is somewhat complicated by the amount of mineralogical contamination over large maria areas originating from non-mare surfaces, including materials that are either dislocated by impact forces or dug out from below the mare. Additionally, fresh impacts produce localised mechanical reworking of the surface layer and implantation of allochthonous ejecta material over an extended area. Unfortunately, the task of interpreting the stratigraphy of the Mare Nubium region by remote sensing is complicated by its close proximity to some of the youngest lunar craters; in particular, from outside the basin, Copernicus, Thyco, and Lalande, and within, Bullialdus.

In order to complement Clementine surface data with high resolution photographs, I scanned, resized, and stretched Orbiter IV prints[1] using standard computer image manipulation software[2]. I then produced a first draft mare/highland map combining both families of images. Major geological features were also noted, such as craters, sinuous rilles, mare domes, lava terraces, and cinder cones.

A few data sets were partially corrupted due to either instrument malfunction or calibration errors; for instance, some regions within the Clementine data offer no computable information; also, a number of Orbiter IV pictures, in particular set IV113, could not be used to ascertain maria boundaries because of film oversaturation caused by high albedo materials.

[1] IV108, IV113, IV120, IV125, IV132; all sets H1 through H3. Bowker D. E. *et al.* (1971)
[2] Adobe © Photoshop and Illustrator.

To help refine my map, Lunar Astronomical Charts (LAC), Lunar Topographic Orthophotomaps (LTO), and photographic reproductions of the Consolidated Lunar Atlas were used extensively (Kuiper *et al.*, 1967). These latter images were captured at different insolation angles (generally lower) than those from the Orbiter satellite, thus helping to distinguish and delineate features of shallow elevation and modest dip angle.

Finally, the maria/upland draft map (Fig. 5.1) was scanned and imported back into the computer for further manipulation. Digitalisation of the image made it possible to gather statistics of the pixel counts within selected areas of the map. Consequently, by knowing the surface area represented by a single pixel, one can derive an estimate of the geographical distribution of the area under question. By applying this method, I found the maria to overlay an area of around 500,000 km^2, representing nearly 60 percent of the whole map region.

I have also introduced a provisional grid system nomenclature (a-f, 1-6) subdividing each map into thirty-six equal quadrants, each side representing five degrees of lat/long (see Fig. 5.1).

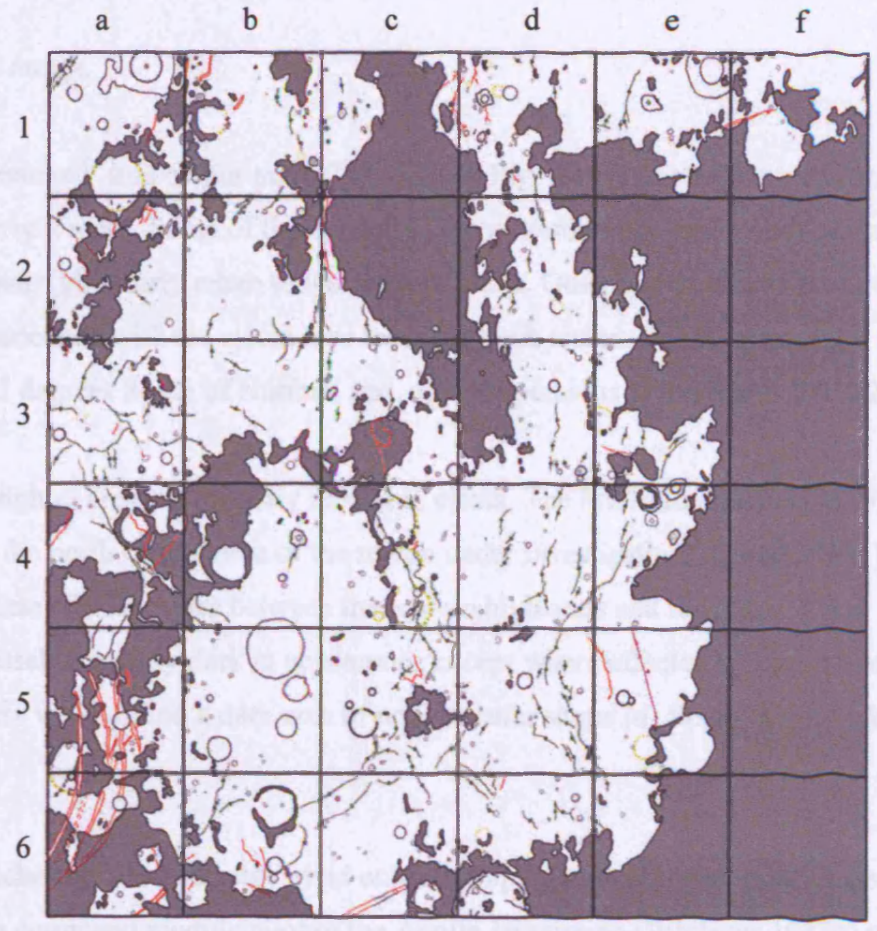

Figure 5.1. Upland, major craters, and grid system within the Nubium region

CHAPTER 6 VISUAL STUDY AND COMPARISON OF THE FeO, TiO_2, DBA, AND FALSE COLOUR MAPS

MARE NUBIUM AND MARE COGNITUM

6.1 DBA image.

In the 'stretched' true colour map, (Fig. 4.1 and Fig. 6.1a) I noticed several contiguous bright areas. Some of them, such as those surrounding crater Bullialdus (*f*) and Lalande (*g*), clearly relate to the craters' ejecta. Other higher albedo features (*k*) are associated with the ejecta rays from the fresh craters Tycho, situated around 15 degrees South of Nubium and, also, Copernicus in the North (10 N 20 W).

Not all brighter areas are directly related to ejecta. The Fra Mauro peninsula (*b*) occupies the north central area of the region under investigation, characterised by intermediate albedo values between the eastern highlands and the maria. Mare Nubium itself is mostly dark in appearance except where affected by ejecta materials. There we also find a dark area of near-circular shape (*d*) South of Guericke B.

Some patches of terrain display vivid colours, in particular (*h*), near crater Lassell. While the command module pilot of the Apollo 16 mission (Whitaker 1972b) was flying over the area he commented: "...right now the southern piece (*of Lassell C*) with a crater in it is a sort of a tan colour, and the northern piece is grey...". Even though this area geographically belongs to the highlands and is consequently, beyond the scope of this research, it is worth noticing as it might represent a site of significant geological value. Another similar bright area (*m*) stands out (in this image) as an archipelago of 'brass tinted' islands near the western shores of Mare Cognitum (*a*).

To summarise, the DBA image (Fig 6.1a) highlights a number of distinctive geomorphologic features, each with their individual colour and albedo characteristics:

1. Dark maria (*c, d,* and *e*), dotted by fresh craters, some deep blue, and some bright green in colour. Lighter or grey maria (e.g. *n* and *d*), representing

more heavily cratered patches of terrain, mostly located near to the borders with highlands.

2. The highlands, bright enough to saturate the Clementine image (e.g. south of *n*).
3. The inferred presence of red glasses of pyroclastic origin characterises areas of possible volcanic origin (*h, m*).
4. The full or partial rim remnants of numerous ghost craters, such as Opelt, Kies, Lubiniezky, etc. (which were inundated by early mare basalt flows). A number of these craters (e.g. Kies) feature bright optical 'tails' originating from the deflection, entrapment, and consequent deposition of brighter ejecta ray materials from nearby fresher impacts.
5. The vibrant blue colours of many craters' rim slopes. These are (relatively) freshly exposed crystalline surfaces, less mature than the surrounding materials, and highly reflective.
6. The large and relatively recent Bullialdus crater (*f*), with its undulated rim terraces and its spectrally complex central peak.
7. The peculiarly heart-shaped Wolf (*i*) crater(s).
8. Brilliant ejecta rays from Tycho, Copernicus, and Lallande (*g*) extending throughout the region.
9. The many morphologic and volcanic features such as wrinkle ridges, channels, and sinuous rilles scattered across the basin. Their presence suggests past crustal dynamics and/or buried geological features. Rupes Recta is a 120 km long scarp that stands out in a landscape of circles and curves, as a long and almost straight thin blue line (*n*). Not far and parallel to it, the Rima Birt rille stretches out for over 50 km over the west side of crater Birt.

6.2 Titanium Map

The Ti map (Fig. 4.2 and Fig. 6.1c) is the image that suffers most from the process of mosaicking original Clementine data. Despite the data having undergone geometric control, radiometric calibration, photometric and phase normalisation, a 'destriping' correction to match month 1 and month 2, and an additional phase-depended function (Lucey *et al.,* 2000a), large regions in the north of the picture

still display sharp compositional boundaries along improbable rectilinear areas. This problem will became more apparent when precise and consistent titanium values will be required in order to tabulate and compare data. Despite its limitations, a considerable amount of elemental information can be ascertained from this image (Fig. 4.2).
At first glance, it appears similar to the iron map. Nevertheless, margins are rather less defined, compositional differences between some uplands and maria are less marked, and many new areas have emerged with little or no correlation to the other maps. Moreover, small patches of highland show unusually high titanium levels. The general impression is that low-Ti material extends into areas neighbouring their probable place of origin (typically uplands and buried crustal rocks), confusing the topographical/geological boundaries.

We find examples of high titanium areas within a patch of highland (*o*) south of Bonpland σ (west off the Fra Mauro peninsula coast), in particular, a mare 'bay' west of the high terrain. It appears to correspond (on the true colour image) to a very low albedo, relatively young and smooth terrain area, probably sheltered from low-Ti ejecta from the surrounding upland, or alternatively representing a later, Ti-rich volcanic episode.

In the southeast, the typically low titanium highland materials appear to extend well into the mare basin, either transported from the highlands by impacts and coastal 'erosion' or reflecting the composition of local lava flows.

We find a chemically distinct and well-defined mare terrain southwest of *m* (*p*). This diamond shaped low-Ti area roughly corresponds to a region covered by ejecta, possibly belonging to Bullialdus. It is also possible that we are looking at a distinct effusive phenomenon, which could explain the origin of its sharp boundaries.

Another feature that does not have a compositional equivalent in the iron map is an oval shaped low-Ti area just north of Wolf (*i*). The colour image hints at a possible correlation with a larger darker area south of Fra Mauro, *d*. Indeed these terrains are both dotted with numerous 'green' coloured craters.

Comparison with features noted in the previous images:

1. Small craters are difficult to distinguish from the surrounding mare terrain, suggesting similar titanium content. Larger craters, such as Guericke B and Nicollet, although still similar in brightness to the neighbouring mare, display thin rims with higher Ti fraction. Within the Nubium basin two areas in particular show higher than average titanium content: one is located south of Lassell (h) and the other relates to Tycho's ejecta ray material (j).
2. The highland in the eastern side shows very low titanium content and appears nearly black. However, unlike the evidence from the iron map, the Fra Mauro peninsula materials seem to extend well into the mare in the west (*l*). By comparison, in the colour image this feature appears to correspond to the ejecta material originating from the north of the region, possibly belonging to either Copernicus or to the earlier Imbrium impact. The discrepancy between the Fe and Ti maps may be related to the similarity in titanium content of both Copernicus ejecta and Fra Mauro materials. On the other hand, it is also possible that the iron content of the ejecta materials, albeit still relatively low, would have been higher than Fra Mauro's minerals, hence the sharper boundaries.
3. The highlands at *m* are located in the centre of an area of relatively high titanium regolith, south of Montes Riphaeus. One can speculate that these uplands might have been the focus of some localised igneous activity, post-dating the lower Ti flow centred near *p*.
4. Ghost and flooded craters are not clearly defined in this multispectral image. Only the faintest and slightly brighter outline of the most prominent crater rims are apparent, for instance those of Opelt and Kies. In a few cases, Fe and Ti images offer a different representation of the compositional and geographical distribution of craters' ejecta. For instance, materials from the Euclides impact (west of Montes Riphaeus) can be detected over a large area in the iron map, but they are much more concentrated around the crater rim if we look at the titanium signature. On the other hand, crater Kundt, next to Guericke, has similar Ti and Fe compositional ejecta range. A crater west of Lassell (*h*) offers the opposite example: its impact materials can be detected over a larger area in the titanium map

than the iron map. It is possible that the materials scattered by these three impacts were characterised by different metal ratios in each case.

5. Crater walls also vary in brightness according to the geology of the target area. Generally, they are not as prominent as in the iron map, possibly because titanium concentration is less affected by maturity or because the Fe reflectance characteristics are more sensitive to the change in the crystalline nature of the regolith.
6. There is little variation in the titanium content within Bullialdus crater. Most of the crater floor is covered with very low-Ti material, and the wall only hints to its terraced character that is so prominent on the optical and Fe images. Bullialdus ejecta also show very little Ti variation and rays structure. The implication is again that the metal concentration was uniform within the local mare stratigraphy.
7. The Wolf's crater area (*i*) follows the general titanium concentration trend of the rest of the region. The prominent 'deviated' Bullialdus' ray that featured so prominently in the iron map, cutting straight across the crater edifice, is no longer clearly visible. An oval-shaped feature just north of the crater has emerged by virtue of its low-Ti content and sharp boundaries.
8. The titanium ejecta signature in the region is complex and diverse in character. It appears to vary according to the type, geological target area, and age of the original impact. Generally, fresh craters' ejecta display high(er) titanium content. For instance, Tycho's materials, contribute considerably to the reflectance characteristic of the southern Nubium regolith (which hindered the chemical investigation of this region's soil). Bullialdus ejecta, along with most of the northeastern side of the region, including Mare Cognitum, are characterised by surface materials with intermediate Ti values.
9. Ridges and rilles are features too small to show clear compositional variations in the titanium map.

6.3 Iron Map

The iron map (Fig. 4.3 and Fig. 6.1b) resembles a black and white negative version of the DBA image. In reality, the brightness of each pixel relates to the Fe concentration in the corresponding regolith area (one pixel representing a lunar surface area of 0.169 km^2, with a resolution of ~ 410 m). Nevertheless, there is a correlation between the lower albedo areas and higher Fe values. Fresher regolith, containing higher percentages of crystalline, basaltic material (richer in Fe and Ti), is usually darker and less 'tanned' than mature one.

Maria show higher iron values around the centre of the basins, grading to lower concentrations towards the borders with highlands. This might be partially due to contamination from highlands materials or just reflect the varying composition and maturity of distinct lava flows. Generally, highland materials appear very dark (low iron) in comparison to the average maria basalts.

Ejecta rays from local and distant craters show much more clearly in this image, their lower Fe values contrasting with the older overlaid areas. Copernicus' rays crown the North of the region, still detectable south of Mare Cognitum (a 25° lat 'journey'). Less dramatic, but still prominent are Tycho's ejecta radiating from south of the image (~ 43° S). Ejecta materials from crater Bullialdus dominate and mantle a significant portion of the western basin. The Eratosthenian-age impact crater is younger than most geological features in the region and, together with the later Copernican events, can be used to unravel the history and chronology of basalt flows in the basin.

Comparison with features noted previously in the DBA image:

1. As has been seen, brighter areas (*m, h,* and *k*) contrast vividly with the black/grey overall tone of the region. Many young craters appear as bright dots, implying high Fe values. Some craters (see *j*, *e* and a few more in *l* for instance) are characterised by dark crater rims. These iron-poor ejecta may be representative of the underlying bedrock (assumed to be anortho-

sitic in character), thus allowing the analysis of composition of these rocks, also helping estimate the maximum depth of the maria at the point of impact.

2. Intermediate iron values are typical of both ejecta materials (*f, g*) and most highland shore regions (*n, h,* left of *c*). Highlands appear very dark, and their relatively low-Fe characteristic makes it easier to distinguish them from the maria.
3. Area *m* is unusual in showing a very sharp contrast in composition against the surrounding maria. This upland might represent the remnants of the original anorthositic bedrock or highland.
4. Ghost craters are here more clearly visible (as low albedo areas) than in the DBA image. For instance, the eastern rim of the large flooded crater near Gould (north of *i*), is now clearly discernable from the background. An example of Fe-rich ejecta being caught, focused, and redirected by the upland is represented by one of Bullialdus' rays, cutting across Wolf crater (*i*) and finally fading out towards the south-western end of Nubium. Other examples are the dark 'streaks' north of the upland patches near Darney crater (14.5 S 24.0 W). Interestingly, they display a similar trend to the northern Copernican rays and nearly intersect within Mare Cognitum. Lastly, I located a number of rays (or better, Fe-poorer straight lines) that cannot easily be associated with fresh craters. One prominent example is represented by a long dark linear features originating from the Lassell region (*h*) stretching for many tens of kilometres towards Bullialdus.
5. Crater walls are bright, suggesting freshly exposed components in the regolith.
6. Bullialdus (*f*) appears very dark, displaying a range of grey shades. The crater's centre is almost uniformly dark. Few faint traces of Fe-rich material hint at a very limited presence of freshly exposed slope minerals. The surrounding grey area, representing ejecta, is asymmetrical in appearance (in the north-western section), suggesting either a low angle impact or, more probably, the result of regional igneous activity postdating the crater formation.
7. One of the many differences between the Fe map and the DBA is shown north of the Wolf crater (*i*). On the colour image, we can see a higher al-

bedo circular area, joined to the crater by a narrow southern appendix. This circular feature is invisible on the iron map except for the appendix itself showing very low iron content. Nicollet, a 15 km crater west of Wolf (*j*), displays a circular low-iron band located at some distance from the crater rim. Looking at the topography of the crater, with its rim standing at 1340 meters above the surrounding maria, it can be seen that the Fe-poor ring lies at the bottom of the impact edifice. The iron map suggests that this high-albedo material may represent ejecta from the nearby crater Birt, (~ 12 km diameter) whose rays extend up to Nicollet. It is possible that, at this distance from the impact (~ 95 km away), the ejecta material had lost most of its momentum and could not 'climb' the crater slope, ending up resting at the foot of the slope.

8. For an account of the region's ejecta please refer to this chapter's introduction.
9. Generally, rilles appear bright, possibly due to slumping over the hanging wall (exposing fresher, more crystalline regolith). The Rupes Recta delineates the easternmost margin of the Nubium Basin. The Wall appears disjointed in several sections and the gaps 'infiltrated' by strips of low-Fe highland materials. It is apparent that whatever the nature of this material might be, its deposition postdates the formation of the Rupes itself.

6.4 False Colour (FC) image.

The previous two Fe and Ti maps display information in two dimensions: spatial distribution and reflectance intensity (Fig. 6.1b and Fig. 6.1c). The False Colour image (FC, Fig. 6.1d) adds hue values, related to composition and soil maturity, as a third dimension. Red and blue hues control the overall chromatic character of this composite because: a) two-thirds of the data originate from mutually enhancing ratios of these two colours; b) the actual visible colour of the typical lunar surface falls between these two extremes. The green and yellow colours instead represent the regolith's reflectance strength in the 1000 (or 950) nm wavelength (NIR) against the 750 nm (red). As explained in detail in the previous chapter, a high ratio can be interpreted as representing an area where the NIR reflectance is particularly weak, a diagnostic sign of the presence of pyroxene and olivine.

In order to facilitate the analysis of the FC image I decided to split it back into its three colour (filter) constituents (RGB) (Fig. 6.2). Unsurprisingly there are similarities between the Ti map (Fig. 6.1c) and the blue channel (6.2d), both sharing a common origin in the ratio 415/750 nm. Nevertheless, only the blue image emphasises the Ti-rich rays from Tycho extending into the highlands to the east. In the northwest (*g*), the crater Lalande displays a set of very bright (i.e. very 'blue') ejecta rays. Overall, the blue channel, with its improved definition, offers the opportunity of fine-tuning the mapping of potential lava flows, especially in those marginal regions close to the mare/highland borders, (e.g. *n*, figure 6.1a).

The red channel map (6.2b) highlands appear very bright because of the presence of a high fraction of agglutinates in the regolith. Within the maria, dark mantling units may also appear bright, because of their high-Fe mineral content. The reddest areas in the image are the uplands *h* and *n*, the southern section of Monte Riphaeus, the maria bordering the lower western coastline of the Fra Mauro peninsula, Bullialdus' crater floor, and the 'horse-shoe' maria *d* into *e*.

The green channel (6.2c) image helped clarify a few unresolved unit flow boundaries, albeit raising a few new questions, for example: why are some craters very blue and others very 'green'? Why does the Fra Mauro peninsula seem to 'fade' into the maria? Why do most craters display 'dark' crater floors, except for Bullialdus and Lalande?

In more detail:

1. In essence, the FC image colour patterns are comparable to the albedo variations of the titanium image. Differences in colour relate to the chemical make up of the regolith: reds to mature and Fe-rich units, mainly uplands and possible volcanic centres; oranges (*l,* and *d)* to the optical expression of a mixture of iron rich (and Ti-poor) soils (similar in tone to the highlands) and a high-density of 'green' craters; blues are the signature of immature and/or Ti-rich soils.

2. The brightest areas in the blue channel are associated to high-Ti regolith units (i.e. *c*), Tycho's ejecta rays (*k*), and Campanus (a6, Fig. 5.1) crater floor.
3. Area *m* holds the reddest units in the map. Only area *h* displays a similar monochromatic intensity.
4. The green channel highlights numerous high-clinopyroxene (cpx) craters and associated ejecta. This reflectance pattern might relate to the chemical signature of either a fresh crater or/and one that has excavated materials from the crystalline bedrock. Four small craters, one north of Lalande (e1), one north of Pitatus (c6), one west of Lassell (d3), and another one east of Lubiniezky (b4) are good examples of this type of excavation.
5. Crater walls are mostly blue/green in character. Some craters, such as crater Birt (e5), are very bright in the colour composite (and in particular the blue/green channels). Nicollet (d5), a similar sized crater on its left, instead appears just as a bright ring, suggesting a flat (filled) crater floor. I interpret this as Birt being somewhat younger; alternatively, Nicollet might have been affected by a different, and more invasive, effusive regime.
6. Crater Bullialdus (*f*) has been extensively studied (e.g.: Tompkins *et al.*, 1994; Pieters 1991) because of its unusual wall and peak stratigraphy. The FC image shows the crater in all its geological complexity: the light blue 'undulated' crater rim; Tycho's 'blue' ejecta ray being funnelled over the north-westerly flank and spilling over the crater rim; the bright red crater floor, similar in colour to parts of the region's highland; the green/yellow central peak, appearing very bright on the green channel. A full geological investigation and interpretation of Bullialdus' genesis and evolution is not among the aims of this work. Nevertheless, one can describe the crater floor as being Fe-rich and mature, lying undisturbed by successive, regional maria phenomena. At this spatial and spectroscopic resolution, Bullialdus' central peak (or geologically distinct peaks, according to Tompkins *et al.*, 1994) appears distinctively enriched in cpx (and also Ti-poor).
7. Wolf's spectral signature is typical of old upland (impact) edifices, red and degraded. More interesting, the oval shaped feature north of the crater (*i*) shows up bright red in the FC image, in sharp contrast to the surrounding

mare. Chemically it is virtually indistinguishable from the 'horseshoe' shaped maria unit south of Fra Mauro peninsula. I suspect that these areas share similar geological histories, but they have become physically separated by either later basaltic flows and/or 'optically', by fresh crater ejecta (mainly from Gould, 4c). A cluster of bright green materials can be seen in the northwestern part of the oval.

8. The red channel shows how extensive is the influence of ejecta on the optical properties of the region. Ejecta rays, appearing bluer than the average soil, criss-cross the whole image. As expected, the green map does not show any ray structures. Tycho's ejecta is very prominent and bright in the blue map, somewhat masking the chemical signature of the underlying regolith in the southern Nubium. Because of this, the mapping of distinct possible unit flows in this region has been more difficult and tentative.
9. I found the green channel of the FC map to be the best Clementine image for mapping rilles and ridges. Rupes Recta, a 120 km long scarp (*n*), described first in this work in the DBA section, shows very interesting cpx-rich head and tail depressions. These could have been the sites of later extrusive phenomena, forming volcanic craters. The wall itself is bright and shows well in both the blue and green filters. I also note, for the first time in this study, two potential domes that have rarely been seen from Earth, located on the northern end of the Rima Birt rille. The hypothesis of a volcanic origin is suggested by the bright red colour of the surrounding area, a sign of possible pyroclastic materials. Wrinkle ridges are also very prominent at this wavelength, for instance around and within *i* and north of Nicollet (5d). One interesting feature within *d* (4d) is the pattern of around seven bright, 'green' spots, arranged in a linear fashion. It might be the remnant of effusive phenomena along a lava channel.

Figure 6.1. Comparisons between DBA, Fe, Ti, and False Colour images:

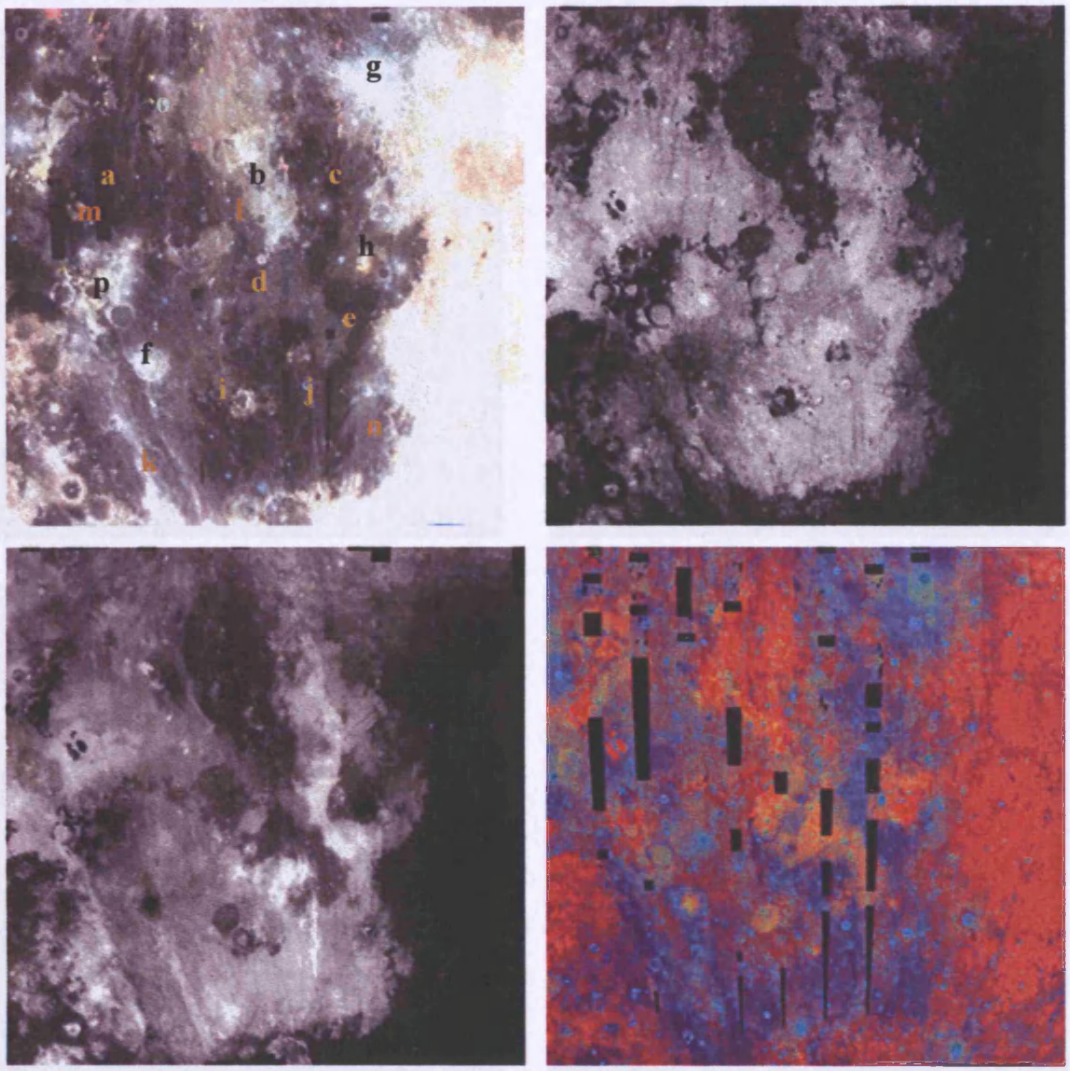

Legend:

DBA (a)	**Fe** (b)
Ti (c)	**FC** (d)

Figure 6.2. False Colour map (FC) and RGB split constituents.

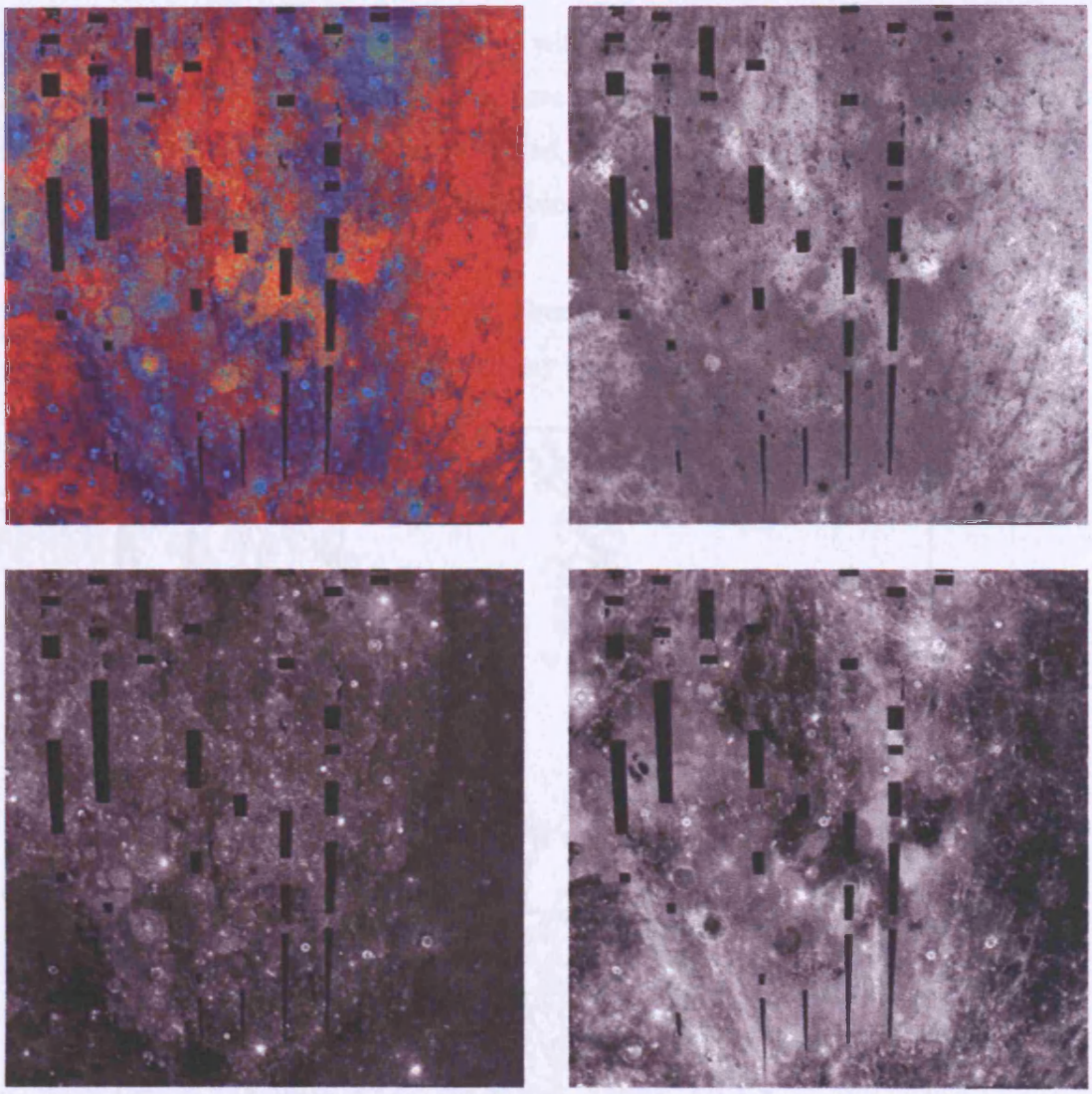

Legend:

FC (a)	**Red** (b)
Green (c)	**Blue** (d)

The 'true' and false colour images, along with the titanium and iron maps, were processed, resized, and printed out as square reproductions of 60.57 cm sides (a scale of 1:1,500,000). I also scanned, scaled, mosaicked, and printed Orbiter IV photographs[1] to match as closely as possible the Clementine maps.

I used tracing paper to sketch albedo and hue differences as possibly distinctive geological flow units. **Figure 7.1** shows my initial map:

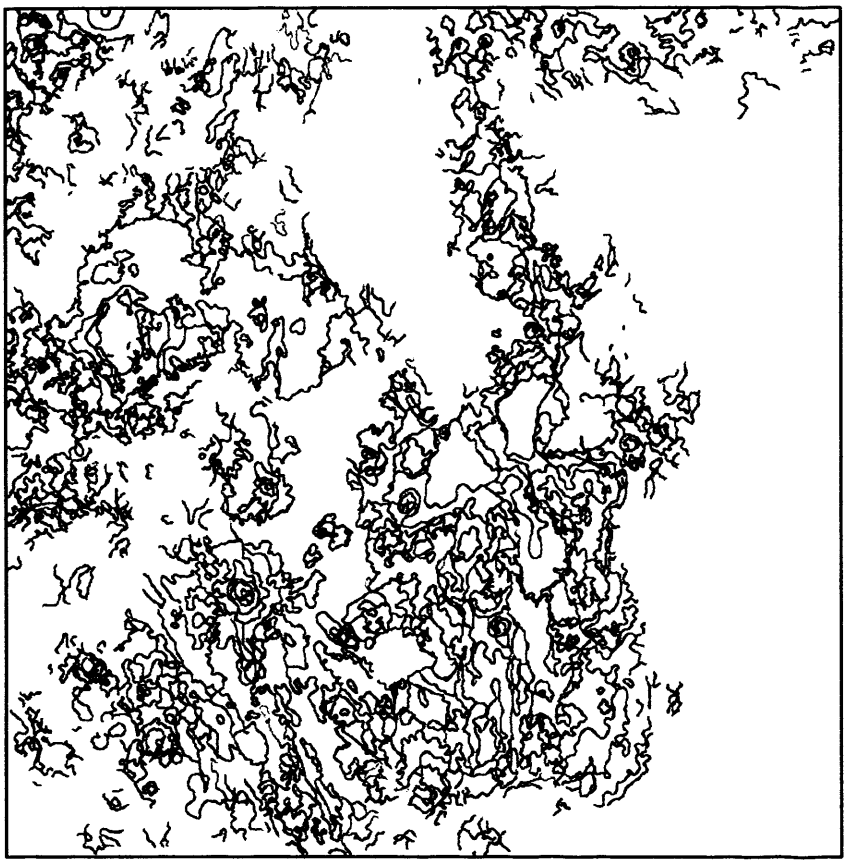

Each time I superimposed the tracing paper onto a different image, more elements were added to the emerging geological map. Toward the end of this task, I noticed an obvious excess of detail and redundancy in the geological data. I then scanned and imported the sketch map into image-manipulation software for further comparisons, enhancements and, ultimately, simplification.

[1] From East to West, Orbiter IV images numbers: 132, 125, 120, 108, and 113. Each number is divided into H1, H2, and H3 subsets.

Two new images were derived from the titanium and iron maps (Figs. 7.2a and 7.2b). I produced these maps by assigning arbitrary colours to spectrum brightness variations. The aim was not to produce a quantitatively accurate or absolute representation of chemical composition of the maria, but a map highlighting differences and similarities in the reflectance characteristics of the regolith: at this stage of my research, it is of little importance or meaning to assign absolute colour values. Figure 7.2a highlights areas of contrasting iron composition. Colours range from blue (very low Fe), through green, yellow, crimson, up to dark red, which represents areas with the highest iron content (*e, h, m,* and *p*, ref. Figure 6.1a). Figure 7.2b shows albedo differences using a complete different palette of colours. This time low-Ti areas appear purple/pink and, at the other extreme, dark green (*e, h, m, j,* and *p*).

Tracing colour boundaries produced unit outlines for each image (Figures 7.3a and 7.3b). As one can see, many areas share similar outlines in both images, but still in a way that makes it rather confusing to combine into a global unit map. In trying to facilitate my task I used standard image processing techniques to produce images that take into account both compositional characteristics.
The two False Colour (FC) maps 7.2a and 7.2b were 'blended' according to arbitrarily chosen parameters, aimed to further enhance colour differences. Using a technique called 'screening', where the two-colour channels information are first inverted and then multiplied together, produced Figure 7.2c. The colours of image 7.2d instead are the result of comparing pixel values from each of the metal images and displaying only the lower albedo ones. Both images were then further blended and manipulated to produce the final false-colour image Figure 7.2e. This map helps redefining potentially related and/or distinct geological units.

All these techniques led to a final unit contour map. I superimposed this onto the original Fe (Fig. 7.3c) and Ti (Fig. 7.3d) maps as a demonstration of their common relevance.

Figure 7.4 represents the resulting map of potential unit flows, numbered accordingly to a random sampling sequence (see following chapter). Also displayed are:

uplands (black), major craters (dark-grey circles), and ejecta blankets (grey). The geology of the greyed-out terrain west of units 72 and 73 will be discussed at a later stage.

Table 7.1 lists the main local geographical features of each unit and their surface area.

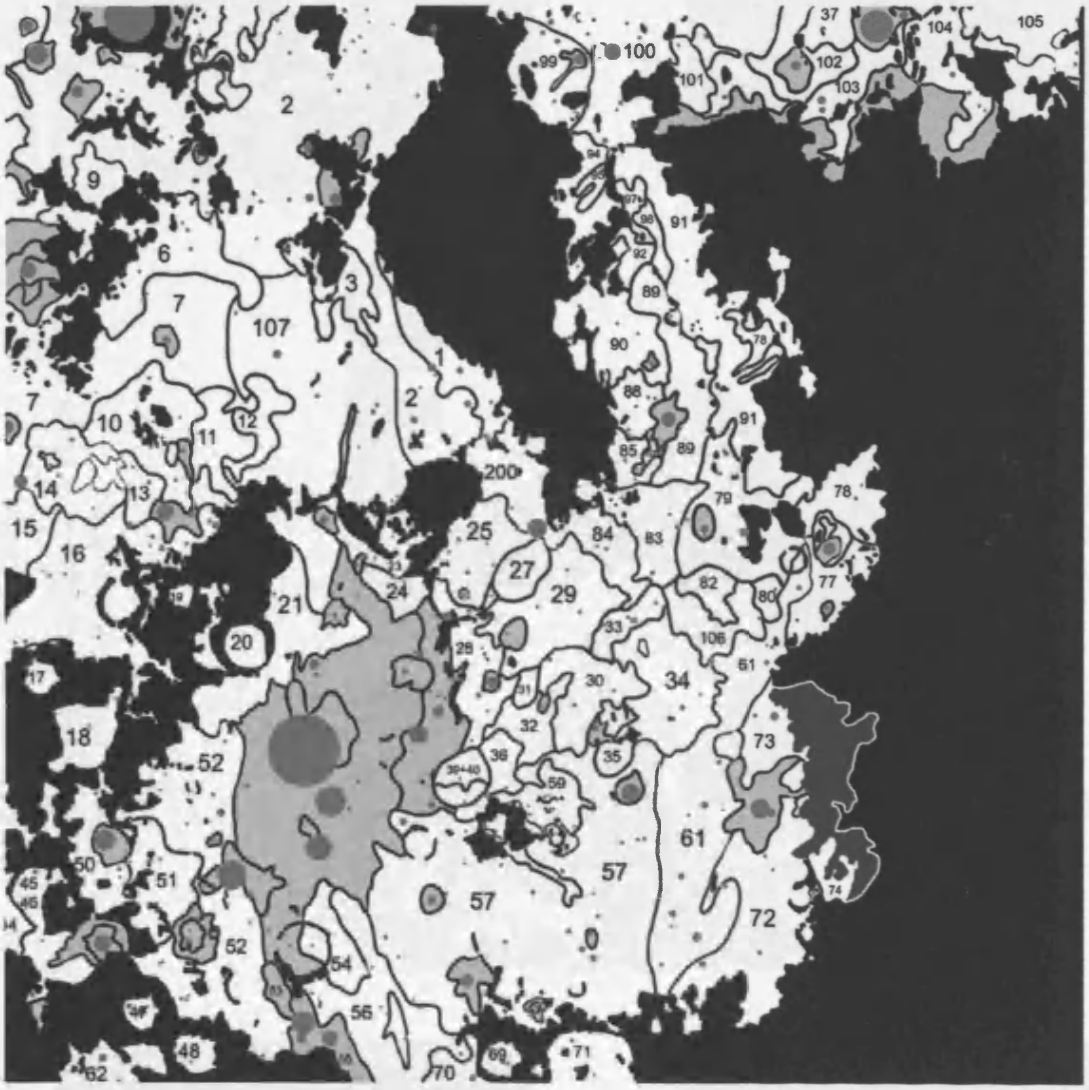

Figure 7.4. Final map of potential unit flows

FeO - albedo colours a)

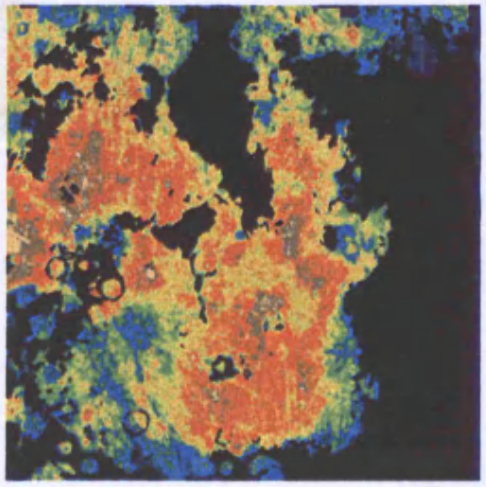

TiO_2 – albedo colours b)

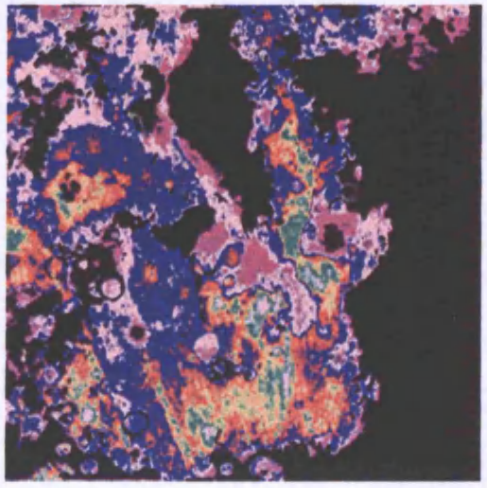

Figure 7.2. Computer-generated colour maps highlighting compositional differences.

Final albedo combination e)

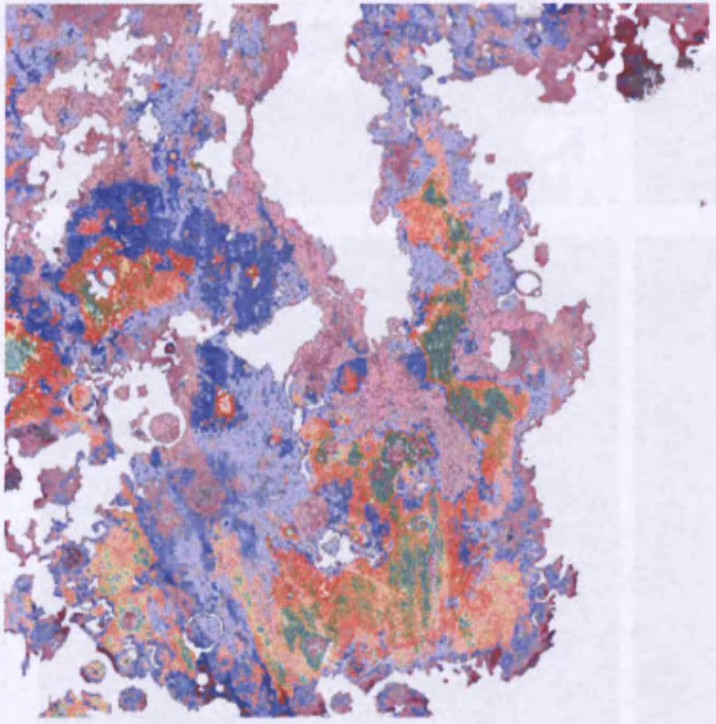

Combination – 'Screen' c)

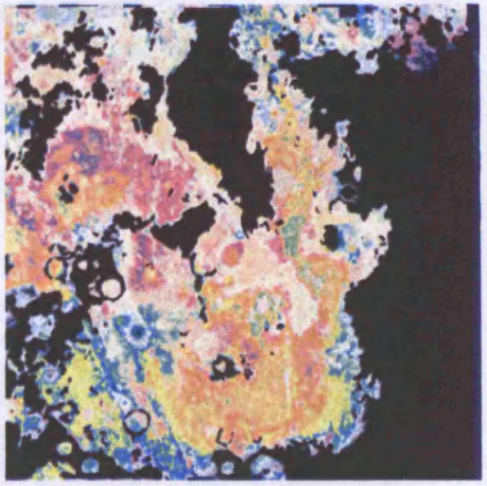

Combination – 'Darken' d)

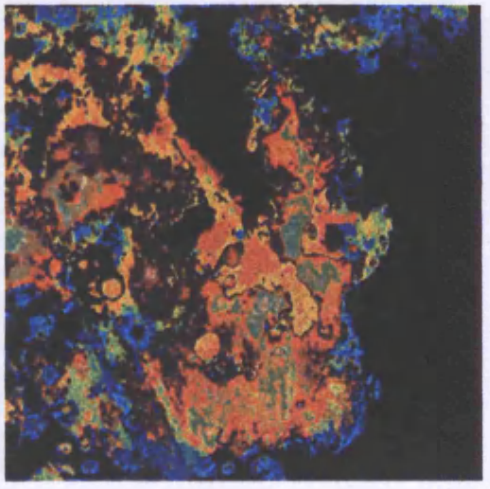

Figure 7.3. Proposed individual and combined units' outlines.

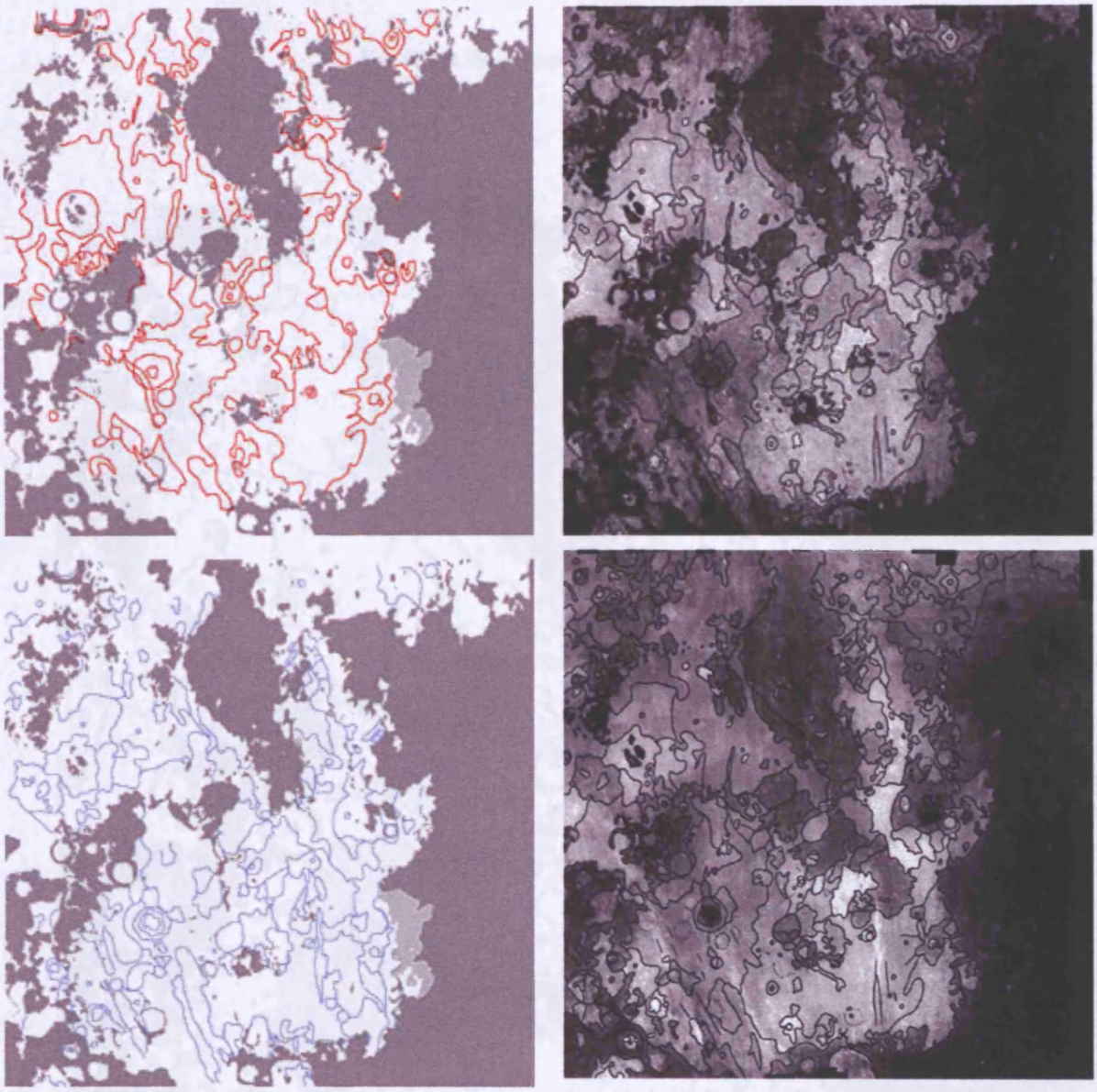

Fe (a) Units outline	**Fe** (c) Combined units outline on Fe map
Ti (b) Units outline	**Ti** (d) Combined units outline on Ti map

Figure 7.4. Final map of potential unit flows.

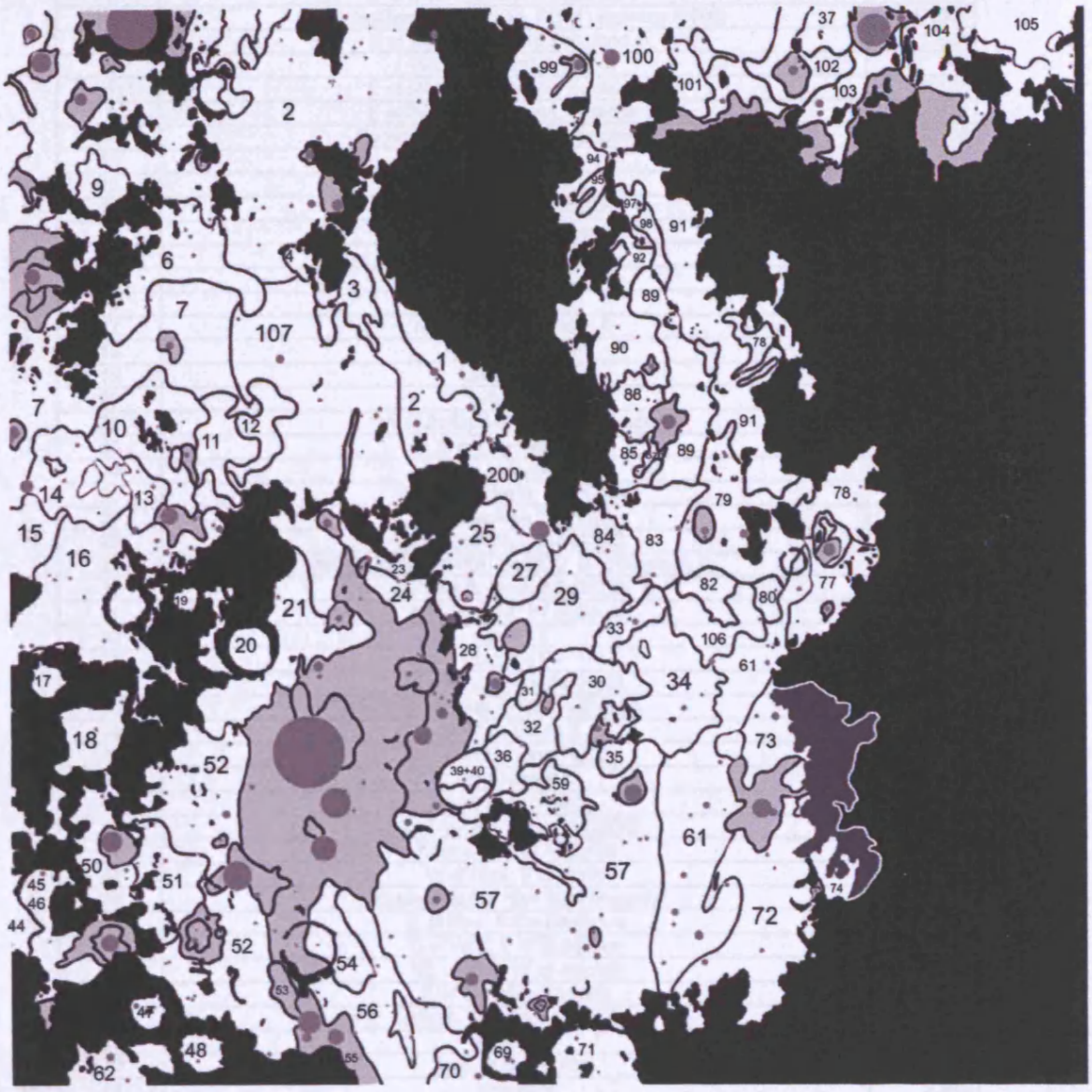

Table 7.1. list of classified flows units including major features and areas

Flow #	**Location - craters, uplands** (elevation in m)	**Area** km^2
1	S Guericke A. N Bonpland F.	3,126
2	Large Northwestern region, SE of Lansberg (4600)	47,609
3	E of Bonpland s and Bonpland m.	1,683
4	W of Bonpland s (3640)	745
6	E of Montes Riphaeus, Euclides E	6,108
7	E of Montes Riphaeus, Euclides D	13,431
9	Euclides P 'basin' (2700). Euclides d.	2,355
10	*Darney c - n.*	4,877
11	E of Dorney E	2,430
12	S of Bonpland E (4000)	1,748
13	N of Dorney D. Dorney F.	1,221
14	Euclides C, CB, and G	4,218
15	S of Euclides C.	1,989
16	Lubiniezky E	11,787
17	NW of Anatharchides P	658
18	Agatharchides P	2,640
19	Lubiniezky A	322
20	Lubiniezky	2,253
21	NW of Bullialdus, SE of Lubiniezky	5,926
23	N of Lubiniezky G	1,626
24	S of Luniezky G	1,267
25	SE f Guericke B. N of Opelt.	3,845
27	S of Guericke B (2880).	1,528
28	Gould (3330), Opelt (4300).	3,384
29	NE of Gould P (900). Gould U. S of Guericke P.	5,929
30	Nicollet B. Lassell E (2620).	3,812
31	W of Gould Z, W of Gould	434
32	Gould Z	1,882
33	Lassell F.	1,378
34	*Nicollet y. Lassell E (550).*	6,021
35	N of Nicollet (2490). Nicollet q.	676
36	Wolf S. Gould X.	1,169
37	S of Sommering	1,418
44	W of Hippalus	751
48	Mercator (3900)	930
50	W of Agatharchides A (2300)	2,845
51	Agatharchides A (2300)	3,506
52	W of Kies, S of Konic	7,634
54	Eastern half of Kies (and beyond)	2,386
56	S of Kies, Rima Hesiodus	7,319
57	S of Wolf, E of Bullialdus	35,251
59	NE of Wolf, W of Nicolett	2,182
61	E of Birt, W of Nicolett	14,105
62	Marth, Mercator A (2870)	2,253
69	Hesiodus	718
70	Hesodius A (2700)	1,258
71	Hesodius	2,988
72	W of Lippershey, S of Birt	10,415
73	N of Birt, Rupes Recta, S of Promontorium Taenarium	2,321
74	E of Rupes Recta	1,039
77	E of Lassell	2,706
78	W of Alphonsus	2,929
79	W of Lassell (4670). C (4300). G (1710). K (530). Lassel H.	6,055
83	N Guericke. S Lassell F (2400). Guericke C	3,945
84	E Guericke B (950). Guericke D12K	2,777
85	Guerike M.	1,086
86	Guerike C	194

88	E of Kundt (3290). S off Guericke E.	1,516
89	E of Guericke C (Kundt, 3290). W of Guericke x. Highest Lat. ~7 S.	4,770
90	W of Parry, M, C, K, and E.	4,949
91	Long area bordering with higland to the East. S of Lalande. N of Palisa	9,465
92	N of Parvy C. W of Lalande i.	738
94	S of Turner x	2,231
95	W of higland peaks, S of Turner x	385
99	Turner (3100)	3,497
100	E of Turner, N of Lalande	12,195
101	W of Turner B	1,745
102	Lalande	2,404
103	S of Mosting	2,373
104	N of Rima Flammarion	1,871
105	E of Mosting	8,995
106	N of Lassell F.	2,581
107	Large central area of Mare Cognitum	20,616
200	S of Guericke	3,454
39+40	N of Wolf A (750) and Wolf B. E of Wolf S.	1,434
45+46	W of Hippalus	2,557
80+82	S of Lassell (4670). Lassell B, T. Rima Lassell I.	1,801
97+98	E of Lalande h (3850).	1,185
	Total mapped mare surface km² (~43% of total image surface, or ~65% of non-upland terrain))	**357,850**
	Total sampled surface area km²	825,554

CHAPTER 8 DETERMINATION OF FeO AND TiO_2 WEIGHT PERCENTAGE FOR EACH AREA

MARE NUBIUM AND MARE COGNITUM

8.1 Method

Each cube image holds multi-layered information on every individual pixel, including its absolute location, displayed as lunar coordinates, and the appropriate metal's reflectance value, expressed in percentage weight. One pixel represents the average reflectance intensity of an area of approximately 168,800 m^2, translating into an average image resolution of 411 m.

As discussed in the previous chapter, I divided the Nubium/Cognitum mare into 105 distinct compositional areas. For each unit, I took twelve spatially random readings of both FeO and TiO_2 weight percentage values. For some larger areas, such as 2 and 57 (Fig. 7.4), it was necessary to double the number of sample points.

Table 8.1, shown as an example, displays the data gathered for unit 1. The iron and titanium maps were linked and synchronised (with a pixel-to-pixel accuracy) in order to obtain spatially coherent sample points. My first sampled area (pixel) gave readings of 19.79 FeO wt% and 1.17 TiO_2 wt%. After every twelve samples, I calculated both the average mean (yellow row) and *standard deviation* (pink row, relating to the gathered samples, and *not* system uncertainties) for each metal in the given unit.

1 FeO wt%	1 TiO_2 wt%
19.79	1.17
17.74	1.47
17.72	1.56
18.99	1.45
19.06	1.25
18.54	1.51
19.04	0.72
18.10	1.71
18.31	1.37
19.46	0.83
19.57	1.16
18.76	0.94
18.76	**1.26**
0.69	**0.31**

Table 8.1. Example of randomly chosen chemical values for sampled unit.

8.2 Results

Table 8.2 lists the results for all units. Typical mare basalts have an average iron* composition between 14 and 20 percent (Lucey *et al.*, 1995). Shkuratov *et al.* (1999) published new global titanium* data for the lunar nearside showing TiO_2 abundances in the range of 1.3 to 6 percent.
My results broadly agree with these estimates: most mare surfaces displayed a FeO and TiO_2 compositions between 18 and 21 percent and between 2 and 5 percent, respectively.

The highest and lowest values for the metals' abundances were found in areas 104 (13.5 %) and 15 (21.9 %) in relation to iron, and in areas 1 (1.3 %) and 106 (5.1 %) to titanium. The arithmetic mean of the standard deviations for all sampled units was 0.27 % TiO_2 and 0.34 % FeO.

Table 8.3.

FeO wt%	Surface km^2
14-15	4547
15-16	10965
16-17	7884
17-18	21716
18-19	35510
19-20	118592
20-21	131638
21-22	26998

Table 8.4.

TiO_2 wt%	Surface km^2
1.5-2.0	26260
2.0-2.5	26482
2.5-3.0	26939
3.0-3.5	104443
3.5-4.0	101327
4.0-4.5	56012
4.5-5.0	16287

Tables 8.3 and 8.4 list the compositional area distribution of each metal in the mare within the studied region and Figures 8.1 and 8.2 are graphical representations of the same data. Figure 8.3 shows most of the maria's iron content (90%) to range between 18 and 22%. Figure 8.5 further simplifies and groups FeO data into four compositional families. Figure 8.1 suggests two general compositional trends for the basalts: a major mafic family containing on average 20% iron, and a much smaller minor one averaging 15% FeO.

* When 'iron and titanium content' terms are used in this research, it always refers to their oxidized compounds (FeO and TiO_2). Native iron is described as Fe^0.

TiO_2 content variations are geographically more evenly distributed. Figure 8.4 shows that 73 % of the mare has a titanium content between 3.0 and 4.5 %. Figure 8.6 merges these data into four ranges, clearly showing the territorial predominance of soils with titanium abundances between 3.0 and 4.0 %. There is a suggestion that we are looking again at two different types of basalts (Fig. 8.2), one with compositions averaging 2.3 wt % TiO_2, and the most widespread type containing a higher percentage of titanium (with an average of 3.5 % titanium).

Table 8.2. Classification of proposed areas according to Fe/Ti average content

Area #	TiO_2 wt%	Ti group	FeO wt%	Fe group
1	1.3	a	18.8	e
3	1.5	a	18.6	e
29	1.6	a	19.3	e
104	1.6	a	13.5	d
79	1.8	a	18.3	e
25	2.0	a	19.7	e
103	2.0	a	17.8	d
33	2.0	a	19.2	e
17	2.1	a	15.7	d
105	2.1	a	17.9	d
19	2.2	a	19.5	e
78	2.2	a	17.5	d
39+40	2.2	a	19.8	e
85	2.2	a	20.3	f
200	2.2	a	19.4	e
70	2.3	a	14.5	d
69	2.4	a	16.3	d
18	2.4	a	16.8	d
71	2.4	a	15.1	d
6	2.5	a	20.3	f
20	2.6	a	19.7	e
95	2.6	a	18.9	e
35	2.6	a	19.9	f
74	2.6	a	16.7	d
44	2.7	a	19.1	e
102	2.8	a	20.4	f
24	2.8	a	20.0	f
9	2.8	a	20.2	f
77	2.8	a	18.5	e
14	2.8	a	20.6	f
84	2.9	a	20.2	f
37	3.0	b	14.6	d
34	3.0	b	19.4	e
36	3.0	b	20.2	f
23	3.0	b	19.8	e
92	3.0	b	19.5	e
99	3.1	b	19.6	e
48	3.1	b	16.4	d
94	3.1	b	19.8	e
101	3.1	b	20.4	f
73	3.1	b	17.4	d
88	3.1	b	19.0	e
54	3.1	b	19.5	e
50	3.3	b	17.4	d
90	3.3	b	19.9	f
27	3.3	b	20.8	f
45+46	3.3	b	16.5	d
2	3.3	b	19.9	f
21	3.4	b	20.5	f
7	3.4	b	20.8	f
56	3.5	b	15.7	d
91	3.6	b	19.6	e
12	3.6	b	19.8	e
80+82	3.6	b	20.3	f
16	3.6	b	20.8	f
107	3.6	b	20.9	f
28	3.6	b	19.8	e
100	3.8	b	19.6	e
11	3.9	c	21.3	f
10	3.9	c	21.2	f
97+98	3.9	c	19.7	e

61	3.9	c	20.5	f
72	3.9	c	18.2	e
52	4.0	c	18.0	e
32	4.0	c	20.2	f
62	4.0	c	17.7	d
51	4.0	c	18.8	e
59	4.0	c	20.3	f
13	4.1	c	21.3	f
86	4.1	c	21.6	f
57	4.4	c	20.3	f
15	4.4	c	21.9	f
4	4.6	c	21.4	f
83	4.7	c	21.5	f
30	4.7	c	21.6	f
31	4.7	c	21.0	f
89	4.8	c	21.1	f
106	5.1	c	21.2	f

Figure 8.1

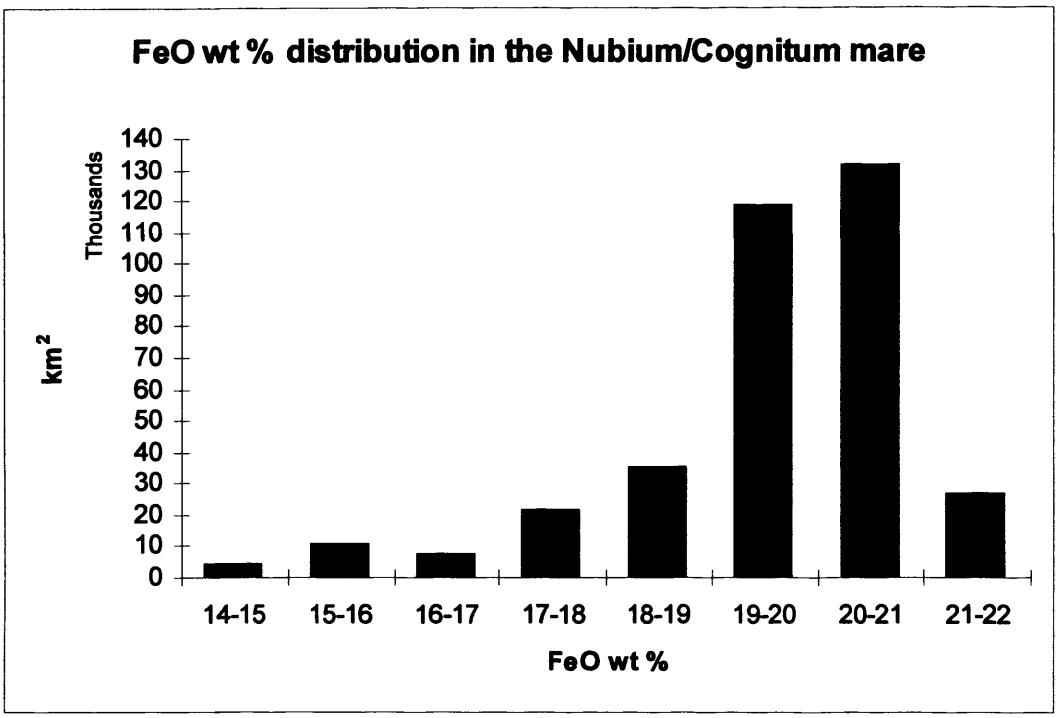

Figure 8.2

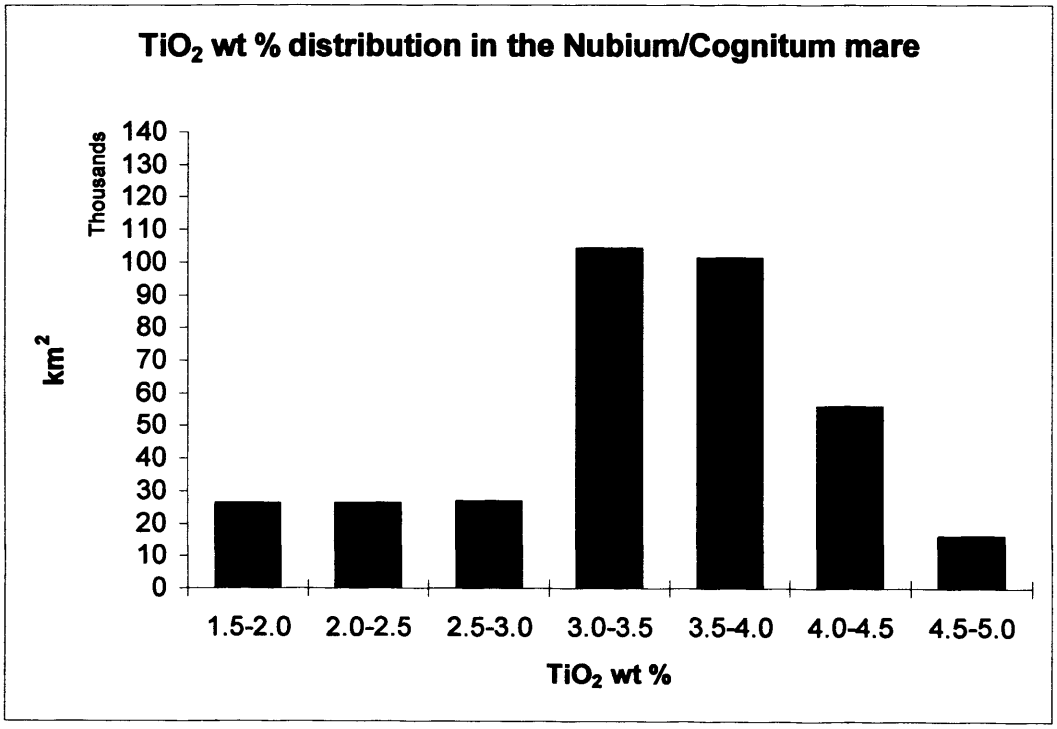

Figure 8.3. Percentage distribution of FeO in the Nubium/Cognitum mare

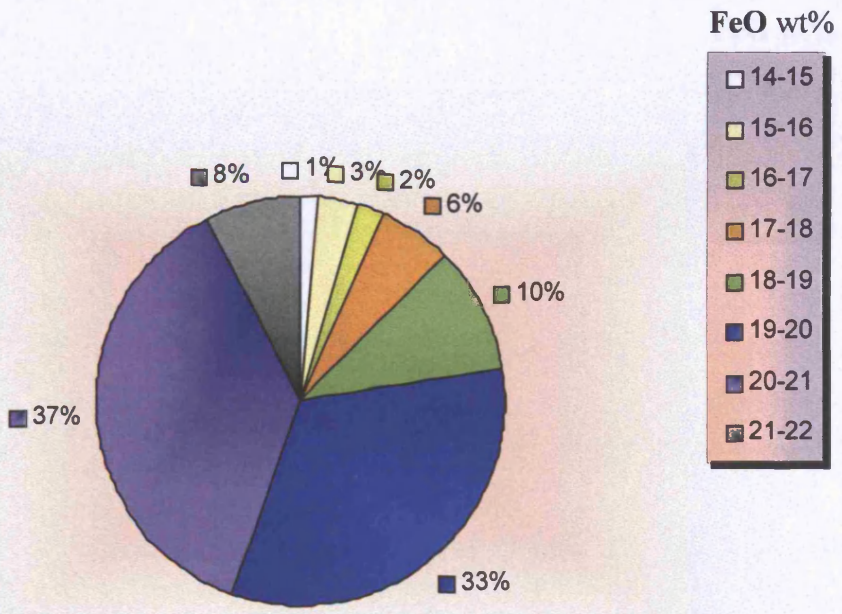

Figure 8.4. Percentage distribution of TiO_2 in the Nubium/Cognitum mare

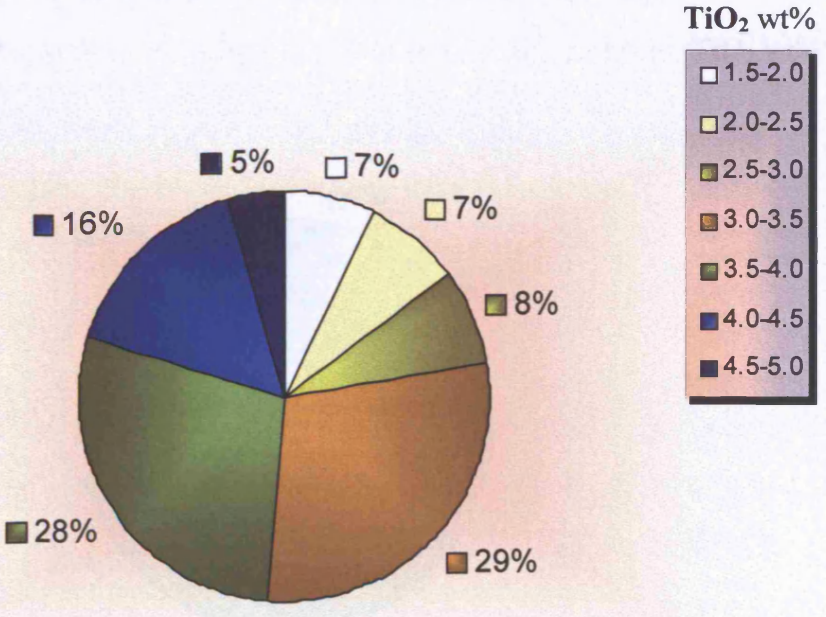

Figure 8.5. Grouped percentage distribution of FeO in the Nubium/Cognitum mare

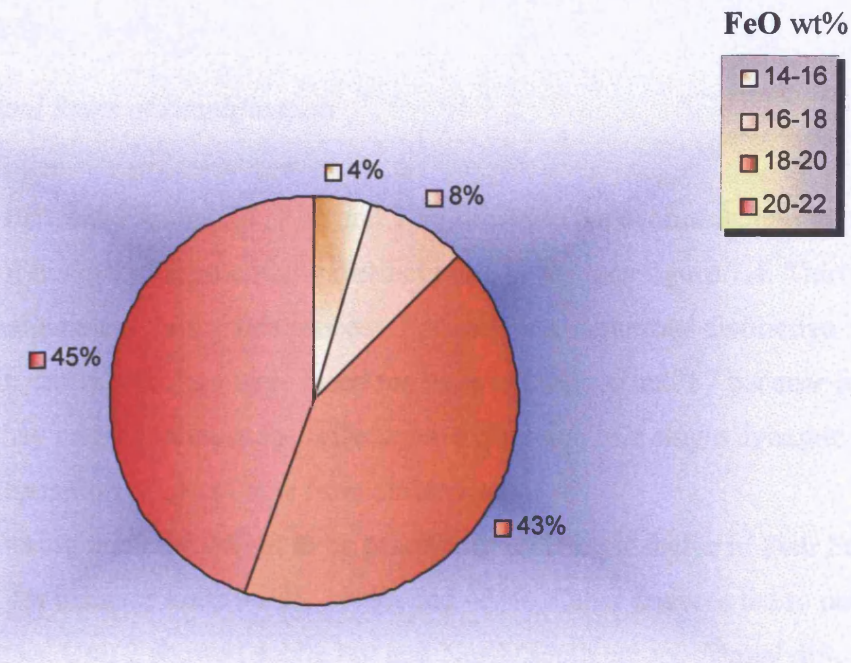

Figure 8.6. Grouped percentage distribution of TiO_2 in the Nubium/Cognitum mare

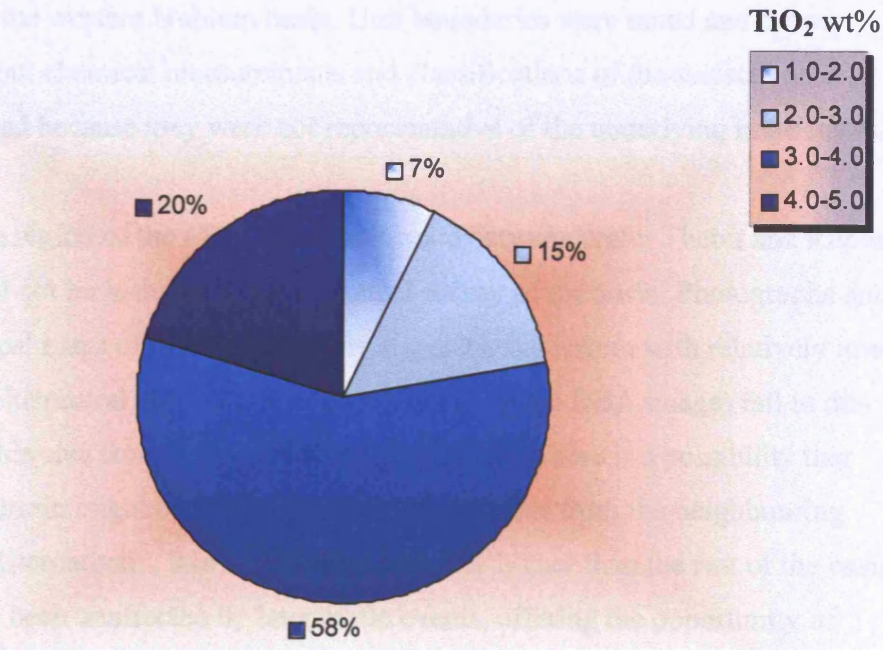

CHAPTER 9 FURTHER COMPARING AND MERGING OF ADJACENT AREAS WITH SIMILAR CHEMICAL SIGNATURE
MARE NUBIUM AND MARE COGNITUM

9.1 Methods and Rules of simplification

Comparisons between Figures 7.1, 7.3c and 7.3d illustrate the evolution, trimming and merging of hundreds of potentially distinct units to produce figure 7.4. Thirty units were amalgamated during this process. For instance, numerous distinctive features within central Nubium were fused together to produce unit 57 because it was felt that they might represent the reflectance expression of a single dynamic process: the deposition of ejecta rays from crater Tycho.
Some neighbouring units turned out to be practically indistinguishable in their Fe-Ti signatures, for instance units 94/95, 39/40, and 45/46. Other features led to new unit subdivisions. Unit 2 showed subtle but real North/South compositional differences; I split it and created a new southern unit 107.
Large areas are blanket over by the ejecta of impact craters. These are the greyed-out units surrounding some large and/or fresh craters. Examples are units 53 and 55 in the South. The ejecta blanketed of Bullialdus crater overlays a significant fraction of the western Nubium basin. Unit boundaries were noted and drawn (Fig. 7.4), but chemical measurements and classifications of the surface material were avoided because they were not representative of the underlying mare flows.

The eastern region of the Mare Nubium located between crater Thebit and Rupes Recta could not be included in the chemical survey of the basin. Photographs and topographical maps of the region clearly suggest a flat terrain with relatively low albedo. Multispectral Clementine images (including the DBA image) fail to differentiate this area from the neighbouring highlands. There is a possibility that this mare terrain might be contaminated with materials from the neighbouring highland. Alternatively, this area, topographically higher than the rest of the basin, might have been unaffected by later mafic events, offering the opportunity of sampling some of the oldest basaltic materials to be observable within the basin.

9.2 Production of abundances maps

I produced preliminary compositional abundances maps based on the gathered data relating to each potential flow units. Figure 9.1 shows FeO average abundances as shades of red (darker = higher abundance). Figure 9.2 represents TiO_2 variations as intensity of colour blue (again, the darker the higher abundance). These maps offer only a qualitative geographical representation of the relative abundances distribution.

9.3 Further grouping and analysis

Comparing and grouping differences in compositions into nine distinctive geochemical 'families' produced Figure 9.3 (based on data from Table 8.2). It is important to stress that when I refer in this work to 'high-Ti' or 'low-Fe' units, it is meant in comparison to the local maria compositional average (please refer to the previous chapter and to Figures 8.1 to 8.6) and not the overall lunar values and official classifications.

I used RGB colours to differentiate between titanium abundances (three categories, 1.3-2.9, 3.0-3.9, and 4.0-5.1 wt %) and colour intensity (hue) for iron (three subdivisions within each titanium group: 13.5-17.9, 18.0-19.9, and 20.0-21.9 wt %). Once again, these families were arbitrarily chosen and they relate only to the local chemical signature of the mare regolith. Nevertheless, the average Ti and Fe composition of the basins (titanium ~3.5 % and iron ~19.0 %) are typical of near-side lunar maria (see previous chapter).

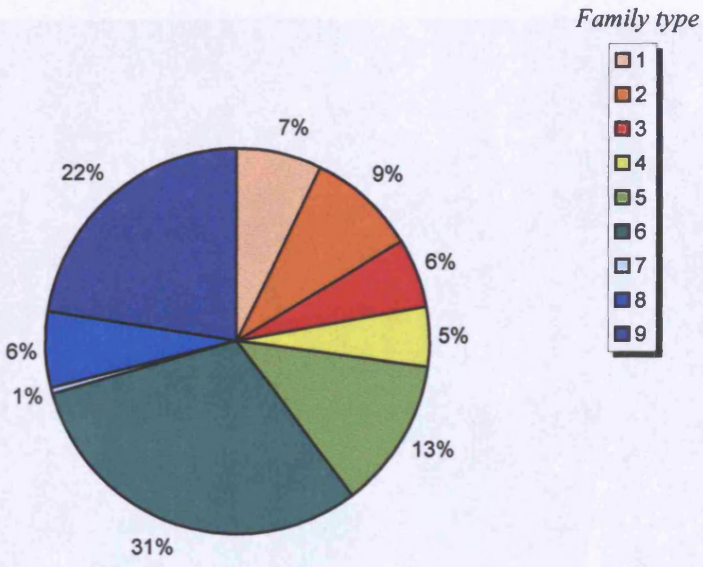

Figure 9.4. Geographical percentage distribution of each family type

Figure 9.4 shows the geographical percentage distribution of each family type (refer to Table 9.1).

Figure 9.5 is a modified version of Figure 9.3. Here neighbouring units with similar Fe and Ti values have been merged to produce a simplified map of chemical abundances. The map suggests a general compositional dichotomy between the north and the south. Mare Nubium materials are somewhat more titanium-rich (and probably more crystalline) than those in the north. In addition, in the south, maria units bordering with the highlands are generally poorer in iron than those further away, a pattern that is not repeated in the northern regions.

A few areas stand out as compositionally distinct: Montes Raphaeus (a2 on the grid map, refer to Figure 5.1) are surrounded by a low-Ti high-Fe type of material that appears different from that of the neighbouring maria. A narrow strip of Fe- and Ti-rich material (9e) runs between the Fra-Mauro peninsula and the highlands to the east. Maria with very low titanium and iron composition (2a) surround the southwestern shores of the Fra-Mauro peninsula extending and expanding towards the centre of the basin.

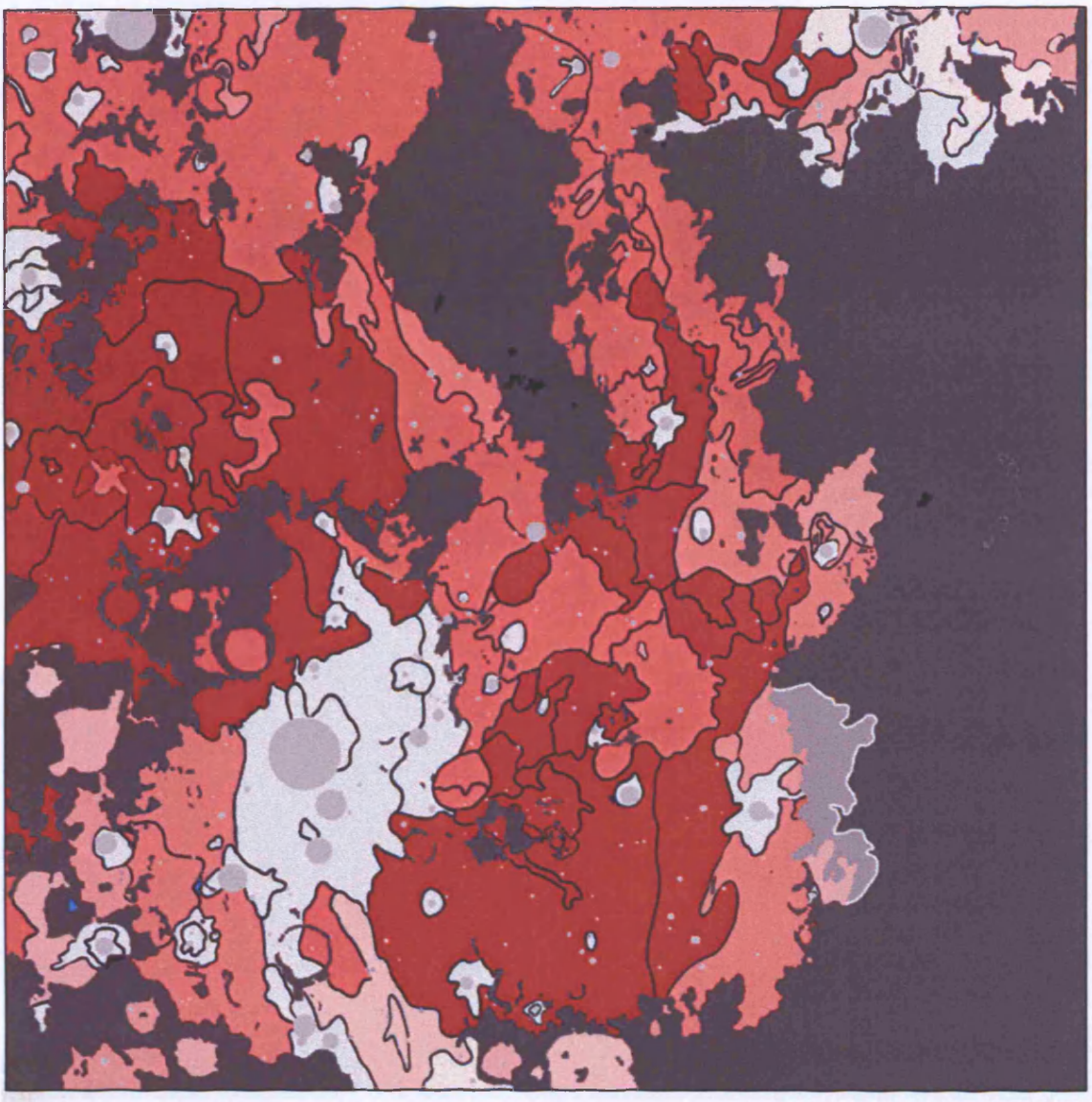

Figure 9.1. Intensity of red indicates FeO average abundance on given unit.

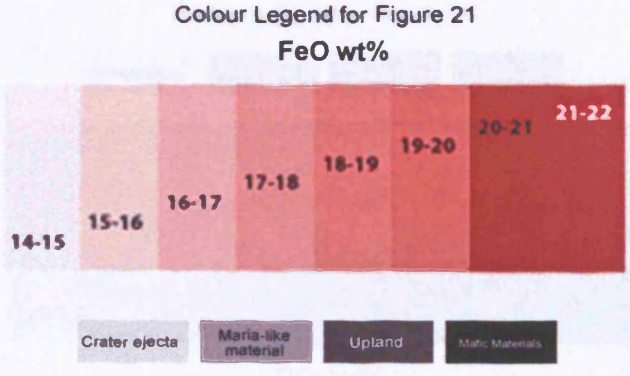

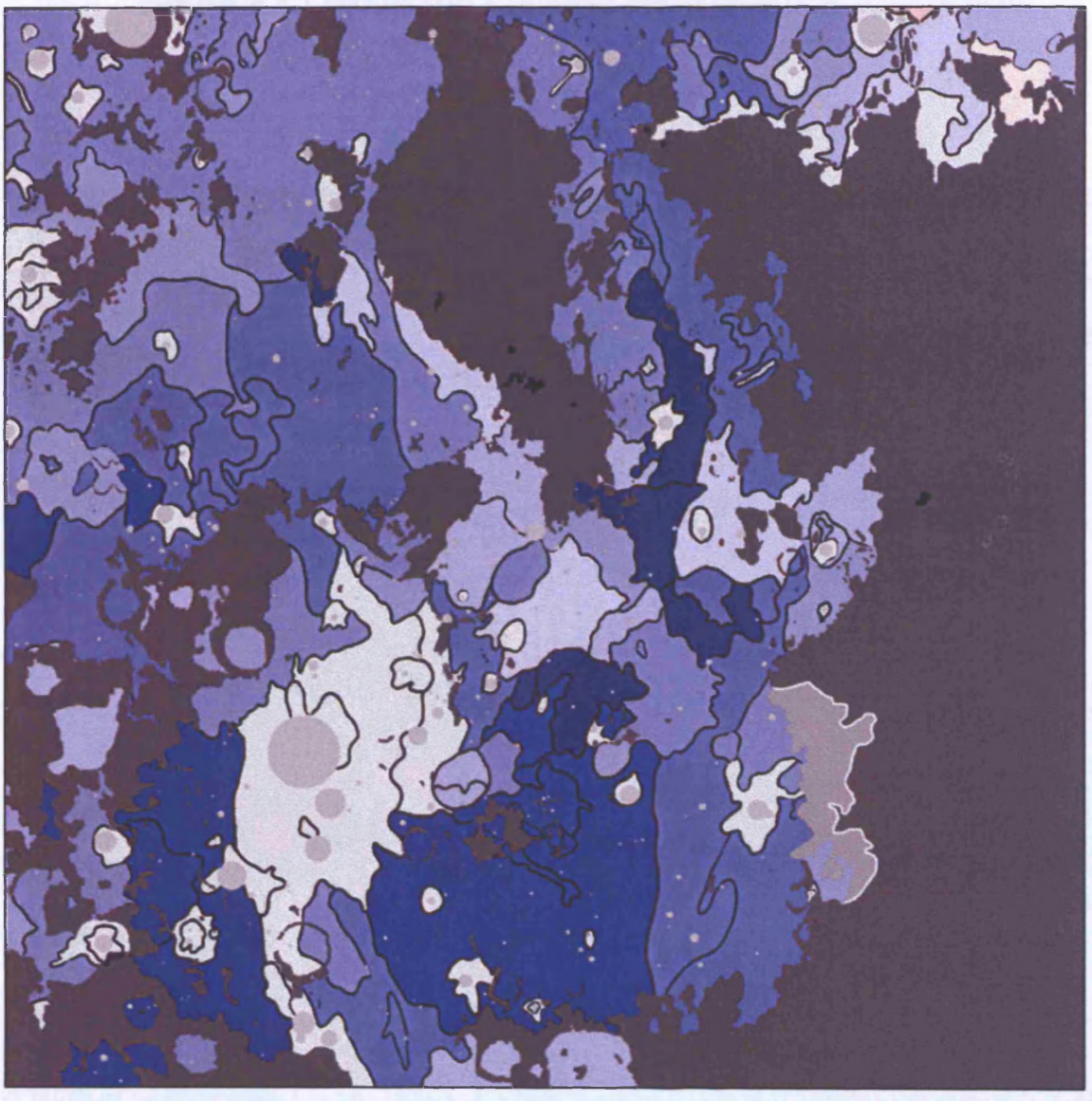

Figure 9.2. Intensity of blue indicates TiO_2 average abundance on given unit.

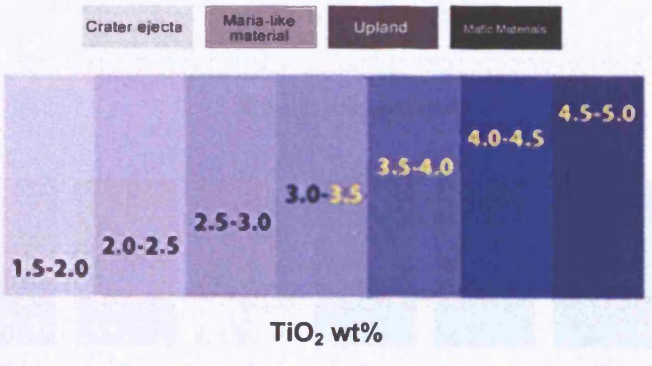

Colour Legend for Figure 22

Figure 9.3. Colours show relative maria chemical abundances

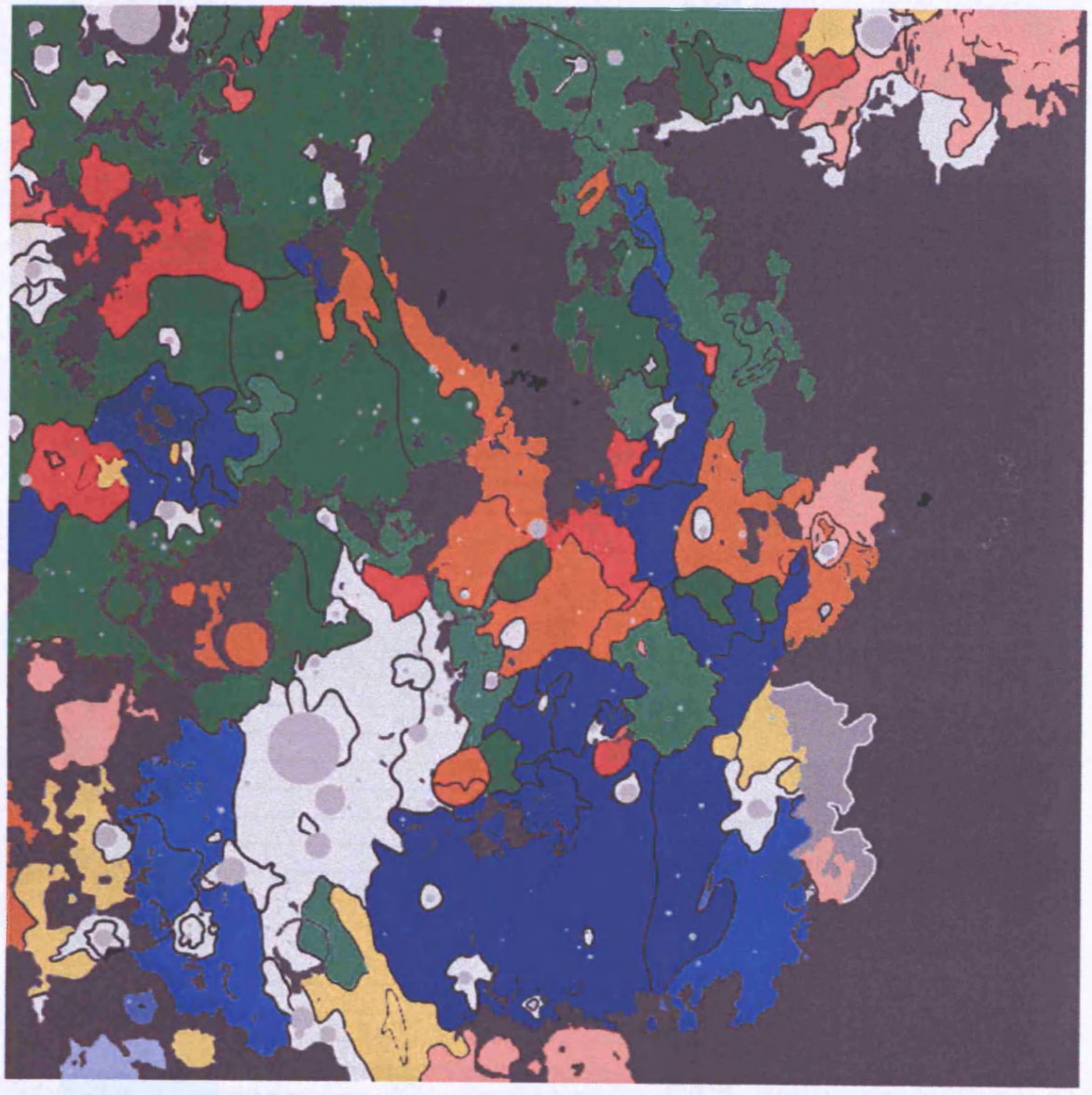

Colour Legend

	1	2	3	4	5	6	7	8	9
TiO_2 wt %	1.3-2.9	1.3-2.9	1.3-2.9	3.0-3.9	3.0-3.9	3.0-3.9	4.0-5.1	4.0-5.1	4.0-5.1
FeO wt %	13.5-17.9	18.0-19.9	20.0-21.9	13.5-17.9	18.0-19.9	20.0-21.9	13.5-17.9	18.0-19.9	20.0-21.9

Table 9.1. New unit classification according to newly grouped areas.

New Units	Units	Area km^2	Unit Surface km^2	%
1a	103, 104, 105	13,239		
1b	78	2,929		
1c	74	1,039		
1d	69, 70, 71	4,964		
1e	17, 18	3,298	**25,469**	7
2a	1, 200, 25, 29, 33	17,732		
2b	79, 77	8,761		
2c	95	385		
2d	39, 40	1,434		
2e	19, 20	2,575		
2f	44	751		
2g	3	1,683	**33,321**	9
3a	102	2,404		
3b	85	1,086		
3c	84	2,777		
3d	35	676		
3e	24	1,267		
3f	14	4,218		
3g	6	6,108		
3h	9	2,355	**20,891**	6
4a	37	1,418		
4b	73	2,321		
4c	56	7,319		
4d	48	930		
4e	45, 46, 50	5,402	**17,390**	5
5a	99, 100, 101, 94, 91, 92	28,126		
5b	34	6,021		
5c	54	2,386		
5d	28, 23	5,010		
5e	12	1,748		
5f	88	1,516	**44,807**	13
6a	101	1,745		
6b	90	4,949		
6c	82, 80	1,801		
6d	36	1,169		
6e	27	1,528		
6f	21	5,926		
6g	16	11,787		
6h	7, 107, 2	81,656	**110,561**	31
7a	62	2,253	**2,253**	1
8a	72	10,415		
8b	51, 52	11,140		
8c	97, 98	1,185	**22,740**	6
9a	57, 61, 59, 32, 30, 106, 83, 89, 31, 86	57,860		
9b	10, 11, 13	8,528		
9c	15	1,989		
9d	4	745		
9e	83, 89, 106	11,296	**80,418**	22

Figure 9.5. Colours show relative maria chemical abundances

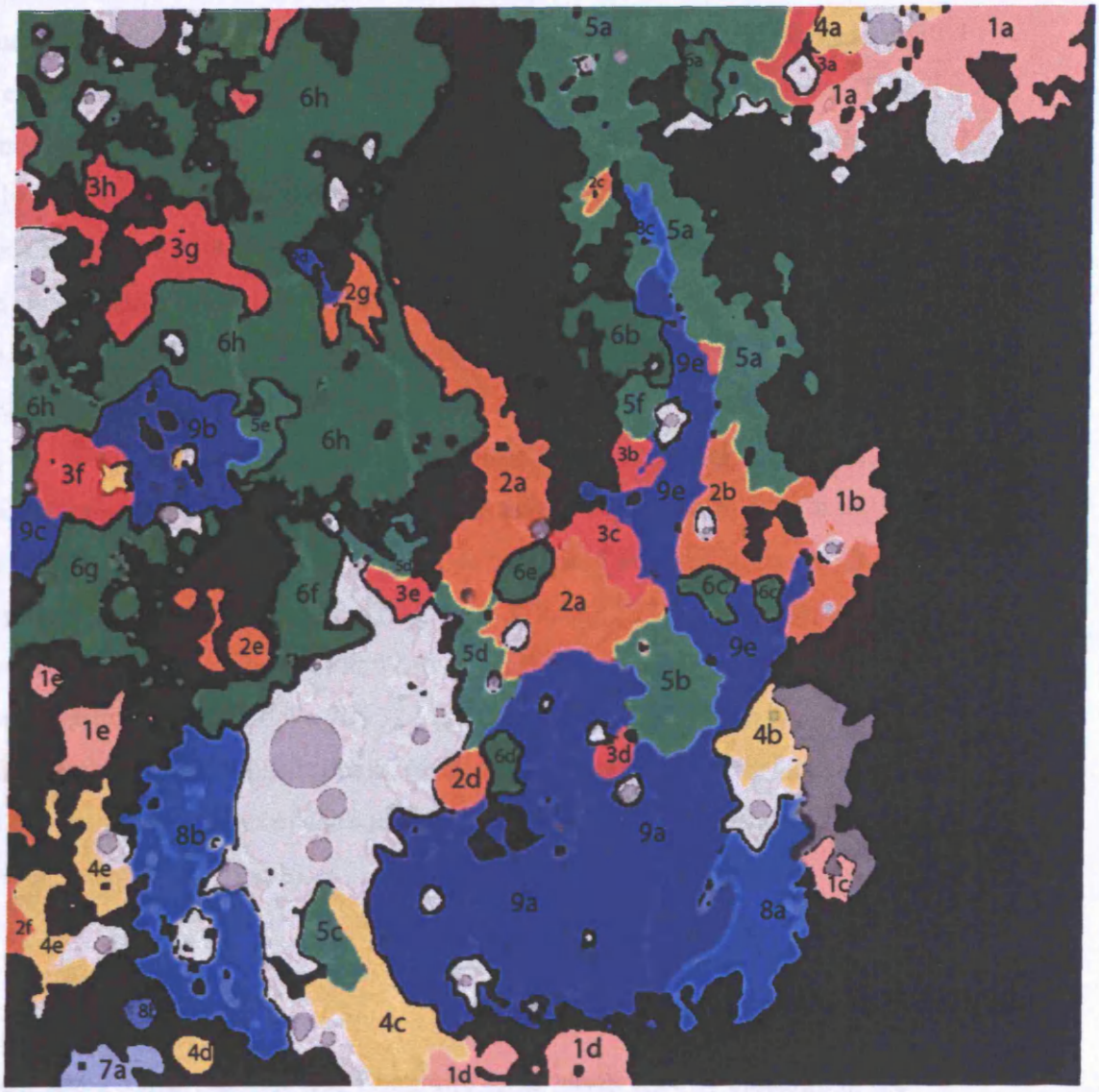

Colour Legend

	1	2	3	4	5	6	7	8	9
TiO_2 wt %	1.3-2.9	1.3-2.9	1.3-2.9	3.0-3.9	3.0-3.9	3.0-3.9	4.0-5.1	4.0-5.1	4.0-5.1
FeO wt %	13.5-17.9	18.0-19.9	20.0-21.9	13.5-17.9	18.0-19.9	20.0-21.9	13.5-17.9	18.0-19.9	20.0-21.9

CHAPTER 10 CRATER COUNTING WITHIN EACH OF THE PROPOSED UNITS. COMPARATIVE AGE DETERMINATION
MARE NUBIUM AND MARE COGNITUM

10.1 Background

A fundamental step in understanding the evolution of the maria is to estimate relative, and ideally absolute, time of emplacement of the proposed lava flows. This enhances our understanding of the geological evolution of the Moon and ultimately leads to the development of a more reliable model of the thermal history of the satellite. There have been many attempts to devise a reliable remote sensing dating method that could be consistently applied to lunar and other planetary surfaces. Boyce and Dial (1975b) were among many lunar scientists who used inferred crater rim erosion rates to estimate the age of the surrounding areas. Lately there has been a concerted multidisciplinary effort to capitalise on the wealth of multispectral data acquired by both terrestrial and orbiting instrumentation. Remote sensing techniques rely on the premise that space weathering acts on the optical properties of the lunar regolith (e.g. McKay *et al.*, 1974). Maturation darkens and reddens the surface material and consequently its spectra exhibit reduced contrast (Fisher and Pieters 1994b, 1996). Much research has gone into developing a reliable method for establishing lunar (and ultimately, planetary) surface maturity from the optical properties of the soil (e.g. Hiroi *et al.,* 1997; Shkuratov *et al.,*1999; Lucey *et al.,* 2000b).

10.2 Method

I investigated Maria Nubium and Cognitum lunar basalt ages by calculating the crater size-frequency distribution for craters down to 500 meters in diameter (for a full account of methodology and background refer to Hiesinger *et al.*, 2000). Clementine data could not be used for this part of the research due to both the relatively low resolution of its UVVIS camera (~ 200 m/px, Nozette *et al.*, 1994) and, crucially, the high phase angle of the images, factors that combined in making it difficult to discern craters <1 km in diameter. Instead, I used images from

the 1967 Lunar Orbiter IV mission, which have spatial resolutions between 60 and 150 m, an incidence angle of 10°-30°, and sharper contrast.

Each photographic print was first scanned at high resolution and imported into Adobe Photoshop©. Substantial tonal range adjustments were required in order to reduce extremes in the contrast/luminosity characteristics[1].

Pixel resolution ranged between 40 and 50m/px. Much care was taken in trying to reproduce and redraw each unit area as proposed in Figure 7.4. A round black dot 10 pixels in diameter was created to mark craters larger than 500 m. In the end, I counted nearly 10,000 craters larger than 500 meters scattered over a sampled mare surface of 225,000 km^2 (see Table 10.1).

I encountered several limitations and uncertainties in my method as the work of identifying suitable craters progressed. Some small sections of the original Orbiter images were overexposed and suffered from poor contrast resolution. In addition, when viewed in high resolution, some areas displayed what appeared to be film-developing 'blotches'. It is also probable that a few volcanic features, such as domes and cones, and natural occurring terrain depressions, were interpreted as craters and included in the count. Nevertheless, the potential errors represent only a tiny percentage of the total crater census. A far trickier task was the differentiation between primary and secondary impact craters. A low-resolution inspection of each area was often enough to estimate and approximate the extent of the 'contamination'. An arbitrary lower crater count was applied for the given area.

The areas occupied by a few individual emplacement units were too small to acquire reliable statistical data of the local crater population size (Craddock and Howard, 2000). Unit *86,* for instance, covers a surface area of only 255 km^2. I counted twelve craters within it, giving a density of 4.7×10^{-2} craters per square km, and a rough estimated age between 3.0-3.2 Ga. If only two of the craters had been the product of nearby secondary impacts, and therefore wrongly included in the count, the new age estimate for the area would be over half billion years

[1] Using 'Curves' option in Adobe © Photoshop © software.

younger! Later in this work, great care will be taken in order to account for the large discrepancies and uncertainties resulting from the study of smaller sample areas.

The size distribution of lunar craters for Mare Nubium has been the focus of several geological studies. Cross (1966) published a detailed paper on three lunar areas, including Mare Nubium, taking advantage of the newly available high resolution surface images sent back by the Ranger 7 satellite. He found that the frequency of crater occurrence is inversely proportional to the square of the crater diameter, and that this relation holds over the whole size range. Three hundred and ninety five crater measurements were taken and used to produce a remarkably consistent cumulative crater frequency graph for Mare Nubium. Subsequently, he derived a formula to enable the total crater area between specified diameter limits to be integrated:

$$N = 10^{10}\, C/X^2$$

Where $C = 1.4$ for Mare Nubium and $X = 500$ m in this study. According to this equation, the number of craters larger than 500 m in diameter in an area of 10^{12} square meters is around 56,000, hence an average density of 5.6×10^{-2} craters per km^2, a value in agreement with my results.

Converting the crater count per square kilometre into an indication of absolute model age requires statistical records on sub-kilometre crater populations plus reliably dated and geographically pertinent soil samples. Most lunar crater chronology is based on statistical records of impacts larger than one kilometre in diameter (e.g. Arvidson 1976; Hiesinger *et al.,* 2000; and *Tables 8.4.1 and 8.4.2 from* BVSP 1981) in the geographical proximities of the few directly sampled areas of the Moon (Apollo 11 to 17, and Luna 16 and 24).

Figure 10.1 is the result of data points collected and compiled from BVSP (tables 8.8.1, 8.4.1, and 8.4.2) and Shultz & Spudis (1983). There are several sources of potential errors in reliable age determination:

1. As explained in detail above, this is the issue of a reliable crater count. Neukum (1975a) estimated the systematic uncertainty of the standard distribution curve to be <10% for 0.8 km $\leq D \geq$ 3 km, and found higher percentages as the diameter of the sampled craters increases. As a result, I took an error of ten percent to be my upper limit of uncertainties for this part of my work.

2. Crater densities relative to lunar maria average and Apollo missions are assumed with a 10% uncertainty (BVSP, table 8.4.2, 1981).

3. Age ranges of sampled lunar rocks are based on listing or individual ages in table 7.3.1 (BVSP) and elsewhere, plus statistical standard deviations.

10.3 Results and discussion

Figure 10.2 focuses on the probable age range of the maria in the mapping region according to my crater count results. Three readings were taken for each of the 48 regions (refer to Table 9.1). Table 10.2 gathers all the results of my research so far. I am rather more confident of the accuracy of my crater density results then of their 'translation' into absolute age estimates. Consequently, in most of my following work I will be offering parallel analysis of my results with reference to both crater frequency and age range.

I plotted the results of these estimated ages against my nine chemical unit types (see figure 9.5). Figures 10.3 and 10.4 suggest an underlying relationship between unit types and their ages, or indeed crater frequency. As we go back in time, Low-Ti areas (groups 1 to 3) appear to become progressively enriched in iron. The opposite is true for all other terrains. Higher titanium units show decreasing iron abundances as they mature (with the exception of group '6').
Figures 10.5 and 10.6 display the age trend for each group (hi-, mid-, and low-Ti). It is clear that, according to my data, more heavily cratered terrains are also less Ti-rich (Table 10.2). At this stage, it is important to take these findings strictly as a qualitative indication of potential age-compositional trends. My data show only

a weak relationship between average units' iron abundances and age differences (figures 10.7 and 10.8). Nevertheless, the overall trend points towards slight iron enrichment in younger soils.

Table 10.2 allows us to compare both the chemical make up and model age among all units. I present two further and progressive levels of amalgamation. Table 10.3 groups all 'original units' (as per table 9.1) that have very similar chemical compositions *and* inferred age. It is unlikely that this region of the Moon has witnessed only seventeen distinctive igneous phenomena throughout its history and left clear evidence just for these processes. Nevertheless, the affinity between certain areas for iron and titanium content and cumulative cratering frequency, combined with their geographical settings and proximity, suggests a number of plausible geological scenarios that will be further discussed and explored later in this work.

I produced further merging and sub-grouping of the seventeen units into eight main potential geological types within the maria (*a-h*, Table 10.4) and a further four (*w-z*) for the remaining terrains. Some minor areas were not included in this final classification: units 16, 7, and 5 are too small, marginal, and too close to either highlands or major craters to be representative of the overall compositional and age trend of the studied area. The soils represented by unit 12 show instead a typical composition of terrains grouped as '*e*' but they are also characterised by a much more cratered morphology (hence, interpreted as older). Nevertheless, all these four groups were 'associated' with their relevant chemical/age group, reflecting my relative reliability bias towards the chemical data. I plotted the data in Table 10.4 to produce Figures 10.9 and 10.10. The best-fit line points and confirms previous findings (Figures 10.5 and 10.6) of a possible trend of soil enrichment in titanium with time. These results disagree in substance with the latest study from Hiesinger *et al.* (2001) who found no correlation between age and titanium abundances in the nearside lunar basalts.

Figure 10.10, derived from crater frequency and Ti data from Table 10.4, suggests three possible eruptive phases with a progressively increasing titanium fraction with time. This relationship is less clear when modelled ages are considered (Fig-

ure 10.9). This is due to the progressive crater saturation of the lunar surface, believed to increase exponentially for soils older than ~3300 Ma (or ~5.0×10^{-2} craters per km^2).

10.4 Conclusions

Table 10.5 and Figure 10.11 show the proposed three major eruptive phases in the Nubium/Cognitum region:

Table 10.5. Proposed three major eruptive phases in the Nubium/Cognitum region.

Family	Ti%	Fe%	Start – End (Ma)
I	2.0-3.0	18.0-20.0	3500-3330
II	3.0-4.0	18.0-20.5	3300-3100
III	4.0-5.0	20.0-21.5	2600-2200

Finally, I used Table 10.4 to produce Figure 10.12, the region's map containing my interpretation of chemical and temporal data for ten distinctive effusive phases.

All age groups represent distinctive periods dating from the Late Imbrian Epoch (I) through the Early Eratosthenian Period (II) and Late Eratosthenian Period (III). Note that I am interpreting only the visible surface units; most of these soil types probably represent only the last of many effusive phenomena witnessed within a geographical area. We have also to consider contamination from highland materials, especially near the 'continental shelves' (e.g. for units 'a' and 'd'), ejecta from local impacts (units near to 'y'), local chemical anomalies (e.g. 'j' at 7°S 22°W), and the general inherent difficulty in acquiring reliable crater frequency data for small geographical areas ('d').

Mare units marked 'x' (Fig. 10.12) are thought to represent the remnants of ancient Imbrian or even Pre-Imbrian flows. We find them mostly in embayed coastal areas and show compositions similar to the neighbouring highlands. Due to the effects of billion of years of erosion plus vertical and horizontal admixing with non-mare material, the multispectral analysis techniques used in this study, being

focused on the topsoil regolith fraction, cannot offer reliable chemical analysis of these ancient mare materials.

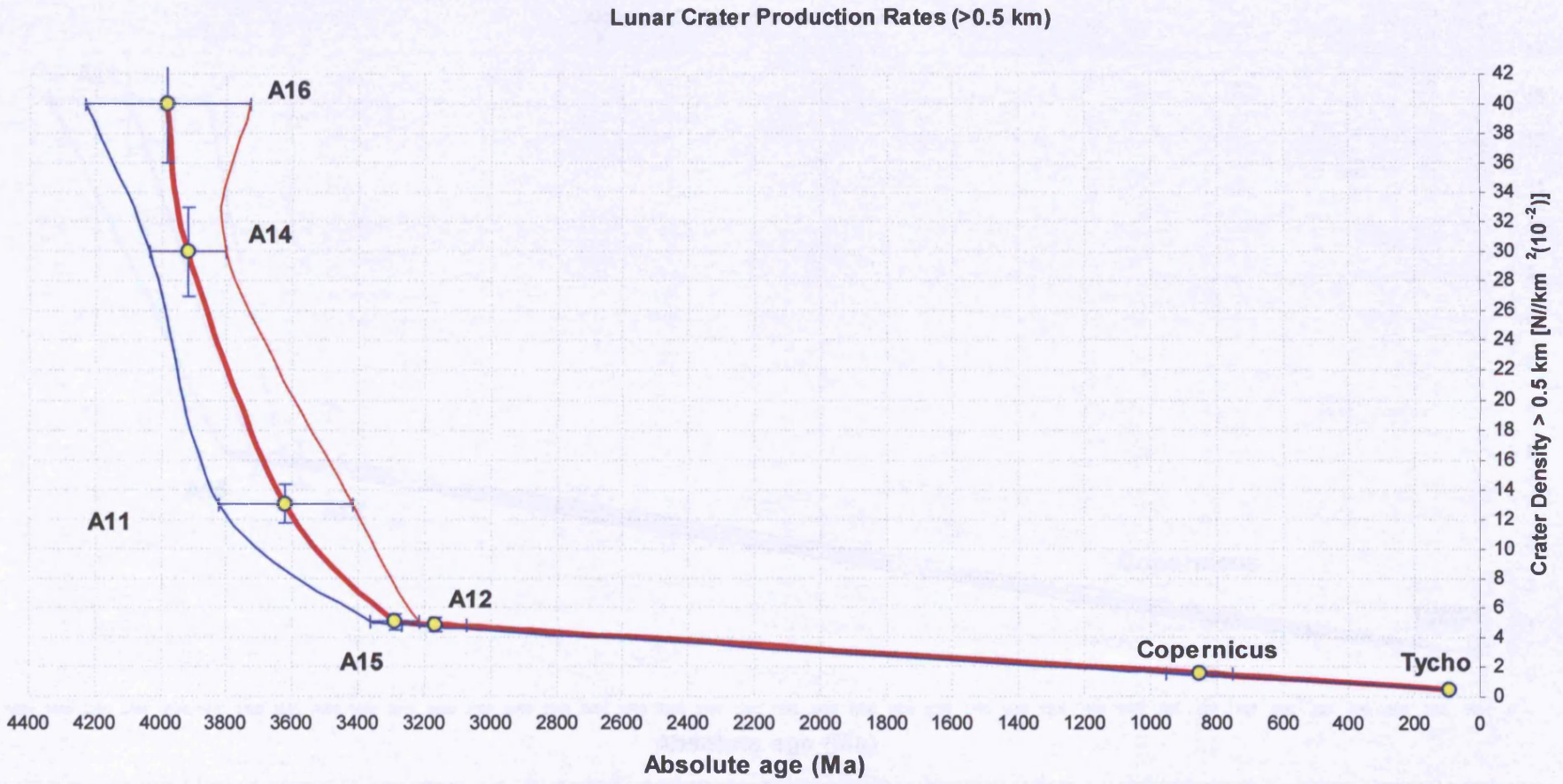

Figure 10.1. Estimated lunar crater production rates (>500m diameter) through the eons
Sampling data obtained from: BVSP (tables 8.8.1, 8.4.1, and 8.4.2) and Shultz & Spudis (1983)

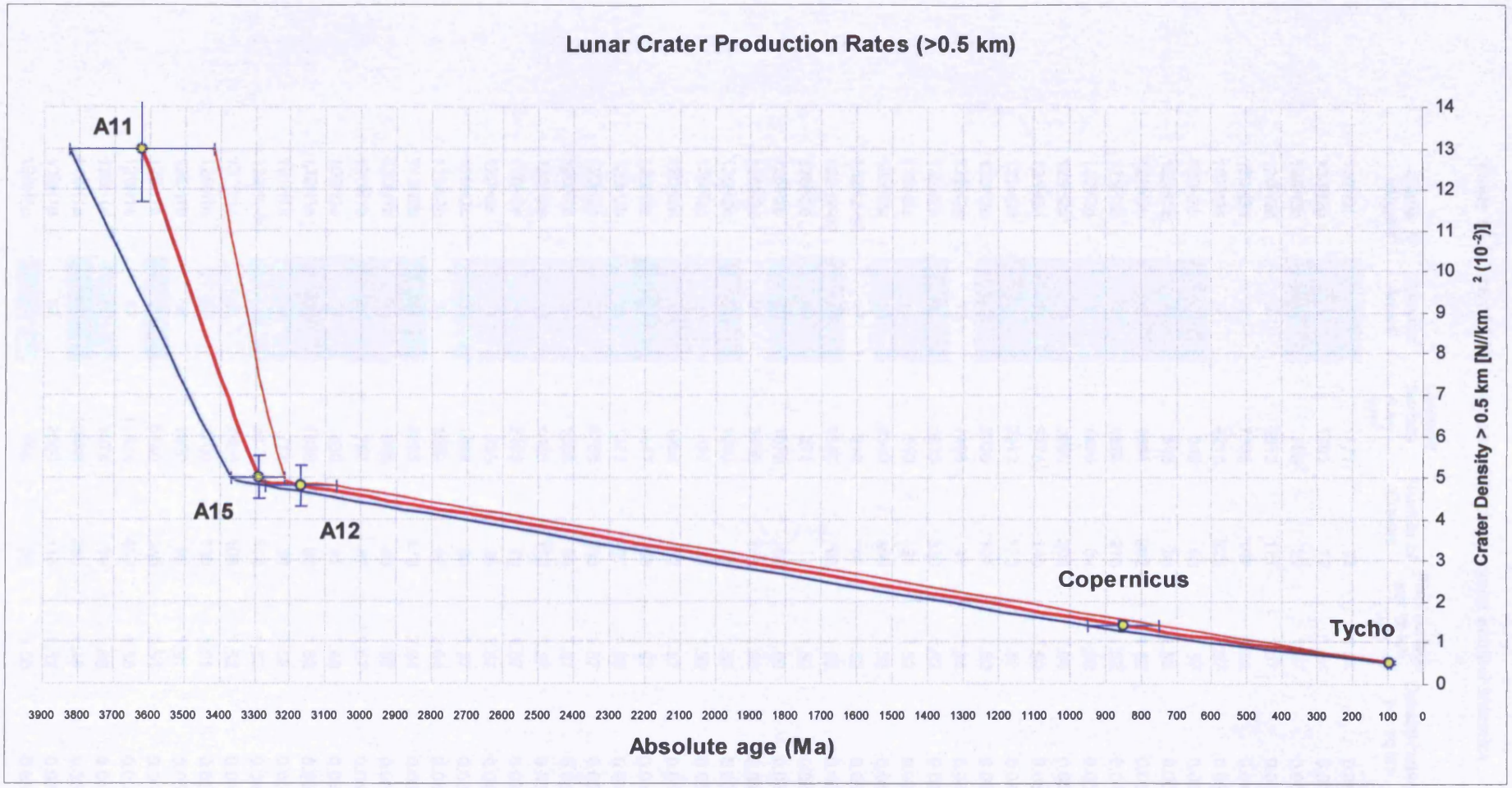

Figure 10.2. Estimated lunar crater production rates (>500m diameter) through the eons
Sampling data obtained from: BVSP (tables 8.8.1, 8.4.1, and 8.4.2) and Shultz & Spudis (1983)

Table 10.1. List of OIV images used to obtain crater number statistics

Orbiter IV Image #	Sampled Area #	Sampled Surface Area Km^2	Number of Craters	Pixel surface per sq km (10^{-3})	Density craters per sq km
120H2f	1	1171	74	1.54	0.063
120H2g	1	1281	77	1.54	0.061
120H3b	1	790	52	1.57	0.066
120H2d	2	3513	171	1.57	0.048
120H3a	2	7438	147	1.52	0.047
132H3a	2	4210	222	1.57	0.053
120H3b	3	845	53	1.57	0.062
125H3a	4	515	33	1.52	0.064
125H3b	6	4661	282	1.52	0.061
125H3b	7	4374	216	1.52	0.048
132H3a	9	1490	84	1.52	0.056
125H2a	10	3660	208	1.54	0.058
125H2d	10	3775	140	1.50	0.037
125H2d	11	2912	123	1.50	0.043
125H2e	12	2070	101	1.50	0.049
132H2a	13	1455	47	1.54	0.047
132H2a	14	5635	339	1.52	0.060
132H2a	15	550	21	1.52	0.038
132H2a	16	9340	486	1.52	0.052
132H2-50	17	910	61	1.52	0.067
132H2-50	18	1550	92	1.52	0.060
125H2b	19	273	17	1.50	0.063
125H2b	20	1073	66	1.50	0.061
125H2c	21	3400	162	1.50	0.048
125H2c	23	1030	58	1.50	0.056
125H2c	24	820	51	1.50	0.062
120H2d	25	1406	81	1.57	0.058
120H2b	27	1447	68	1.57	0.047
120H2b	28	1351	67	1.59	0.049
120H2c	29	4786	255	1.57	0.053
120H2d	29	1000	64	1.57	0.064
120H2e	29	1965	122	1.57	0.062
120H2c	30	2165	76	1.57	0.036
120H2c	31	635	25	1.57	0.040
120H2c	32	1566	60	1.57	0.038
113H2b	33	1532	97	2.64	0.063
113H2b	34	3285	179	2.64	0.055
120H1a	35	658	40	1.57	0.061
120H1b	36	767	37	1.57	0.048
108H3a	37	630	41	1.48	0.066
132H1a	44	1638	83	1.52	0.058
131H1b	48	712	38	1.52	0.053
132H1-50	50	2370	114	1.52	0.048
132H1d	51	2466	108	1.52	0.044
125H1c	52	2700	136	1.51	0.051
125H1b	54	1860	93	1.51	0.051
125H1b	56	6480	345	1.51	0.053
120H1e	57	11824	403	1.58	0.035
120H1d	59	1678	79	1.58	0.047
113H1a	61	10880	380	1.48	0.035
132H1a	62	2500	118	1.52	0.047
120H1c	69	468	26	1.58	0.061

120H1c	70	886	47	1.58	0.053
120H1d	71	2852	152	1.58	0.053
113H1c	72	5920	285	1.48	0.047
113H2-73	73	3147	184	1.50	0.059
113H1c	74	516	32	1.48	0.062
113H2d	77	1321	78	1.57	0.060
113H2c	78	1640	102	2.67	0.062
113H2a	79	4313	275	2.74	0.063
113H2d	80	630	33	2.70	0.053
113H2b	82	1030	54	2.74	0.053
113H2a	83	2920	113	2.74	0.039
113H2b	83	1327	51	2.64	0.038
113H2b	84	1079	61	2.64	0.056
113H2a	85	1150	70	2.74	0.061
113H2a	86	255	12	2.74	0.045
113H2a	88	303	18	2.74	0.061
113H2a	88	957	51	2.74	0.053
113H2a	88	1617	98	2.74	0.061
113H3a	89	1840	74	2.64	0.040
113H3b	89	704	32	2.74	0.046
113H3b	89	1141	41	2.74	0.037
113H3b	89	1930	85	2.74	0.043
113H3a	90	3135	167	2.64	0.053
113H3c	91	5382	286	1.50	0.053
113H3a	92	876	51	2.64	0.058
113H3a	94	944	49	2.64	0.053
113H3a	95	437	26	2.64	0.061
113H3e	99	1650	78	1.50	0.047
113H3e	100	5440	231	1.50	0.043
113H3e	101	2050	99	1.50	0.048
108H3a	102	1800	104	1.48	0.058
108H3a	103	1870	113	1.48	0.060
108H3a	104	2400	160	1.48	0.067
125H3a	105	3374	196	1.47	0.058
113H2b	106	2583	102	2.64	0.040
113H2d	106	955	38	2.70	0.040
125H2e	107	8937	422	1.50	0.047
120H1b	39-40	1432	85	1.57	0.063
132H1a	45-46	2371	129	1.52	0.060
113H3a	97-98	921	39	2.64	0.043
120H2d	200	3400	192	1.57	0.056

Units	Crater Count (10^{-2}N km^{-2})	Lower Age Limit (Ma)	Average Age (Ma)	Higher Age Limit (Ma)	*SD in Age* (Ma)	Surface (km^2)	TiO_2 %	FeO %	Original units (Fig. 7.4)
1a	6.8	3275	3380	3485	*105*	13,239	2.0	17.3	103, 104, 105
1b	6.2	3260	3350	3430	*85*	2,929	2.2	17.5	78
1c	6.2	3260	3350	3430	*85*	1,039	2.6	16.7	74
1d	5.3	3225	3315	3380	*78*	4,964	2.4	15.1	69, 70, 71
1e	5.3	3225	3315	3380	*78*	3,298	2.3	16.6	17, 18
2a	6.2	3260	3350	3430	*85*	17,732	1.8	19.3	1, 200, 25, 29, 33
2b	6.1	3255	3345	3428	*87*	8,761	2.1	18.4	77, 79
2c	6.1	3255	3345	3428	*87*	385	2.6	18.9	95
2d	6.0	3250	3340	3425	*88*	1,434	2.2	19.8	39, 40
2e	6.1	3255	3345	3428	*87*	2,575	2.6	19.7	19, 20
2f	5.8	3245	3330	3415	*85*	751	2.7	19.1	44
2g	7.4	3295	3400	3510	*108*	1,683	1.5	18.6	3
3a	5.8	3245	3330	3415	*85*	2,404	2.8	20.4	102
3b	6.1	3255	3345	3428	*87*	1,086	2.2	20.3	85
3c	5.6	3235	3320	3400	*83*	2,777	2.9	20.2	84
3d	6.1	3255	3345	3428	*87*	676	2.6	19.9	35
3e	6.2	3260	3350	3430	*85*	1,267	2.8	20.0	24
3f	6.0	3250	3340	3425	*88*	4,218	2.8	20.6	14
3g	7.1	3290	3390	3490	*100*	6,108	2.5	20.3	6
3h	6.8	3275	3380	3485	*105*	2,355	2.8	20.2	9
4a	6.6	3270	3370	3470	*100*	1,418	3.0	14.6	37
4b	6.4	3260	3360	3450	*95*	2,321	3.1	17.4	73
4c	5.3	3225	3315	3380	*78*	7,319	3.5	15.7	56
4d	5.3	3225	3315	3380	*78*	930	3.1	16.4	48
4e	5.1	3150	3250	3350	*100*	5,402	3.3	17.0	45, 46, 50
5a	5.3	3225	3315	3380	*78*	28,126	3.5	19.7	99, 100, 101, 94, 91, 92
5b	5.5	3230	3318	3390	*80*	6,021	3.0	19.4	34
5c	5.1	3150	3250	3350	*100*	2,386	3.1	19.5	54
5d	5.3	3225	3315	3380	*78*	5,010	3.4	19.8	23, 28
5e	6.9	3280	3385	3490	*105*	1,748	3.6	19.8	12
5f	6.0	3250	3340	3425	*88*	1,516	3.1	19.0	88
6a	4.8	3070	3170	3270	*100*	1,745	3.1	20.4	101
6b	5.3	3225	3315	3380	*78*	4,949	3.3	19.9	90
6c	5.3	3225	3315	3380	*78*	1,801	3.6	20.3	80, 82
6d	4.8	3070	3170	3270	*100*	1,169	3.0	20.2	36
6e	4.7	3010	3100	3200	*95*	1,528	3.3	20.8	27
6f	4.8	3070	3170	3270	*100*	5,926	3.4	20.5	21
6g	7.4	3295	3400	3510	*108*	11,787	3.6	20.8	16
6h	4.8	3070	3170	3270	*100*	81,656	3.4	20.3	7, 107, 2
7a	4.7	3010	3100	3200	*95*	2,253	4.0	17.7	62
8a	4.7	3010	3100	3200	*95*	10,415	3.9	18.2	72
8b	4.7	3010	3100	3200	*95*	11,140	4.0	18.3	51, 52
8c	4.5	2850	2950	3050	*100*	1,185	3.9	19.7	97, 98
9a	3.5	2200	2300	2400	*100*	57,860	4.3	20.5	57, 61, 59, 32, 30, 31, 86,
9b	4.6	2950	3025	3130	*90*	8,528	3.9	21.3	10, 11, 13
9c	3.8	2450	2550	2650	*100*	1,989	4.4	21.9	15
9d	6.4	3260	3360	3450	*95*	745	4.6	21.4	4
9e	3.8	2450	2550	2650	*100*	11,296	4.8	21.3	83, 89, 106

Table 10.2. List of each unit's crater count and inferred average age

Figure 10.3. Graph showing unit numbers against ages

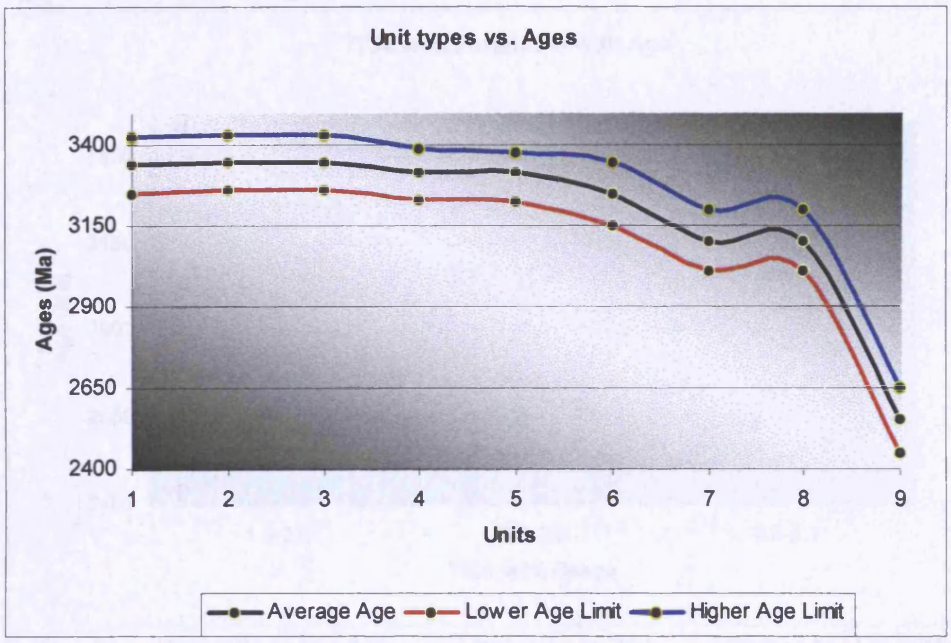

Figure 10.4. Graph showing unit numbers against crater count

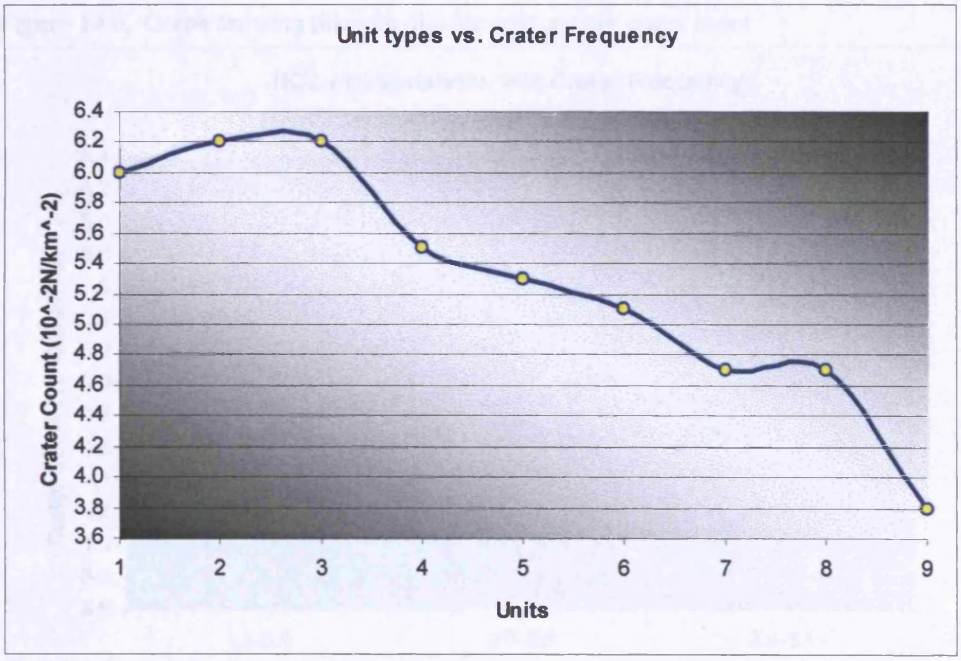

Figure 10.5. Graph showing titanium dioxide wt% against age estimates

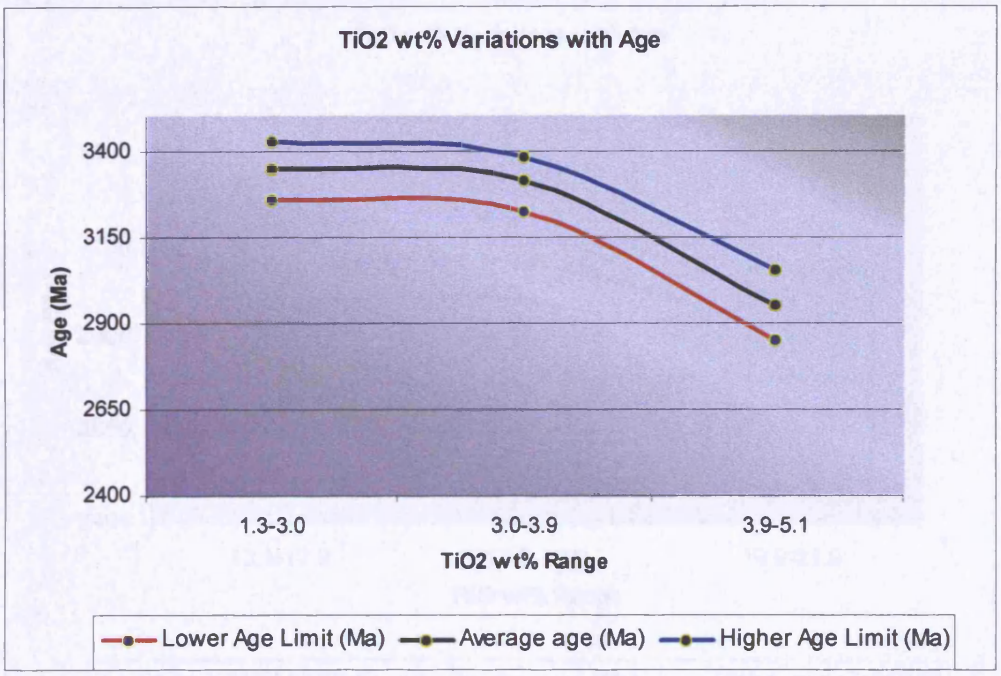

Figure 10.6. Graph showing titanium dioxide wt% against crater count

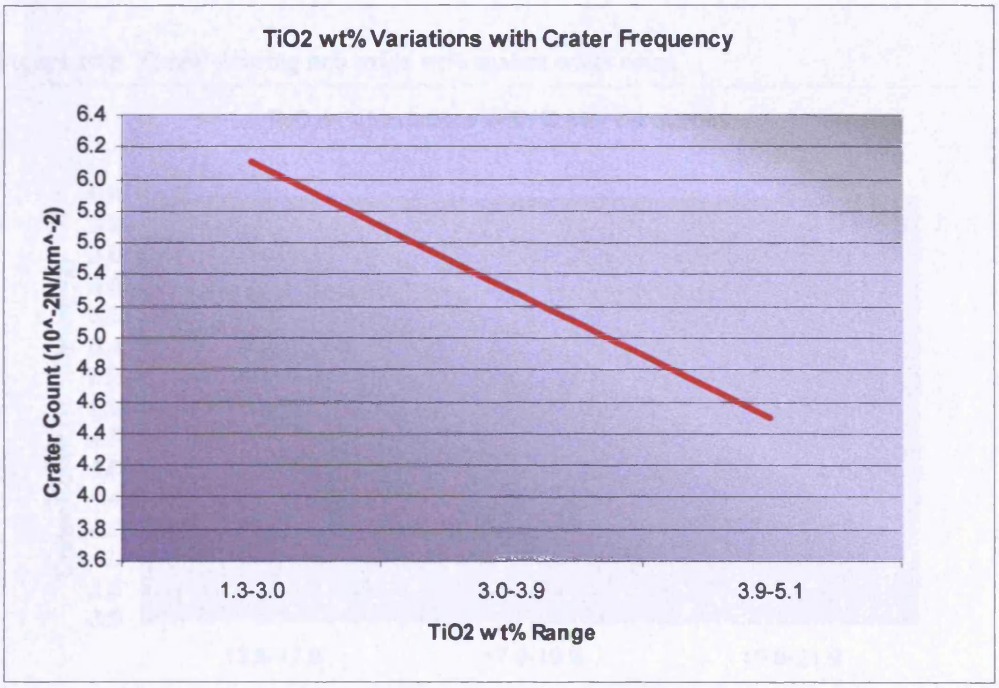

Figure 10.7. Graph showing iron oxide wt% against age estimates

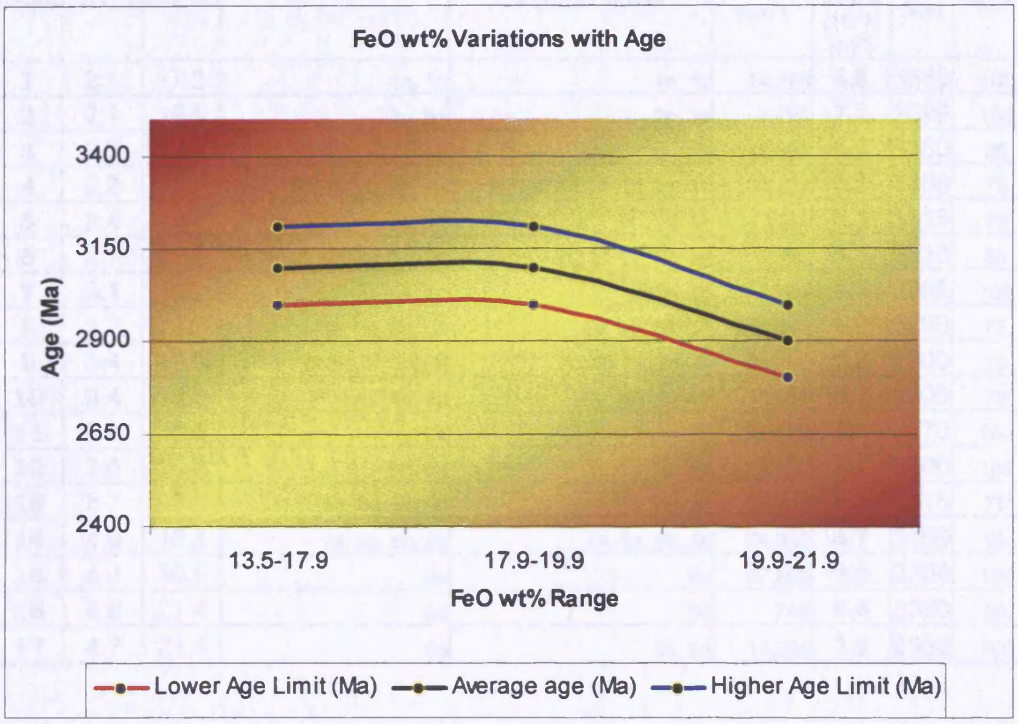

Figure 10.8. Graph showing iron oxide wt% against crater count

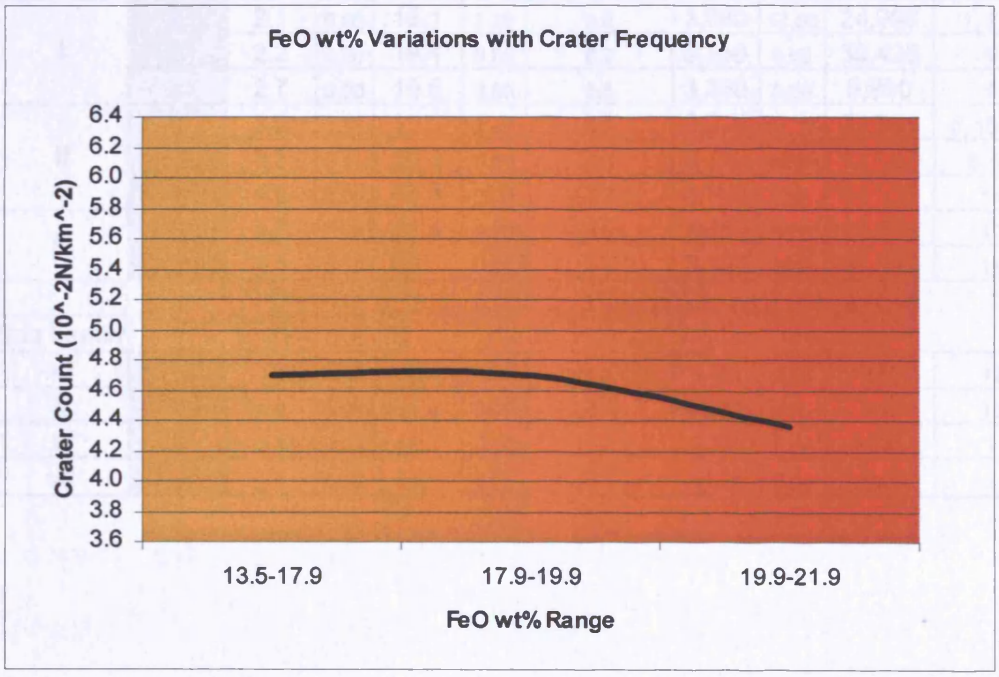

Table 10.3. Original sample units grouped into 17 new units

Units	TiO^2%	FeO%		Original units	Surface (km^2)	Sample Crater Count ($10^{-2}N\ km^{-2}$)	Age (Ma)	Age SD
1	2.1	17.2	1a, 1c	1a, 1c	14,278	6.8	3380	105
2	2.1	19.5	2g, 3g	2g, 3g	7,791	7.2	3390	100
3	2.2	17.5	1b	1b	2,929	6.2	3350	85
4	2.2	19.4	2a, 2b, 2e, 3b, 3f, 3e, 3h	2a, 2b, 2d, 2e, 3b, 3f, 3e, 3h	39,428	6.2	3350	75
5	2.4	15.7	1e, 1d	1d, 1e	8,262	5.3	3315	78
6	2.7	19.8	2a, 2b, 2f, 3a, 3c, 3d	2c, 2f, 3a, 3c, 3d	6,993	5.8	3330	85
7	3.1	16.2	4a, 4b	4a, 4b	3,739	6.5	3365	100
8	3.2	20.3	6a, 6e, 6b, 6d	6a, 6b, 6d, 6e	9,391	5.0	3290	75
9	3.4	19.8	6f, 5b,5f, 5c, 5d	6f, 5b, 5c, 5d, 5f	20,859	5.2	3300	78
10	3.4	16.3	4d, 4e, 4c	4c, 4d, 4e	13,651	5.2	3300	78
11	3.4	20.3	6h	6h	81,656	4.8	3170	100
12	3.6	20.4	5e, 6g	5e, 6g	13,535	7.3	3400	108
13	3.7	20.9	5a, 6c, 9b, 9c	5a, 6c, 9b	38,455	5.3	3315	78
14	4.0	18.3	7a, 8a, 8b, 8c	7a, 8a, 8b, 8c	24,993	4.7	3100	95
15	4.3	20.5	9a	9a	57,860	3.5	2300	100
16	4.6	21.4	9d	9d	745	6.4	3360	95
17	4.7	21.4	9e	9c, 9e	13,285	3.8	2550	100

Table 10.4. Further grouping of units into three compositional/age families

Family	Groups	TiO_2%	TiO_2 SD	FeO%	FeO SD	Crater Count ($10^{-2}N\ km^{-2}$)	Age (Ma)	Age SD	Surface (km^2)	Orig. Groups
I	a	2.1	0.06	18.1	1.25	6.8	3,380	17.56	24,998	1, 2, 3
	b	2.2	0.00	19.4	0.00	6.2	3,350	0.00	39,428	4
	c	2.7	0.00	19.8	0.00	5.8	3,330	0.00	6,990	6
II	d	3.5	0.17	19.0	2.40	5.3	3,315	31.75	72,965	9, 10, 13
	e	3.3	0.14	20.3	0.00	4.9	3,170	45.96	91,047	8, 11
	f	4.0	0.00	18.3	0.00	4.7	3,100	0.00	24,993	14
III	g	4.7	0.00	21.4	0.00	3.8	2,550	0.00	13,285	17
	h	4.3	0.00	20.5	0.00	3.5	2,300	0.00	57,860	15
Sub Family										
IV	d	3.6	0.00	20.4	0.00	7.3	3,400	0.00	13,535	12
V	g	4.6	0.00	21.4	0.00	6.4	3,360	0.00	745	16
VI	b	3.1	0.00	16.2	0.00	6.5	3,365	0.00	3,739	7
VII	a	2.4	0.00	15.7	0.00	5.3	3,315	0.00	8,265	5

Figure 10.9. TiO_2 abundances vs. model age.

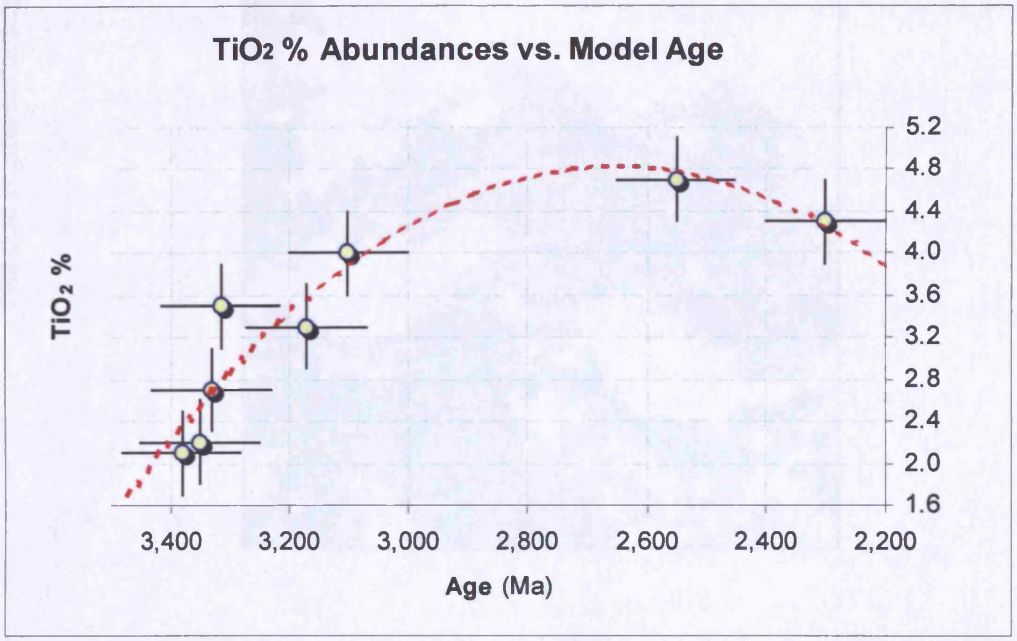

Figure 10.10. TiO_2 abundances vs. crater frequencies.

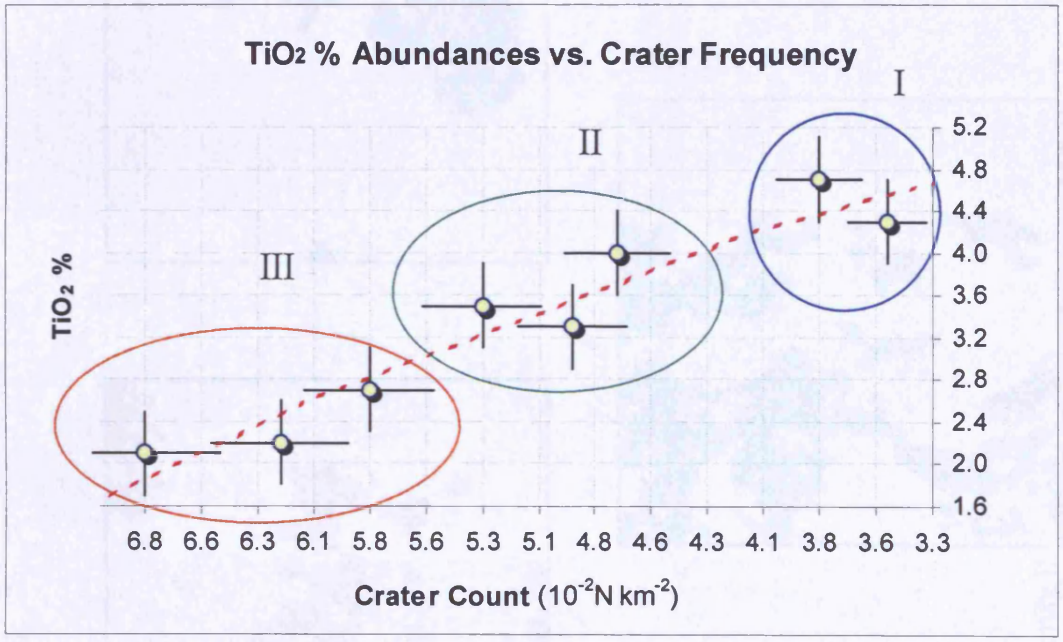

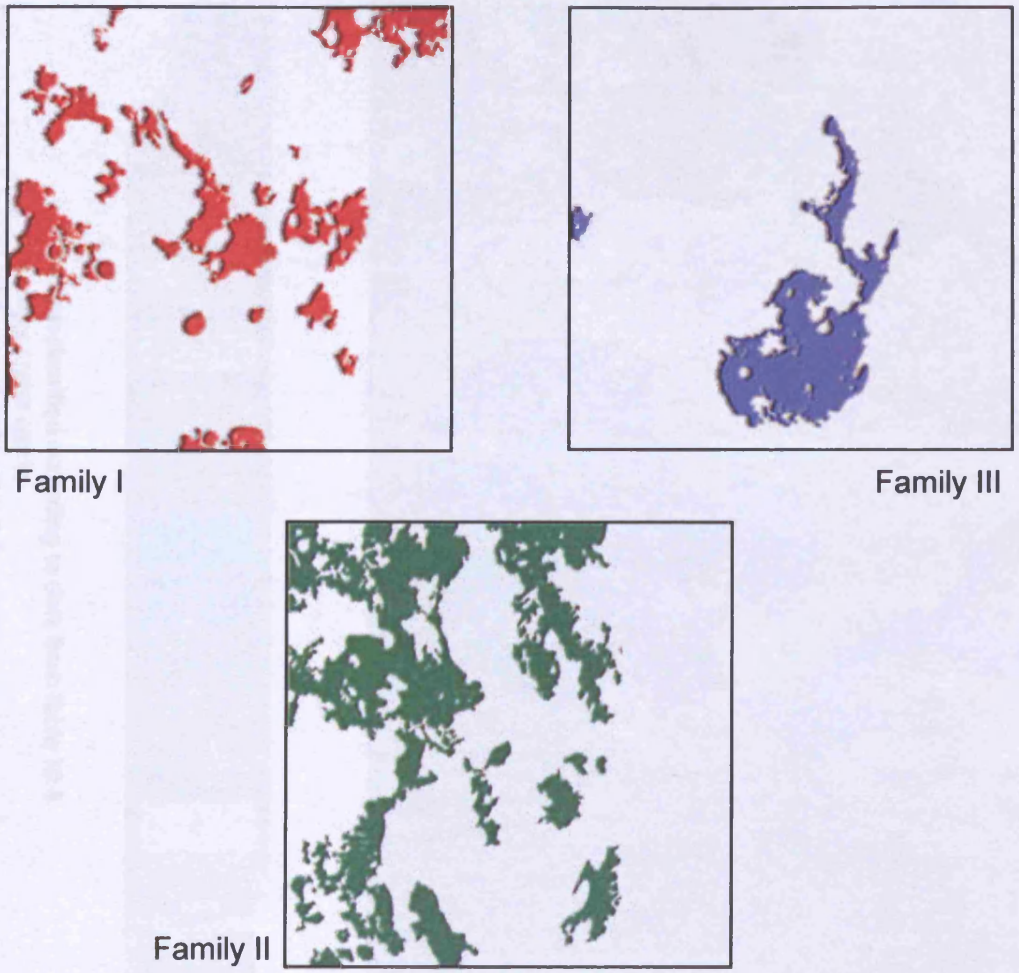

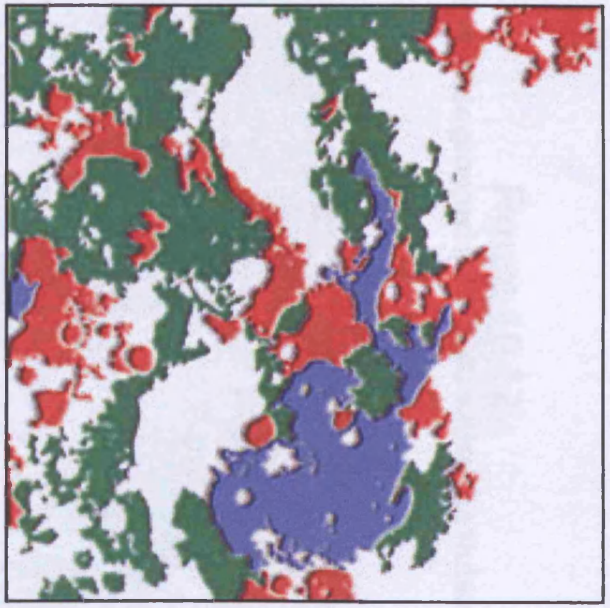

Figure 10.11. Distribution map of maria in the Nubium region according to age

Figure 10.12

Map of the possible grouped mare units within the Nubium region

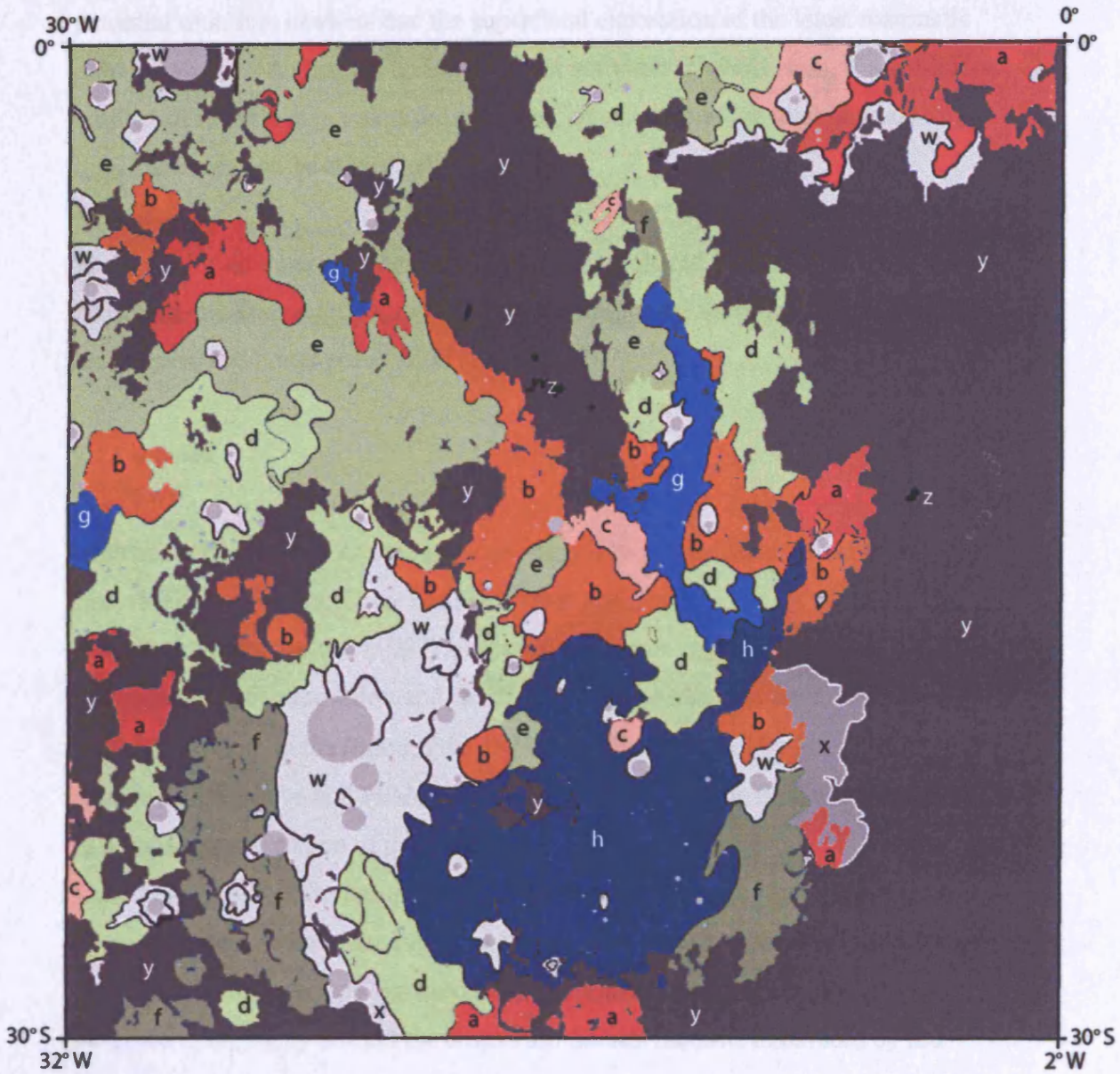

Units a-h classified according to data from Table 10.4.
w = major crater ejecta
x = obfuscated mare materials
y = highlands
z = basalt-like material within highland regions

CHAPTER 11 BASALT THICKNESS DETERMINATION
MARE NUBIUM AND MARE COGNITUM

11.1 Background

In order to estimate the cumulative volumetric igneous output in the region under study, it is necessary to acquire data on the total thickness of the basalts for each potential unit. It is obvious that the superficial expression of the latest magmatic outpourings may not reflect underlying past activities. Nevertheless, if a sufficient number of reliable data points are acquired, an estimate of the total igneous activity for the area can be attempted.

A number of alternative techniques have been employed to determine mare thickness: stratigraphic and topographic relationships, crater morphology, geophysical techniques, and crater penetration (Head 1982).

11.2 Method

Meteorites can be used as probes for piercing through the maria down to the mare/highland contact. There has been much research into the dynamics of high-velocity impacts. Melosh (1989) suggested an approximate relationship of 1/10 between depth of excavation and the diameter of the transient crater for simple craters (≤ 14 km on the Moon, Pike 1974), results confirmed by later studies (e.g. Spudis 1993; Grieve and Pilkington 1996). At this scale, the final crater diameter is a good approximation of the transient excavation.
Crater ejecta reflect the composition of the excavated target. If an impact penetrates the maria down to the highland bedrock, we would expect the ejecta blanket to contain a proportion of highland material. Various researchers have proposed a reversed stratigraphy around the crater rim: the last material excavated by the penetrating body will also be the last being deposited nearest to the rim (Shoemaker 1962; Stöffler *et al.*, 1975; Melosh 1989; Budney and Lucey 1998).
Using the UVVIS Clementine data set, I am able to differentiate between these two types of ejecta through their different iron spectra. Fe-poor highland material, mixed with the iron-rich local basalts, will result in the darkening (within the FeO map) of part of the ejecta blanket nearer to the crater rim.

It is beyond the scope of this work to offer a detailed analysis of the basins' depths. Here, I estimate the effusive volumes for the proposed basaltic units.

The degree of admixing of subsurface highland material with mare basalts is a function of the depth of excavation and contamination (after Thomson *et al.*, 1998):

$$\frac{Ch}{Mh} = \frac{FCE - H}{E - H} \qquad \text{eq. 1}$$

where:

	Definition	***Scale***
Ch	Max. excavation depth	Meters
Mh	Estimated maria depth	Meters
FCE	Fresh Crater Ejecta (pristine mare basalt)	Fe %
E	Dark mix material (mare + highland bedrock)	Fe %
H	Nearest highland material	Fe %

I obtained accurate crater diameter measurements from the same image Cubes used to determine FeO wt%. I rearranged the equation to find the estimated maria depth in meters:

$$Mh = 20(L_2 - L_1)\frac{E - H}{FCE - H} \qquad \text{eq. 2}$$

where L_x is the line number (*count*) in the 'Cube' co-ordinates system.

Figure 11.1 is a practical and graphical representation of the elements involved in solving the equation. I chose crater '*5*' (table 11.1) to illustrate my method. I used a small crater close to the highlands as an example of a relatively young crater with exposed fresh basalt (FCE), which supplied us with a measure of iron content in pristine local maria (~23%). Crater *5* has a diameter of 4,200 m and it is surrounded by a dark(er) crater ring 1,680 m wide. Iron readings outside the rim averaged to a figure of ~18%. The highlands were Fe-poorer with ~12% Fe. The crater depth was estimated at around 420 m giving an estimate for the mare depth of around 250 m.

I applied this technique to a further 73 craters spread across the area under investigation (table 11.1). Only a handful of craters actually feature a clear darker ejecta ring. I decided to supplement my data with values from craters that showed a relatively low-albedo crater floor. Their interpreted lower iron content could be a consequence of the presence of highland material within the allochthonous breccia.

11.3 Results

Figure 11.2 shows the inferred mare depths. Results from craters that displayed dark haloes are shown in red. It is clear that, due to both the paucity of the data and the uncertainties in measuring crater floors' compositions, it is necessary to be cautious about the reliability of the results. Nevertheless, the distribution of basalt thickness in Mare Nubium broadly agrees with past studies (e.g. De Hon 1977), with my estimates generally some 20% shallower than others. In particular, I confirmed a possible thickening of the basalt layers in the centre of the Nubium basin (~17 W 23 S), the northern eastern region (~10 W 20 S), and northern border (~18 W 17 S).

I am also reporting two areas of maria thickening in Mare Cognitum: one just north of Dorney D (26 W 12 S) and another near the middle of the basin (23 W 10 S).

As noted before, because I used a much simplified version of the crater excavation method, and due to the lack of a sufficient number of sample 'points', I can only offer a rough estimate of the basalt thicknesses, and consequently volumes, for each of the geological unit (groups). Table 11.2 shows the estimated volumes and thicknesses of mare materials for each effusive groups.

Table 11.2. Estimate volume of maria thickness for each effusive groups.

Age Group	Sub Groups	TiO_2 wt%	FeO wt%	Age (Ma)	Surface Area (km^2)	Min. Depth (km)	Volume estimate (km^3)
III	h	4.3	20.5	2,300	57,860	0.64	37,000
	g	4.7	21.4	2,550	13,285	0.12	1,600
II	f	4.0	18.3	3,100	24,993	0.10	2,500
	e	3.3	20.3	3,170	91,047	0.59	54,000
	d	3.5	19.0	3,315	72,965	0.53	39,000
I	c	2.7	19.8	3,330	6,990	N/A	N/A
	b	2.2	19.4	3,350	39,428	0.46	18,000
	a	2.1	18.1	3,380	24,998	0.16	4,000

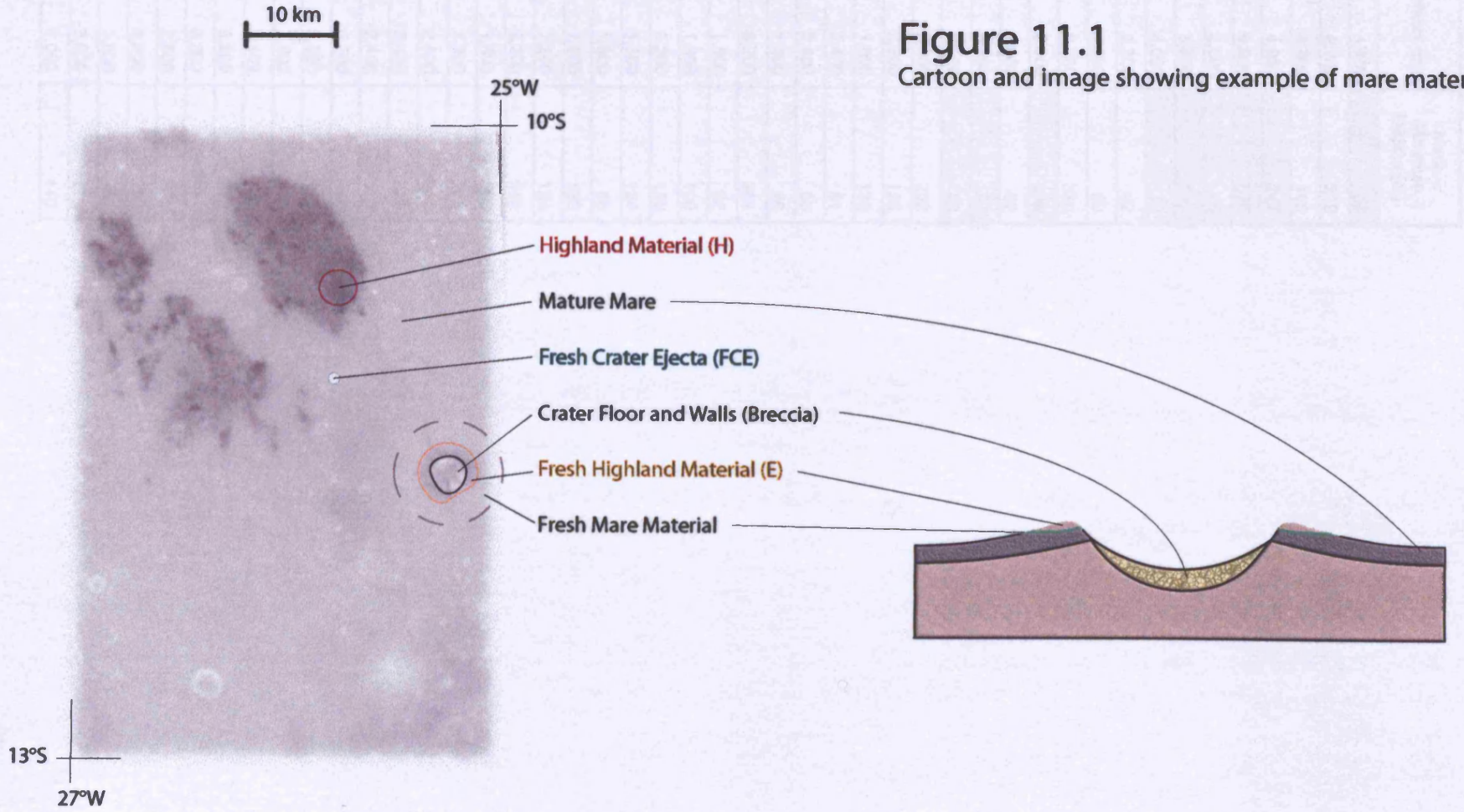

Figure 11.1

Cartoon and image showing example of mare materials

Table 11.1. List of craters and their minimum excavation depths

Crater #	Diameter (m)	Maria - Minimum Depths (m)
2	4,400	54
3	4,200	212
4	4,200	169
5	4,200	247
6	9,800	586
7	2,000	25
8	3,600	188
9	4,000	39
10	2,200	92
11	3,000	59
12	5,000	330
13	5,000	258
14	2,000	52
15	8,000	157
16	3,800	46
17	2,600	232
18	2,200	128
19	1,800	136
20	2,400	91
21	3,400	53
22	1,400	88
23	6,200	261
24	1,800	92
25	1,800	100
26	2,200	159
27	1,800	124
28	1,600	88
29	1,800	135
30	2,200	124
31	3,200	242
32	1,800	160
33	3,200	276
34	2,800	244
35	12,400	526
36	2,400	168
37	6,200	456
38	2,000	173
39	2,800	217
40	2,400	175
41	2,200	140
42	6,800	371
43	2,600	201
44	3,200	280
45	3,800	254
46	3,600	279
47	2,000	140

48	1,800	128
49	3,000	199
50	2,600	191
51	2,000	196
52	2,600	139
53	2,400	177
54	6,000	463
55	14,600	635
56	5,200	292
57	2,400	195
58	2,800	174
59	3,400	227
60	5,200	367
61	2,800	198
62	7,000	394
63	1,800	39
64	2,600	214
65	5,600	384
66	1,600	101
67	2,000	94
68	2,200	102
69	3,200	30
70	3,200	216
71	3,800	164
72	1,600	116
73	1,800	117
74	3,600	154
75	3,000	196
Average	***3,538***	***196***

Figure 11.2

Distribution and location of sampled craters

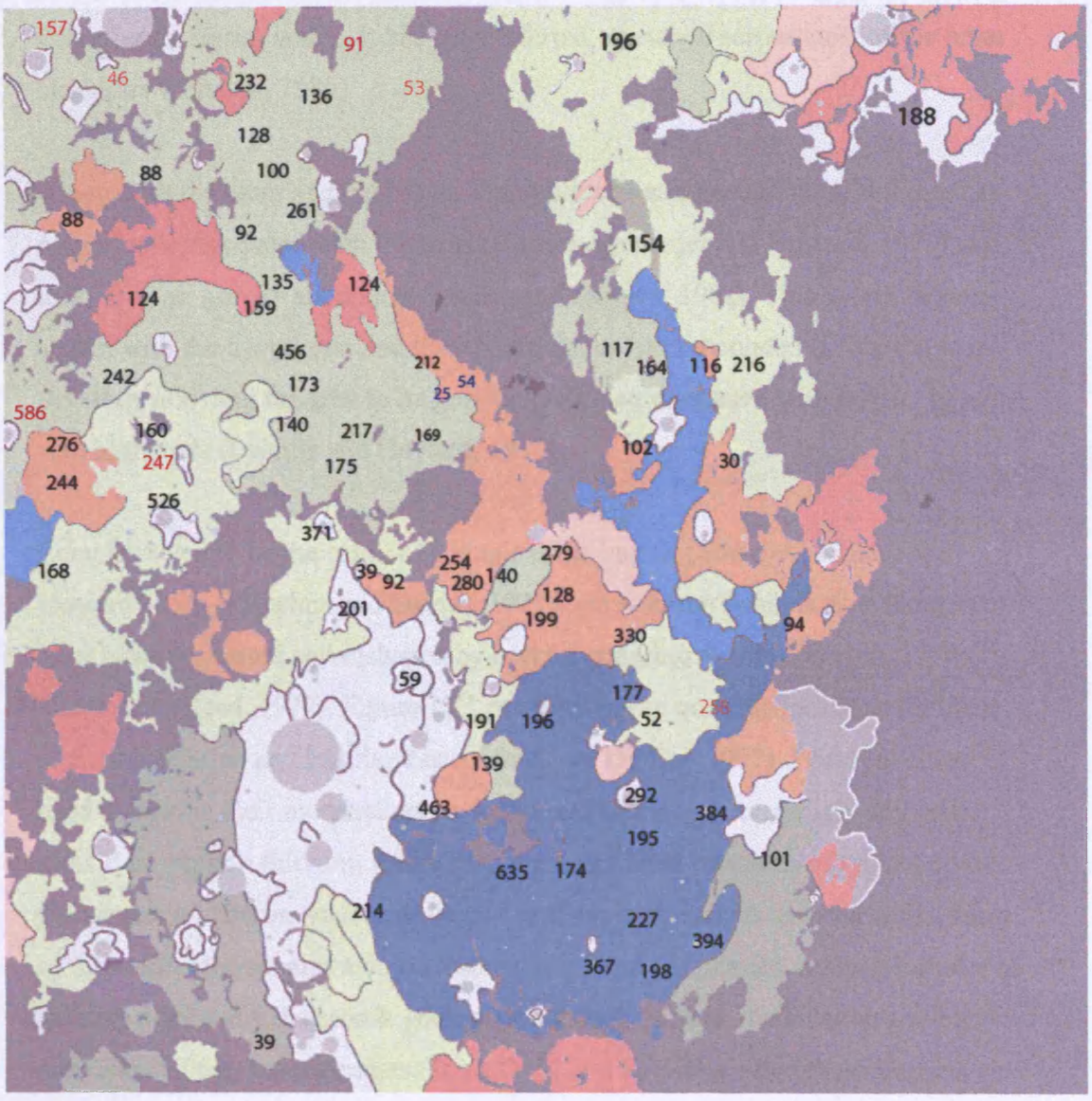

Depths (m)

12.1 Pre-Nectarian impacts - Basin formation

The Nubium basin has long been recognised as belonging to the pre-Nectarian system (Wilshire and Jackson, 1972). Centred at around 19 S 17 W, it has a diameter of ~750 km. It was excavated within the southernmost edge of the older Procellarum Basin, which, it has been inferred, stretched across most of the lunar nearside (Whitaker, 1981).

Along with the other ancient basins Tranquillitatis and Fecunditatis, Nubium has no mascons associated with the maria (Stuart-Alexander and Howard, 1970) and lacks free-air gravity anomalies (Muller and Sjogren, 1968). This would be consistent with the hypothesis that the impact basins had rebounded before the mare flooding, allowing the area to be gravitationally compensated with respect to adjacent highlands (Desiree and Howard, 1970).

Long believed to be the result of a single giant impact (Stuart-Alexander and Howard 1970; Wilhelms and Davies, 1971), the Nubium Basin is now thought to have been excavated and reshaped by several cratering events (De Hon, 1977; Hawke and Head, 1977). Figure 12.1 proposes seven possible locations for these ancient Nectarian and Imbrian craters (also see De Hon 1977). Principal clues used to outline their morphology include mountain ranges seemingly arched around a common fulcrum, which may represent local remnants of typical complex crater's features, such as scalloped circular outlines and terraced walls. Most of these elevated terrains also represent maria/terra boundaries, making it easier to identify potentially diagnostic geological patterns. Indeed, the location and characteristics of the eastern craters (B, C, D, E, and F) indicate that these impacts occurred near or across the ancient highland seashores, i.e. the primordial Nubium Basin's eastern boundaries. Ultimately they contributed in modifying the likely original circular appearance of the Nubium Basin to its present oval shape. Their formation also allowed post-excavation basalt flows to fill in the newly formed

terrain depressions. My results from basalt thickness measurements indeed hint at a possible thickening of the maria near these basins centres (Chapter 11).

A number of wrinkle ridges also appear to follow the proposed circular outlines, suggesting a basin-related seabed morphology expressed on the surface as crustal thrust faults, tension cracks (Hodges, 1973), or local strike slip ridges (Wilson, 1970). Indeed, it is the very absence of concentric curved rills around the margins of the whole Nubium mare, and the central presence of the Wolf crater complex, that points to a punctuated formation the basin.

The largest impact is represented by the remnants of the West Nubium basin (A), a 340 km complex crater (centred around 23 S 23 W) survived by its western mountainous range (also Hartmann and Wood, 1971). On the opposite side of Nubium we can still infer the outlines of a second major impact (B) that excavated a 240 km crater. Subsequently, three smaller objects landed around the same region producing a circular feature (C) of 200 km in diameter (26 S 14 W), including two other smaller craters (D and E, 160 and 55 km, respectively). A 150 km long scarp with a 300 meters drop (Rupes Recta) nearly dissects the larger of these two (D). Still within the Nubium basin (16 S 8 W), one observes a 150 km circular outline (F) that has been extensively modified by later geological events. Hawke and Head (1977) named this crater "west Alphonsus" and proposed a somewhat later formation than the other major impacts.

Mare Cognitum (10 S 23 W, 376 km diameter) is located northwest of Mare Nubium and west of the Fra Mauro peninsula, and it is recognised as being a possible contemporary (Pre-Nectarian) structure to the Nubium basin. If we interpret Montes Riphaeus to the west, together with various other positive relief features in the area, to be product of an ancient massive large impact, we can extrapolate a potential crater size of around 180 km (G), centred at 8 S 23 W. Other surviving major craters from this period also include Fra Mauro, Bonpland, Parry, Deslandres, and Davy *Y*.

The major impact structures listed above do not represent a full survey of pre-Imbrian potential basin locations (see Hawke and Head, 1977 for a more detailed

and alternative account). Figure 12.1 is only a sketch of the most prominent 'circular' shorelines as noticed by the author. Indeed, impacts continued flagellating this region throughout its history, albeit with an exponential decrease with time in both impact rate and projectile size.

12.2 Nectarian Impacts

In Nectarian time, a 20 km cosmic body collided with the Moon at a speed of over 11 km per second, thus excavating a crater of 430 km in diameter just east of the Nubium Basin: the Humorum Basin. Lunar material[1] was ejected radially for hundreds of kilometres, forming a layer some 500 meters deep around the western Nubium Basin (McGetchin *et al.,* 1973). This event also produced a prominent system of concentric grabens across the highland and mountains bordering the Western Nubium (~ 25 S 30 W). These non-sinuous rilles have been interpreted (Shultz, 1974) as products of synthetic and antithetic faulting along lines of geological weaknesses caused by the Humorum basin subsidence in the early stages of basalt flooding.

One of the key characteristics of the Nubium Basin is the large number of buried and partially buried craters scattered across its surface (also described as ghost craters and ringed plains). The basin witnessed extended periods of basaltic flooding which buried all but the largest of the ancient Nectarian structures. Only the breached and eroded rims of craters larger than thirty kilometres protrude above the mare. Examples are Lubiniezky (38 km), Gould (33 km), Opelt (45 km), and Kies (44 km). These observations helped De Hon (1977) to estimate the thickness of mare basalts around these craters of having depths between 600 and 950 meters, compared to a basin average in excess of 500 meters. These figures are somewhat larger than my calculations, but comparable in geographical distribution and mode (Chapter 11).

[1] Ejecta named the 'Vitello Formation' (De Hon, 1977).

12.3 Imbrian Impacts

3.9 billion years ago the Moon received a direct hit by a ~60 km meteorite. It struck the northern hemisphere of the lunar near side creating a 1250 km crater (the Imbrium Basin) while ejecting great volumes of high-energy material. This affected the morphology and surface geology of more than 15% of the whole satellite. Because most of the record of its ejecta falling on both Cognitum and Nubium lowlands has been long hidden by later mare flows, we can only estimate the contribution to its present geology as marginal. On the other hand, parts of the local highlands north of ~10S were extensively modified as a consequence of the Imbrium impact, producing a series of nearly linear ridges and troughs, called the Imbrium Sculpture, extending radially for more than 1000 km from the rim of the basin (Scott, 1972). The deposited material has been named the Fra Mauro Formation. The Imbrium impact also produced vast volumes of ejecta (i.e. Spudis, 1984) that are still exposed largely as flat plains in local depressions (such as the floor of the Parry crater) and 'sheltered' and elevated terrains (Cayley Formation).
Mare infill might have started long before the Imbrium event, but samples brought back by the Apollo and Luna missions indicate massive volcanic activity following this period of heavy bombardment. Vast flows of low-viscosity basaltic materials flooded lunar basins and plains (Wilhelms and McCauley 1971, also units 'x'). In the meantime, meteorites of many sizes and composition were still pounding the lunar surface. Craters Davy (32 km) and Lassell (22 km) probably are surviving examples from this epoch. I estimated that the mare under investigation was hit no less than 18,000 times by objects larger than one kilometre in diameter since the Upper Imbrian time, based on the cratering data from my research.

A small concentric crater, east of Hesiodus (45 km), might have formed when the mare was still in a fluid or at least non-solid state. It features a mounded floor within the inner ring. This type of nested crater is typically found adjacent to or within highly fractured craters bordering the maria (Shultz, 1974).

12.4 Eratosthenian Impacts

During the Eratosthenian Period space bombardment continued to decline, but not before delivering a last, massive strike at the heart of the Western Nubium Basin: the Bullialdus impact. It produced a complex crater of 61 km in diameter displaying the typical morphology for this type of structure; multiple central peaks, a hummocky floor, and a continuous ejecta blanket radiating approximately 15 km away from the crater rim, giving away to a series of grooves and ridges grading into a system of secondary craters (Tompkins *et al.*, 1994).

Figure 12.2 shows the distribution of around thirty large (> 10 km) craters and their associated ejecta belonging to the Early Eratosthenian Period (displayed as colourless craters surrounded by a 'purple' apron). I based my age estimations on the degree, extent, and degradation of the ejecta relatively to the surrounding mare. I also made use of the Clementine multispectral data to investigate their chemical characteristics. Major craters belonging to this group are: Mösting (1 S 6 W, 26 km) and Lansberg (1 S 27 W, 35 km), both characterised by slumped walls and well developed central peaks. Younger craters include Birt (23 S 9 W, 18 km), a deep crater intersected on its eastern rim by an older and smaller crater (7 km). Another interesting crater belonging to this group is located north of the crater Campanus (23 S 29 W, 17 km); it formed over Rimae Hippalus, splitting the round rille into two sections.

12.5 Smaller and fresher craters

I used the diagnostic reflective properties of pyroxene (due to its characteristic 'one micron' absorption signature) to spot and highlight fresh(er) craters resident on the region's mare. Freshly exposed basalts are richer in pyroxene and olivine and appear green/yellow in the 'false colour' (FC) mosaic elaborated from Clementine data. I further filtered and processed this map in order to highlight the geographical distribution of these minerals. Figure 12.3 shows most of the bright (green/yellow) craters and materials scattered across the region.

Multispectral analysis of regolith composition can be complemented by the study of surface albedo variations. There are many physical mechanisms that produce darkening of the lunar surface; in essence, the albedo characteristic of a given regolith is mostly dependent on the average composition of its constituent minerals (mafic or felsic) and its petrological setting (crystalline or vetrified). Both local and exogenic geological events determine soil composition, events which are by definition periodic, relatively short-lived, and often unrelated. In contrast, regolith's petrological properties dynamically change and mutate with time, because of continuous external factors.

I grouped and assigned a wide range of crater and associated ejecta units to three broadly encompassing family types found in the Nubium basin:

(a) High albedo crater floor, walls, and ejecta. Radial rays with similar spectral signature to the materials in the crater are often present.

(b) As *(a)* except for possible impact melt and ray pattern, which have degraded considerably, or even disappeared, on the 1 μm composite. The ejecta blanket may still be visible on the DBA (figure 4.1) image (drawn as a 'purple' apron, in Figure 12.2).

(c) These craters have faded 'green' interiors. In some cases only the crater's walls have exposed fresh material, making the formations appear as bright 'rings'. Ejecta, when visible, follow the same pattern as *(b)*.

It is important to reference Figure 12.2 (an interpretative drawing) with Figure 12.3 (an image) because the apparent diameter of the green 'craters' on the latter often includes materials (impact melt) extending beyond the rim boundary.

As stated before, surface brightness variations may correlate with the age of impact. Subsequent degradation, aging, and gardening of surface material produce 'colour' variations with time. I propose, with due exceptions, type *a* as representing the freshest craters and *c* the oldest.

Type *(c)* has been described earlier in this work as craters belonging to the Early Eratosthenian Period. Even though Bullialdus is the most prominent crater of this type in the region, crater Nicollet (15 km, 22 S 13 W) represents the best example of this characteristic colour pattern. In the multispectral composite it appears as a distinctive and bright green ring in the middle of East Nubium. The colour probably reflects new exposure of relatively pristine subsurface crystalline basalt. The unveiling was most likely caused by gravitationally driven slumping of mature wall surface material. The resulting debris could have contributed to the infilling of the crater floor. Ray material from Tycho was deposited around the crater rim and over the crater floor. An alternative explanation to Nicollet's present morphology would place the time of impact prior to the latest basaltic flooding of the neighbouring region, accompanied by a breach through the northwestern rim and subsequent partial infill of the circular depression. The similar chemical signature of both the crater floor and surrounding regolith would support this hypothesis.

Type *(b)* is the most common amongst younger craters less than ten kilometres in diameter. This might be partly due to the relative size of their ejecta blankets and crater diameters. At this resolution, these formations appear as roughly circular, bright points. Kundt (12 S 12 W) is a 12 km crater east of Guericke. It sits within an older basalt flow (albeit probably one the youngest in the region, according to my study); it is characterised by a very high albedo, typical of 'recent' craters, and an ill defined but still quite visible ejecta blanket. On the FC mosaic the ejecta appears to be of a similar composition to the surface material west of the crater, and altogether much less distinct than its optical counterpart. Instead, the crater disk is very clearly defined and bright green throughout, except for a small circular area in the centre (<13% of the total radius). I interpret this as representing the present crater floor, therefore giving the cavity an almost conical profile. Steep walls encourage gravitationally driven surface material slumping, hence the 'fresh look' of the crater. Alternatively, if the impact had penetrated young crystalline basalts without excavating underlying terra material, we would expect the ejecta to be similar in composition to the surrounding geology and reflect the spatial distribution of the target basalts. Indeed, this seems to be the case, with a chemical east-west asymmetry resulting from the meteorite impacting the bordering region between two distinct lava flows.

Most bright-ray systems darken slowly with apparent crater age (e.g. Shoemaker *et al.*, 1962), mainly due to regional re-equalisation of surface porosity of terrains previously compacted by the energy of the blast. I based my assumptions of age discrimination on this plausible physical model. Nevertheless, it is clear that other factors influence the rate of degradation and darkening of this lunar material. In particular one should include the deposition of secondary debris, which mineralogical composition and physical structure relates to the primary impact, and the properties and composition of the subregolith layers they subsequently excavate (Shultz, 1974). The two most visible large-rayed lunar craters are Copernicus (93 km) and Tycho (85 km). The former was directly dated, following the Apollo missions, at 810 Ma old, while Tycho is believed to be around 100 Ma old (Wilhelms 1987). Both craters' ejecta reached the study region, supplying an invaluable tool for comparing and dating affected geological features.

12.6 Copernican Impacts

Type *(a)* craters are largely represented by impacts smaller than 10 km in diameter. Despite their relatively modest size, they stand out against the background by virtue of their contrasting ejecta composition, exposed less-gardened soil, and ray system patterns. These bright features may represent the youngest impact events, stretching from the late Eratosthenian period to the Copernican Period (last billion years), with some examples not older than a few million years. High-albedo ejecta blanket characterises most of these youngest impacts. A small, 2 km (*a*) simple crater (14 S 11 W) displays a complex system of concentric and radial albedo patterns (figure 12.4). The first (*b*) of these extends beyond the uplifted rim for ~1.5 km and it is characterised by rillelike features that possess rims. It appears extremely bright in the optical image and vivid green in the FC composite.

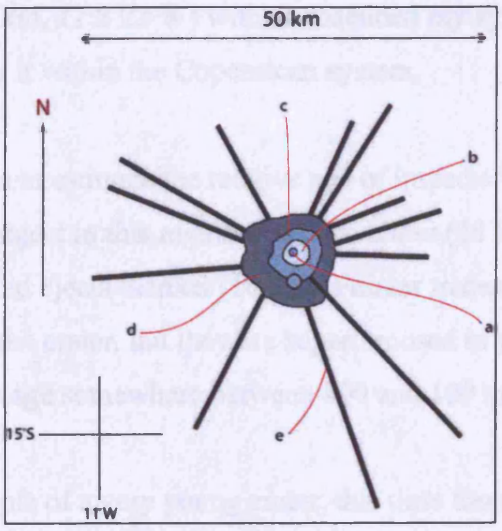

Figure 12.4. Ejecta units a-e

A continuous lower-albedo terrain (*c*), extends a further ~4 km from *b*: chemically similar to inner materials, its distribution appears to reflect the (inferred) pre-existing terrain morphology. The outermost continuous ring of ejecta *(d)* stretches out for a further 7 km, and it is characterised by an asymmetric distribution of materials, found to be darker in the west quadrant, and somewhat brighter in the east. A system of rays (*e*) can be detected up to ~50 km from the centre of impact, overlaying two chemically distinct terrains, thus suggesting a younger age than both. The rays appear better preserved than those of Tycho, to the south, suggesting an age of impact perhaps much more recent than 100 million years. The high-albedo character of the (primary) ejecta could be in part explained by the chemical composition of the excavated material. Chemical and morphologic characteristics of the impacted mare lead us to believe it to be relatively shallow. Consequently, even a small impact would have penetrated down to the potential high-albedo crustal rock layer and incorporated it with the ejected materials. This would imply that the observed brightness of the ejecta to be largely due to contrasting mineralogy rather than maturity of the regolith. Nevertheless, the FC image suggests a strong 1 μm absorption band material covering a ~13 km radius, nearly ten times the actual crater diameter. This indicates a strong basaltic composition, still at least crystalline in character. All this evidence points to a geologically recent impact.

A larger crater (~4.5 km, 17 S 22 W) with an extended ray system lies within Bullialdus ejecta, placing it within the Copernican system.

Tycho's rays allow us to estimate the relative age of impacts within Southern Nubium. The brightest object in this region is a 3 km crater (28 S 19 W, north of Pitatus) and its associated ejecta blanket (10 km). Fainter traces can be detected up to 30 km away from the crater, but they are superimposed in places by rays from Tycho, suggesting an age somewhere between 800 and 100 million years.

Lastly, another example of a very young crater, this time found in the northern part of my region close to the lunar equator (2 S 8 W). This 4 km crater clearly postdates both the Eratosthenian crater Lalande and Copernicus, suggesting a time of formation within the last 800 Ma.

Figure 12.1

Map showing proposed ancient craters' locations

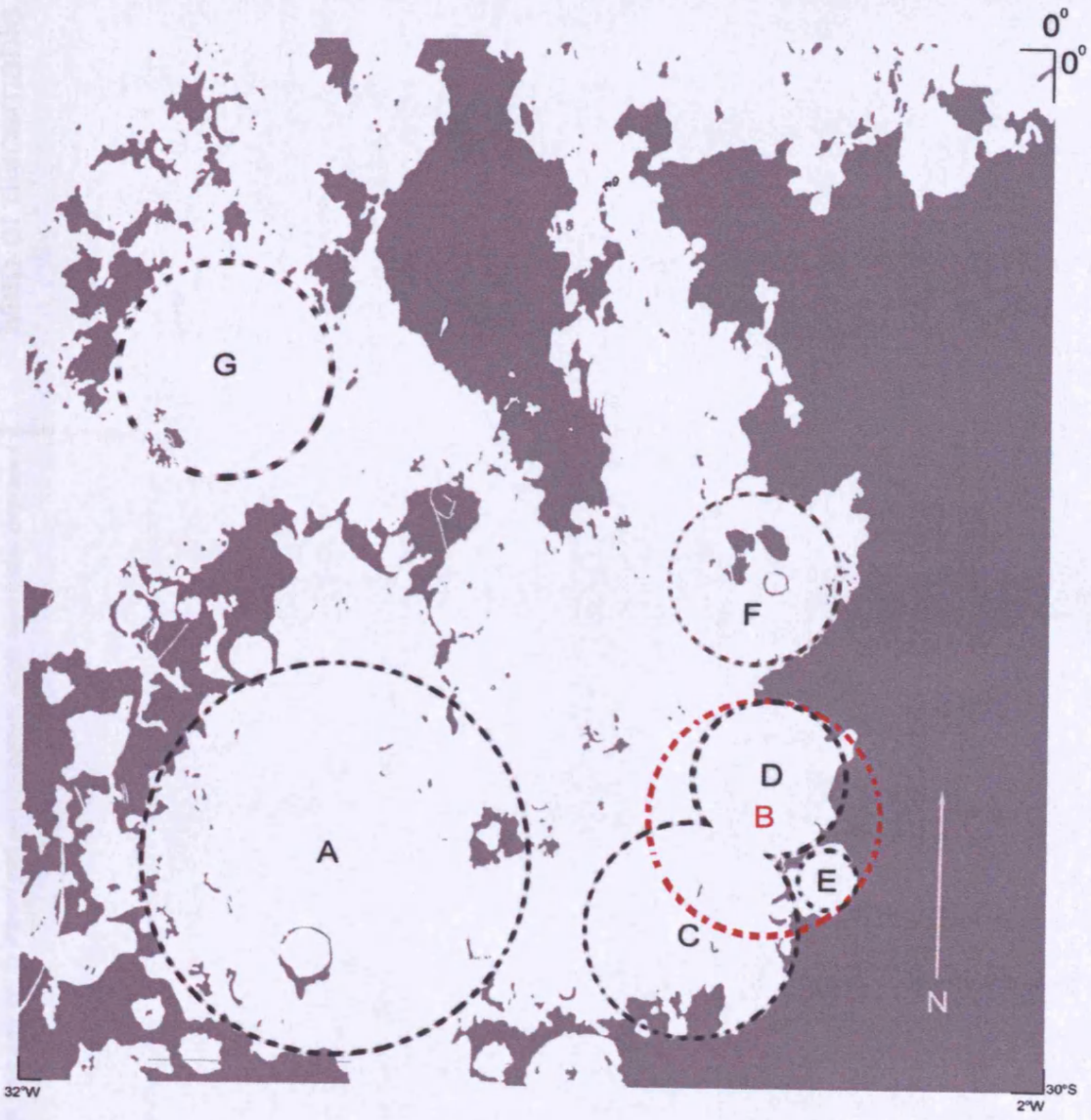

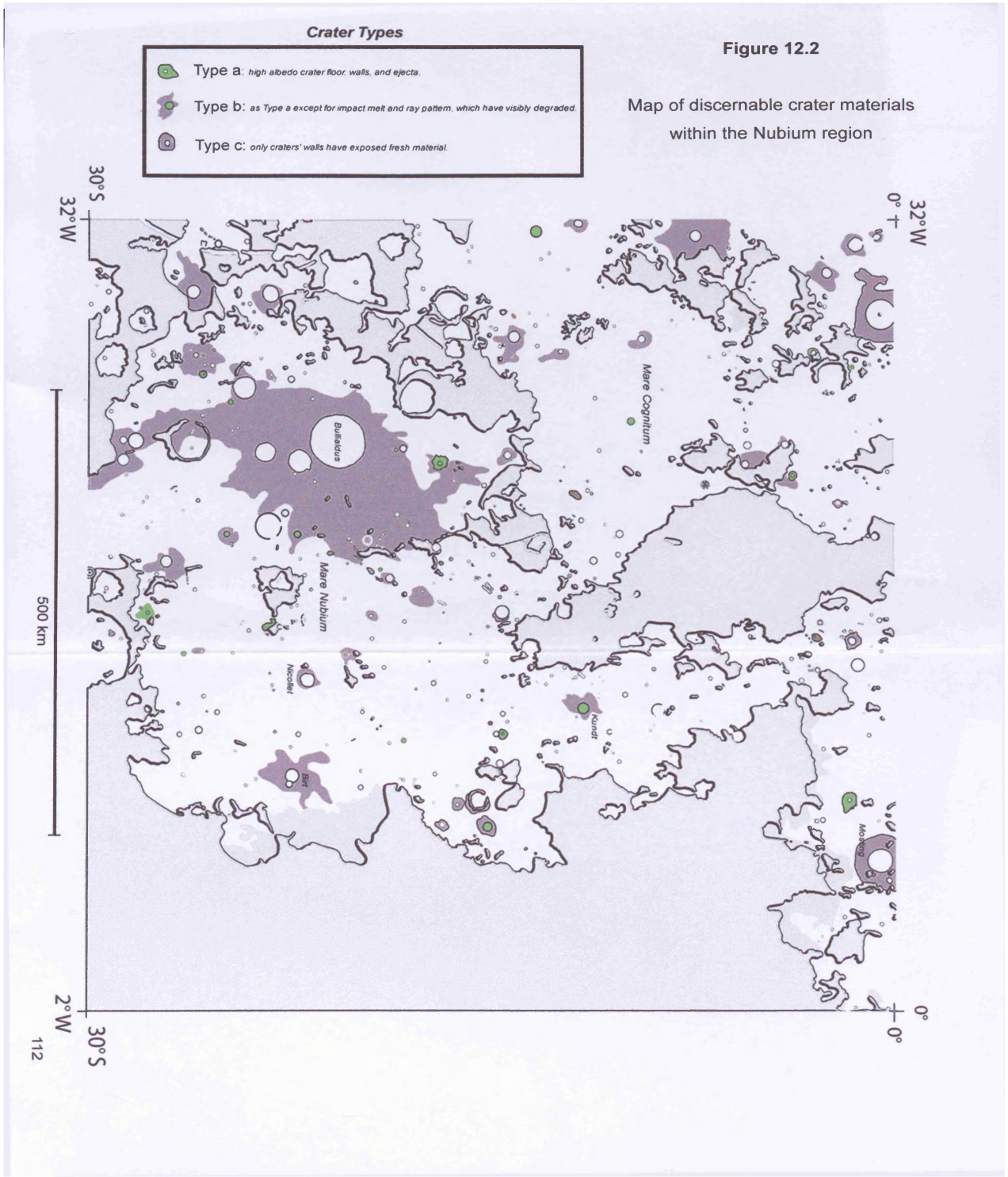

Figure 12.2

Map of discernable crater materials within the Nubium region

Figure 12.3

Location of 'fresh' crystalline material within the Nubium basin

CHAPTER 13 GEOLOGY AND GEOMORPHOLOGY (PART I)

MARE NUBIUM AND MARE COGNITUM

The area under study offers examples of many geological and morphological features typical of the lunar surface. Following my previous study of craters and various circular depressions in the region, I am now going to focus on other characteristic mare features in some detail.

13.1 Rilles

Mare Nubium shares its western border with Mare Humorum, a Nectarian basin mainly flooded by basaltic materials in late Imbrian time. Rimae Hippalus, a system of regular round rilles, cuts across parts of the region just west of Nubium (Figure 13.1). They are concentric and parallel to the Humorum basin, suggesting a related origin. These U-shaped valleys, up to 3 km wide, stretch across both highlands and maria with no apparent change in morphology, indicating a later formation. Nevertheless, there is some evidence that the easternmost rilles (~25 S 28 W) might have been partially infilled by later basaltic flows, an assumption based on their apparent shallower depth and flatter graben floor. There are no obvious compositional differences with the surrounding terrains except for the innermost ring (relating to Humorum) outlined by 'brighter' levées, possibly caused by gravitational slumping of surface materials down the steepest walls. It is understood that these circum-maria rilles represent tensile features that developed along extensional crustal weaknesses (Solomon and Head, 1979) because of subsidence within the basin following inundation.

Another example of wide nonsinuous rille is found in the proximity of crater Hesiodus, cutting across Rupes Mercator (~30 S 20 W), and continuing into Palus Epidemiarum. It progressively widens to over 3 km towards the southwestern end. The origin of this formation is less clear, since it does not seem to reflect any obvious local morphology. It is possible that it might have formed as a tension fracture or boundary fault caused by shear stresses following the early mare flooding of the West Nubium basin. On closer inspection, the rille shows an identical

chemical signature and cratering frequency to those of the surrounding terrain, placing its formation to a period prior to the latest local flood volcanism. High-resolution Orbiter images reveal many more nonsinuous rilles scattered across the region. Most are located near terra-mare boundaries; some cut across these boundaries (Rimae Hippalus, rille centred at 16 S 27 W, etc.), but most tend to follow the coastal topography. One of the best examples is located east of Fra Mauro (5 S 21 W), stretching north to south for nearly 100 km. It is also joined halfway by an eastern 'tributary', originating from the nearby terra-mare boundary (or, less likely, 'flowing' from the main rille to the highland). This evidence leads to an interpretation of these rilles as either: a system of collapsed lava tubes or channels (Greeley, 1971), or the result of erosion caused by large volumes of lava flowing southwards (Carr, 1974). Some rilles do not follow the distribution patterns described above, and they can be used as diagnostic indicators of centres of igneous activity.

13.2 Rima Birt

One of the best known rilles on the nearside of the Moon can be found in the Eastern Nubium, northwest of the crater Birt, from which it takes its name: Rima Birt (figure 13.2). It is a two-headed rille just over 60 km in length with elongated craters at each end. There is also a complex of three domes at the south end of the Rima, further supporting an endo-genetic origin of this formation (Salimbeni *et al.*, 2002). Rima Birt, along with the nearby Rupes Recta (an eastern parallel scarp, ~120 km long), probably are related geological expressions both located within a massive flooded crater (~160 km diameter, 'D', figure 12.1), now a constituent part of the East Nubium Basin. This ancient crater is delineated in the east by highland morphology, in the north by Promontorium Taenarium, and in the east by a system of concentric mare ridges, which may correspond to the ancient main rim. High resolution images reveal the rille to consist of a system of three distinctive sections (figure 13.2c): rille 'a' is a shallow linear depression, around 6 km long, possibly representing an earlier graben formation that was subsequently partly infilled by mare basalts. Alternatively, it might represent a rectilinear rille carved by basaltic output from vent 'b'. A large area of darker material surrounds this elongated depression (Figure 13.2a). Clementine FC image shows this area as bright red and the walls of the caldera green/yellow (Figure 13.2b).

The superposition of this low-albedo material over the surrounding maria suggests a relatively recent igneous activity (late Eratosthenian?). Eruptions were probably in the form of fissure eruptions with characteristic pyroclastic falls (Lucey *et al.*, 1986). Magmas were channelled and flowed south along paths governed by local gradient and morphology. It is plausible that volcanic material filled pre-existing depressions created by ground extension (as in the nearby Rupes Recta) and subsequent faulting.

Fig. 13.2a

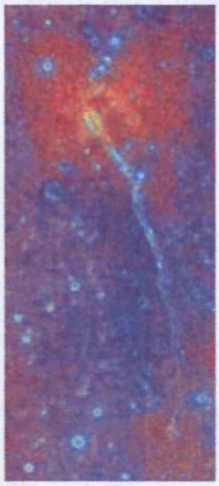

Fig. 13.2b

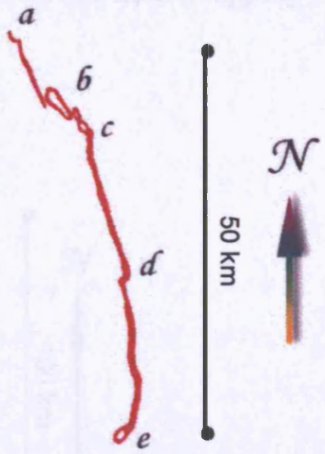

Fig. 13.2c

Figure 13.2. Rima Birt

Discontinuities *'c'* and *'d'* are offsets that suggest a punctuated origin for the rille, rather than a singular and continuous flow feature. There is also some weak photographic evidence that *'c'* might represent an area of igneous activity, suggested by caldera-like depressions. Fig. 13.2a indeed displays some dark terrain surrounding it. Closer study of high-resolution images does not offer conclusive evidence for this hypothesis.

North of *'b'*, leading to the circular crater *'a'* I notice a shallow, nearly rectilinear 'U' shaped channel. I believe it to be a flow channel originating from a secondary vent on the western flanks of volcano *'b'*. This relatively modest lava outpouring flowed north towards impact crater *'a'*, where it split around the depression and terminated its journey. Depression *'e'* defines the southernmost end of the rille. Both optical and composite images hint at it being another fissure crater that witnessed an earlier and possibly less extended eruptive phase than *'b'*. It is plausible that this vent might have fed the southern section of the rille. In this scenario,

lavas that flows from *'b'* (plus *'c'*?) and *'e'* might have met around *'d'*, embaying a local geographical hollow.

13.3 Rupes Recta

As mentioned above, about 40 km east of Rima Birt we find another outstanding geological formation: Rupes Recta (or Straight Fault). It stretches for ~120 km, dipping down 240-300 m towards the West with an apparent width of 2500 m. Thus, it is not a steep scarp but a moderate slope (a thrust) dipping 7 degrees (1:9) west-southwest.

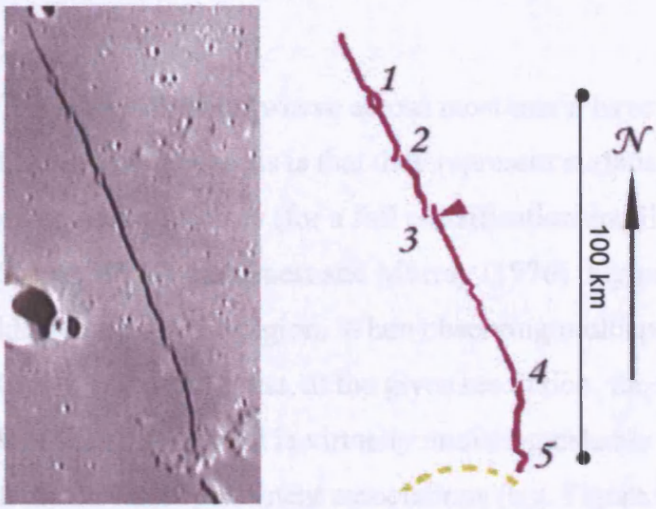

Figure 13.3. Rupes Recta

On closer inspection the fault shows discontinuities and meanderings away from an ideal straight line. Extensive lava flooding of the Eastern Nubium basin may have disturbed the isostatic conditions across the projected crater 'B' (figure 12.1). Differential basaltic uploading towards the centre of Nubium would have challenged the tensile strength of the peripheral maria. By looking at the regional morphology, one can draw an ideal line from the tip of Promontorium Taenarium to the Southern edge of crater 'D'. This line, corresponding to the fault, can be interpreted as the result of extensional faulting produced by differential movement of the mare terrain away from the highland. I speculate that the location of the fracture might relate to the ancient terra-mare coastal line, subsequently obliterated by impact 'B'. While the fault's footwall might have been part of the surrounding highland to the east, the hanging wall was progressively sinking west,

seemingly uncoupled from the underlying structure. These contrasting forces produced shear fractures that eventually created Rupes Recta. Figure 13.3 shows the fault in some detail. Notice discontinuities and offsets (2, 3, and 4) typical of this type of listric faults; an extensional duplex can be seen at 1, with its characteristic 'horse' to the west of the fracture. In its southern end, the fault continues across elevated terra material. This suggests a relatively recent formation of the fracture. It also appears to validate the hypothesis of the origin of the fault prior to the formation of crater 'D' and related to the projected primordial terra-mare boundary at the time of impact 'B'. In essence, Rupes Recta is the result of deep-seated morphology.

13.4 Wrinkle Ridges

The ridges that interweave across most maria have been extensively studied and the present consensus is that they represent surface expressions of a number of geological processes (for a full classification and list of references, please refer to Shultz (1974) and Guest and Murray (1976). Figure 13.1 sketches the major wrinkle systems in the region. When observing multispectral images of the maria, it becomes apparent that, at the given resolution, the composition make up of each wrinkle arrangement is virtually undistinguishable from the surrounding basalts. Only the most prominent associations (e.g. Figure 13.4a, 17-23 S 10 W) appear brighter (in this case, due to their lower Ti content, Figure 13.4c) than the surrounding mare.

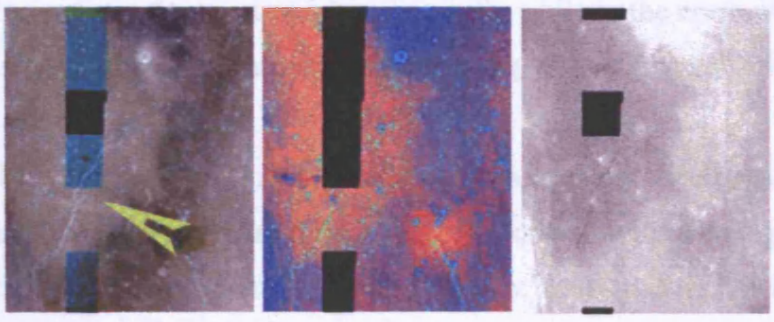

Figure 13.4. ***a.*** Enhanced 'true colours'. ***b.*** False colour composite. ***c.*** Ti map.

Comparing with medium resolution Orbiter IV images ($113H_1$ and H_2) of the same region, one can see that this wrinkle ridge system, spreading in an arcuate geometry for nearly 400 km, is intimately linked with the regional morphology

and petrology of the terrains it 'crosses'. The ridge appears much smoother and subdued away from the highlighted area. I interpret this change in chemistry as the result of later and regional basaltic flooding which affected the area around Figure 13.4. The high albedo characteristic of this section of the complex may represent a relatively pristine example of the original ridge. This system (no more than a few tens of meters high) can be associated with the geometry of the impacts that created and shaped the East Nubium basin. As we have seen, Rupes Recta might represent an extensional fracture resulting from slippage or mare crusting over deep-seated terrain boundaries, triggered by sagging of the central part of the basin. Subsidence would have generated compressional stresses further west of the area, resulting in buckling and low angle thrusting. The arcuate and antithetic character of the entire ridge system may also in part reveal buried structures such as the western rims of structures 'b' and 'c' (Figure 13.2c), brought into relief by differential compaction of overlying deposits (Shultz, 1974).

Apart from the ridge considered above, most other complexes in the eastern part of our region run parallel to the coastal outlines. None of these ridge associations appear to have been modified by the basaltic flows that presumably followed their formation. They clearly overlap regions of different age and compositions, sharing their varying surface chemistry and crater frequencies.
Some ridges often reflect buried structures as in the case of the partially exposed craters near crater Davy (13 S 10 W); their presence is betrayed by a broken circular system of terra material in the south, while in the north we observe a partial continuation of the ancient rim by contiguous ridge association.

Towards the centre of the Nubium Basin, south of the Fra Mauro peninsula, there is an area rich in mare ridges. A system of semi-circular ridges appears to follow the projected eastern rims of the partially buried craters Opelt and Gould. Indeed, a curved ridge suggests the presence of a further fully buried crater just south of Gould. The progressive higher degree of embayment and submersion would confirm the suspicion that mare thickness in this area increases southwards, towards the centre of the basin.

The ridge east of Opelt appears to branch north straight through 60 km of highland terrain where it then develops into a system of rilles. It is possible that the rille belonged to a large network of lava channels and tubes that extended beyond the existing area. Following later stages of mare flooding, the lower laying terra to the south was embayed by advancing lavas, subsequently burying the existing uncollapsed lava tubes. The wrinkle ridge may represent the positive relief of the underlying structure.

A mare ridge more than 100 km long cuts across the same three buried craters. It is apparent that its origin may reside outside the immediate neighbouring area. If we examine Figure 13.1, a drawing of the major morphological characteristics of the region, we notice how most ridges in the Western Nubium are distributed in a circular pattern with epicentre Bullialdus, around 140 km west of its crater rim. It is likely that this major impact event might have triggered massive compressional forces away from the blast, causing buckling of crustal material out to a given radius. There is some evidence to suggest (here and De Hon 1977) that the west Nubium basin is characterised by a central thick lens of basalt (750 m). It is therefore possible that the ridge system could have developed only where the lens thinned out to a shallower depth (~200 m in my estimates), allowing eastern bound radial tectonic movements of the decoupled plate, causing it to collide and buckle against other mare plates. Ultimately, this would have produced crustal thrust faults.

Another arrangement of ridges can be found just SW (25 S 18 W) of the Wolf crater. 30 km west of the crater we can clearly see the outline of a large (~30 km), completely embayed crater; it is difficult to classify this positive relief structure either as an actual rim remnant of the ghost crater, or the high relief mare pattern betraying the underlying topography. The Fe image suggests rim material to be still exposed in the northern part of the formation, but the southern portion's composition is virtually indistinguishable from the surrounding mare. It is probable that this section of the rim was draped over by later flooding events, and is still detectable by virtue of changes in mare elevation.

A few kilometres south of this formation, a local ridge system appears to form a broken circular pattern of around 40 km in diameter. Again, this might betray the presence of another buried structure, deep within the mare strata. The origin of this complex (either igneous, impact, or some combination) is impossible to ascertain only from surface expressions.

Despite my observations so far, it is important to stress that most ridge systems do not follow obvious genealogical patterns. For instance, an extended *en èchelon* ridge association, nearly 160 km long, appears to stretch from within the mare north of Lubiniezky (16 S 21 W), straight through remnants of the concentric mountains created by shock waves from the west Nubium impact, and continuing north towards Mare Cognitum.
Detailed examination of high-resolution photographs (Orbiter IV $125H_2$) and Clementine 'true' colour image (figure 4.1), leads to the conclusion that the relationship between the sections of the ridge appears to be only superficial and coincidental. The southern branch may represent either common compressional folds or thrust faults. There is a possibility that we might be looking instead at a lava flow front, by virtue of the fact that the mountain range that separates the basins would have been embayed and flooded by incoming igneous material. Random heavy cratering, following the formation of the west Nubium Basin, could have locally 'flattened' this part of the range, allowing mare to invade the area. In this scenario, the present day ridges would just mirror pre-existing contours and underlying topography.

Further west on the other side of the mountains, a rather complex system of braided ridges appear to head in a northerly direction. This system displays relatively high albedo and figures prominently on several lunar maps (e.g. Schimerman, 1975). The enhanced brightness of the local high-relief geological features is mostly due to the effects of channelled ejecta from the Tycho crater. This indeed represents a crossroad region, where an ocean (Oceanus Procellarum) meets both an ancient sea (Mare Cognitum) and a relatively young one (Mare Humorum). Photographic evidence suggests the existence of a large volcanic centre, with associated eruptive edifices, further west of this complex (17 S 32 W) pointing to a possible cogenesis with the ridges. More likely, the actual braided nature of this

ridge complex might be diagnostic of a tectonic origin, a hypothesis based on local topography. This includes a system of crustal fractures, plus deep-seated faults and rills stretching across diverse terrains (maria, highlands, and crater basins), and the nearby edifice of the Humorum basin.

Mare Cognitum is relatively devoid of an extensive ridge system. Only a subdued concentric band of compressional ridges suggest down warp of the basin under successive basalt fillings. A more prominent (elevated) northwestern section of this system may indicate a mare ridge formed by compaction (thrust fault), rather than compression (an antiform).

Ultimately, the formation of large-scale wrinkle ridges across the lunar surface (including highlands) can be associated with global thermal stresses. During the first billion of years, the Moon's crust experienced a period of thermal expansion, mainly fuelled by latent accretion and radiogenic heat, in association with strong tidal stresses, followed by a progressively cooling regime (Solomon and Head, 1979). During this latest phase, which started approximately 3.6 Ga, the lunar surface rocks compacted and contracted, resulting in progressive accumulation of compressional stresses, which eventually manifested as thrust faults and folds along lines of crustal weaknesses.

Figure 13.1

Main geological features within
the Nubium region

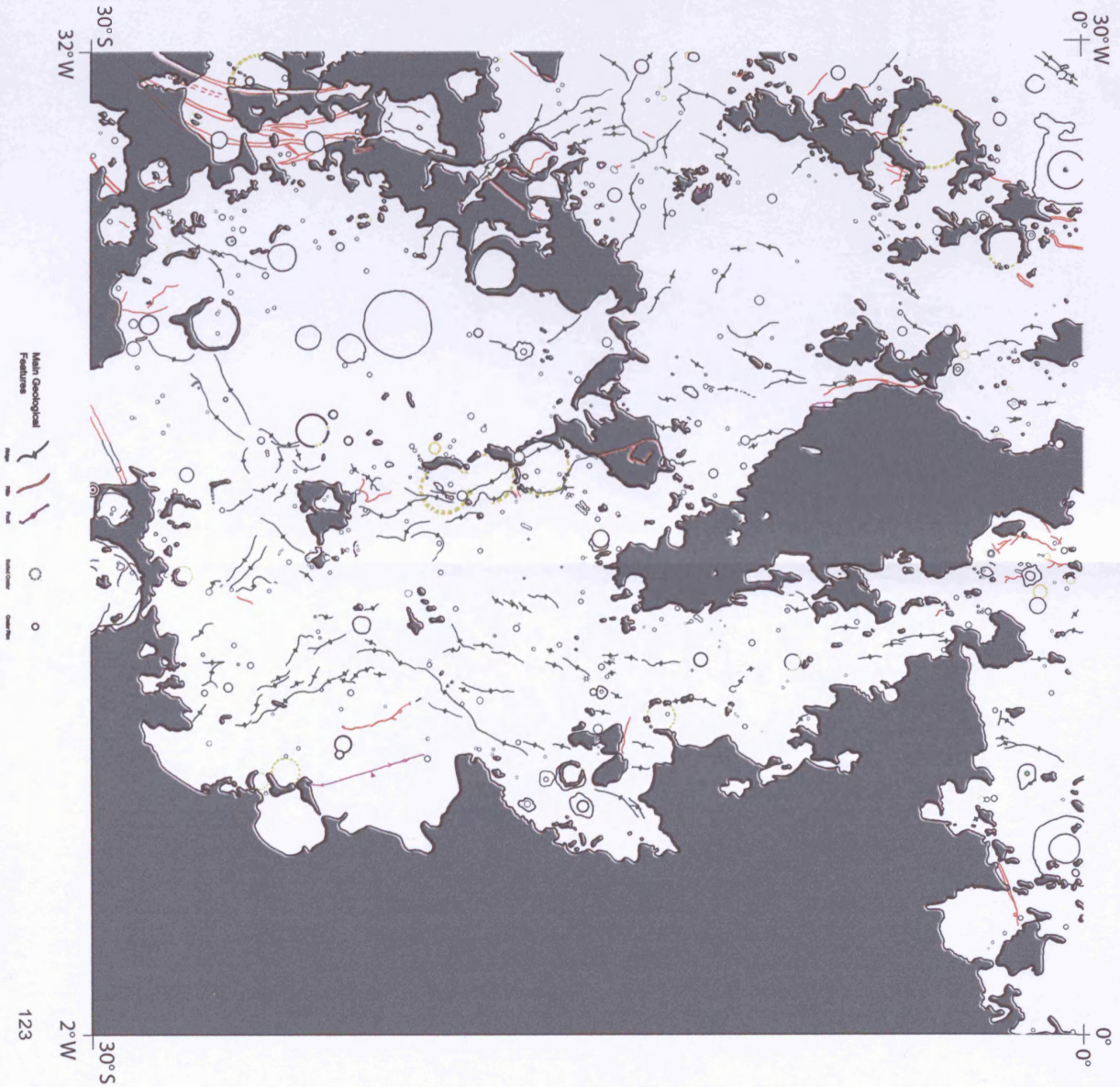

14.1 Positive relief volcanic landforms

Basaltic mare covers 43% (~358,000 km^2) of the region under study. Such large-scale distribution of deposits suggests massive outpouring of low-viscosity lava, which embayed and infilled areas of low-relief topography. By taking an average lava thickness of 600 meters (e.g. Head, 1975; this work chapter 11), one can estimate a volume of about 0.22 x 10^6 km^3. This can be compared to major flood basalt provinces on Earth; according to Yoder (1988) the Columbia River basalts took around 10 million years to build up a volume of about 0.20 x 10^6 km^3 over an area of approx. 160,000 km^2 (a rate of extrusion averaging 0.02 km^3/yr).

There is geological and direct petrological evidence (i.e. Apollo missions' samples) that indicates a start of the eruptive phase perhaps as early as 4.3 Ga (Shultz and Spudis 1983), volumetrically peaking between 3.6 and 3.2 Ga (BVSP 1981), and gradually grinding to a virtual halt around one billion year ago. Nevertheless, there is also some evidence of minor eruptive phenomena postdating the Copernicus impact (e.g. Shultz and Spudis, 1983).

The apparent paucity of point source igneous centres suggests monogenetic volcanoes of the fissure type, where lava is extruded from linear cracks over a protracted, albeit single, eruptive phase. Some postulate that several wrinkle ridges may represent fissures through which the bulk of the mare basalts erupted (e.g. Fielder and Fielder, 1968). Because of the relatively low elevation of fissure vents, albedo variations are often absent or subtle at best. Unfortunately, multispectral remote sensing also fails to unveil these potential igneous sources because of their compositional affinity with the body of the flow. Nevertheless, elevated volcanic structures are generally much easier to spot optically: when pyroclastic material is present, either as building material or pyroclastics, volcanic constructs become clearly identifiable against the surrounding terrains.

14.2 Central Vents

Figure 14.1 shows a positive relief feature (a). The edifice appears darker than the (higher) surrounding upland islets. Based on my study of Lunar Orbiter medium resolution images, I believe it to be an example of a mare dome, or shield volcano. The 6 km edifice has a summit crater 1.5 km in diameter. Unlike its neighbouring islands, both the albedo and chemical signatures of the basaltic material appear identical to the composition of the surrounding mare, suggesting a related origin. Figure 13.1 shows an extended system of sinuous rilles to the west of this area, following the Fra Mauro terrain contour (e.g. (f)).

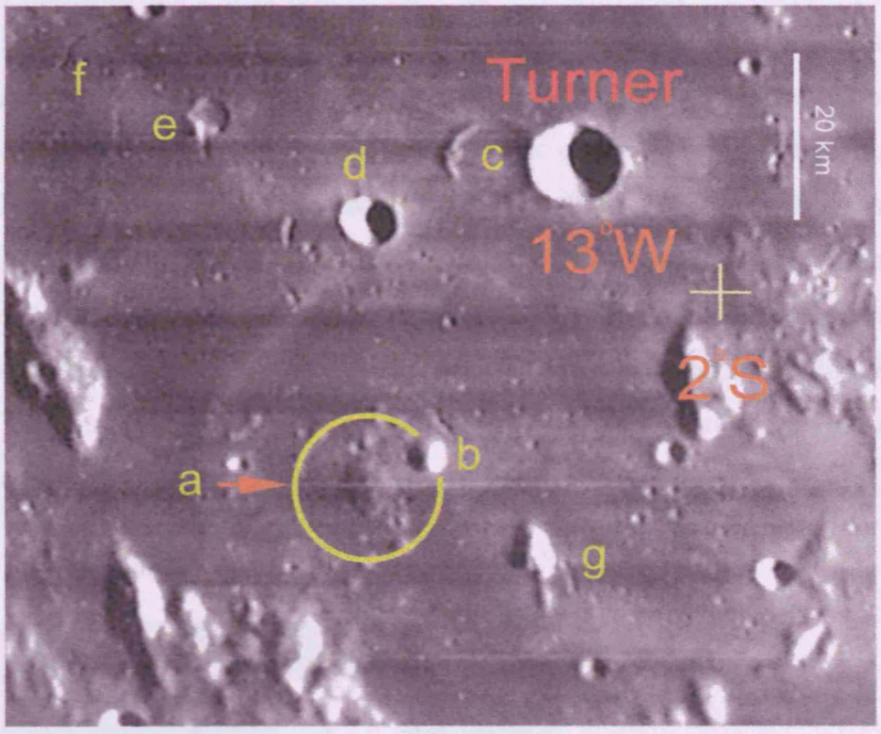

Figure 14.1. Proposed volcanic edifice (Orbiter IV 114H_3, NASA)

(e) represents a circular depression feature, possibly an ancient and flooded crater. The obvious lack of a rim and its irregular plan suggests an origin by collapse (caldera). A deep, rectilinear rille crosses its southern rim, probably genetically related to the caldera. Alternatively, it might be associated with a sinuous rille that terminates (or originates?) on the northern rim of the depression.

This near-equatorial area also offers many more examples of the complex and dynamic events that shaped the lunar surface. The meteorite that created Turner nearly impacted a more ancient crater (c), probably pre-Imbrian in age, and filled

almost to its rim by successive basaltic flows. One can also argue that the asymmetric relief of the relic crater rim may be the result of material accumulation from the Turner excavation.

Only a few kilometres away, a fresher crater (d) still clearly displays an asymmetrical ejecta pattern, with a well-developed ray pointing southwest. The iron image (Figure 4.3) suggests a composition similar to the neighbouring highlands, possibly due to admixing of melted mare material with excavated crustal rock. If this hypothesis were to be correct, it would explain in part the survival history of the ejecta pattern as a function of both its age and composition.

I mapped (g) and (b) as catenæ, strings of closely spaced depressions created by secondary impacts. Alternatively, the absence of clearly related main cratering events nearby may indicate an endogenetic origin, possibly the product of collapsed sections of a lava tube (e.g. Greeley, 1971). This hypothesis is made even more intriguing by the presence of narrow, rectilinear oblong structure protruding south of the nearby upland fragment (g), possibly an uncollapsed lava tube. (b) could also be interpreted as volcanic in origin and associated with the neighbouring pitted linear depression. This mare dome might represent an intrusion such as a shallow subsurface laccolith.

14.3 Tephra Cone

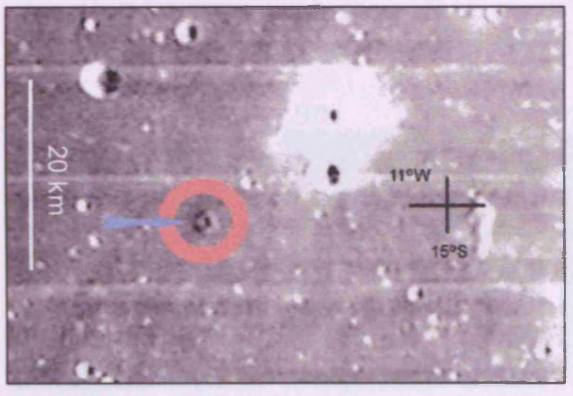

Figure 14.2. Tephra cone (Orbiter IV 113H_2, NASA)

Figure 14.2 shows a potentially different kind of single vent. This cone, around 3 km in diameter, stands out very clearly from the surrounding mare plains because of its low albedo, nearly perfectly circular outline, and summit crater 1.2 km

across. This type of volcano on Earth originates from the explosive eruption and consequent accumulation of pyroclastic material.

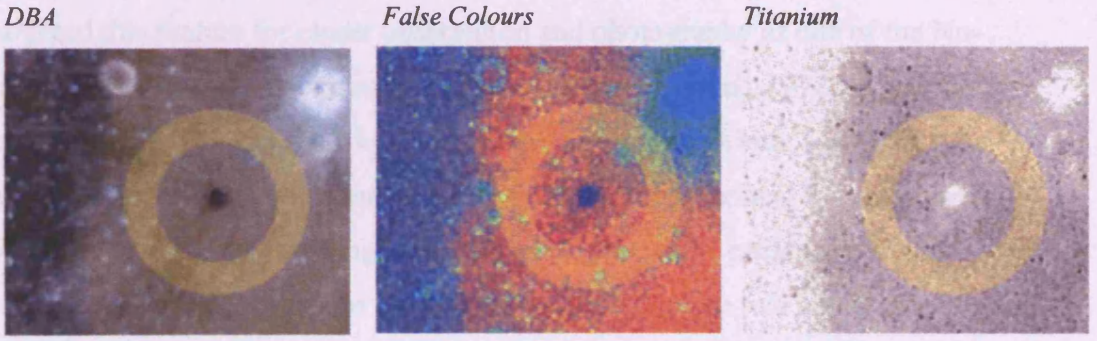

Figure 14.3. Clementine multispectral images.

This cone was known from ground-based observations and visually confirmed by the command module pilot of the Apollo 16 (Whitaker 1972c). Clementine images confirm the nature of this eruptive centre. Both the FC and Ti images (Figure 14.3) indicate a basaltic composition similar to the mare unit further to the west. It also appears that the ejecta material from the nearby fresh impact has not affected the volcanic edifice. I suspect this to be the result of the relatively high elevation of the cone, rather than an origin post-dating the impact.

The titanium-rich composition would probably reflect both the age of the formation, i.e. much more recent than the latest mare flooding of the area, and composition, similar to the later Ti-richer basaltic flows.

14.4 Lassell-Guericke region

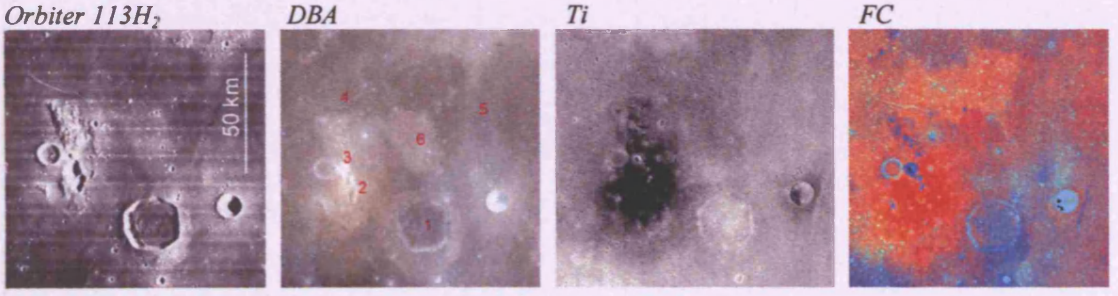

Figure 14.4. Lassell-Guericke region - **15S 7W**. Each frame 'band' in Orbiter image is ~11.35 km wide.

20 km northwest of the polygonal crater Lassell ((1), Figures 14.4 and 14.5) is another noteworthy geological formation. This area effectively belongs to the upland

terrain (i.e. (6)), and as such, is outside the scope of this research. Nevertheless, further analyses of multispectral data suggest a possible geological link with the extrusive history of the region. The scientific team behind the Apollo 16 mission targeted this feature for closer observation and photography as one of the Nubium/Cognitum maria's 'strange' red soils (Mattingly *et al.*, 1972), consequently named Lunar Red Spots (Hawke *et al.*, 2001). Both the Orbiter and DBA (enhanced Clementine colour image) photographs show an upland formation nearly 50 km long. The most striking aspect of this terrain is the presence of a number of overlapping deep depressions on its southern half (2). The two halves converge in the middle towards a small crater (~1.5 km) next to Lassell *C*, and its related ejecta (3). A 27 km long rille (4) appears to originate close to the eastern flank of the northern upland and follows its contour in a northeasterly direction. A well-defined system of radial ridges 'connects' this area to the highlands in the north (5). Clementine maps indicate that the upland area has a similar Fe content to that of the nearby highlands. Nevertheless, the False Colour image, designed to dramatically enhance differences in the reflectance characteristic of the regolith, shows a remarkably intense 'red' mantling of the terrain leading to Lassell (2). The area is also extremely low in titanium (<1.5% TiO_2). The little crater (3) stands out as a bright blue dot, which includes its immediate ejecta. Rille (4)'s 'head' can now be observed as a blue spot within the upland formation; also the channel maintains a similar width along its length.

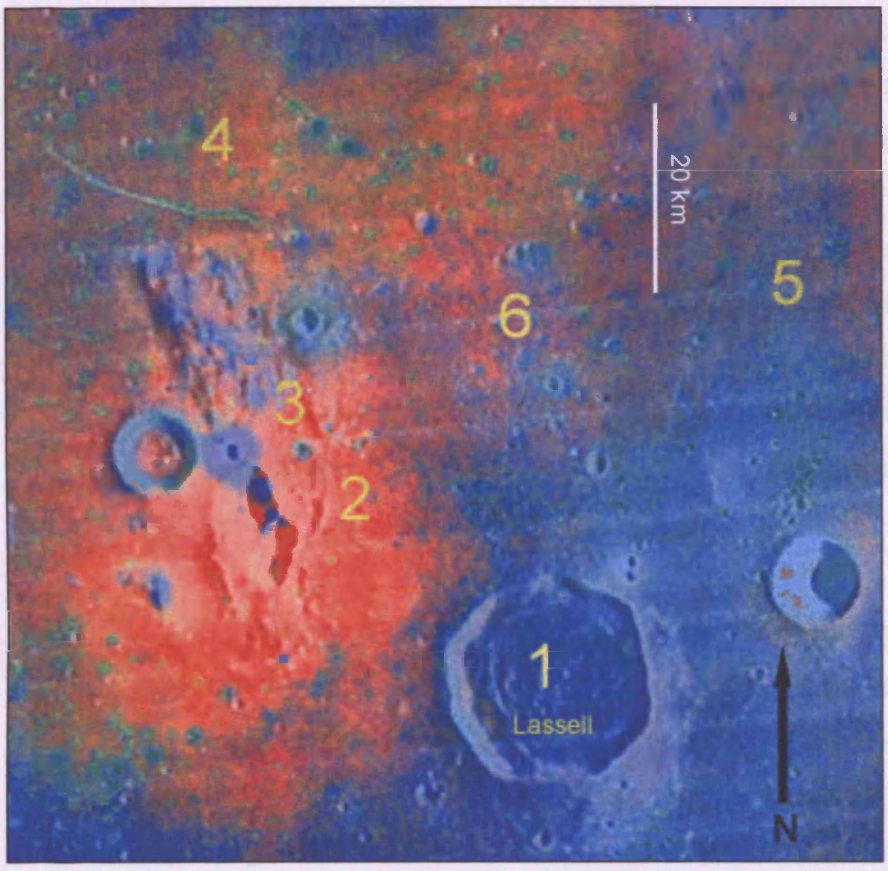

Figure 14.5. FC composite superimposed on Orbiter IV image.

My interpretation is that the two overlapping craters and the connected oblong depression represent the remains of collapse craters (calderas). The red soil might owe its colour to the presence of glassy scoria ejected from the eruptive centres as original volcanic ash and cinders (McEwen *et al.*, 1994). This volcanic material should not be confused with the "mysterious" 'orange glasses', which are mainly composed of black crystalline droplets containing ilmenite, olivine, spinel, and native iron (McKay *et al.*, 1991). Its low titanium composition also suggests that we are looking at an example of Very-Low-Ti (VLT) mare basalt, which is comparable in composition to green-glass pyroclastic deposits (McKay *et al.*, 1991). The asymmetrical distribution pattern of this material points to a progressive migratory trend of active vents. Indeed, the centre of the red soil blanket appears to coincide with the southernmost caldera. The titanium image also tells us that pyroclastics barely spilled over Lassell *C*'s eastern rim, failing to alter its crater floor (superficial) composition. This evidence reinforces the hypothesis that the volcano to erupt last was the one furthest away from it.

Alternatively, but in my view, much less likely, the nearby fresh crater (Figure 14.2, north of the tephra cone) might have caused admixing of the uppermost lunar soil west of Lassell *C*, causing partial dilution and masking of the original soils.

Crater (3) is probably unrelated to the igneous history of the region, and of impact origin. Its fresh ejecta material extends one crater-radius away from the excavation and it can be seen spilling over the oblong caldera in the south. More crystalline material is exposed on the eastern flanks of the depression, possibly caused by partial collapse and denudation of this section of the wall triggered by the nearby impact event.

Rille (4) is one of the most clearly defined in the whole of the Nubium/Cognitum region. Clementine composites confirm the presence of fresh basalt exposed on the rille walls, which appears bright green in colour (FC) and of low-Ti content (Ti image). Its southern cobra head is located near the upland, and it might be associated with the igneous activities within the local area. I speculate that the rille may be related to a less violent period of volcanic activity, accompanied by the outpouring of larger volumes of basaltic material. Photographic evidence points to a time of formation postdating the neighbouring igneous events.

In synthesis, the origin of this centre of igneous activity may relate to its location within an ancient impact basin (Fig. 12.1, basin 'F'). Structural fractures, created by the excavation process and subsequent crustal readjustments, would have made it possible for fractionated melts to rise to the surface. The range of effusive phenomena would reflect varying basaltic compositions, volatile content, and volumetric outputs throughout the geological history of this area.

14.5 Area near Nicollet crater

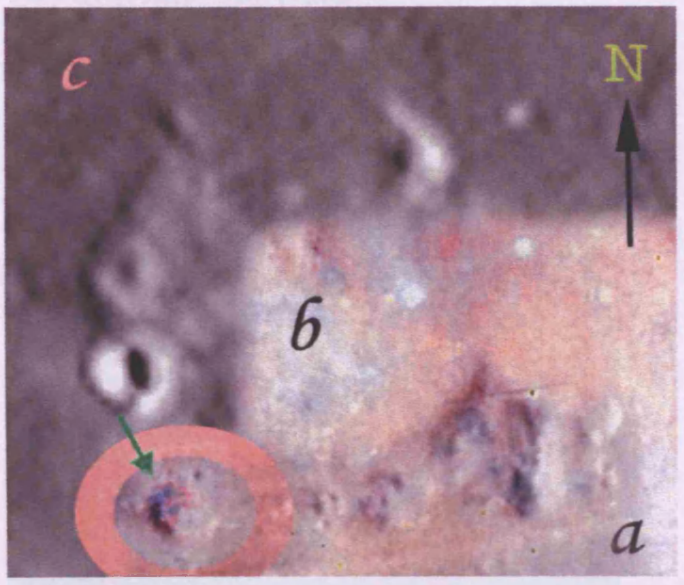

Figure 14.6. Images from: a) Orbiter VI; b) Clementine FC; c) NASA Consolidated Atlas.

Photo composite figure 14.6 (20 S 13 W) shows an area in central East Nubium, 37 km north of crater Nicollet, of around 2,500 km^2. The most prominent upland terrain in the south may represent the remains of either an ancient mountain range or highland, later reshaped and partially submerged by mare infill. Indeed this terra appears heavily reworked and cratered.

The land next to '*b*' is more modest in relief, but features two adjacent craters through different stages of degradation. One could interpret this upland as volcanic in origin, the smaller of the cones as a potential vent, the source of the relatively (to the average mare) viscous lava that spread eastwards.

Further south in the image I highlighted a round edifice four kilometres in diameter. Its morphology and geological settings suggest an extrusive origin. This lunar dome stands out from the surrounding plains because of its low titanium content and highly pitted surface. Judging by its topography, the most likely scenario is that it represents a mare dome, probably the lunar equivalent of a small terrestrial lava shield.

14.6 Area near Wolf crater

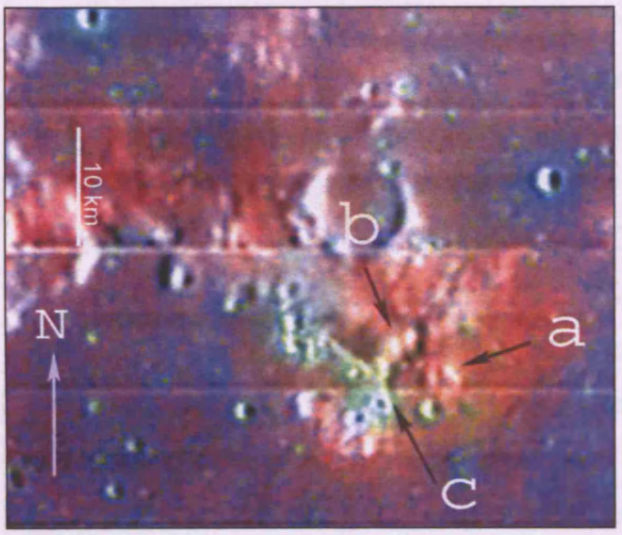

Figure 14.7. Photo composite (Clementine FC + Orbiter VI $120H_1$)

The elevated edifice of the Wolf crater dominates the central Nubium Basin (23 S 17 W). This 'clover leaf' shaped depression has an infilled floor with similar materials to the surrounding mare. The crater rim is clearly breached in several points, most noticeably in the northwest and southwest. Various episodes of lava flows might have exploited these locations and equalised the crater floor to the outside plains. Wolf could be interpreted as the remnant of a pre-Imbrian impact. Isostatic compensation of the Nubium Basin would have produced tectonic movements and readjustments likely to deform, and in places fracture, the original circular morphology of the crater. Compressional surface forces, following the filling of the basin by dense basaltic material, would have also contributed to down warping and subsidence of the basin floor, along with localised inundations of the uplifted rim and impact ejecta (e.g. Desiree *et al.,* 1970). Its present morphology would be the result of billion of years of geologic modification of the underlying crustal material and overlying mare.

Shultz (1974) classifies Wolf as an ancient caldera, an interpretation that could explain the irregular shape of the hypothetical collapsed volcanic structure, without resorting to the agency of external tectonic forces. In contrast, Spudis (personal communication, 2003) believes the Wolf complex to have formed by the impact of material from the Imbrian basin excavation.

East of Wolf crater there is a smaller area with a complex morphology dominated by a 7.5 km inundated crater (Fig. 14.7). Many circular depressions less than 1.5 km in diameter characterise this upland. I observe two sets of crater chains converging at point 'c', the one to the right ('b') showing much larger pit diameters. It is likely that these formations represent dissimilar effusive phenomena. Crater chain 'b' is probably an example of a relatively recent collapsed lava tube, which will probably degrade into a sinuous rille. The Clementine composite shows regolith around the area to be similar in composition to that found around Lassell *C* (Fig. 14.5). I propose 'b' as the source of this material, erupted in the style of lava fountaining, scattering pyroclastic materials over the surrounding area.

Further evidence that this might be a complex eruptive centre is represented by 'a', a kilometre wide volcano just south of 'b'. It is possible, albeit unlikely, that this tephra cone might be the major source of the red material, giving the geometry of propagation of the ejected fragments of fluid lava.

14.7 Low-albedo areas

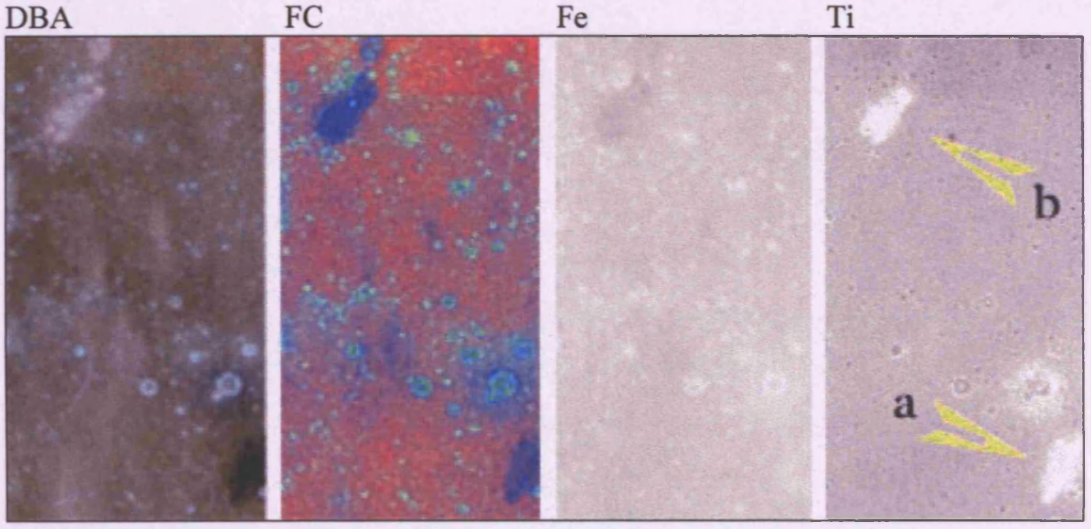

Figure 14.8. Clementine multispectral composites.

Clementine (stretched) real colour images (DBA) feature numerous areas of exceptionally low albedo. One of these can be found near the southernmost edge of Mare Cognitum (~ 12 S 19 W, 'a', Fig. 14.8). This dark mantle, covering an area of around 90 km^2, appears dark blue in the FC image and it shows much higher

titanium content than the surrounding terrain (a). It is interesting to compare this area with a similarly sized one further north in the images (b). Although displaying very similar titanium content, (b) is much brighter in appearance than (a) and with a significantly lower iron signature.

Figure 14.9 merges an Orbiter IV photo-composite with its corresponding Clementine multispectral image (FC image from Fig. 14.8). (b) displays a similar composition and morphology to elevated terrains belonging to partially-flooded, large ancient craters, such as the exposed western rim of Opelt. Their flatter continuum (blue) may be the result of exposure of fresher material caused by gravitational removal of surface cover. This terrain would contain a higher percentage of crystalline minerals that have yet to suffer from the same degree of weathering as the maria covering the surrounding plains. (c) is a section of a well-developed wrinkle ridge system stretching across the region. Whatever the origin of this feature might be, it is clear that its present composition and degradation is similar to the mare, suggesting either a contemporary formation (extrusive), or a later tectonic deformation.

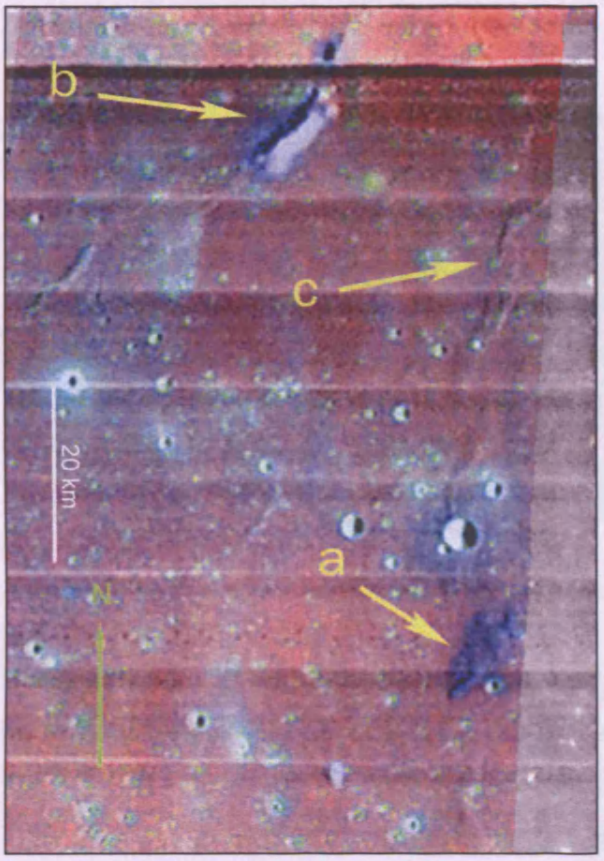

Figure 14.9. Photo composite (Clementine FC + Orbiter VI 125H_2)

(a) is the most intriguing geological feature on this image. Compositionally, it has very low albedo and high 415/750-nm ratio. Its elevated topography appears to be the result of interconnecting steep domes, all terminating in flat plateaus except for a possible cone situated at the tail end of the scorpion-shaped unit.

This formation appears relatively young, at least in comparison to the surrounding mare, due to its low crater density and 'fresher' colour. Evidence suggests the hypothesis that we might be observing a post-Imbrium extrusive edifice(s), namely a post-mare mafic emplacement along the general trend of crustal weakness in the region. The morphology of this volcanic edifice would be controlled by the rate of effusion rather than viscosity of the lava. Alternatively, the formation could be much older than the mare. In this case, it would represent early-Imbrian eruptions of more viscous, Ti-rich basaltic lavas (Hiesinger *et al.*, 2001) originating from shallow subsurface laccoliths.

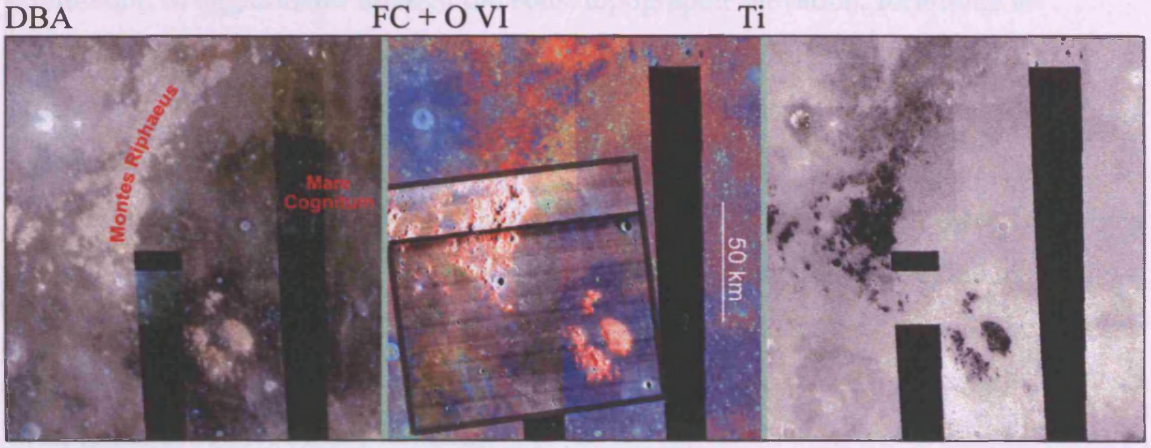

Figure 14.10. Clementine images and montage (Clementine FC + Orbiter VI 132H_2)

Ewen Whitaker, the command module pilot on the Apollo 16 mission, was asked to take colour pictures of parts of the western side of the Mare Cognitum, including Montes Riphaeus. This location, among a few other sample areas, was deemed of special geological interest because of its distinct coloration (one of the Lunar Red Soils) in comparison to similar morphologies (a very strong ultraviolet absorption).

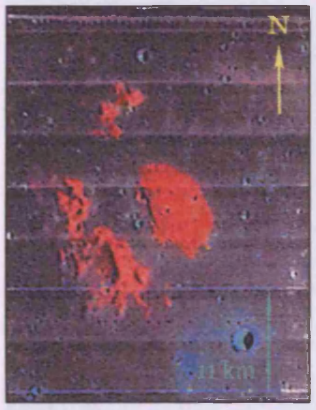

Figure 14.11. Photo composite (Clementine FC + Orbiter VI 125H_2)

Indeed, the southern half of the mountains and the patches of highland within Cognitum (Fig. 14.11) are of particular high albedo. Their chemical signature is very distinctive even from the other terra formations scattered across the region. The regolith contains high percentage of lithologies rich in plagioclase feldspar (Al-Ca silicate) and low in mafic (iron-bearing) minerals. The redness of the regolith (Figs. 14.10 and 14.11), and the high crater frequency on the surface, points

to the classification of these uplands as mature soils. Relatively undisturbed accumulation of agglutinates through the eons, topographic elevation, fortuitous location away from major ejecta deposition and igneous centres, and a well-defined placement among relatively dark, young Ti-rich mare conjured the present striking appearance of these lands.

The original mineralogy might have also contributed to the formation of these Lunar Red Spots (LRS). Malin (1974) interpreted LRS as surface manifestation of pre-mare KREEP basalts. Wood and Head (1975) proposed that the origin of the red materials might be traced back to post-Imbrian extrusive volcanic activity prior to major regional mare flooding.

14.9 Area within Montes Riphaeus

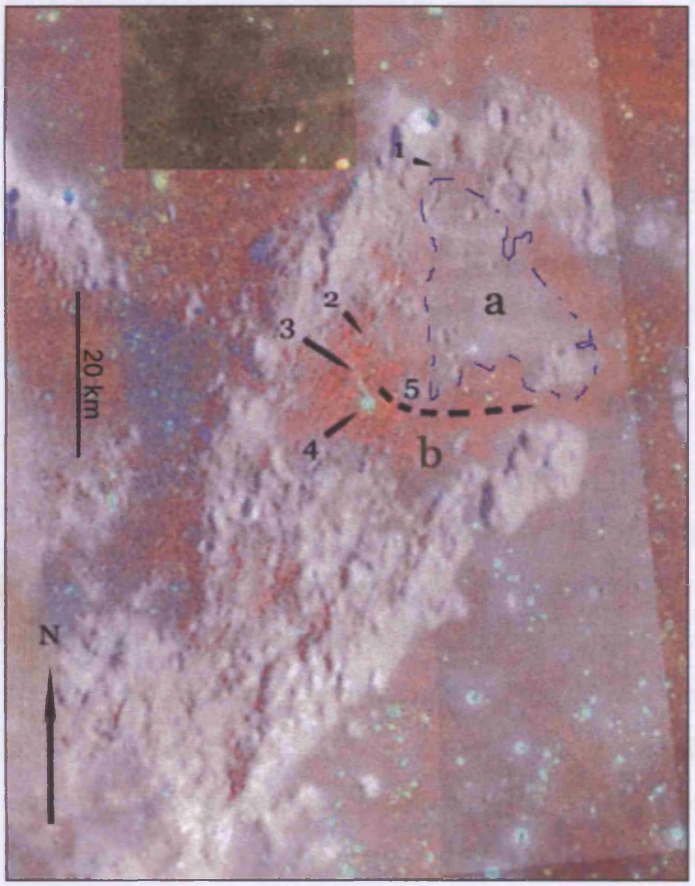

Figure 14.12. Photo composite (DBA, Orbiter IV 125H_3, and FC) of northern Montes Riphaeus.

Figure 14.12 reveals one more potential centre of igneous activity in the region. The northernmost section of the Montes Riphaeus encloses a low topography, smooth terrain valley partially flooded by maria apparently originating from the

eastern plains. I also noticed a complex system of rilles, with a major sinuous channel meandering at the foot of the mountain ridge (1-2).

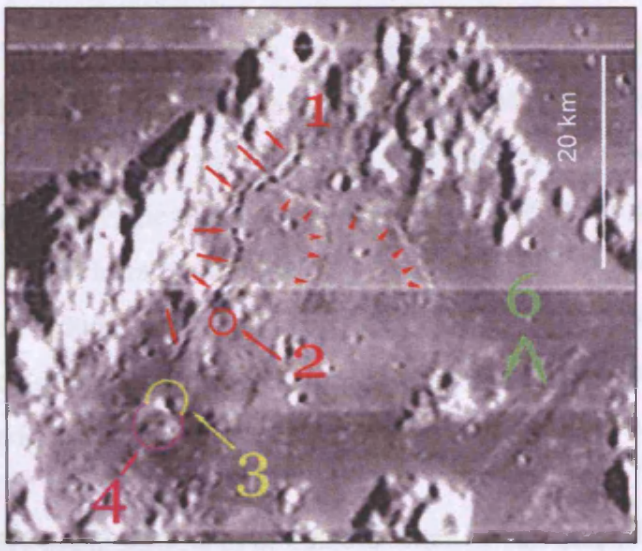

Figure 14.13. Orbiter IV image ($125H_3$) of northern Montes Riphaeus.

The lava channels branching to the right of the main rille are somewhat smaller and with sections still partially roofed over (Fig. 14.13). 3 is a rimless circular depression and 4 is a relatively fresh crater surrounded by bright ejecta. Two large nonsinuous rilles (6) can also be found within the mare in the east. Collapsed pits of the lava tubes are clearly visible on the shorter rille on the left.

The Clementine False Colour image (layer in Fig. 14.12) suggests two different lithologies within the bay: bright red material covering most of the soil (a) surrounded by orange regolith (b). The redder material is chemically and chronologically related to highland rocks (Fe-poor and highly cratered) but of flatter topography. It might represent an example of the Cayley Formation, terra plains of Imbrian age (Morris *et al.*, 1967). A possible source of the orange material, as described in this work as containing a high percentage of volcanic glass, is crater (3), a rimless circular depression at one end of the rille (1). It is plausible that larger volumes of lavas accompanied the eruption of pyroclastics, spreading from the igneous source eastward (as suggested by arrow '5', Fig. 14.12). Rilles (6) appear to follow the general morphological trend of the area and may represent surface expressions of deep-seated crustal weaknesses, possibly relating to the Cognitum Basin, and ultimately controlled by tectonic forces.

15.1 Introduction

Using Clementine data, I produced a preliminary map of compositionally distinct flow units within the mare (figure 7.1). Most of these early units were later discarded as being the product of gaps and errors in the original data and, more significantly, the result of erroneous inclusion of exogenetic geological phenomena, such as terrain mantling by crater ejecta. Indeed, the name of the basin itself, Sea of Clouds, relates to the confusing optical lithology caused by the regional criss-crossing of ejecta from fresh major craters, both nearby (Copernicus and Tycho) and within (Bullialdus and Lalande, among others).

By using subsets of scanned Orbiter IV images, I determined the relative age of each potential unit flow by establishing the size and frequency distribution of its crater population (craters >0.5 km). A trend of correlation between age and chemistry of each area was observed (Figs. 10.3-10.10). I made further use of the Clementine multispectral images (Fe sensitive waveband) to sample and estimate mare thickness in various locations where impacts have excavated highland material (Chapter 11).

All the results for the potential 82 distinctive units (Table 10.1) were then tabulated and ordered in accordance with their chemical signature and inferred age (Table 10.2). Further grouping and incorporations led to my final estimate of eight distinctive principal mare unit types (table10.4), each belonging to a distinctive age group. Plotting the geochemical results against age of deposition produced Figure 10.9. This invited a further grouping into three major periods of igneous activity in the area (Table 10.5, Fig. 10.11)
Potential igneous centres were also identified and discussed, along with other major geomorphological formations (Chapter 12, Fig. 12.1). Table 11.2 gathers all the data accumulated in this research and Figure 15.1 represents the final map incorporating my findings.

15.2 Titanium

The composition of the liquid produced by the melting of typical mantle rocks (such as peridotite) depends both on the degree of partial melting and on the conditions of melting (i.e. pressure, temperature, and volatile content, Hall 1996). Titanium is an important elemental indicator in mare basalt petrogenesis, reflecting the composition and state of the partial melt at depth (Elphic *et al.*, 2001a). Generally, higher melting temperatures (and consequent increasing percentage of melting) will yield progressively lower concentrations of TiO_2 in the liquid (e.g.. Mysen and Kushiro,1977).

Analysis of lunar rock samples initially suggested a strong bimodal distribution of titanium contents in mare basalt (peaks at ~2.5-3 wt% TiO_2 and, the least abundant, at 12-13 wt%). Multispectral data from Earth-based observations and various remote-sensing missions (mostly Galileo, Clementine, and Prospector), have been exploited to estimate the overall distribution of titanium in the lunar regolith (e.g. Lucey *et al.,* 1998, 2000a). These studies have suggested a continuous gradation from very-low-Ti to high-Ti mare basalts (Giguere *et al.*, 2000).

My results (Chapter 8) place the Nubium/Cognitum basalts in the low-Ti category (1-5 wt% TiO_2), with nearly 80% of the data in the range of 3-5 wt% (Fig. 8.4). These values should be shifted upwards (~20% according to Giguere *et al.*, 2000) because of admixing and 'contamination' of the mare regolith with materials excavated or ejected from underlying and neighbouring highland rocks. Taking into account these adjustments, my figures are still comparable with samples of low-Ti basalts and the inferred unimodal trend.

15.3 Iron

Hand-specimens of low-titanium lunar basalts average ~20.2 wt% FeO (Jolliff *et al.,* 2000). Multispectral Clementine data indicate that the majority (~90%) of the mare region under investigation has iron content between 18 and 22 wt% (chapter 8). In particular, Fe variances tend to concentrate towards two compositional poles of ~20 wt% and, a much smaller one, of ~15 wt% (figure 8.5). The latter

low FeO concentration in the regolith is probably due to 'contamination' by horizontal and/or vertical admixing with iron-poor highland material.

15.4 Ages

My crater count averages a frequency of 5.6×10^{-2} km^{-2} for craters larger than 500 m in diameter (Chapter 10). This translates into an inferred mean age of 3320 ± 100 Ma for the majority of the exposed lava flows. Ages range between 2300 (±100) Ma and 3400 (±100) Ma. These figures are translations from my crater counting frequency data (Table 10.1) to the estimate age of known lunar sites (Apollo and Luna, Fig. 10.2). Due to the uncertainties of this method, crater densities per unit area were used as a more reliable comparative tool.

15.5 Mare Thickness

My results confirm previous studies on mare thickness variations (e.g. De Hon, 1977): a possible thickening of the basalt layers in the centre of the Nubium basin (~17 W 23 S), the northern eastern region (~10 W 20 S), and northern border (~18 W 17 S). I am also reporting two areas of mare thickening in Mare Cognitum: one just north of Dorney D (26 W 12 S) and another near the middle of the basin (23 W 10 S).

15.6 Below the sea

The western side of the basin has been studied in greater detail thanks to the exposed geology around and within the Bullialdus crater, the product of a large Eratosthenian-age impact. By making use of ground-based near-infrared spectra images to estimate the composition of the impact's ejecta and central peak, Tompkins *et al.* (1993, 1994) proposed the following stratigraphy for the Western Nubium basin, shown as Fig. 15.2:

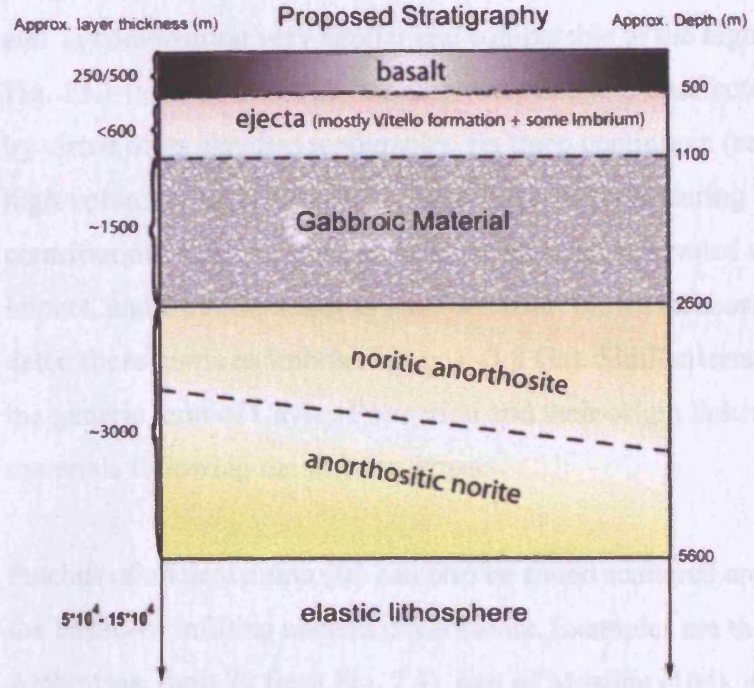

Figure 15.2. Proposed stratigraphy (adapted from Tompkins *et al,* (1994) and Hall and Solomon (1986).

15.7 Basaltic Flows

Basaltic flood volcanism to form the mare appears to have taken place many times throughout the lifetime of the region. Evidence is provided by hundreds of embayed and emplaced morphological features, such as ghost craters, partially infilled craters, buried uplands, locally obliterated ejecta mantles and so on. Figure 15.1 shows nine types of exposed mare basalts, igneous centres and associated flow units, surface morphologies such as ridges, rilles, and faults, countless craters that formed either before, during, or after mare emplacement, and ejecta materials from far and within the basin. Based on cratering frequency and distribution, along with degradation stage of the regolith, one can infer a chronological order of the potential flows. My dating results are in broad agreement to previous studies of the region (e.g. Boyce, 1975a), but they are now associated and compared to analysis of soil compositions.

The most ancient and degraded maria are found in Fig. 15.1 (x) either next to terra or within ancient craters (Fra Mauro). The largest example of this type of terrain can be located east of the Rupes Recta; albeit virtually indistinguishable in optical

images from the rest of the neighbouring mare, spectral analysis indicates a Fe and Ti composition very similar and comparable to the highlands to the east in Fig. 15.1 (y). I believe that this area was relatively unaffected by later mare flows by virtue of its elevated topography. Its steep continuum (red) might reflect the high volume of agglutinates accumulated in the soil during billion of years, plus contributions from the west as bedrock material excavated and ejected by the Birt impact, and from the south as terra material 'blown offshore' by the Tycho blast. I dated these maria as Imbrian in age (~3.8 Ga). Similar terrains have been given the generic term of Cayley Formation and their origin linked to ejecta and melting materials following the Imbrian impact.

Patches of ancient maria (Ia) can also be found scattered around the periphery of the basins or infilling ancient crater floors. Examples are the bay next to Davy and Alphonsus, (unit 79 from Fig. 7.4), east of Mosting (104), east of Bonpland *s* (3), next to Montes Riphaeus, and within the craters Pitatus (71) and Mercator (18). All these areas either border or are enclosed by terra. Contamination and overspill of highland materials contributed partially to the enhanced affinity in mineralogy of the constituent basalts (lower than average Fe and Ti). Another factor dictating the chemical signature of the uppermost regolith layer might have been the physical barrier to ejecta admixing offered by the elevated topography surrounding these units. These sheltered areas would have been left relatively undisturbed by superficial rejuvenation and mixing caused by the aftermath of major nearby impacts (mainly Tycho and Copernicus).

The remnant units belonging to group I feature some of the most distinctive lava flow units on the lunar surface. In particular, the terrain stretching south from the western side the Fra Mauro peninsula to the Nicollet crater in Eastern Nubium, and west towards Lassell, is clearly detectable even on relatively low-resolution Earth-based images of the Moon. It stands out very clearly from the darker maria as a consequence of sharply defined borders. Closer inspection reveals a highly cratered surface, with low titanium content but nearly average mare iron signature. Indeed TiO_2 concentration in the regolith of units 1, 25, 29, and 79 is comparable to that in the nearby highlands (Fra Mauro and south of Guericke). Both the high crater count and Ti-Fe content (according to the findings from this research) sug-

gest a relatively old age for these terrains (Upper Imbrian Series). One also notices how some areas of these units have been consequently mantled over by later flows (Ic, such as 84) or presumably, a series of basalt units (from IId 34, up to IIIh 61). A tentative chronology of these units is offered on Figure 15.3, with unit 0 representing the oldest and 7 the youngest.

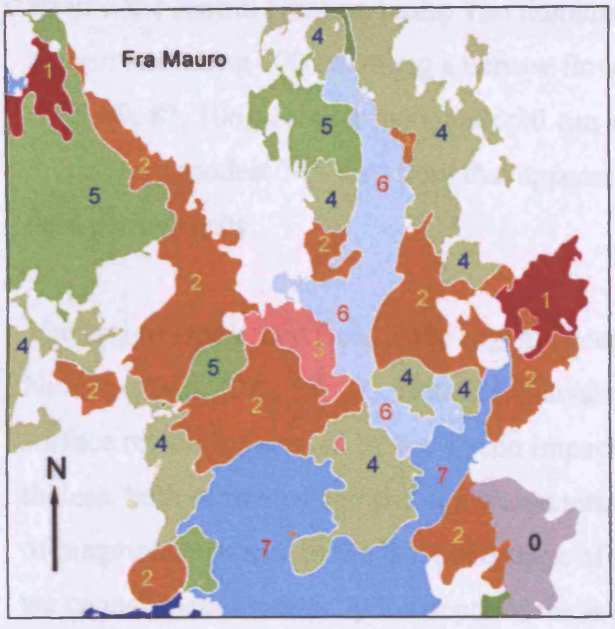

Figure 15.3. Chronological order (0 to 7) of unit flow emplacement (where 0 representing the oldest).

I propose that units I are representative of the major basaltic infill of the basins and neighbouring lowlands during the Late Imbrian Epoch. Most of the northern and eastern parts of the region (15 S 20 W) are overlaid by basaltic materials belonging to the Early Eratosthenian Period. Within Nubium, ejecta from the 61 km Bullialdus crater and associated secondary impacts cover and mask most of the pre-existing terrains in the western Nubium basin. Only small patches of Imbrian soils are still visible (Ib, 24, 20, and 39-40). Following the impact event, fresh basaltic flows covered some of the ejecta itself. Most apparent is the IId mare east of Lubiniezky.

Mare Cognitum shows an intricate pattern of flow units. Old Imbrian basalts are confined to the mare near Montes Riphaeus (6 and 9), further south of the mountains (14), and east of Bonpland s (3). Most of the area is covered with regolith belonging to the IIe unit type except for a large area south of the basin, which is

dominated by older Ti-richer basalts (IIe, 16, 10, 11, 12). We find soils of similar composition on the other side of the mountains (21), possibly a related and contemporary mare flow. Regolith of a similar composition covers most of the low-topography mare corridor between Fra Mauro and the highlands in the east.

The last major mare flows (Late Eratosthenian) were confined to large areas around the central Nubium basin. The titanium composite reveals a high-Ti basaltic unit stretching 400 km along a narrow flow on the eastern side of Fra Mauro (IIIg, 89, 83, 106). Similar mare material can also be found west of Bonpland *s*, a much more modest 745-km^2 flow that appears extremely smooth and dark in standard photography.

The largest single unit flow in the region occupies most of the central part of the Nubium Basin (IIIh, 57, 61). Detailed analysis of this regolith is complicated by surface reworking caused by the Tycho impact energy and ejecta material. Nevertheless, both estimated age and soil characteristics point to a massive outpouring of magmatic material in the late infill stage of the Nubium Basin. Unfortunately, we cannot measure directly the depth of these emplacements and consequently estimate the volume of the erupted lava. These flows appear to have infilled areas of lower topography, which were already relatively flat. This could explain the large geographical distribution of the relatively modest effusive phenomenon so late in the thermal history of the Moon.

Research based on terrestrial volcanoes has established that rate of effusion rather than viscosity is the primary control on igneous flows (e.g. Walker *et al.*, 1975; Greeley and Womer, 1981). There is evidence that the final eruptive mare-filling eruptions may have been mafic pyroclastic flows, roughly five meters deep, in the form of an aerosol of gas and liquid droplets, the basaltic equivalent of nuée ardentes (O'Hara, 2000). The fluidity and dynamics of the emplacement would explain the uninterrupted morphology of geological features such as wrinkle ridges, which overlap many a distinctive flow. This would point to an origin of these folds either prior to most emplacements, and subsequently mantled over repeatedly by later flows, or, more likely, later than most eruptions. In the study region,

this would imply a time of formation of most mare ridges around the late Eratosthenian Period.

There is evidence that effusive activity continued well into the Copernican Period as sporadic igneous centres distributed across the region (i). I found possible signs of relatively recent volcanic activity around a number of areas of crustal weakness or displacement. For instance Rima Birt is terminated by two depressions surrounded by freshly deposited mafic material. I also noticed several positive relief features such as cone-like edifices with distinct composition from the surrounding maria.

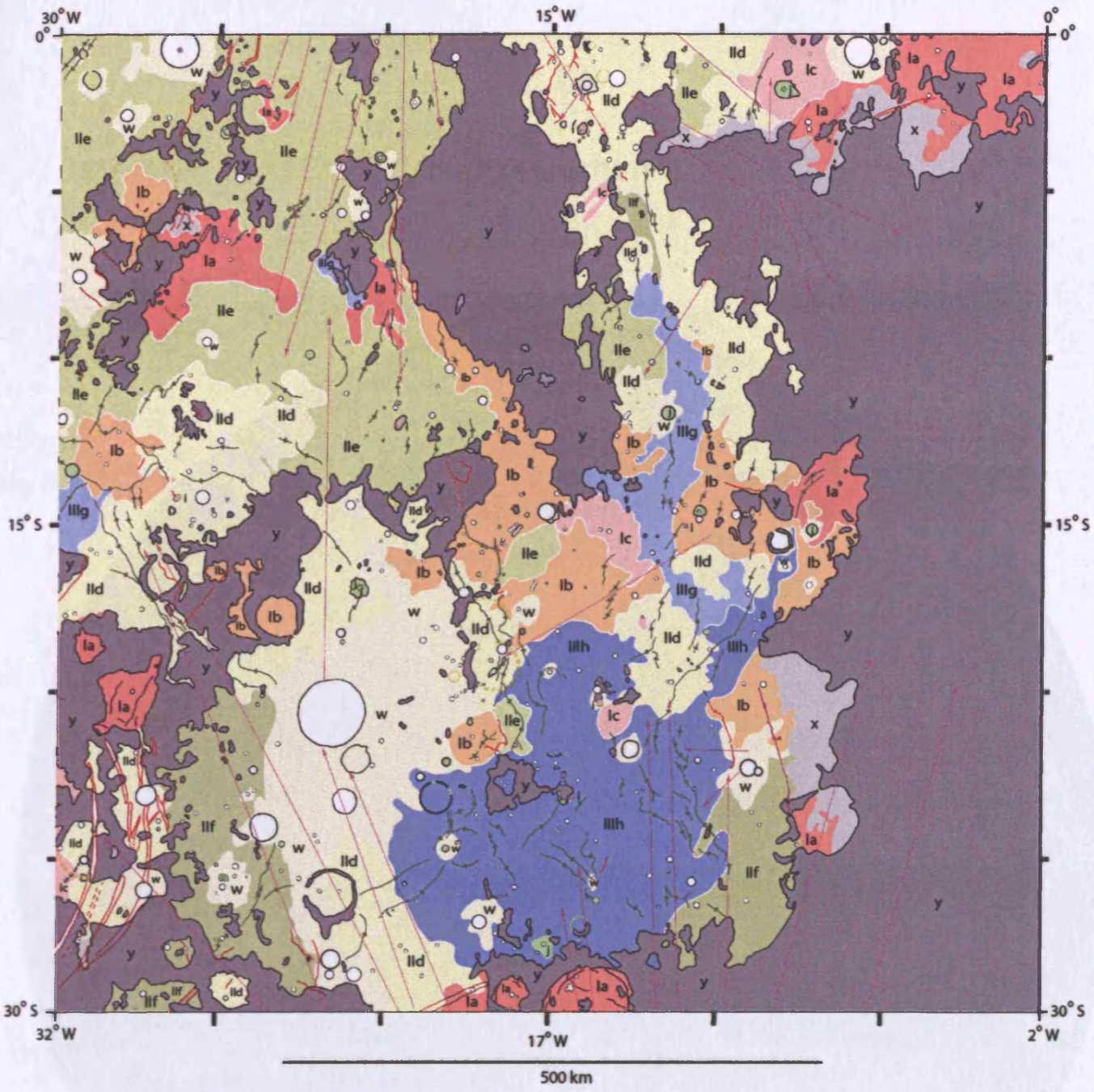

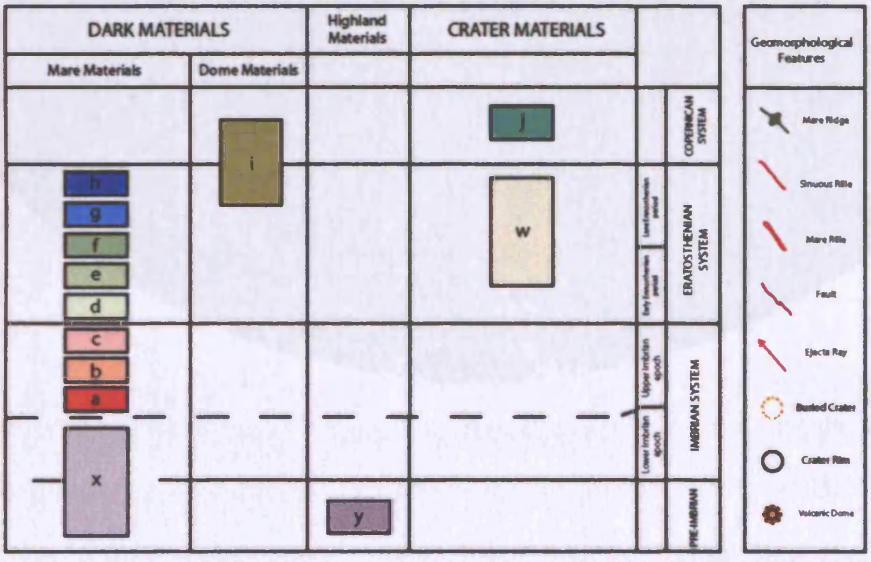

Figure 15.1
The Nubium Basin

Part III

Mare Imbrium

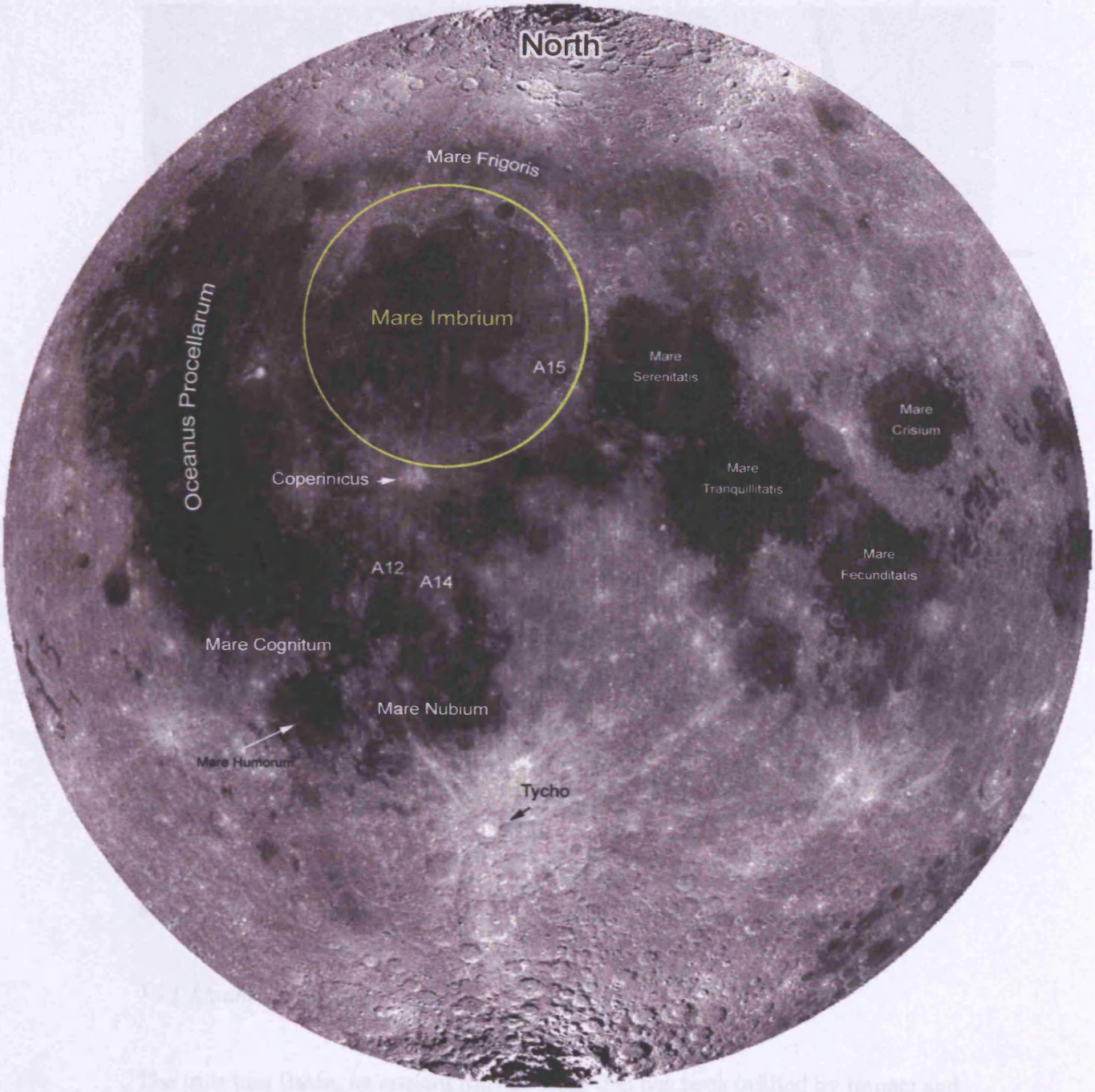

The area covered by this study is a quadrangle with 1400 km sides and coordinates 53 N 53 W and 10 N 38 W (see Fig. 16.1) giving a total surface area of approximately two million square kilometres.

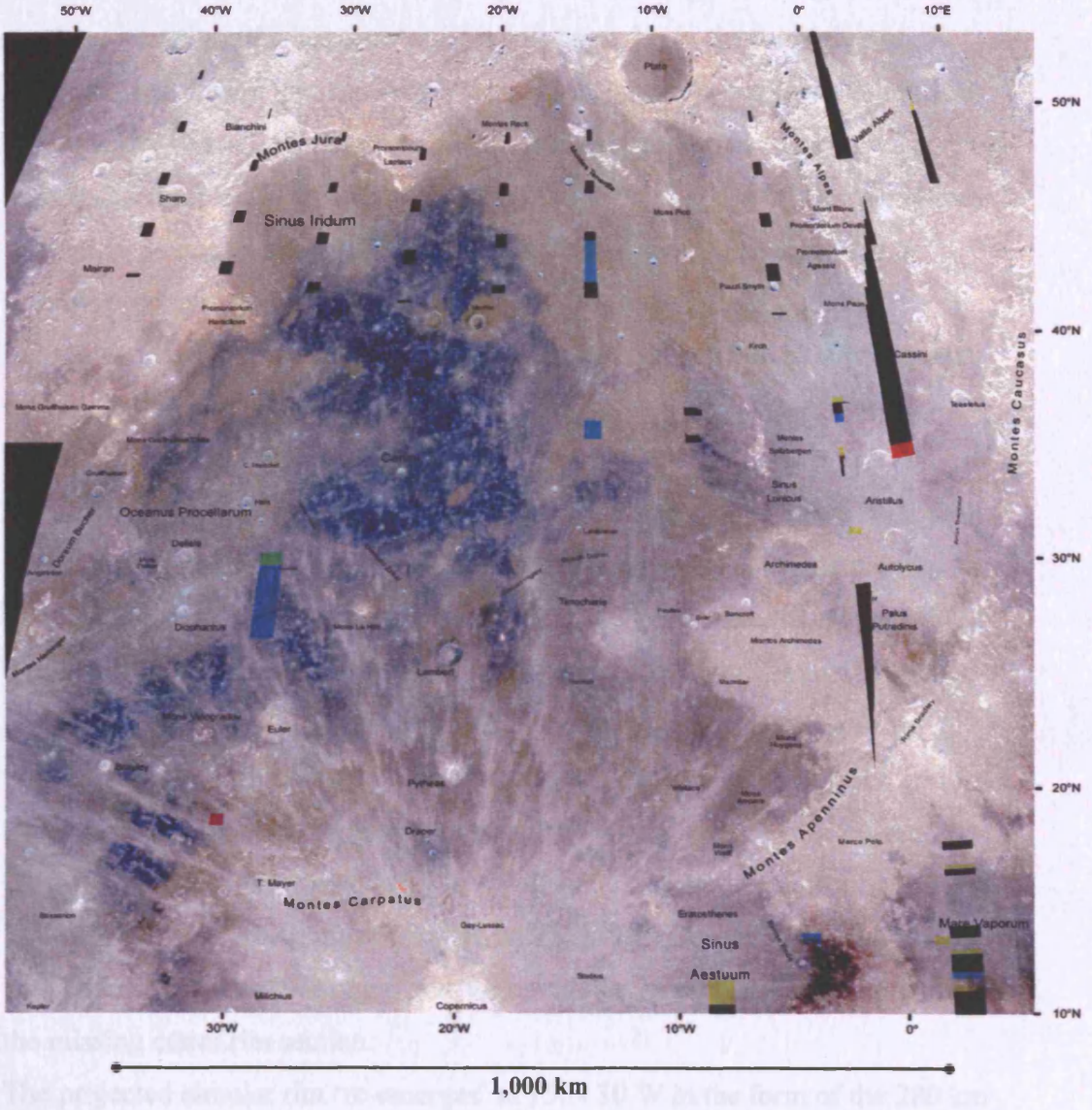

Figure 16.1. Filter-enhanced Clementine DBA image of the Mare Imbrium region.

16.1 Mountain Ranges

The Imbrium Basin, an ancient impact basin that has been infilled by impact and volcanic materials since its formation, dominates the morphology of this region. Mountain ranges with peaks up to 5500 meters above the mean lunar radius

(Montes Apenninus in the S-SE) define most of the circular morphology of the basin.
Further north, stretching for around 200 km with peaks of 3650 meters, Montes Caucasus delineate the border between mare Imbrium and mare Serenitatis in the east (360,000 km^2). Continuing in an anticlockwise direction, we meet another mountain chain: Montes Alpes. The progressive infilling of the basin and the nearby excavation of a large crater (Cassini) gave rise to the formation of promontories Deville and Agassiz. Vallis Alpes, a nearly rectilinear valley 130 km long and 10 km wide, dissects the mountain range and features a lava channel linking Imbrium Basin and Mare Frigoris in to the north. We find similar valleys at other large impact basins on the Moon and these are often interpreted as grabens produced by faulting at the time of formation of the raised rims. Subsequent lava flows infilled the depression, as demonstrated by a prominent rille occupying the centre of the valley.

Further west, we encounter the semi-circular mountain chain Montes Jura, with peaks reaching 3800 meters. They outline a secondary circular structure that has 'lost' its southeastern rim: Sinus Iridium. This 260 km crater was excavated not long after the formation of the Imbrium basin. Subsequently, the newly formed circular depression, 600 meters lower than the average neighbouring mare topography, was infilled by numerous lava flows. Promontories Laplace and Heraclides terminate the semicircular mountain chain. Montes Gruithuisen Gamma and Delta today give away to a vast stretch of maria connecting the Imbrium Basin with Oceanus Procellarum. Dorsi Bucher and Arduino, together with Montes Delisle, Harbinger, and Vinogradov may represent the remnants of the missing crater rim section.
The projected circular rim 're-emerges' at 15 N 30 W in the form of the 280 km long chain of Montes Carpatus. This is characterised by peaks of around 2400 meters, craters Tobias Mayer (35 km) and Gay-Lussac (24 km), and in the north, the promontory Cape Banat.

Smaller mountain chains are also found within the basin, for instance the northern Montes Recti (2020 m high), Teneriffe (1450), and eastern Spitzbergen (1450).

Mons Pico and Mons Piton, both around 2400 meter high, are two isolated mountain peaks that stand out in the northeast.

16.2 Major Craters

Along with Sinus Iridum, the region under study features many other well-known large craters. Mare Imbrium is dominated in the south by the bright rays of Copernicus (107 km, 10 N 20 W), which can be still detected nearly to the centre of the basin (~30 N). Eratosthenes (60 km) is located just south of the Montes Apenninus near Sinus Aestuum and it is characterised by an elevated crater rim (3900 m). Archimedes and Plato are both flat-floored craters, infilled by mare materials, and of comparable age and dimensions (~100 km diameter and 2000 m height). Aristillus and Autolycus are two major craters found in the west of the basin, the former characterised by a system of valleys radiating towards Mare Imbrium and Palus Nebularum. Other major craters within the mare are Cassini (29 km – 2400 m), Timocharis (40 – 2870), Lambert (29 – 2400), Euler (28 – 2200), Delisle (26 – 2420), Diophantus (21 – 2590), Le Verrier (18 – 2450).

16.3 Marginal Areas and Neighbouring Regions

Palus Nebularum and Palus Putredinis represent two marginal mare locations that have become 'isolated' following the major impacts Archimedes, Aristillus, and Autolycus.

Mare Imbrium borders in the north with Mare Frigoris (251,000 km^2) and Sinus Roris, Mare Serenitatis in the East, Sinus Aestuum (25,000 km^2) and Mare Insularum in the South, and in the west with Oceanus Procellarum (4,000,000 km^2).

I used the same techniques and steps as in my previous work (Chapter 5) to propose a map of the exposed basaltic flows within the Mare Imbrium region. More than 35 Lunar Orbiter IV prints were employed in conjunction with LAC airbrush maps, LTO topographic maps, photographic reproductions of the Consolidated Lunar Atlas, and Clementine images to produce Figure 17.1.

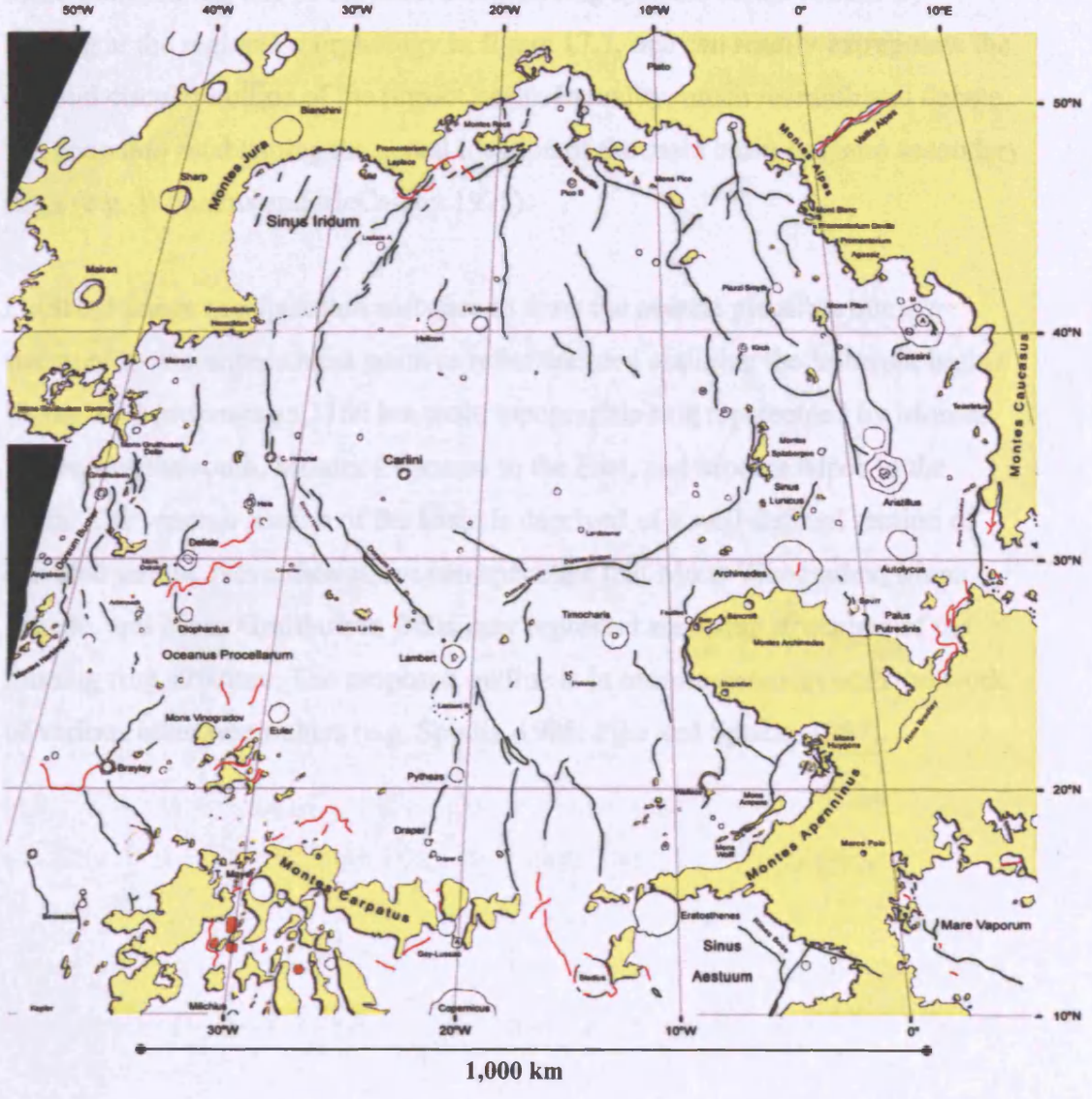

Figure 17.1. Sketch map of the Mare Imbrium region where:
White - maria/lowland, Yellow - highland/upland, Red - rilles, Green - ridges.

This map also outlines major geological features such as crater edifices (not including their ejecta blankets), and the most prominent rilles and ridges. I differentiated between mare and non-mare terrain by noting variations in topographic elevation, albedo, geographical and geological context, and contrasting mineralogical signatures (using Ti, Fe, and FC Clementine data). I calculated that maria overlie around 63% of the region under study (1.23×10^6 km^2).

Mare Imbrium has one of the most complex ring systems on the Moon. By looking at the regional morphology in figure 17.1, one can readily extrapolate the original circular outline of the impact basin. In reality, much research and debate has gone into establishing the actual location of the main basin ring and secondary rings (e.g. Wilhelms and McCauley 1971).

I utilized image manipulation software to draw the nearest plausible circular structure to encompass most positive relief features outlining the Imbrium basin. Figure 17.2 proposes an 1160 km main topographic ring represented by Montes Appeninus the south, Montes Caucasus in the East, and Montes Alpes in the north. The western section of the basin is deprived of a well-defined section of elevated terrain. Nevertheless, we can speculate that Mons Vinogradev, Mons Delisle, and Mons Gruithuisen Delta may represent surviving structures of the missing ring structure. The proposed outline is in broad agreement with the work of various other researchers (e.g. Spudis, 1986; Pike and Spudis, 1987).

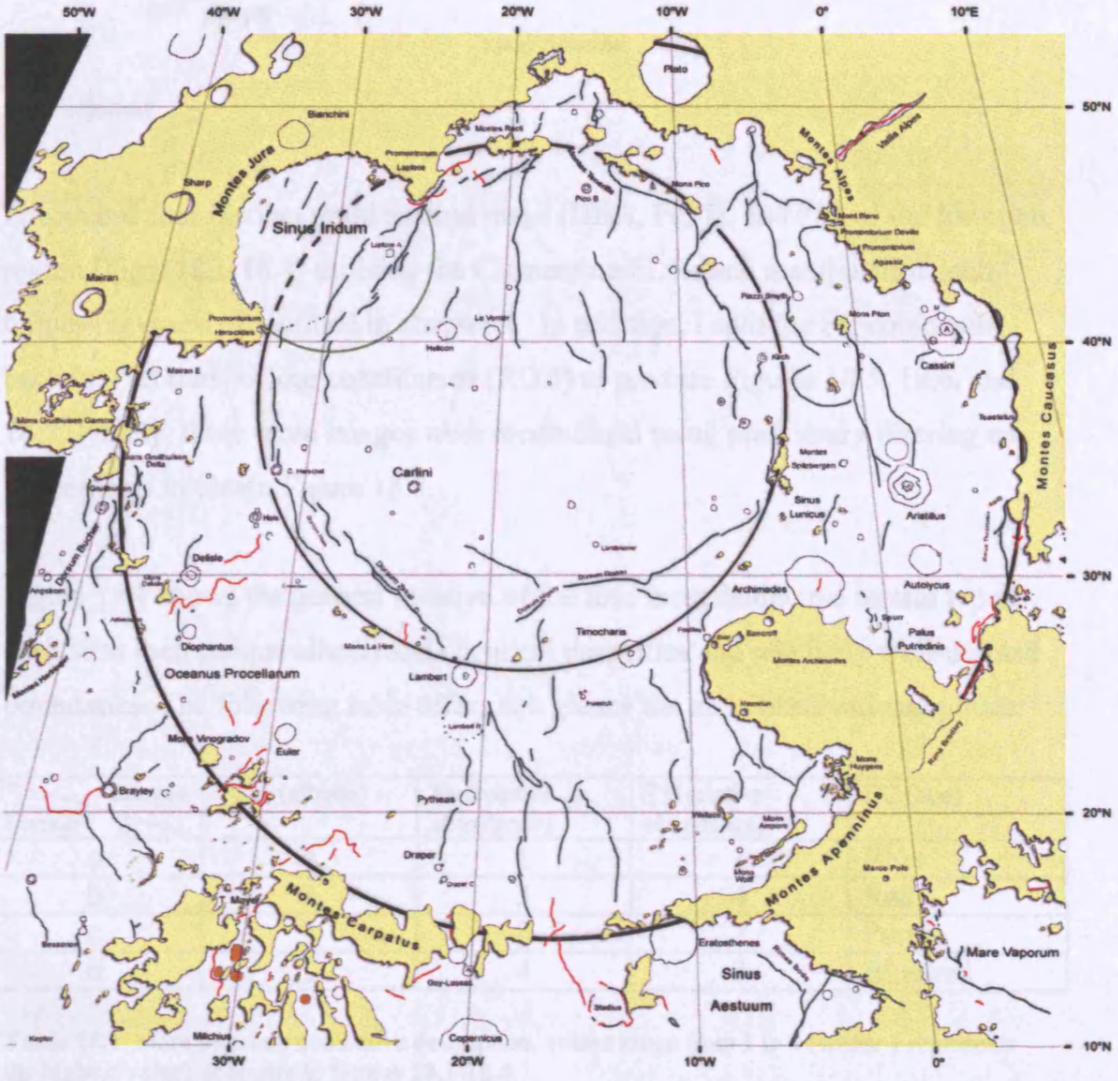

Figure 17.2. Proposed multiring outlines in the Imbrium Basin (1160 and 670 km in diameter).

Spudis (1986) proposed five additional rings: two inside the topographic rim (550 and 750 km in diameter) and three outside. I have not been able to match either of these internal rings with the material at my disposal. Nevertheless, I detected a topographical circular trend of elevated terrains that includes Montes Recti and Teneriffe along with Mons Pico in the north, and Montes La Hire and Spitzbergen, plus various scattered islands, in the south (Fig. 17.1). A series of ridges located just inside the circumference, such as dorsi Grabau, Higazy, Zirkel, and Heim demark this proposed rim of 670 km in diameter.

I have also highlighted the Iridum impact crater rim and its 'missing' section (260 km in diameter).

CHAPTER 18 VISUAL STUDY AND COMPARISON OF THE FeO, TiO_2, DBA, AND FC MAPS

MARE IMBRIUM

18.1 Method

I produced four distinct multispectral maps (DBA, Fe, Ti, and FC) of the Imbrium region (Figs. 18.1-18.4) utilising the Clementine EDRs and manipulation techniques previously described in chapter 4. In addition, I split the FC composite back into its three colour constituents (RGB) to produce Figures 18.5, 18.6, and 18.7. Finally, these three images were recombined using proprietary filtering enhancements to obtain Figure 18.8.

Figure 18.1 shows the general location of the four most distinctive terrain types, each with their unique albedo and chemical properties and relatively well-defined boundaries. The following table offers at a glance the main observational points:

Images / Terrain	DBA (albedo)	Fe (relative abundance)	Ti (relative abundance)	FC (hue)
a	4	1	1	Blue
b	3	3	4	Red
c	2	2	2	Purple
d	1	4	3	Blue/red

Table 18.1. Mare Imbrium qualitative description: values range from 1 to 4 (where 1 represents the highest value). It relates to figures 18.1-18.4.

At this point, it is worth noting that I applied several filtering techniques (contrast, levels etc.) to the original Clementine DBA map in order to emphasise albedo variations.

18.2 Discussion

The Clementine images suggest distinct geographical distribution of the four surface materials: the western half is characterised by low albedo regolith with the highest contents of both Fe and Ti in the region (a). By looking at Figure 18.1 we can speculate that this terrain once extended further south within the basin, but it was probably hidden and reworked following the Copernicus impact (d); its ejecta

rays can be traced up to 30 N and obfuscates most of the area's pre-impact spectrographical signature.

Terrain (b) extends throughout the northeastern half of the basin including Sinus Iridum. It is characterised by regolith containing the least amount of titanium in the basin and by a low iron concentration. As per terrain (a), I hypothesise a larger geographical distribution of this lunar material prior to further mare emplacements, perhaps caused by the Aristillus impact. This would have scattered a large quantity of ejecta material in the area, consequently obliterating much evidence of the pre-event mineralogy.

Located between the predominant terrains types (a) and (b), and impact material (d), we find mare material (c), characterised by a spectral signature falling somewhere in between the (relatively) high and low iron and titanium soils; the regolith might represent just an admixture of these two mineralogical extremes. Nevertheless, it is worth noting its characteristic purple hue in the FC image, suggesting a distinct mineralogical band of mare terrain extending southwesterly Montes Caucasus towards Montes Carpatus.

I also noticed how the boundaries between soil types in the titanium map appear much sharper than in the iron map. This is probably due to the presence of ejecta from major craters, such as Copernicus and Aristillus, and from the myriad of smaller impacts scattered across the basin. Impacts excavate subsurface material that is by definition fresher and less weathered than the average topsoil. It also contains a higher percentage of crystalline, basaltic material (relatively richer in Fe than Ti), which contributes in making the rays appear 'darker' in the iron maps and, consequently, 'contaminate' (darken) most of the affected mare (see chapter 4). The titanium data succeed in piercing through the ejecta 'clouds' to reveal well-defined compositional boundaries and fresh (low-Ti) impact ejecta.

One small mare region east of Sinus Aestuum stands out on all images: in DBA the regolith appears of extremely low albedo, i.e. an area of relatively high iron and titanium contents (opaques).

18.3 Further manipulation of FC image: Blue and Red filter channels

The FC image greatly exaggerates the true colour of the lunar surface by stretching the blue and red extremes of its spectral properties. Additionally, the green and yellow colours are a diagnostic sign of the presence of pyroxene and olivine in the regolith (see Chapter 4).

The blue channel image (Fig. 18.5) and the titanium map (18.3) share a common origin in the ratio 415/750 nm. Nevertheless, because the FC image is a combination of pure filter ratios (see Table 4.1), i.e. has not been normalised for albedo variations (they do not contain quantitative information on mineralogical values), the resulting image displays far larger hue variations than the corresponding oxide maps.

Aristillus' ray system (33.9 N 1.2 E) is shown here in much detail and extends radially away from the crater (55 km diameter) for around 200 km. Some rays are still visible in the northeast, at a distance of ~600 km from the impact.
The southern section of the Mare Imbrium proposed main ring (see Fig. 17.2) can be followed nearly continuously clockwise from Montes Caucasus (40 N 15 E) to Mons Vinogradov (23 N 30 W).

Figures 18.5 and 18.6 both hint to the possibility of a buried circular structure of around 70 km in diameter that is difficult to notice either in photographs or albedo maps (18 N 27 W).

Copernicus crater displays a peculiar chromatic duality with an east-west contrasting composition. The eastern side shows typical Fe-Ti values for a crater of its size and age (see Aristillus); the western side instead is much 'redder' than its opposite half. This dichotomy may have arisen from the complex nature of the pre-impact terrain and sub-soil mineralogy. Alternatively, each side may have been the theatre of distinct igneous histories, with one half being more effected by either neighbouring or in-crater geological processes.

A few craters in the 'bright' (bluer) western half of the basin show a darker apron of material outside their raised rims (e.g. Carlini, 10 km, ~34 N 24 W). The ejecta are easily distinguishable from the surrounding mare because of their particular mineral content, the source possibly traceable to Fe- and Ti-richer material buried below later lava flows.

By the very nature of the filter ratio chosen to represent the red end of the spectrum, that is to say, an inversion of the blue filter values, Figure 18.6 can be view as a 'negative' print of Figure 18.5. Nevertheless, it is interesting to notice how the mare material north of the basin (including Sinus Iridum) appears brighter than the highland terrain further north, unlike other maria on the Moon. This regolith when viewed in the False Colour composite, does indeed appear redder in comparison to most other basalts, and in places (such as in the northeast), emphatically so.

18.4 Further manipulation of FC image: Green filter channel

Figure 18.7 is a representation of the 'green channel' used to construct the FC photo concentrations of clinopyroxene and olivine in the regolith, minerals that can be diagnostic of the presence of fresh mafic minerals in the lunar soil. Whereas in Figure 18.1 large craters represent most of the brightest spots (e.g. Aristillus, Timocharis, Pytheas, Euler, and Copernicus), in Figure 18.7 we see a constellation of randomly set bright circles and points. These smaller and relatively young craters and associated ejecta formed across the lunar surface after the end of the latest widespread mare infill. It is difficult to detect a non-random geographical distribution pattern except for a possible paucity of bright spots in the high titanium area (west basin).

The most outstanding of these bright features is a little crater that 'outshines' all the others in the region. Located halfway between craters Cassini and Kirch, the 3 km excavation is barely distinguishable in the other Clementine images. Here it is surrounded by a 22-km ring of fresh ejecta material outside its rim. An identically sized crater, a few km further north, is nearly 'obliterated' by materials from this later impact.

In relatively recent times, the Cassini crater, along with the two younger impacts located inside its circumference, was effected again by a large third impact, close to its northern rim.

Diophantus (~28 N 34 W, 17 km) is one of the few larger craters that appear bright in figure 18.7. Nevertheless, a few kilometres north, a little 2 km crater scattered and exposed fresher regolith material in a 5 km radius from its centre. Moreover, a twin set of ejecta rays can be seen extending up to 60 km in each direction away from the impact. The rays appear to have followed the local topography, trapped within the 'valley' between the raised impact edifices of Diophantus and Delisle.

Some larger craters show bright annular rings just inside their rims. They probably represent freshly exposed crystalline material, resulting from gravitationally driven slumping on the crater walls.

Rima Bradley also appears bright. This might be due again to freshly exposed materials on the levees of the rille. Alternatively, but less probably, there is the possibility that more cpx and olivine rich minerals might be present within the fissure.

18.5 Further manipulation of FC image: colour reassignment

I produced an alternative false colour image (Fig. 18.8) by assigning hues to each RGB channel that would further highlight differences in compositions. This time red shows the 'pyroxene' channel, the intensity of the green colour is proportional to the blueness of the soil, and blue stands for the red. This map will help identifying the geographical distribution of different mineralogies, and the location, within the mare, of freshly exposed mafic materials.

Figure 18.1
The Imbrium Basin

DBA Map

Figure 18.2
The Imbrium Basin

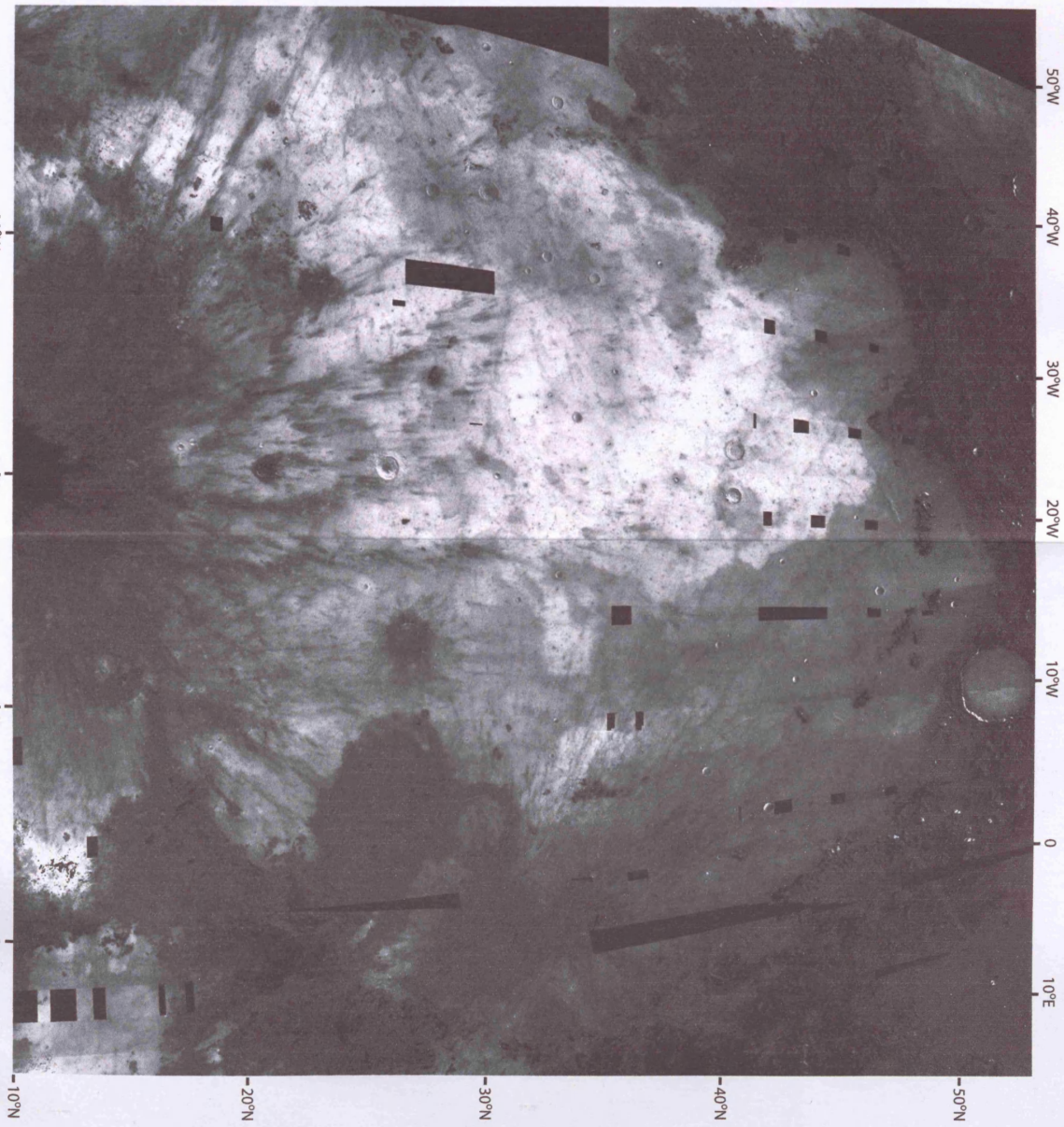

Figure 18.3
The Imbrium Basin

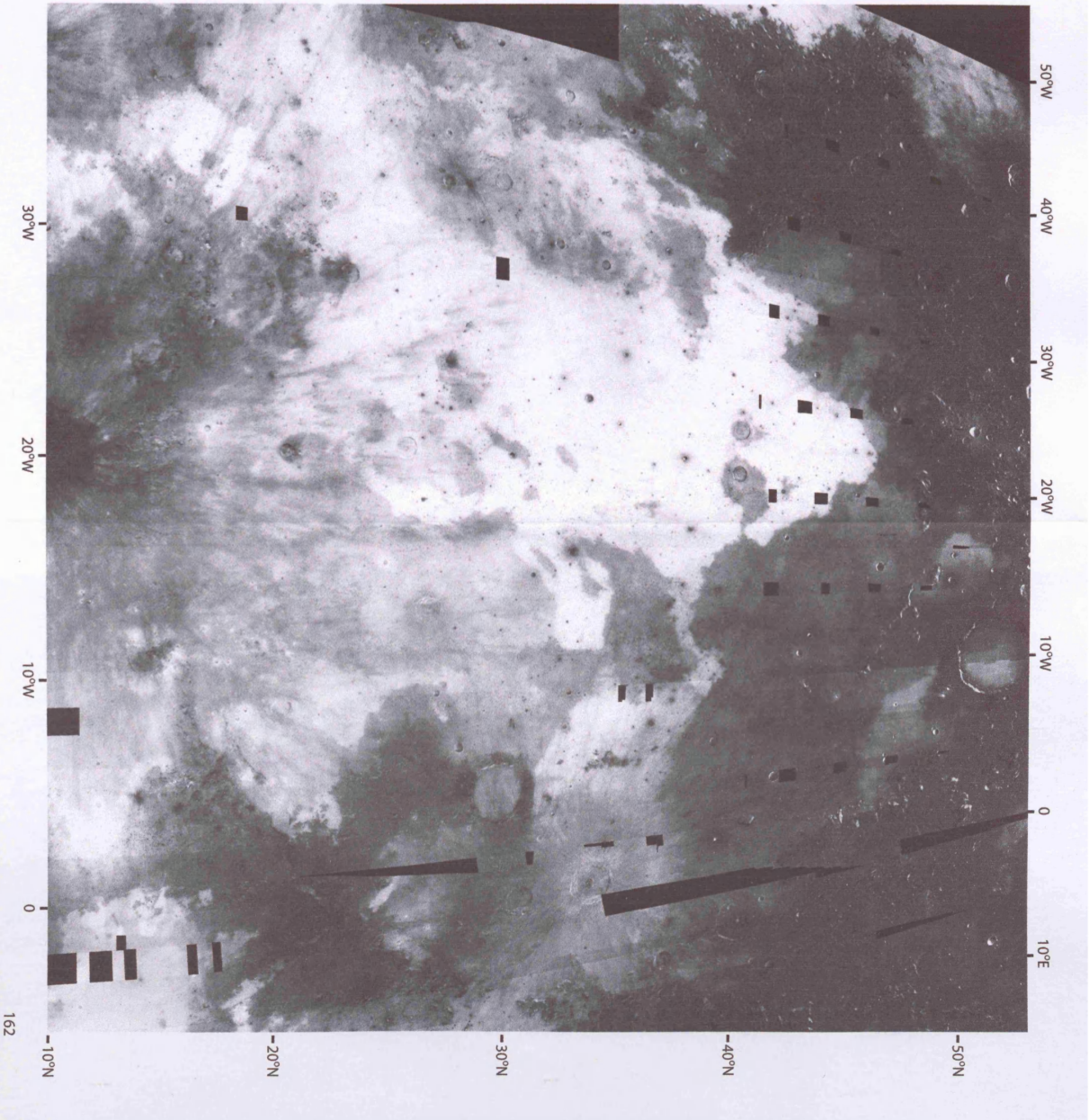

Figure 18.4
The Imbrium Basin

False Colour Image (FC)

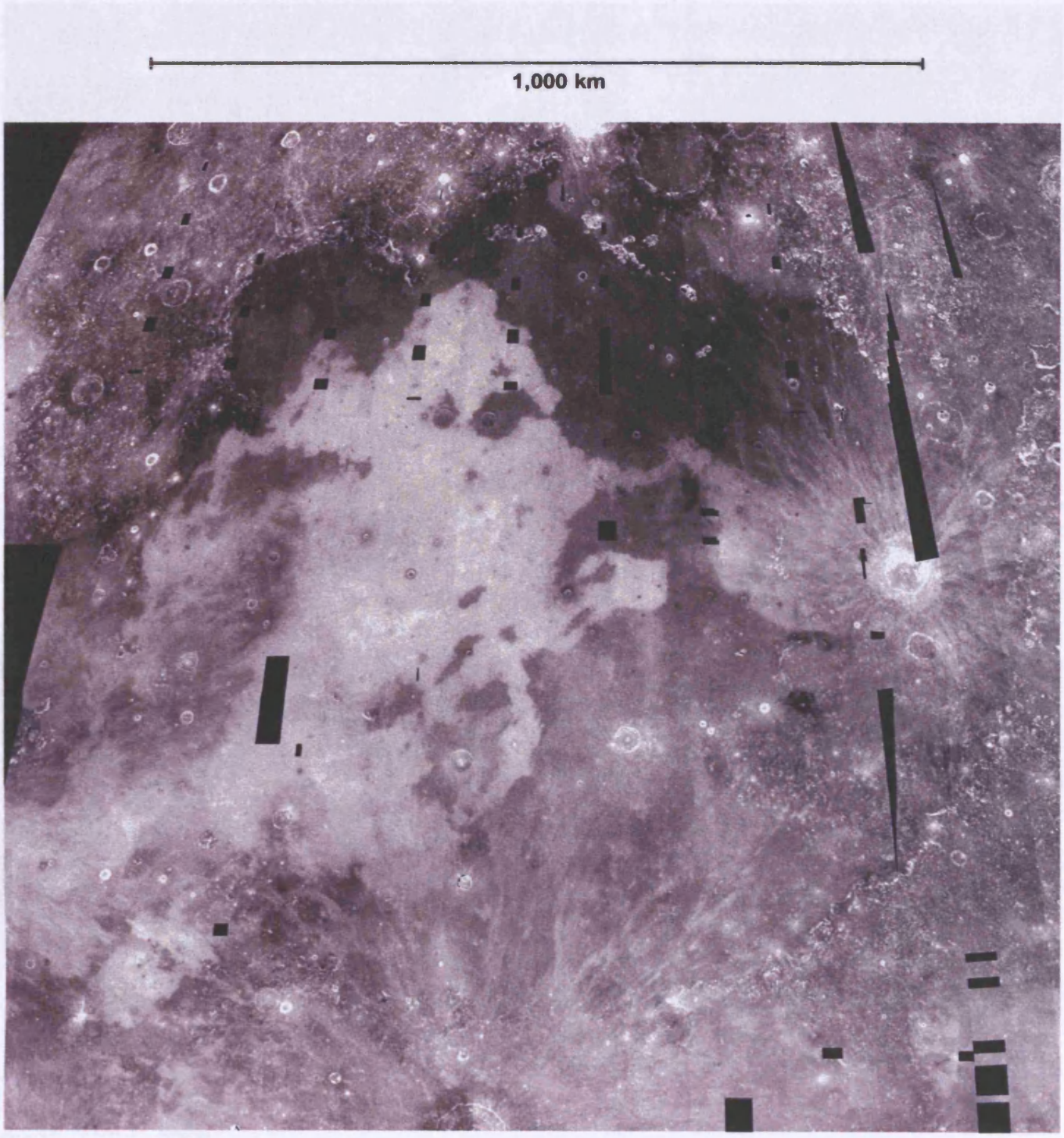

Figure 18.5. Blue filter component extracted from FC image (Fig. 18.4). Imbrium region

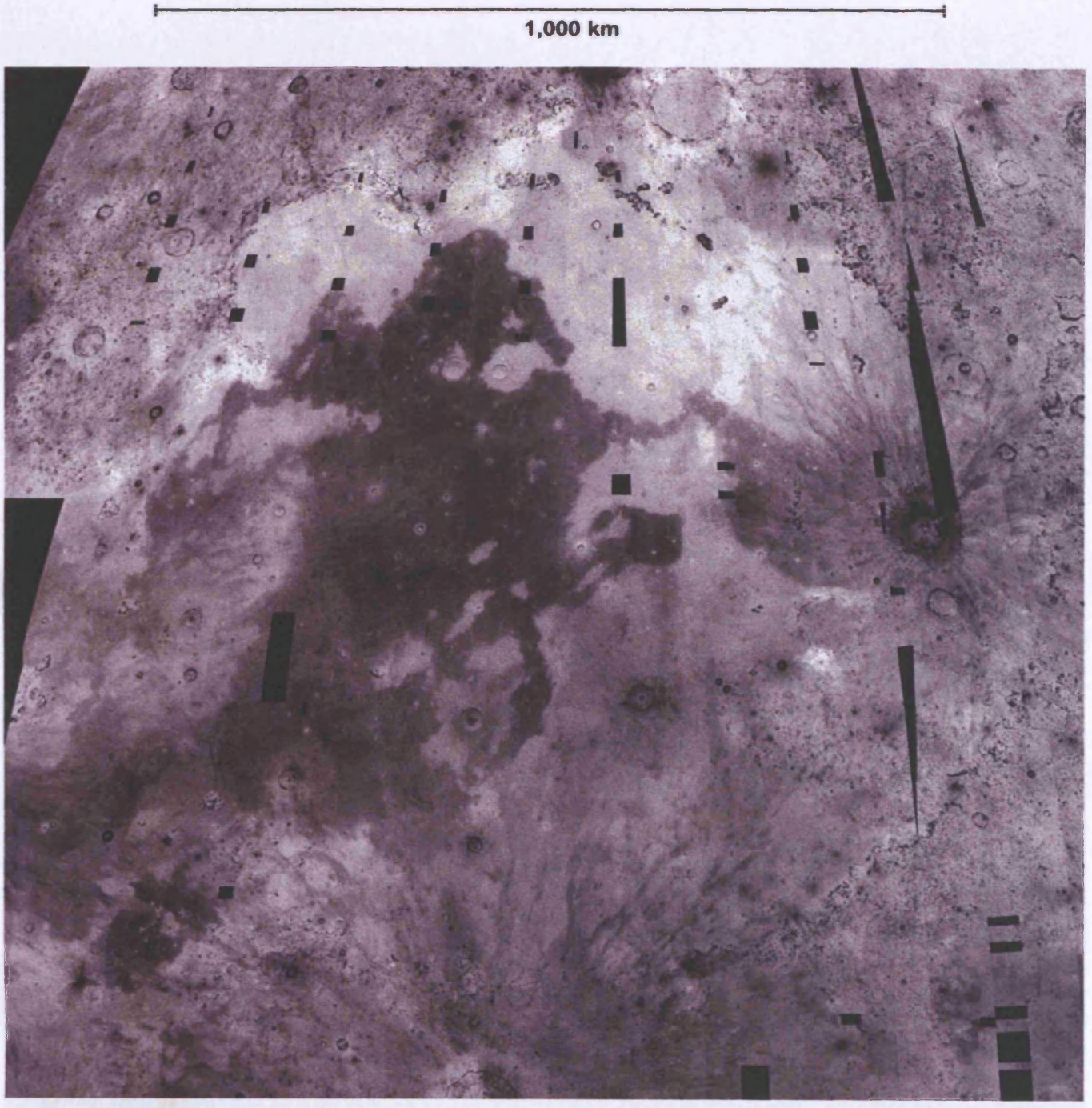

Figure 18.6. Red filter component extracted from FC image (Fig. 18.4). Imbrium region

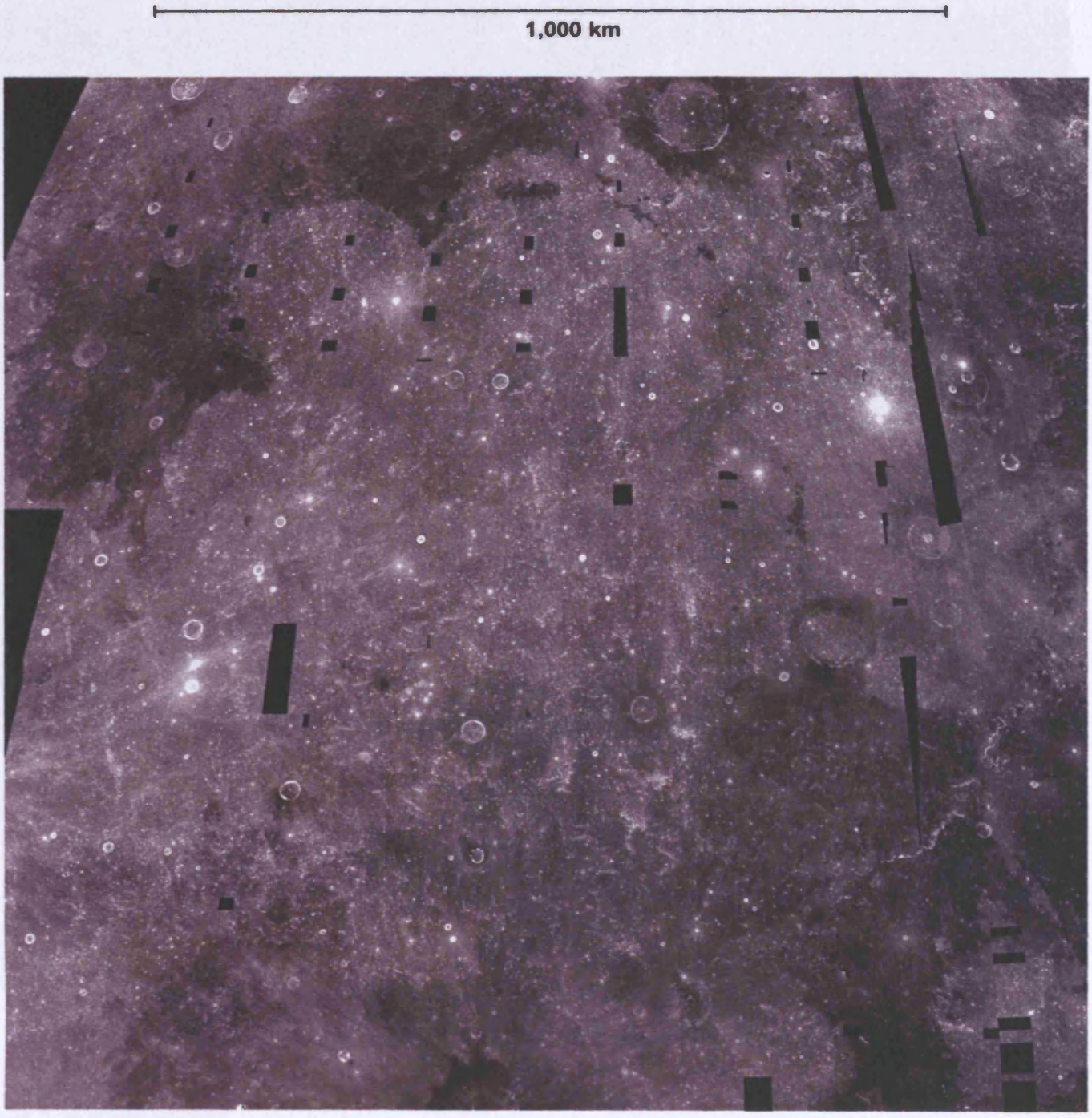

Figure 18.7. Green filter component extracted from FC image (Fig. 18.4). Imbrium region

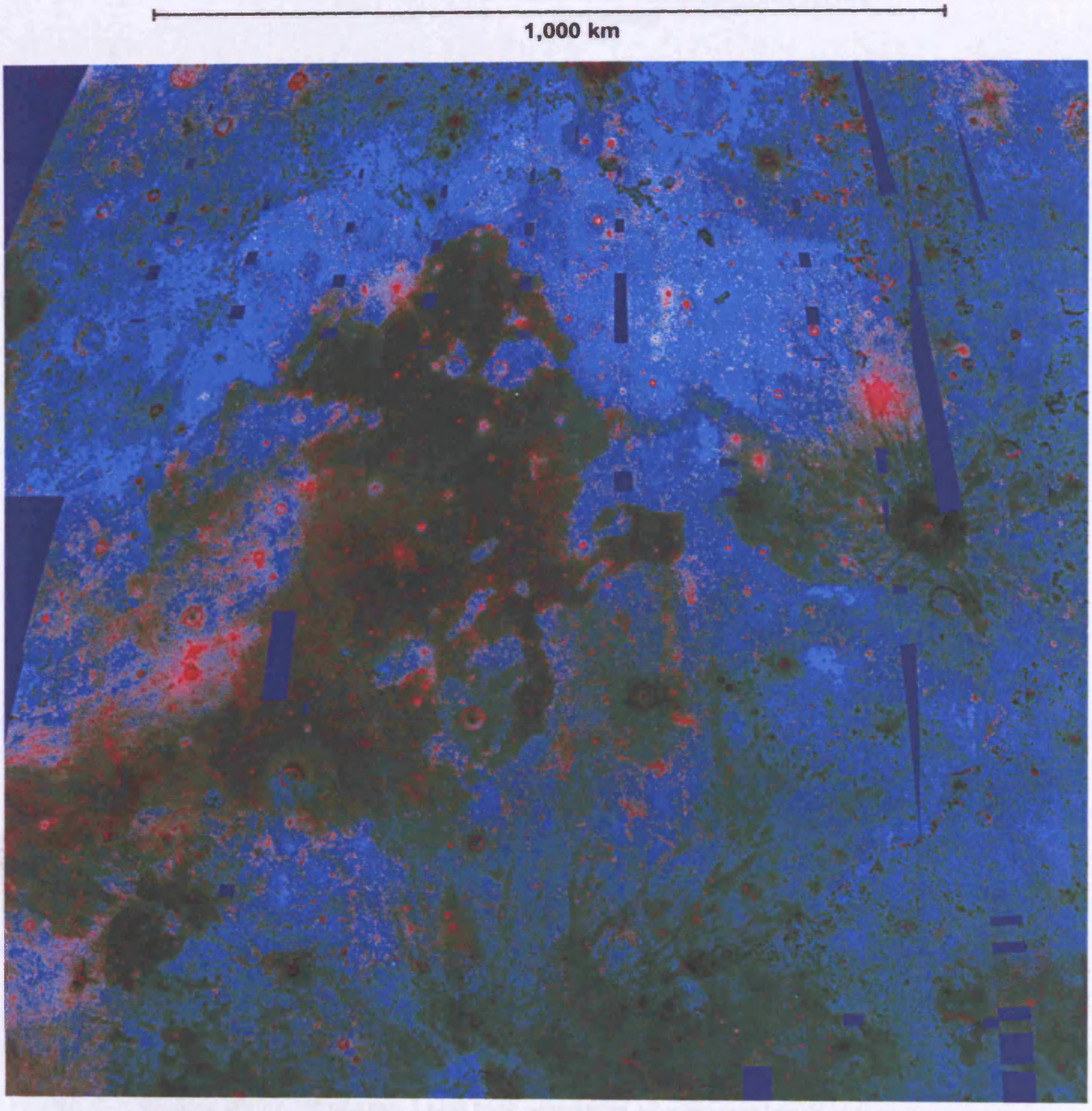

Figure 18.8. RGB filter composite version of Fig. 18.4 produced in order to emphasising unit boundaries. Imbrium region.

I resized the 'true' and false colour images, along with the titanium and iron maps to produce a printout of 50 × 49 cm sides (a scale of 1:2,800,000). I also scanned, scaled, mosaiced, and printed Orbiter IV photographs[1] to match as closely as possible the Clementine maps.

I used tracing paper to sketch albedo and hues differences as potentially distinctive geological units. Figure 19.1 shows my first sketch draft:

Figure 19.1. Sketch map of optically distinct potential unit flows

This map was consequently scanned at high resolution and superimposed to the original computer images. I also took advantage of computer image enhancing and manipulation tools to produce exaggerated colour maps (e.g. Figure 18.8). This helped to better define chromatic variations and confusing boundaries.

Figure 19.2 shows the final sketch map of potential distinct mineralogical units and their relation to the original Clementine images. It is very likely that, as the

[1] From East to West, Orbiter IV images numbers: 109, 110, 114, 115, 121, 122, 126, 127, 133, 134, 138, 139, 144, and 145. Each number is divided into H1, H2, and H3 subsets.

study of this area progresses, a number of units will be either merged or discarded following a better understanding of local geological settings.

I decided to focus the chemical analysis of potential unit flows on 102 areas (Fig.19.3). My choice was based on geochemical relevance, affinity with neighbouring units, and size of the sampled area. I also either discarded areas obviously affected by ejecta material and rays altogether, or selected smaller unit samples to complement the overall geological study of the mare basin.

Crater rims were broadly categorised and associated into two chemical groups (see following chapter).

Figure 19.2. Chemical boundaries superimposed on Clementine multispectral images.

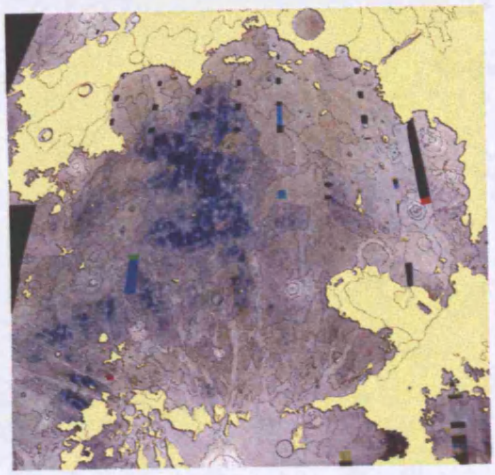

DBA image

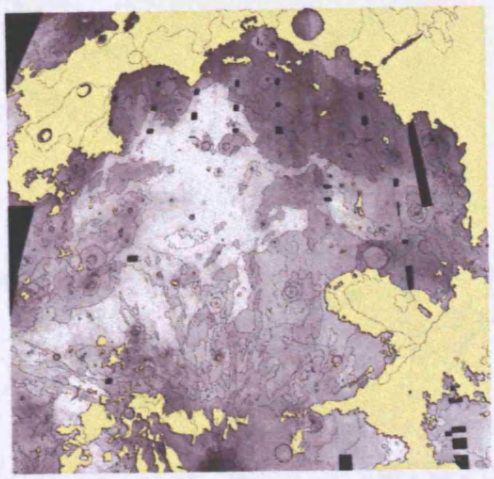

Titanium map

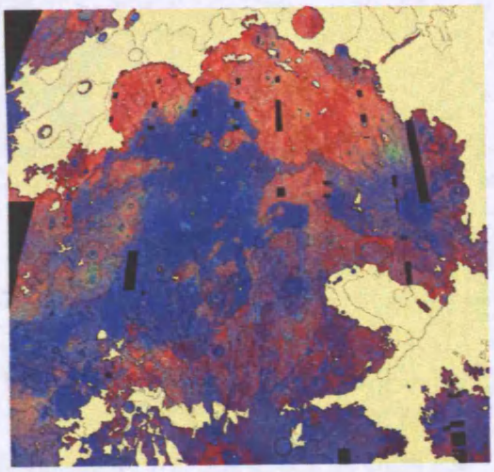

FC map

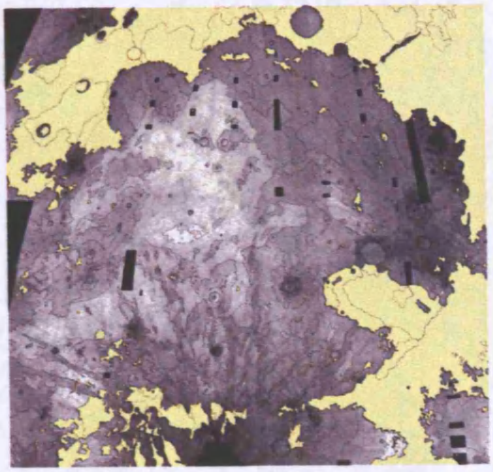

Iron Map

Figure 19.3. Final map of potential unit flows within and around Mare Imbrium

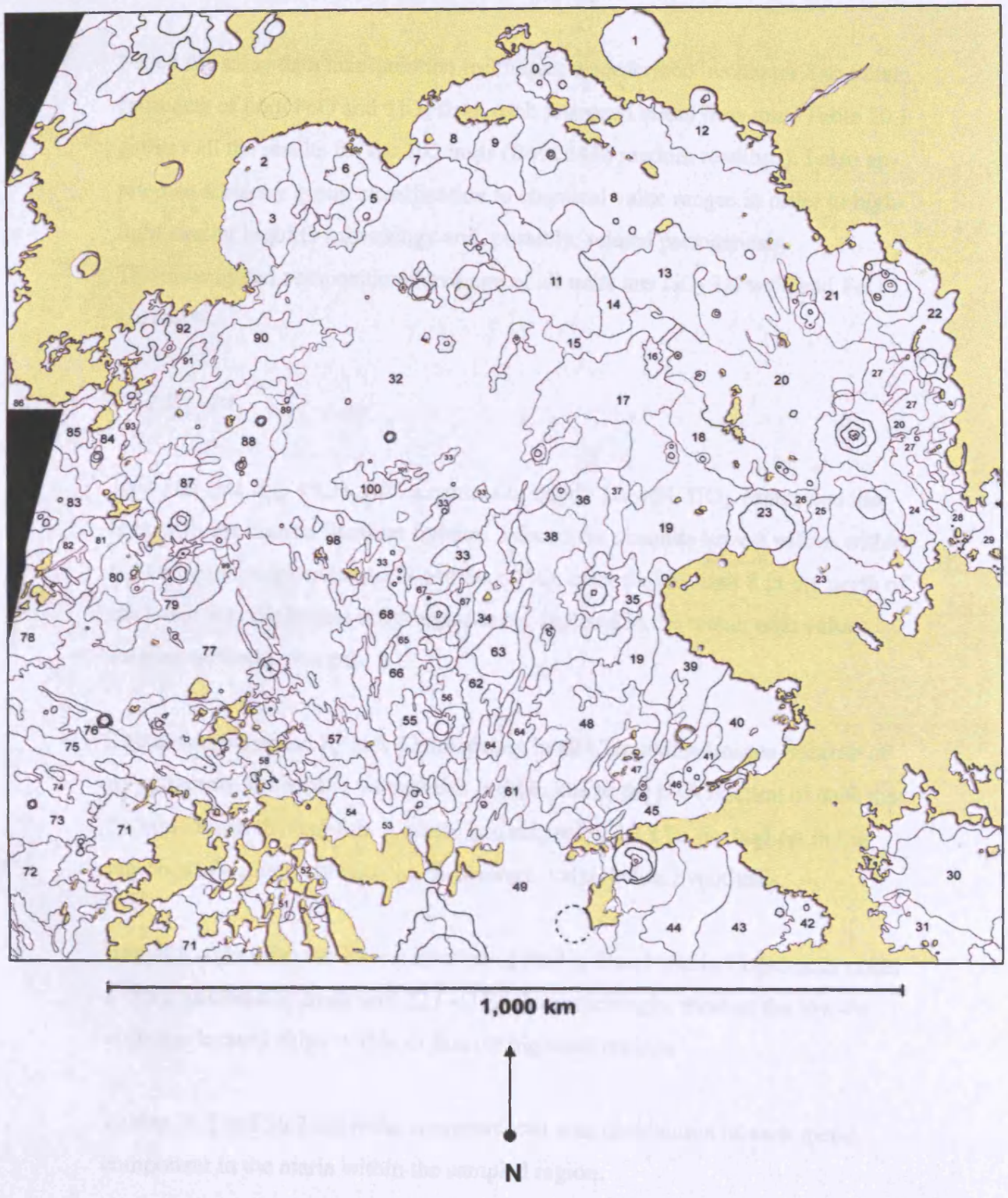

CHAPTER 20 DETERMINATION OF FeO AND TiO_2 WEIGHT PERCENTAGE FOR EACH AREA

MARE IMBRIUM

20.1 Method

I used the same data manipulation techniques as described in chapter 8 to obtain estimates of both FeO and TiO_2 from each proposed maria flow unit. Table 20.1 gathers all the results for the 102 units (from 2448 random readings). I also applied an arbitrary group classification to chemical value ranges in order to highlight similar regolith mineralogy and, possibly, related petrogenesis.
The unweighted compositional average of all units are TiO_2 3.6 wt% and FeO 16.1 wt%.

20.2 Results

Unit 100 (see Fig. 19.3), with a content of nearly 10 wt% TiO_2, represents the area with the highest titanium fraction. I found the absolute lowest values within the Copernicus crater (units 59 and 60, <1%); nevertheless, unit 8 in the north of the basin was the largest mare region most depleted in the metal, with values ranging around 1 percent.

The area represented by unit 42 stands out in all Clementine images because of its extremely low albedo values; this is often due to the high fraction of dark mafic minerals in the regolith. A mean iron content of 19.3 %, the highest in the region, and a relatively high 9.0 % titanium, validate this hypothesis.

Regolith containing the lowest fraction of FeO is found within Copernicus crater (~5%), followed by mare unit 22 (~11%). Unsurprisingly, most of the low-Fe areas are located either within or just off highland regions.

Tables 20.2 and 20.3 show the compositional area distribution of each metal component in the maria within the sampled region.

Table 20.2

FeO %	Surface km^2
<14%	15,300
14-15	33,800
15-16	125,800
16-17	271,500
17-18	273,900
18-19	267,300

Table 20.3

TiO_2 %	Surface Km^2
1-2	220,700
2-3	139,100
3-4	109,600
4-5	121,600
5-6	48,800
6-7	53,100
7-8	104,900
8-9	156,500
9-10	33,300

Figures 20.1 and 20.2 translate the data from Tables 20.2 and 20.3 into a graphical representation of the geographical distribution of regolith types in the region. I reduced the range of compositional families in order to represent these data in a clearer format. Figure 20.3 suggests that more than half of the sampled regolith contains FeO in the region of 16-18 % and the rest within 2% of these values in both extremes (albeit with a slight bias towards more iron rich values, see figure 20.5). The absolute average of all 102 units stands at FeO 16.1 wt%.

After looking at the sampled areas in detail, I decided to 'prune' certain units that are clearly not representative of the whole basin chemistry, either because of their modest size or because of their proximity to obvious sources of contamination (craters, highlands, etc). In this scenario, the average iron content was raised to 17.3 %. These values are consistent with known average lunar mare basalt compositions of between 14 and 20 percent (see Chapter 8).

Figure 20.4 suggests wider compositional variations of titanium fractions among the lunar maria. Alongside Figure 20.6, we see that most regolith contains TiO_2 in values between the two ranges 1-5 and 7-9 percent, with the fraction between 1 and 2 percent being the most common. In later Chapters I will discuss the geological implications of these findings. The average titanium abundance in the sampled region is 3.6 %, and for the weighted sample units 4.6 %. Again, these values fall well within the average nearside mare basalts titanium abundances of 1.3 to 6 percent.

20.3 Iron-Titanium abundance ratio trend

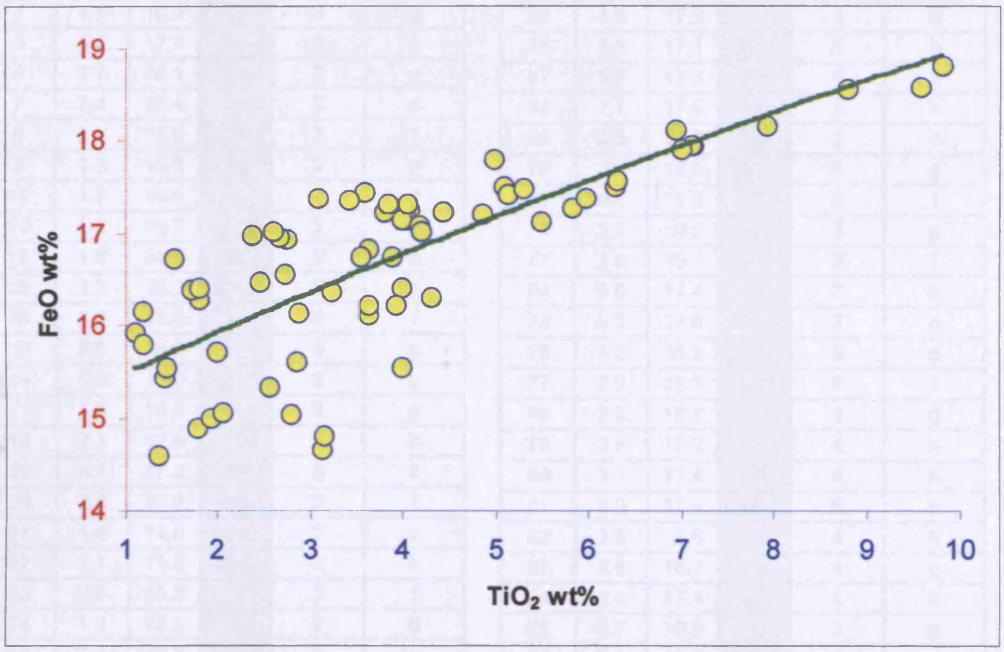

Figure 20.7. Graph suggesting possible abundance correlation between titanium and iron content in the regolith.

I noticed a possible compositional parallel trend between the variations of iron and titanium. By plotting these values (Fig. 20.7), a trend line can be sketched to highlight a potential correlation between the two metals' mineralogical implementation and petrogenesis, especially for materials with TiO_2 and FeO content broadly above 5 w% and 17 wt% respectively. Other researchers have found similar compositional correspondence between titanium and iron content in several igneous provinces on the Moon (e.g. Hackwill *et al.*, 2004). These findings are consistent with models of the formation of source regions for the lunar magmas involving, among other mechanisms, comparable dynamic mixing of sinking dense Ti-rich and Fe-rich late-stage cumulates (e.g. Dowty, 1975; Hess and Parmentier, 1995). Relatively Ti- and Fe-rich magmas (~> 4.5 wt%) might originate in less heterogeneous melt sources or/and they might have experienced a more limited amount of contamination, fractionation, and admixing on their way up from a relatively shallow source.

Area #	TiO_2%	FeO%	Family	Ti Group	Fe Group
0	2.5	16.4	3g	3	g
1	1.4	15.4	2f	2	f
2	1.5	15.5	2f	2	f
3	2.4	17.0	3h	3	h
4	1.5	16.3	2g	2	g
5	2.3	17.3	3g	3	h
6	1.7	16.1	2g	2	g
7	2.4	16.4	3g	3	g
8	1.1	15.9	2f	2	f
9	1.8	16.3	2g	2	g
10	1.9	16.6	2g	2	g
11	1.5	16.7	2g	2	g
12	1.8	14.9	2e	2	e
13	1.2	16.2	2g	2	g
14	1.2	15.8	2f	2	f
15	3.9	16.8	4g	4	g
16	1.3	16.0	2g	2	g
17	1.9	16.5	2g	2	g
18	7.1	17.9	8h	8	h
19	4.1	17.3	5h	5	h
20	2.8	15.0	3f	3	f
21	1.4	14.6	2e	2	e
22	1.1	11.2	2b	2	b
23	2.6	15.3	3f	3	f
24	1.8	13.1	2d	2	d
25	1.4	12.2	2c	2	c
26	1.1	12.8	2c	2	c
27	2.9	15.6	3f	3	f
28	1.9	15.0	2f	2	f
29	3.2	16.4	4g	4	g
30	6.3	17.5	7h	7	h
31	4.0	16.4	5g	5	g
32	8.8	18.6	9i	9	i
33	3.6	17.4	4h	4	h
34	7.9	18.2	8i	8	i
35	3.9	16.2	4g	4	g
36	4.0	17.1	5h	5	h
37	4.5	16.8	5g	5	g
38	5.1	17.5	6h	6	h
39	5.1	17.4	6h	6	h
40	4.9	17.2	5h	5	h
41	5.6	17.5	6h	6	h
42	9.0	19.3	9i	9	i
43	6.1	17.6	7h	7	h
44	4.0	15.5	5f	5	f
45	3.1	14.7	4e	4	e
46	3.2	14.8	4e	4	e
47	3.6	16.1	4g	4	g
48	4.0	17.2	5h	5	h
49	1.8	12.3	2c	2	c
50	2.3	13.5	3d	3	d
51	2.2	14.1	3e	3	e
52	2.2	14.6	3e	3	e
53	2.6	14.8	3e	3	e
54	1.5	14.3	2e	2	e
55	5.3	17.5	6h	6	h
56	3.4	17.3	4h	4	h
57	2.5	16.5	3g	3	g
58	3.6	16.2	4g	4	g
59	0.3	5.4	1a	1	a
60	0.7	5.2	1a	1	a
61	4.2	17.1	5h	5	h
62	2.6	14.4	3e	3	e
63	4.4	17.2	5h	5	h
64	4.2	17.0	5h	5	h
65	3.9	17.2	4h	4	h
66	5.5	17.1	6h	6	h
67	5.8	17.3	6h	6	h
68	7.1	17.9	8h	8	h
69	2.3	13.9	3d	3	d
70	3.6	16.8	4g	4	g
71	9.6	18.6	9i	9	i
72	2.7	16.6	3g	3	g
73	2.0	15.7	3f	3	f
74	6.0	17.4	7h	7	h
75	6.3	17.6	7h	7	h
76	4.3	16.3	5g	5	g
77	7.0	18.1	8i	8	i
78	2.9	16.1	3g	3	g
79	3.8	17.2	4h	4	h
80	3.1	17.4	4h	4	h
81	5.0	17.8	6h	6	h
82	3.6	17.6	4h	4	h
83	3.6	16.7	4g	4	g
84	3.4	17.4	4h	4	h
85	2.7	16.9	3g	3	g
86	1.9	16.4	2g	2	g
87	3.9	17.3	4h	4	h
88	2.7	17.0	3h	3	h
89	4.1	17.3	5h	5	h
90	2.6	17.0	3g	3	h
91	2.4	16.7	3g	3	g
92	1.7	16.4	2g	2	g
93	2.1	15.1	3f	3	f
94	3.7	14.9	4e	4	e
95	6.7	17.7	7h	7	h
96	2.6	15.6	3f	3	f
97	2.8	15.8	3f	3	f
98	7.0	17.9	8h	8	h
99	4.4	17.1	5h	5	h
100	9.8	18.8	9i	9	i
101	9.1	18.7	9i	9	i

Table 20.1. Results from random readings of both FeO and TiO_2 weight percentage values. Groups' range are shown below:

TiO_2%	Ti group	FeO%	Fe group
0-1	1	<10	a
1-2	2	11-12	b
2-3	3	12-13	c
3-4	4	13-14	d
4-5	5	14-15	e
5-6	6	15-16	f
6-7	7	16-17	g
7-8	8	17-18	h
8-10	9	18-19	i

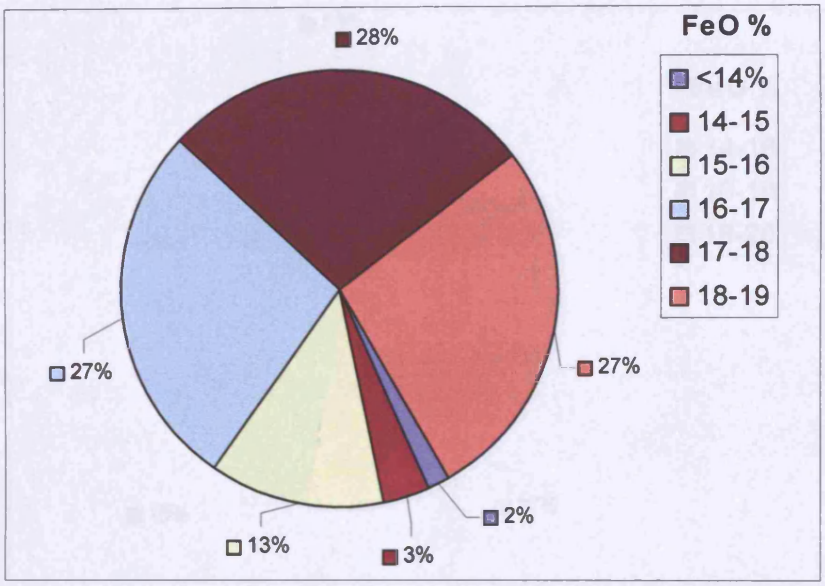

Figure 20.1. Percentage distribution of FeO in the Mare Imbrium region

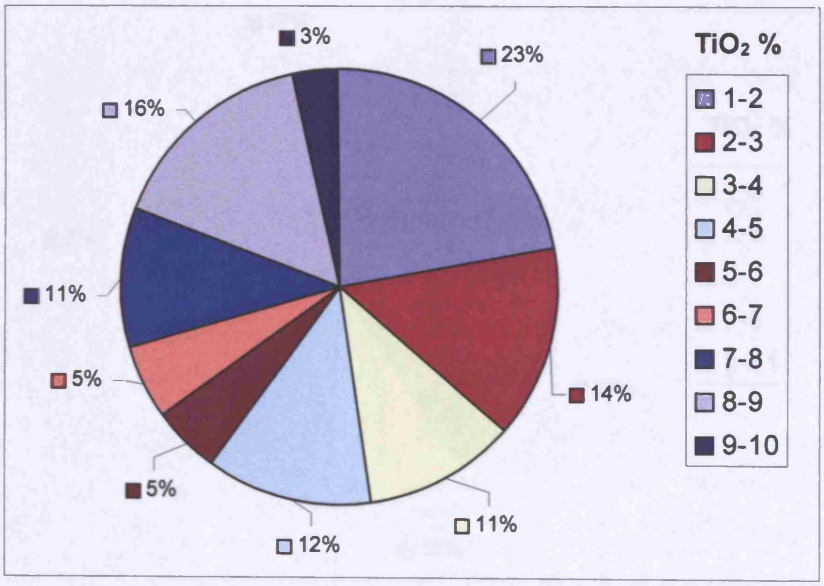

Figure 20.2. Percentage distribution of TiO_2 in the Mare Imbrium region

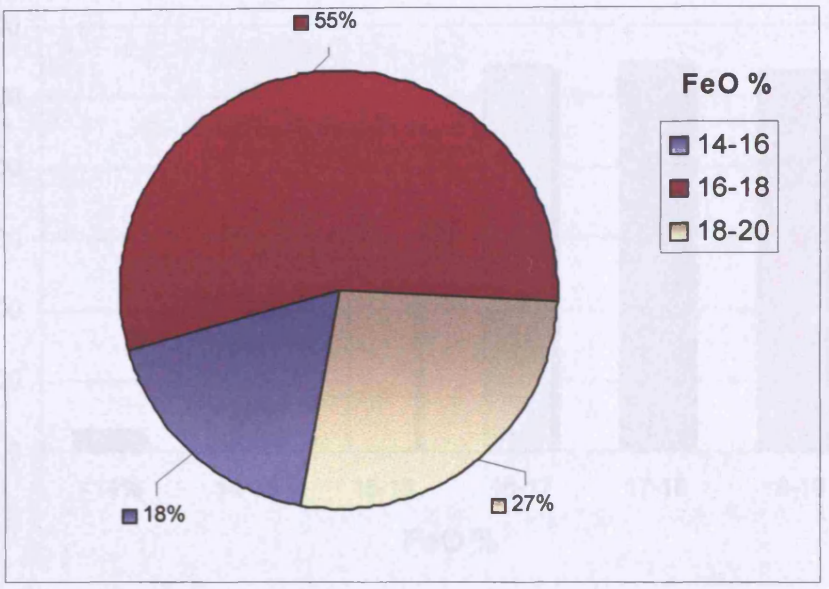

Figure 20.3. Percentage distribution of FeO in the Mare Imbrium region

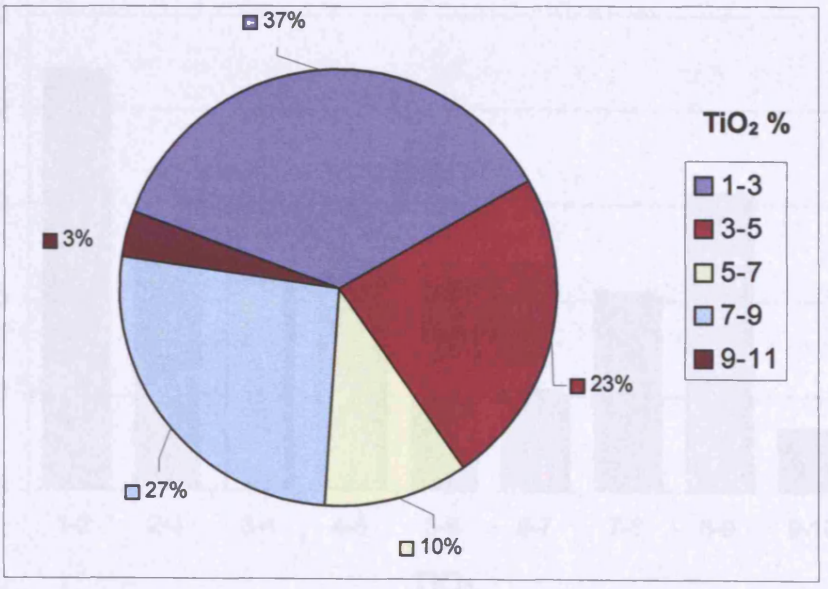

Figure 20.4. Percentage distribution of TiO_2 in the Mare Imbrium region

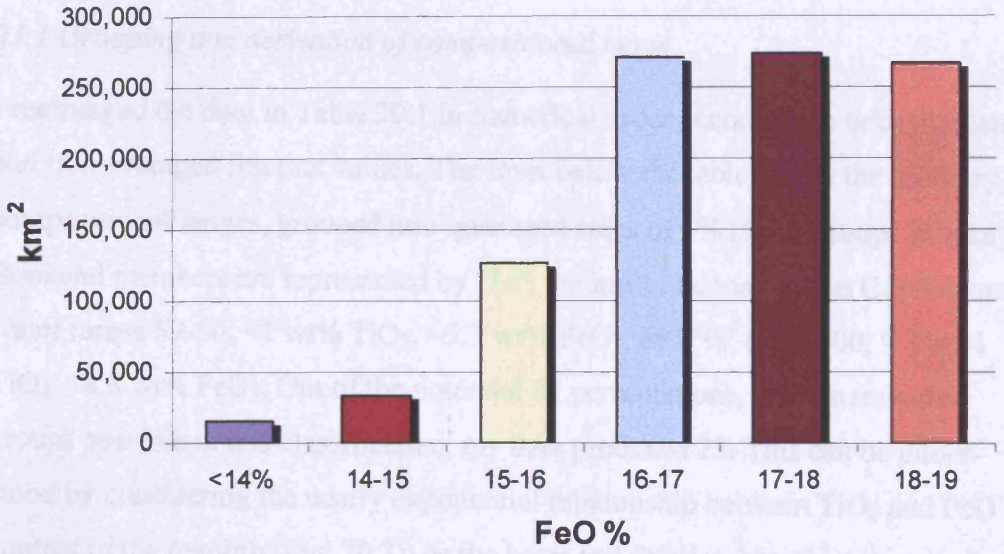

Figure 20.5. FeO wt% distribution of in the Mare Imbrium region

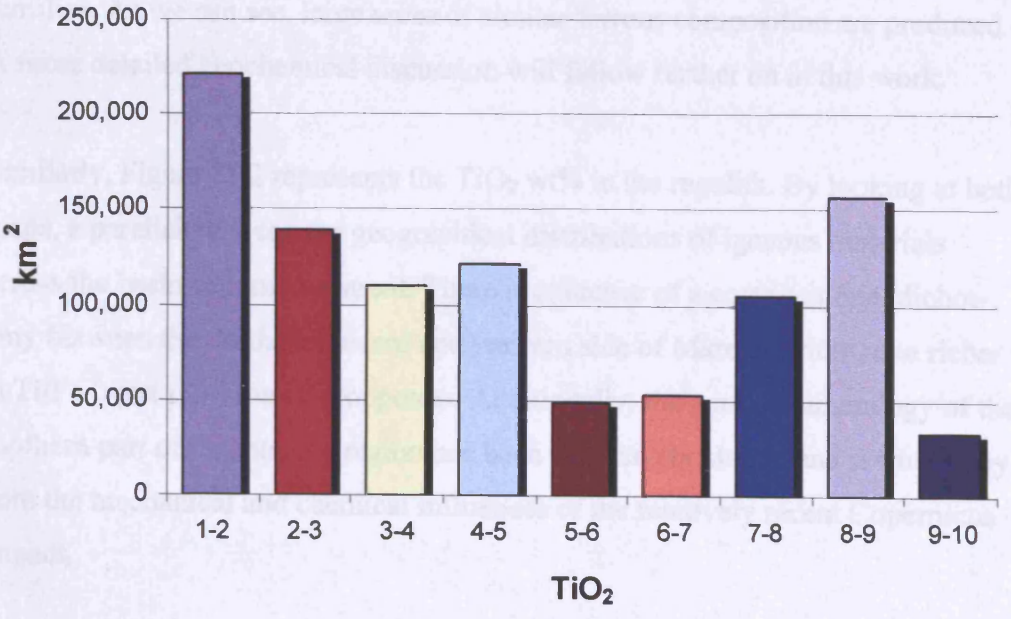

Figure 20.6. TiO_2 wt% distribution of in the Mare Imbrium region

21.1 Grouping and derivation of compositional maps

I rearranged the data in Table 20.1 in numerical order according to both titanium and iron averaged fraction values. The inset below the table shows the arbitrary compositional ranges, grouped into quantised steps of 1% (9 × 2 groups in total). Bookend members are represented by '1a': the infill material within Copernicus crater (areas 59-60, <1 wt% TiO_2, ~5.3 wt% FeO), and '9i' (area 100, 9.8 wt% TiO_2, 18.8 wt% FeO). Out of the potential 81 permutations, i.e. mineralogical groups possible in this classification, my data produced 23. This can be understood by considering the nearly exponential relationship between TiO_2 and FeO content in the regolith (Fig. 20.7): as the lunar soil fraction becomes progressively 'enriched' in titanium dioxide, we are met with a narrower range of possible iron values (high end range).

Figure 21.1 maps the geographical distribution fraction of FeO wt% in the maria. In aid of clarity, the nine iron groups were amalgamated further into five main families. As we can see, large areas of similar ferrous composition are produced. A more detailed geochemical discussion will follow further on in this work.

Similarly, Figure 21.2 represents the TiO_2 wt% in the regolith. By looking at both maps, a parallel between the geographical distributions of igneous materials across the basin become apparent. There is evidence of a compositional dichotomy between the northern eastern and western side of Mare Imbrium, one richer in Ti/Fe (west side) than the opposite. Additionally, the surface mineralogy of the southern part of the mapped region has been extensively altered and reworked by both the mechanical and chemical influences of the relatively recent Copernicus impact.

Regolith found within or just beyond major crater rims was noted for its relative Ti content only, and not included in the geochemical classification of the mare soils.

21.2 Further analysis and amalgamation of unit flows

My next step was to look for similar Ti/Fe values (same groups) in adjacent unit flows. When deemed appropriate, and the geological setting plausible, said units were merged. Examples are units 25 and 26 near Archimedes, both showing similar titanium and iron values, adjoining location, and comparable geomorphology. They were joined in this new group by unit 49 (Fig. 19.3), part of the Copernicus upland system, very similar in composition ('2c') and, probably, petrology.

Other groups cover much larger areas and include many a once distinctive unit. '3g' is an amalgamation of 14 of these areas that comprise several marginal plots scattered across the outer reaches of the basin. '2e' includes 'shore' material off Montes Jura and Alpes, and Plato's infill. Some areas could not be compared directly with others in the region.

Unit 22 is probably related to units '2c' and '2d', but its smaller Fe content precludes direct merging. A similar scenario is presented by unit 24, this time a narrow stretch of mare found between Montes Apenninus and Copernicus upland, which displays a lower than typical iron content, possibly a result of contamination from these areas.

Table 21.1 lists the 19 'remaining' chemically distinct groups, representing an average value from the 100 mare readings (Copernicus inner crater materials, readings 59-60, will be omitted from further analysis). It is unlikely that these units represent the only exposed igneous rock types present in the basin. It is also plausible that, as mentioned above, some of these flows may be directly related to some others on the ground, but they now appear different after undergoing a dissimilar weathering regime, and/or contamination.

Table 21.1. First grouping of mare units with similar chemical characteristics

Areas	TiO_2%	FeO%	*Chemical Family*
22	1.1	11.2	2b
25-26-49	1.5	12.3	2c
24	1.8	13.1	2d
1-2-12-21-28-54	1.6	14.8	2e
4-6-8-9-10-11-13-14-16-17-86-92	1.5	16.3	2g
50-51-52-53-62-69	2.4	14.2	3e
20-23-73-93-96	2.5	15.4	3f
0-3-5-7-27-29-57-72-78-85-88-90-91-97	2.7	16.4	3g
45-46-94	3.3	14.8	4e
15-35-47-58-70-83	3.7	16.5	4g
33-56-65-79-80-82-84-87	3.6	17.4	4h
44	4.0	15.5	5f
31-37-76	4.3	16.5	5g
19-36-48-61-63-64-89-99	4.7	17.3	5h
38-39-40-41-55-66-67-81	5.3	17.4	6h
18-30-34-43-68-74-75-77-95-98	6.8	18.7	7i
32-42-71-100-101	9.3	18.8	9i

My next task was to further analyse the data displayed in Table 21.1, recognise potentially related chemical families and 'discard' units deemed unrepresentative of the overall geology of the region, mainly because of their physical location, limited geographical extension, peculiar topography, or possible contamination (ejecta, rays, material slumping, surface reworking, etc.).

Area 22 was not included in the new classification of related lava flow units because of its composition being more closely related to the adjacent highlands than the rest of the mare (typical composition of direct sampled melt rocks and glasses from the Montes Apenninus averages TiO_2 1.3 wt% and FeO 9.1 wt%, Spudis, 1993). Furthermore, its proximity to the Cassini craters meant the surface would also have been subject to extensive admixing with excavated materials. The decision to exclude families 2c and 2d was based on similar arguments. Further analysis of the geological settings and soil compositions of individual units (Table 20.1), in conjunction with Table 21.1 data, resulted in the removal, relocation, or reclassification of some of these unit flows. New family 3f includes units 20 and 27, which cover a geographical region (around craters Archimedes and Autolycus) with unusual composition (lower FeO, similar to areas of low TiO_2 content).

The main aspect of my reclassification relates to the shift in detail regarding the grouping of areas with higher titanium values. I amalgamated (or discarded) units with very low Ti content because of the petrological implications (contamination, admixing etc.) and error margins (a reading of 0.5 TiO_2 wt% ± 0.5 % cannot be considered very representative of a true value). Concurrently, I expanded or refined the higher titanium unit members' classification. Whereas in Table 21.1 potential unit flows with TiO_2 values larger than 5.3% were split in two chemical families, the new classification creates a further three.

21.3 Derivation of eight compositional groups

Table 21.2 lists 13 distinctive compositional categories. Titanium and iron values were derived from the geographically weighted mineralogical contribution from each unit flow. Finally, I created eight compositional groups from areas belonging to similar chemical families.

Table 21.2. Further grouping of mare units with similar chemical characteristics

Area	TiO_2%	FeO%	*Chemical family*	Area size km^2
1, 2, 8, 12, 14, 21	1.4	15.2	2f	*129,300*
13	1.2	16.2	2g	*12,600*
4, 6, 9, 11, 16, 17, 92	1.7	16.4	2g	*54,700*
20, 27	2.8	15.2	3f	*45,500*
7, 23, 57, 72, 73, 91	2.5	16.0	3g	*30,200*
0, 3, 5, 88, 90	2.5	16.9	3g	*41,900*
31, 36, 76, 87, 89	4.0	17.4	5h	*42,800*
19, 39, 40, 48, 61, 63, 64	4.2	17.1	5h	*74,600*
30, 43, 74	6.2	17.5	7h	*47,200*
18	7.1	17.9	8h	*8,200*
34, 68, 77, 98	7.2	18.0	8i	*96,700*
32, 42, 101	8.9	18.8	9i	*162,400*
100	9.8	18.8	9i	*2,500*

Figure 21.3 represents the geographical distribution of the eight groups listed in Table 21.2. There are large areas of uncharted terrain. As discussed earlier on, the composition of these soils' does not display a Fe/Ti trend comparable to that of the majority of the regional mare. Most of these regoliths were somewhat recently reworked or gardened by nearby cratering events, making the surface material less representative of its pristine composition. Nevertheless, for a fuller interpretation

of the mineralogical distribution of surface materials in the region, we should complement the study of Figure 21.3 with compositional maps 21.1 and 21.2.

Finally, Figure 21.4 represents the geographical extension of each 'new' group in the region.

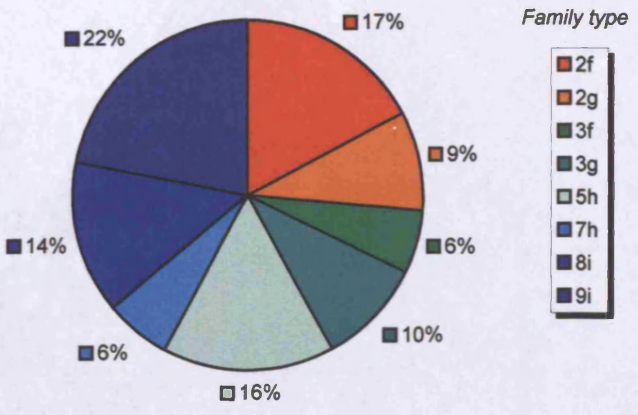

Figure 21.4. Geographical percentage distribution of each chemical family.

21.4 Results

Figure 21.4 shows that there is an almost even distribution of regolith types, ranging from 2f (1.4 wt% TiO_2 – 15.2 wt% FeO) to 9i (9.8 wt% TiO_2 – 18.8 wt% FeO).

Figures 21.1 and 21.2, along with data from table 21.2 suggest a further simplification of the classification of soil composition: one with relatively low-Ti (1-2 wt% TiO_2, 2f, 2g, 'red' colours), average titanium (2-4 wt%, 3f, 3g, 5h, 'greens'), and high-Ti (6-10 wt%, 7h, 8h, 8i, 9i, 'blues'). Their relative territorial distributions are, respectively, 26 wt%, 32 wt%, and 42 wt%).

Figure 21.1. FeO map with original unit boundaries

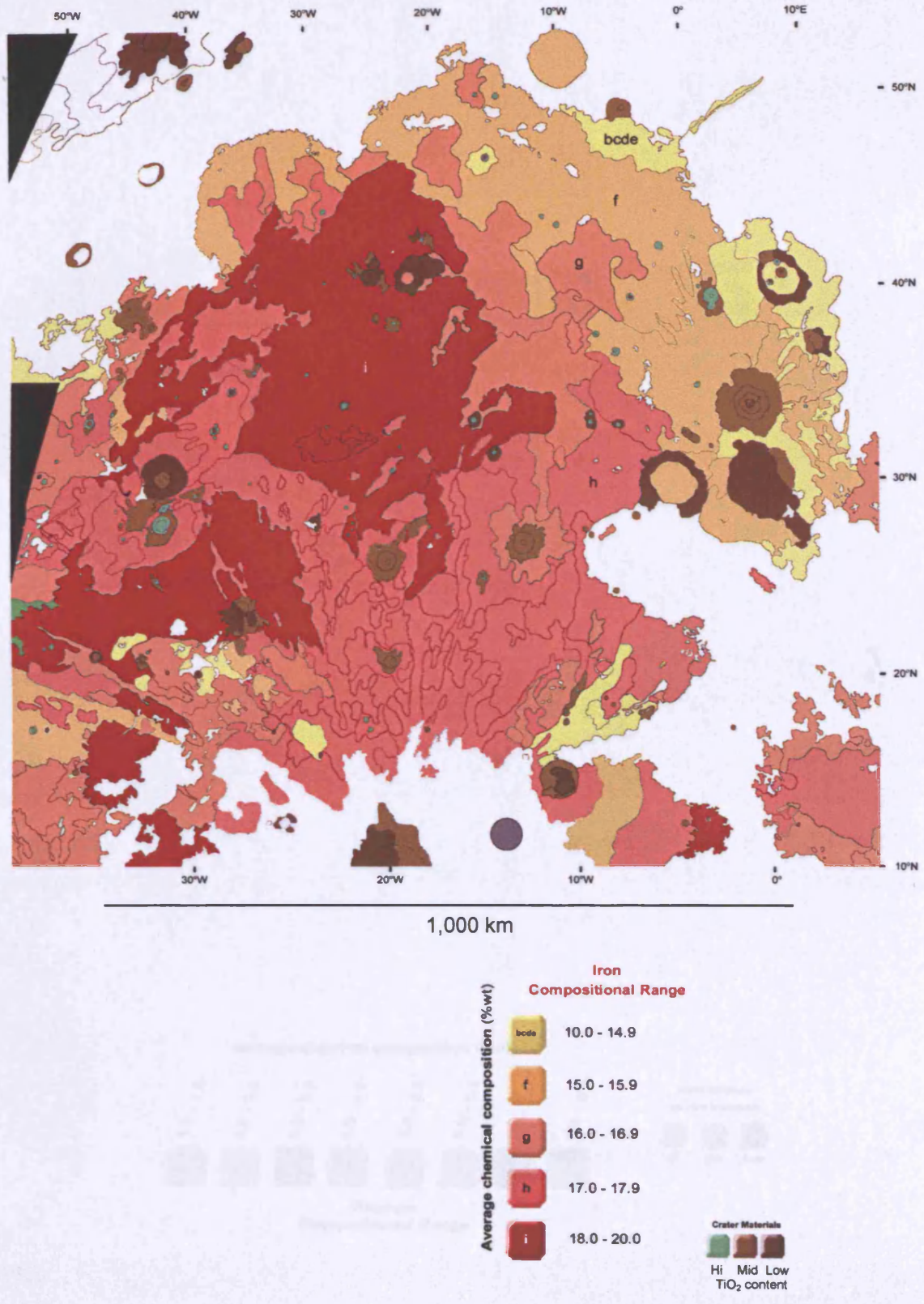

Figure 21.2. TiO_2 map with original unit boundaries

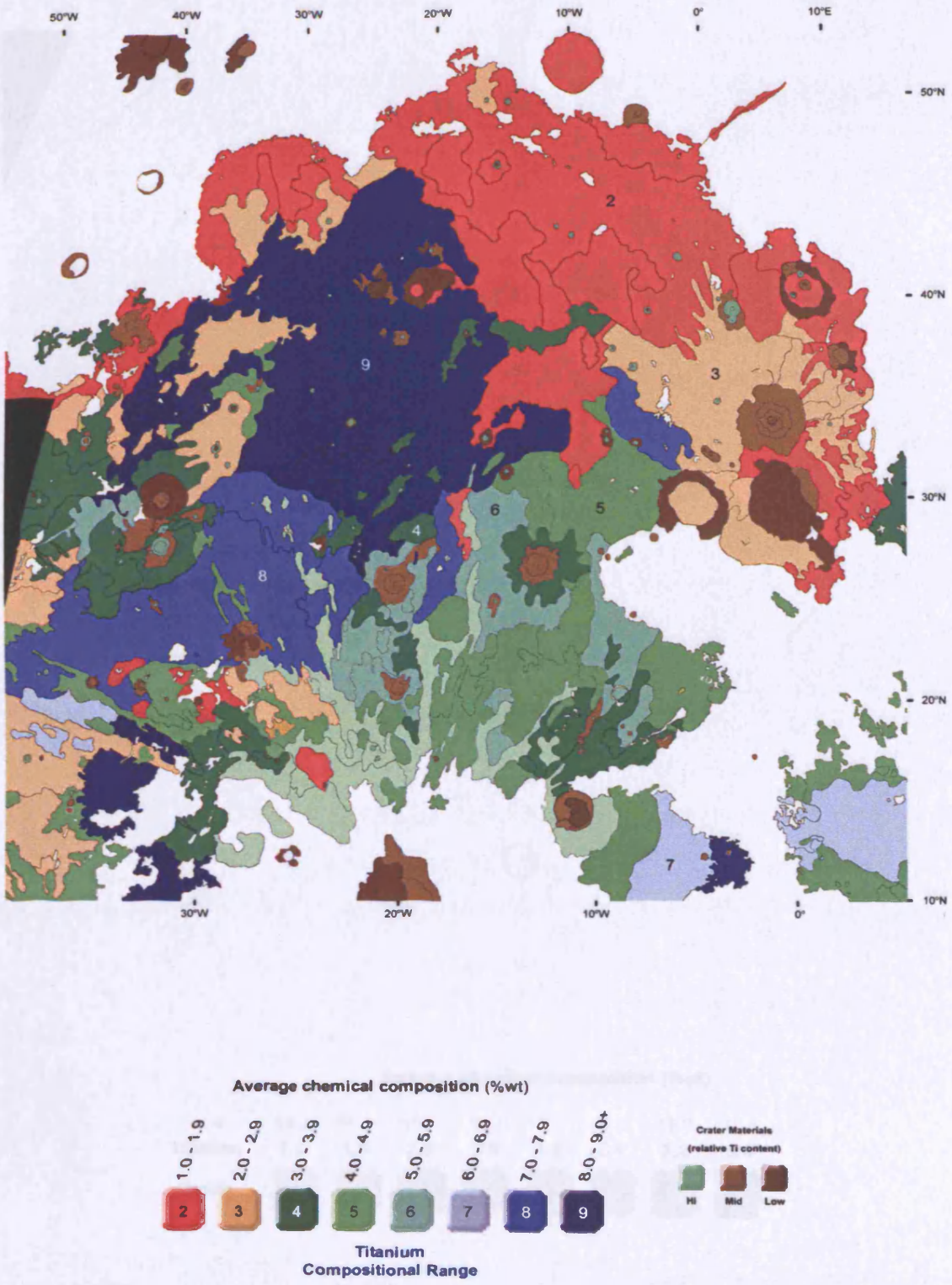

Figure 21.3. Grouped units with similar FeO-TiO_2 content.

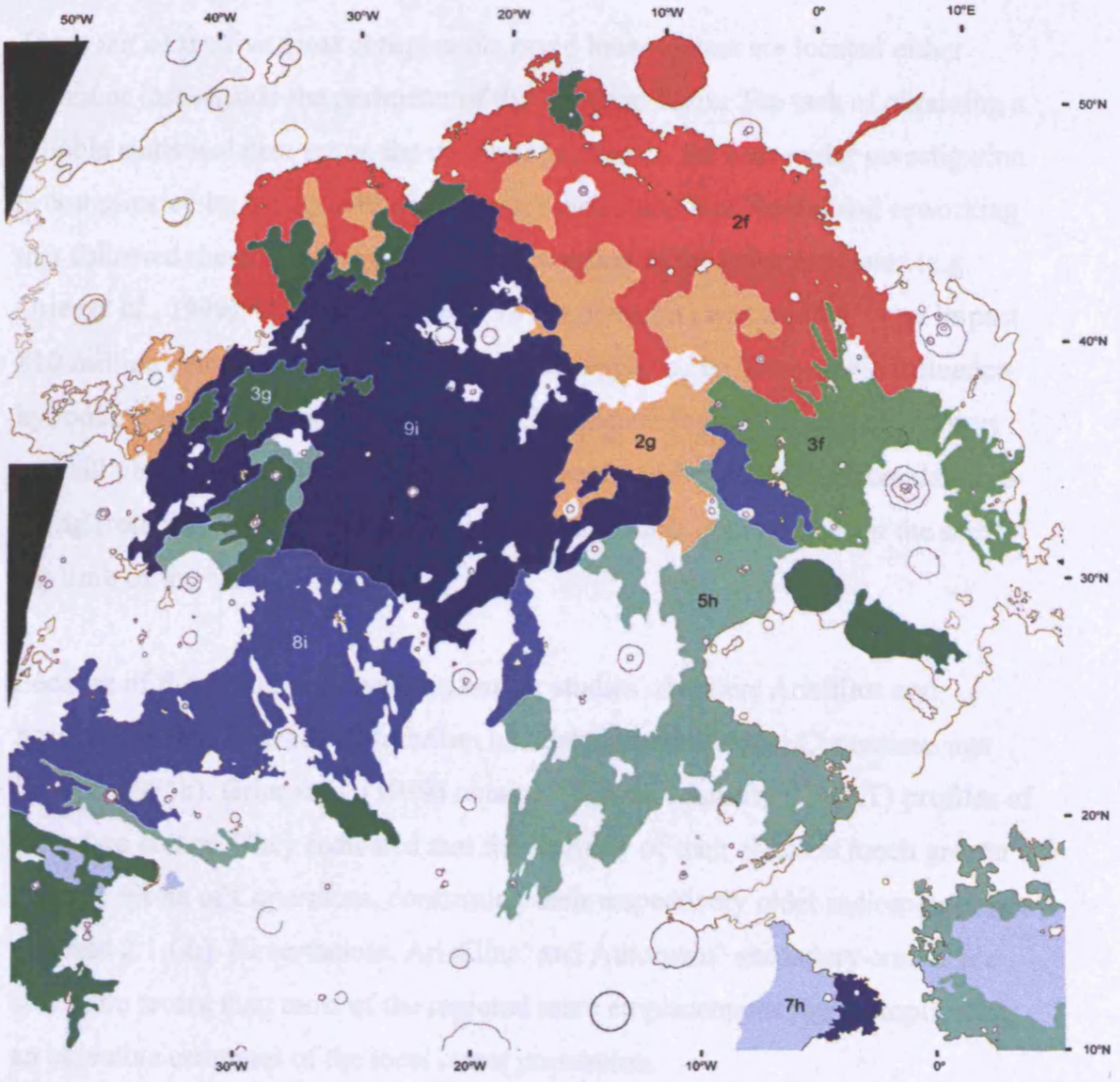

Average chemical composition (%wt)

Iron	15.2	16.3	16.5	15.2	17.3	17.5	18.0	18.8
Titanium	1.4	1.5	2.5	2.8	4.1	6.1	7.2	9.4
Group	2f	2g	3g	3f	5h	7h	8i	9i

CHAPTER 22 CRATER COUNT WITHIN EACH OF THE PROPOSED UNITS – COMPARATIVE AGE DETERMINATION

MARE IMBRIUM

22.1 Background and method

Three out of the five most conspicuous rayed lunar craters are located either within or just outside the perimeter of the Imbrium basin. The task of obtaining a reliable statistical data set on the crater population of the area under investigation is complicated by the amount of secondary ejecta and mechanical soil reworking that followed these post-mare impacts. According to the latest estimates (e.g. Grier *et al.*, 1999), Copernicus crater (93 km diameter) was created by an impact 810 million years ago. We can appreciate the extent of its geomorphic influence by looking at the Clementine images, for instance at Figure 16.1. Its ejecta rays are still visible just north of 30° N, well inside the Imbrium basin. Secondary cratering from this impact seriously jeopardises a reliable crater census at the southern limb of the basin.

Because of their bright ray systems, earlier studies of craters Aristillus and Autolycus in the east side of Imbrium had dated them to a post Copernicus age (Boyce, 1975b). Grier *et al.* (1999) obtained Optical Maturity (OMAT) profiles of these two craters. They indicated that the maturity of their ejecta is much greater than the ejecta of Copernicus, confirming their respectively older radiometric ages (1.3 and 2.1 Ga). Nevertheless, Aristillus' and Autolycus' secondary craters are still more recent than most of the regional mare emplacements thus complicating an objective estimates of the local crater population.

I followed the same technique and data sources as those employed for the Nubium region and described in Chapter 10 of this work to obtain data on crater frequency in Mare Imbrium.

22.2 Results

Table 22.1 shows all the crater count results (i.e. crater density) of each unit area. Some of the originally mapped units were either too small to obtain a reliable crater count figure (i.e. 25, 26, and 46), or severely scarred and effected by secondary

impacts (50, 51, 52, 69, or geographically marginal (85 and 86). Ultimately, 81 units were analysed, representing 981,100 km^2, or 80% of this study's spectrally sampled mare.

The most heavily cratered units are located, somewhat unsurprisingly, not far from major craters (i.e. 58, 37, 70 etc.). There is no doubt that although great care was taken not to include as many 'suspicious' secondary craters as possible in the count, many were included. Nevertheless, the modelled ages (see Figure 10.2) give us an estimate of 3.4 ± 0.1 Ga.

The units dated as the youngest in the basin are found scattered across the whole basin, with most prominent of these located near the centre of Mare Imbrium. In particular, units 98, 100, 101, and 33 appear somewhat younger (~ 2.2 ± 0.1 Ga) than the surrounding terrain (2.3 ± 0.1 Ga). This is consistent with early studies (e.g. Schaber *et al.*, 1975, Hiesinger *et al.*, 2000), which give values in the region of 2.3 ± 0.2 Ga.

The average unweighted crater density is 0.047 craters (>0.5 km) per square kilometre (3.1 ± 0.1 Ga).

Table 22.2 rearranges the data of table 22.1 according to a descending crater density order. I then subdivided the units into nine groups of comparable cratering patterns (a-i), choosing $0.5 \times 10^{-2}N\ km^{-2}$ as an arbitrary incremental step (except for endmember group a).

These nine families are mapped in Figure 22.1 with Table 22.3 listing their geographical coverage. Figure 22.2 is a graphic representation of the percentage share of each group.

Table 22.3. List of nine compositional families within Mare Nubium

Family	a	b	c	d	e	f	g	h	i
Surface Km^2	8,400	50,900	42,700	75,900	213,900	115,700	60,800	365,500	47,300
Crater density >0.5 km $10^{-2}N/km^2$	7.0 - 8.0	6.5 - 6.9	6.0 - 6.4	5.5 - 5.9	5.0 - 5.4	4.5 - 4.9	4.0 - 4.4	3.5 - 3.9	2.9 - 3.4

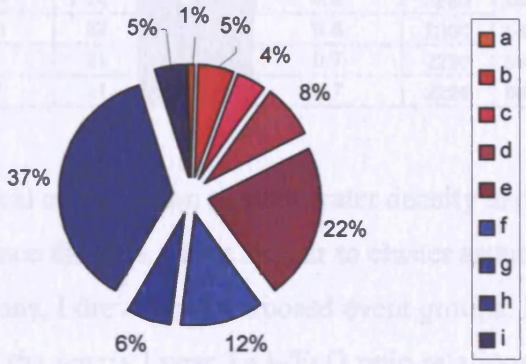

Figure 22.2
Area distribution of crater density in maria

Three quarters of the mare shows a crater density population within groups h and e ($3.5 - 5.5 \times 10^{-2}$N km^{-2}), giving an estimated age between 2.5 and 3.3 Ga. I further categorised a-i families into four major groups, using crater density unit increments:

Using data taken from Tables 22.1 and 22.2, I associated units with comparable Ti-Fe composition and crater density. Naturally, not every unit could be easily assigned to a common chemical/age group. I used my previous list of 13 distinctive compositional categories (from a pool of 51 selected units), grouped it into eight encompassing families (Table 21.2, Fig. 21.3), then further enhanced it with new crater density data, to produce Table 22.4. The crater count/density figure represents a weighted average of the original units' values.

Table 22.4. Grouping of eleven compositional units into eight

Units	TiO_2 %	FeO %	Chemical/ age group	Crater count	Crater Density $10^{-2}N\ km^{-2}$	One-Sigma error +/- $10^{-2}N\ km^{-2}$	Age (Ma)	+/-	% +/-	Area size km^2
1, 2, 8, 12, 14, 21	1.4	15.2	2f/e	34	5.4	0.9	**3310**	*185*	5.6	*129,300*
13	1.2	16.2	2g/g	27	4.3	0.8	**2830**	*500*	17.0	*12,600*
4, 6, 9, 11, 16, 17, 92	1.7	16.4	2g/e	34	5.4	0.9	**3310**	*185*	5.6	*54,700*
7, 23, 57, 72, 73, 91	2.5	16.0	3g/f	28	4.5	0.8	**2980**	*445*	15.0	*45,500*
0, 3, 5, 88, 90	2.5	16.9	3g/h	23	3.7	0.8	**2420**	*545*	22.5	*30,200*
20, 27	2.8	15.2	3f/h	22	3.5	0.8	**2300**	*540*	23.5	*41,900*
31, 36, 76, 87, 89	4.0	17.4	5g/h	22	3.5	0.8	**2300**	*540*	23.5	*42,800*
19, 39, 40, 48, 61, 63, 64	4.2	17.1	5g/e	33	5.3	0.9	**3310**	*220*	6.7	*74,600*
30, 43, 74	6.2	17.5	7h/e	31	5.0	0.9	**3300**	*310*	9.4	*47,200*
18	7.1	17.9	8h/f	28	4.5	0.8	**2980**	*445*	14.9	*8,200*
34, 68, 77, 98	7.2	18.0	8i/h	22	3.5	0.8	**2300**	*540*	23.5	*96,700*
32, 42, 101	8.9	18.8	9i/i	21	3.4	0.7	**2220**	*540*	24.3	*162,400*
100	9.8	18.8	9i/i	21	3.4	0.7	**2220**	*540*	24.3	*2,500*

I plotted the variations in chemical composition against crater density and obtained Figures 22.3 and 22.4. Since the data points appear to cluster around relatively narrow cratering populations, I drew three proposed event groups. It is important to notice that because of the nearly linear TiO_2/FeO ratio relationship as shown in Figure 20.7, the two graphs display a very similar trend.

Figures 22.5 and 22.6 share the same chemical compositional axis with the previous figures but this time they are plotted against inferred ages (see Fig. 10.2). Three cluster families emerge again, as shown in Table 22.5:

Table 22.5. Classification of Mare Imbrium flows into three eruptive periods

Period		TiO_2 wt%	FeO wt%	Average age (Ga)
I	Middle Imbrian	1.4-6.2	15.2-17.5	3.3 ± 0.1
II	Late Imbrian	2.5-7.1	16.0-17.9	3.0 ± 0.2
III	Early Eratosthenian	2.5-9.8	15.2-18.8	2.3 ± 0.5

Figure 22.7 brings together the chemical distribution of the eight regolith compositional groups from Figure 21.3 and their inferred age as in Table 22.5.

22.3 Discussion

Figure 22.1 shows the two endmenbers (a-i) crater density units to be confined to small geographical areas. In particular, the older (by definition) basalts are found not far from major impacts (Copernicus, Timocharis etc). Interestingly, adjacent to the west of the old terrain north of Timocharis, we find some of the freshest

looking regolith in the area. We also see potentially contemporary soils further west, south of Carlini. Unit 98 (see Fig. 19.3) is one of these 'young' terrains and it appears to be 'severed' in its northeasterly limb by the Dorsum Zirkel.

Most heavily cratered maria are concentrated in the eastern half of Mare Imbrium, except for a radial area around Aristillus and Autolycus. The vast amount of ejecta distributed by these two relatively recent events, in addition of the mechanical effects of the blasts on the surrounding surface materials, may have 'reset' the apparent age of the pre-existing units. The sharp decline in bombardment rates in the last two billion years would have caused the basalts to appear much younger than their estimated age. The freshest units (h) cover just over 40% of the whole basin and are found mainly in the western section of the basin. Pockets of heavily cratered terrains away from major blasts are located within Sinus Iridum and west of Kirch.

Figure 22.7, together with the data in Figures 22.3 to 22.6, depicts eight distinctive basalt mineralogies representing the exposed, and locally youngest, lava flows.
According to this study, three major periods of mare infill are exposed in the Imbrium basin; despite each period showing a range of basaltic compositions (classified according to their titanium content), it is apparent that, at least in narrow geological settings, the igneous petrogenesis shifted with time towards more mafic melts (higher Ti and Fe fractions).

Figure 22.8 reconstructs a possible chronology of the major mare infill in the basin. Clearly, periods I and III represent the two principal eruptive phases in the region, broadly divided between Middle to Late Imbrian epochs and Early to Late Eratosthenian periods (as classified by Neukum and Ivanov, 1994). Earlier flow remains can still be found against the basin's prominent coastlines and promontories. Later infills flooded the topographic lows of the centre of the basin. I will discuss in more depth the chronogeology and petrology of the region in later chapters.

22.4 Comparison with previous studies

My results are in broad agreement with earlier findings regarding the dating of potential unit flows. Boyce (1975a) built a chronology of flow units in western maria based on crater morphology (also Boyce, 1976). My results broadly agree with his by recognising three major flow periods (see Table 22.6). We disagree nevertheless on the geographical distribution of these mare materials, albeit agreeing on the general conclusion that fresher basalts are mostly found in the western side of the basin, with the latest flows occupying the central part of the basin.

Hiesinger *et al.* (2000) published the results of a large study aimed at unravelling the ages of mare basalts on the lunar nearside. They confirmed the younger ages of the western basalts compared to the eastern ones. In detail, however, many units do not correspond to or match in my analysis. It is interesting to note how such divergent data would have been generated from the study of similar material sources (chromophotography and Orbiter IV images). The differences are probably due to the subjective interpretation of the crater as a primary or secondary feature. Major discrepancies relate to the ages of broadly comparable units around craters Aristillus, Autolycus, and Archimedes (units 20, 27 etc., Fig. 19.3, in this study, and I6, figure 6.2, Hiesinger *et al.*, 2000). I took into consideration the relatively young age of the two smaller impact events, with all the constraints on the timing of basaltic cover on the ejecta, plus the predictable scattering of vast quantities of secondary craters and materials in the neighbouring areas, and finally the spectral signature of the terrain. As a result, I interpreted this area to be much younger (~2.3 ± 0.5 Ga) than the 3.5 Ga in their study. Overall, the discussed differences in the interpretation of our results stem from the availability and choice of multispectral images of the basin. They used data from the Galileo Earth/Moon Encounter 2 (EM2) with < 2 km/px spatial resolution, whereas the Clementine data set which benefits from a resolution of a factor of 10 higher (~0.2 km/px). This allowed a finer subdivision of potential flow units in this work, obviously still liable to subjective and often contrasting interpretations of chromographic differences.

Table 22.6 gathers a range of estimates for the ages of flow units in the Imbrium Basin. Most workers agree on a three major phases of igneous outpouring, and broadly confirm their chronological distribution. Nevertheless, because some of these works aimed at dating previously spectrally defined flows (i.e. this work), and others concentrated on building a mare emplacement history from the varying ages of surface terrains (i.e. Boyce, 1975), we find minor differences in the interpretation of geographical distributions of these flow 'periods' I, II, and III.

Table 22.6. Comparison of different estimates for ages of flow units

Papers / Period	**Head** (1975) (Ga)	**Boyce** (1976) (Ga)	**Whitford-Stark & Head** (1980) (Ga)	**Friedman** *et al* (1996) (Ga)	**Hiesinger** *et al* (2000) (Ga)	**Bugiolacchi** (2005) (Ga)
I	3.6 ± 0.1	3.6 ± 0.1	3.5 ± 0.3	3.5 ± 0.1	3.5 ± 0.2	3.3 ± 0.1
II	3.3 ± 0.2	3.1 ± 0.2	3.3 ± 0.3	3.0 ± 0.4	3.1 ± 0.2	3.0 ± 0.2
III	2.8 ± 0.3	2.6 ± 0.3	2.5 ± 0.3	2.6 ± 0.4	2.6 ± 0.3	2.3 ± 0.5

Table 22.1. Full list of each unit's crater count and inferred average age

Units	Crater Density >0.5 km 10^{-2}N km^{-2}	Crater count (in a area of 625 km^2)	One-Sigma error +/- 10^{-2}N km^{-2}	TiO_2 wt%	FeO wt%	Approx. Area size km^2	OIV Images #
0	3.7	23	0.8	2.5	16.4	*2,700*	127h3a
1	5.3	33	0.9	1.4	15.4	*7,300*	127h3b
2	5.6	35	0.9	1.5	15.5	*18,600*	145h2a
3	4.0	25	0.8	2.4	17.0	*4,900*	139h2c
4	6.4	40	1.0	1.5	16.3	*1,800*	145h2
5	3.8	24	0.8	2.3	17.3	*3,400*	139h2d
6	5.3	33	0.9	1.7	16.1	*3,200*	127h3d
7	4.2	26	0.8	2.4	16.4	*1,800*	134h2
8	5.3	33	0.9	1.1	15.9	*83,800*	115h2a
9	5.3	33	0.9	1.8	16.3	*5,100*	127h2d
11	5.3	33	0.9	1.5	16.7	*14,700*	122h2d
12	5.8	36	1.0	1.8	14.9	*8,700*	115h2b
13	4.3	27	0.8	1.2	16.2	*12,600*	115h2a
14	6.7	42	1.0	1.2	15.8	*3,500*	122h2d
15	6.4	40	1.0	3.9	16.8	*6,200*	122h2d
16+17	5.1	32	0.9	1.8	16.4	*23,000*	115h1c
18	4.5	28	0.8	7.1	17.9	*8,200*	115h1c
19	5.6	35	0.9	4.1	17.3	*17,900*	114h3d
20	3.7	23	0.8	2.8	15.0	*37,000*	115h2
21	5.1	32	0.9	1.4	14.6	*7,400*	110h2
22	3.5	22	0.8	1.1	11.2	*15,300*	126h3b
23	4.5	28	0.8	2.6	15.3	*12,000*	109h3b
27	3.4	21	0.7	2.9	15.6	*4,900*	110h3
28	3.7	23	0.8	1.9	15.0	*6,300*	103h3
29	4.0	25	0.8	3.2	16.4	*4,300*	103h3
30	4.8	30	0.9	6.3	17.5	*26,400*	112
31	3.5	22	0.8	4.0	16.4	*20,900*	122h2
32	3.5	22	0.8	8.8	18.6	*156,500*	139h2a
33	3.5	22	0.8	3.6	17.4	*6,300*	127h1a
34	3.8	24	0.8	7.9	18.2	*5,800*	126h3c
35	4.5	28	0.8	3.9	16.2	*7,000*	122h1
36	3.4	21	0.7	4.0	17.1	*5,400*	122h1
37	7.5	47	1.1	4.5	16.8	*3,000*	122h1
38	6.1	38	1.0	5.1	17.5	*15,800*	121h3a
39	5.3	33	0.9	5.1	17.4	*10,100*	114h3d
40	5.6	35	0.9	4.9	17.2	*12,600*	114h3c
41	4.6	29	0.9	5.6	17.5	*2,100*	114h3c
42	3.2	20	0.7	9.0	19.3	*5,000*	109h2a
43	5.1	32	0.9	6.1	17.6	*16,700*	109h2a
44	6.2	39	1.0	4.0	15.5	*15,100*	114h2
45	4.5	28	0.8	3.1	14.7	*11,000*	114h3d
47	5.9	37	1.0	3.6	16.1	*6,000*	114h3d
48	5.1	32	0.9	4.0	17.2	*16,200*	121h3c
54	3.2	20	0.7	1.5	14.3	*2,500*	126h2
55	3.8	24	0.8	5.3	17.5	*4,900*	126h3b
56	5.3	33	0.9	3.4	17.3	*2,500*	126h3d
57	4.8	30	0.9	2.5	16.5	*7,900*	133h3c
58	8.0	50	1.1	3.6	16.2	*5,400*	133h2c
61	5.4	34	0.9	4.2	17.1	*11,000*	121h2
63	5.0	31	0.9	4.4	17.2	*3,200*	121h3a
64	5.3	33	0.9	4.2	17.0	*3,600*	121h3
65	5.1	32	0.9	3.9	17.2	*2,000*	126h3a

66	**4.0**	25	0.8	5.5	17.1	*7,000*	126h3c
67	**4.6**	29	0.9	5.8	17.3	*3,500*	126h3c
68	**3.7**	23	0.8	7.1	17.9	*6,600*	126h3a
70	**6.9**	43	1.0	3.6	16.8	*12,500*	133h2c
71	**6.7**	42	1.0	9.6	18.6	*24,900*	133h2c
72	**4.2**	26	0.8	2.7	16.6	*13,600*	138h2a
73	**4.8**	30	0.9	2.0	15.7	*19,600*	138h2
74	**5.3**	33	0.9	6.0	17.4	*4,100*	138h2a
75	**2.9**	18	0.7	6.3	17.6	*5,900*	144h3b
76	**3.4**	21	0.7	4.3	16.3	*8,500*	144h3b
77	**3.8**	24	0.8	7.0	18.1	*71,700*	139h1a
78	**5.9**	37	1.0	2.9	16.1	*5,200*	144h3a
79	**4.0**	25	0.8	3.8	17.2	*10,300*	139h1a
80	**4.0**	25	0.8	3.1	17.4	*6,300*	144h3a
81	**4.6**	29	0.9	5.0	17.8	*5,400*	144h3a
82	**4.6**	29	0.9	3.6	17.6	*5,900*	144h3a
83	**6.6**	41	1.0	3.6	16.7	*10,000*	145h1
84	**4.8**	30	0.9	3.4	17.4	*5,300*	145h1
87	**3.5**	22	0.8	3.9	17.3	*4,400*	139h1
88	**3.8**	24	0.8	2.7	17.0	*9,800*	139h1a
89	**3.8**	24	0.8	4.1	17.3	*3,600*	139h1a
90	**3.5**	22	0.8	2.6	17.0	*9,400*	139h2c
91	**4.5**	28	0.8	2.4	16.7	*1,400*	145h2a
92	**5.8**	36	1.0	1.7	16.4	*6,900*	145h2
94	**6.1**	38	1.0	3.7	14.9	*3,200*	145h2
98	**3.2**	20	0.7	7.0	17.9	*12,600*	139h1b
99	**6.2**	39	1.0	4.4	17.1	*600*	139h1b
100	**3.4**	21	0.7	9.8	18.8	*2,500*	134h1d
101	**3.5**	22	0.8	9.1	18.7	*900*	134h1d

Table 22.2. Classification of mare units according to crater density

Units	Crater Density >0.5 km 10^{-2}N km^{-2}	Crater count	One-Sigma error +/- 10^{-2}N km^{-2}	TiO_2 wt%	FeO wt%	Approx. Area size km^2
58	8.0	50	1.1	3.6	16.2	*5,400*
37	7.5	47	1.1	4.5	16.8	*3,000*
70	6.9	43	1.0	3.6	16.8	*12,500*
14	6.7	42	1.0	1.2	15.8	*3,500*
71	6.7	42	1.0	9.6	18.6	*24,900*
83	6.6	41	1.0	3.6	16.7	*10,000*
4	6.4	40	1.0	1.5	16.3	*1,800*
15	6.4	40	1.0	3.9	16.8	*6,200*
44	6.2	39	1.0	4.0	15.5	*15,100*
99	6.2	39	1.0	4.4	17.1	*600*
94	6.1	38	1.0	3.7	14.9	*3,200*
38	6.1	38	1.0	5.1	17.5	*15,800*
78	5.9	37	1.0	2.9	16.1	*5,200*
47	5.9	37	1.0	3.6	16.1	*6,000*
12	5.8	36	1.0	1.8	14.9	*8,700*
92	5.8	36	1.0	1.7	16.4	*6,900*
2	5.6	35	0.9	1.5	15.5	*18,600*
19	5.6	35	0.9	4.1	17.3	*17,900*
40	5.6	35	0.9	4.9	17.2	*12,600*
61	5.4	34	0.9	4.2	17.1	*11,000*
1	5.3	33	0.9	1.4	15.4	*7,300*
8	5.3	33	0.9	1.1	15.9	*83,800*
6	5.3	33	0.9	1.7	16.1	*3,200*
9	5.3	33	0.9	1.8	16.3	*5,100*
11	5.3	33	0.9	1.5	16.7	*14,700*
56	5.3	33	0.9	3.4	17.3	*2,500*
64	5.3	33	0.9	4.2	17.0	*3,600*
39	5.3	33	0.9	5.1	17.4	*10,100*
74	5.3	33	0.9	6.0	17.4	*4,100*
21	5.1	32	0.9	1.4	14.6	*7,400*
16+17	5.1	32	0.9	1.8	16.4	*23,000*
65	5.1	32	0.9	3.9	17.2	*2,000*
48	5.1	32	0.9	4.0	17.2	*16,200*
43	5.1	32	0.9	6.1	17.6	*16,700*
63	5.0	31	0.9	4.4	17.2	*3,200*
73	4.8	30	0.9	2.0	15.7	*19,600*
57	4.8	30	0.9	2.5	16.5	*7,900*
84	4.8	30	0.9	3.4	17.4	*5,300*
30	4.8	30	0.9	6.3	17.5	*26,400*
82	4.6	29	0.9	3.6	17.6	*5,900*
41	4.6	29	0.9	5.6	17.5	*2,100*
67	4.6	29	0.9	5.8	17.3	*3,500*
81	4.6	29	0.9	5.0	17.8	*5,400*
23	4.5	28	0.8	2.6	15.3	*12,000*
91	4.5	28	0.8	2.4	16.7	*1,400*
45	4.5	28	0.8	3.1	14.7	*11,000*
35	4.5	28	0.8	3.9	16.2	*7,000*
18	4.5	28	0.8	7.1	17.9	*8,200*
13	4.3	27	0.8	1.2	16.2	*12,600*
7	4.2	26	0.8	2.4	16.4	*1,800*
72	4.2	26	0.8	2.7	16.6	*13,600*
3	4.0	25	0.8	2.4	17.0	*4,900*

29	4.0	25	0.8	3.2	16.4	4,300
79	4.0	25	0.8	3.8	17.2	10,300
80	4.0	25	0.8	3.1	17.4	6,300
66	4.0	25	0.8	5.5	17.1	7,000
5	3.8	24	0.8	2.3	17.3	3,400
88	3.8	24	0.8	2.7	17.0	9,800
89	3.8	24	0.8	4.1	17.3	3,600
55	3.8	24	0.8	5.3	17.5	4,900
34	3.8	24	0.8	7.9	18.2	5,800
77	3.8	24	0.8	7.0	18.1	71,700
28	3.7	23	0.8	1.9	15.0	6,300
20	3.7	23	0.8	2.8	15.0	37,000
0	3.7	23	0.8	2.5	16.4	2,700
68	3.7	23	0.8	7.1	17.9	6,600
22	3.5	22	0.8	1.1	11.2	15,300
90	3.5	22	0.8	2.6	17.0	9,400
33	3.5	22	0.8	3.6	17.4	6,300
87	3.5	22	0.8	3.9	17.3	4,400
31	3.5	22	0.8	4.0	16.4	20,900
32	3.5	22	0.8	8.8	18.6	156,500
101	3.5	22	0.8	9.1	18.7	900
27	3.4	21	0.7	2.9	15.6	4,900
76	3.4	21	0.7	4.3	16.3	8,500
36	3.4	21	0.7	4.0	17.1	5,400
100	3.4	21	0.7	9.8	18.8	2,500
54	3.2	20	0.7	1.5	14.3	2,500
98	3.2	20	0.7	7.0	17.9	12,600
42	3.2	20	0.7	9.0	19.3	5,000
75	2.9	18	0.7	6.3	17.6	5,900

Figure 22.1. Crater density map

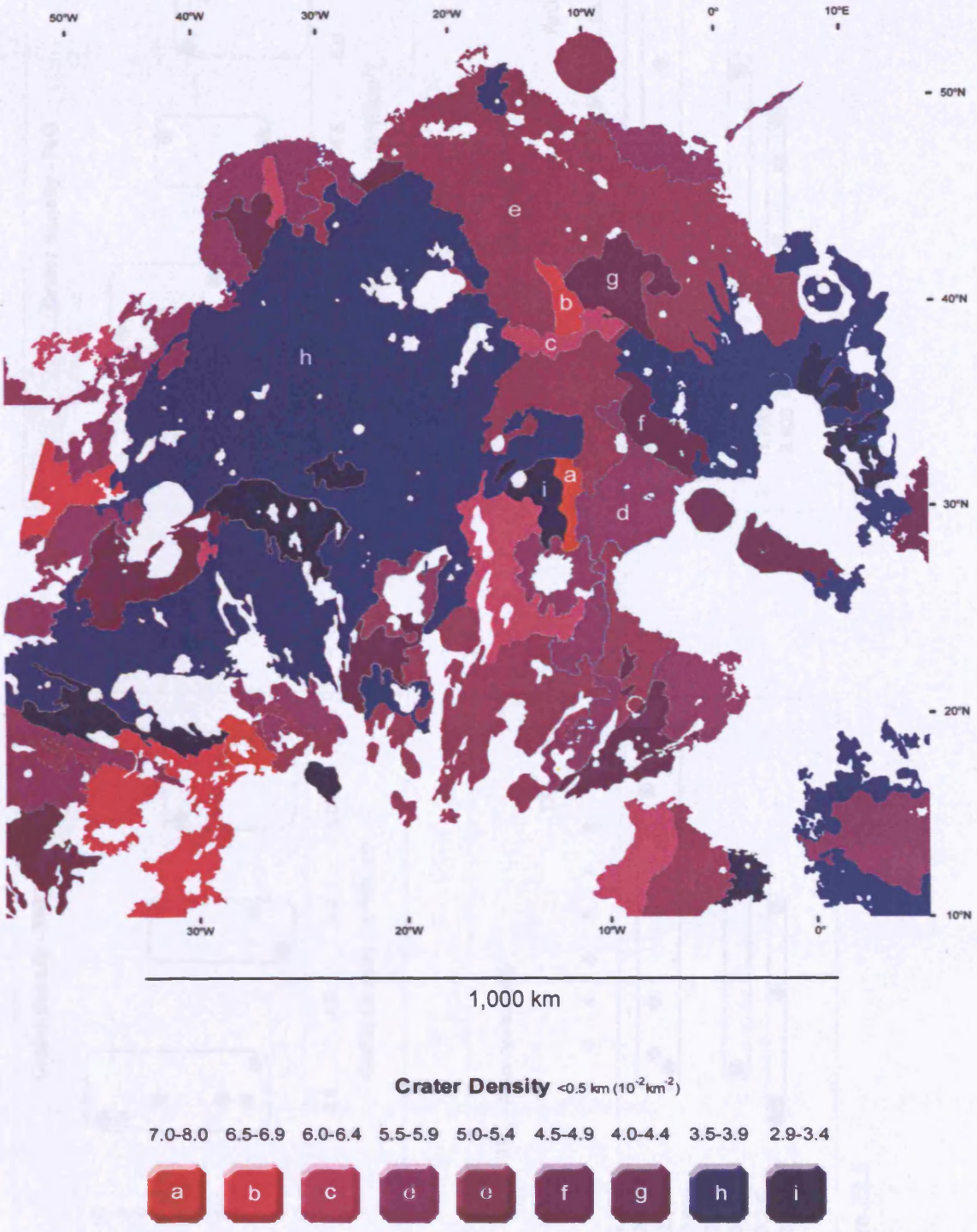

Figure 22.3

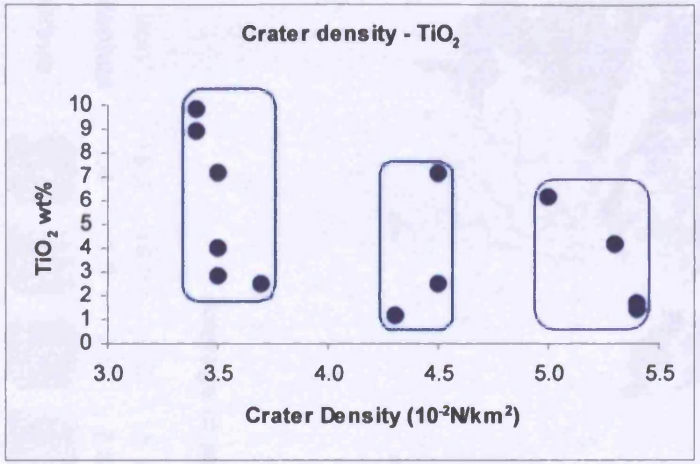

Figure 22.4

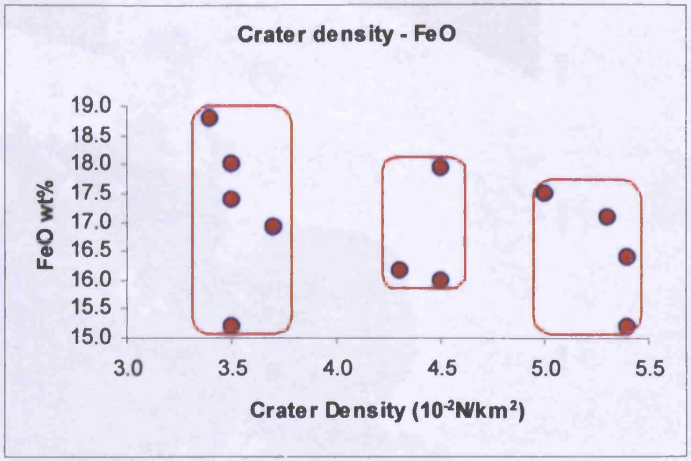

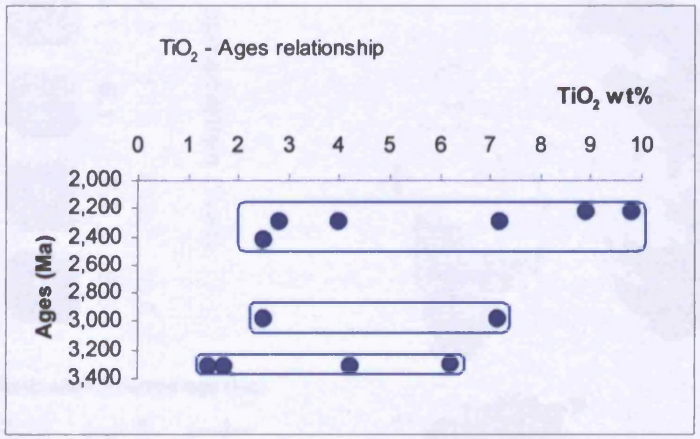

Figure 22.5

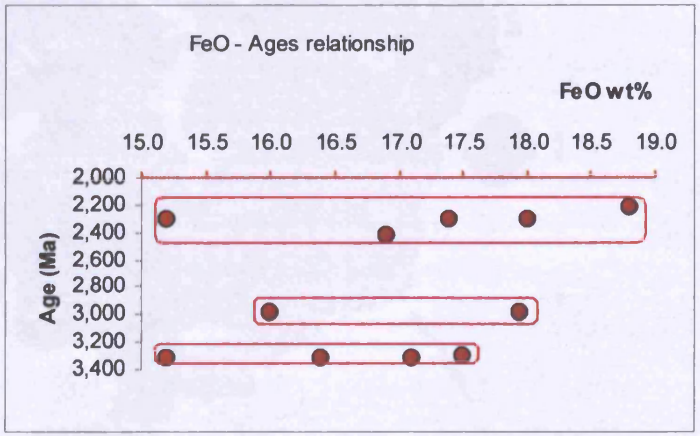

Figure 22.6

Figure 22.7. Combined chemical/ages map

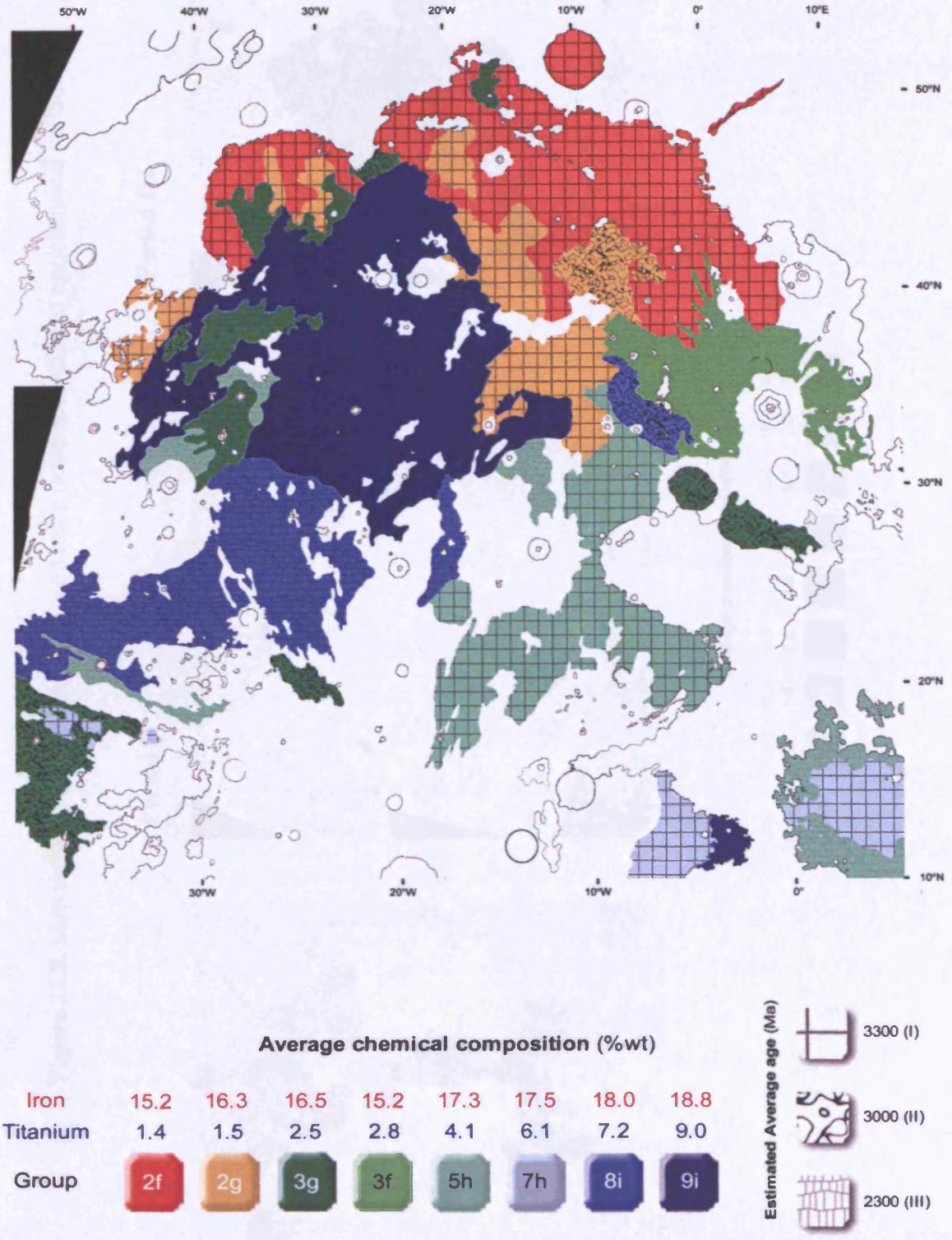

Figure 22.8. Map showing distribution of mapped mare flows according to age/chemical variations

Period I

Period II

Period III

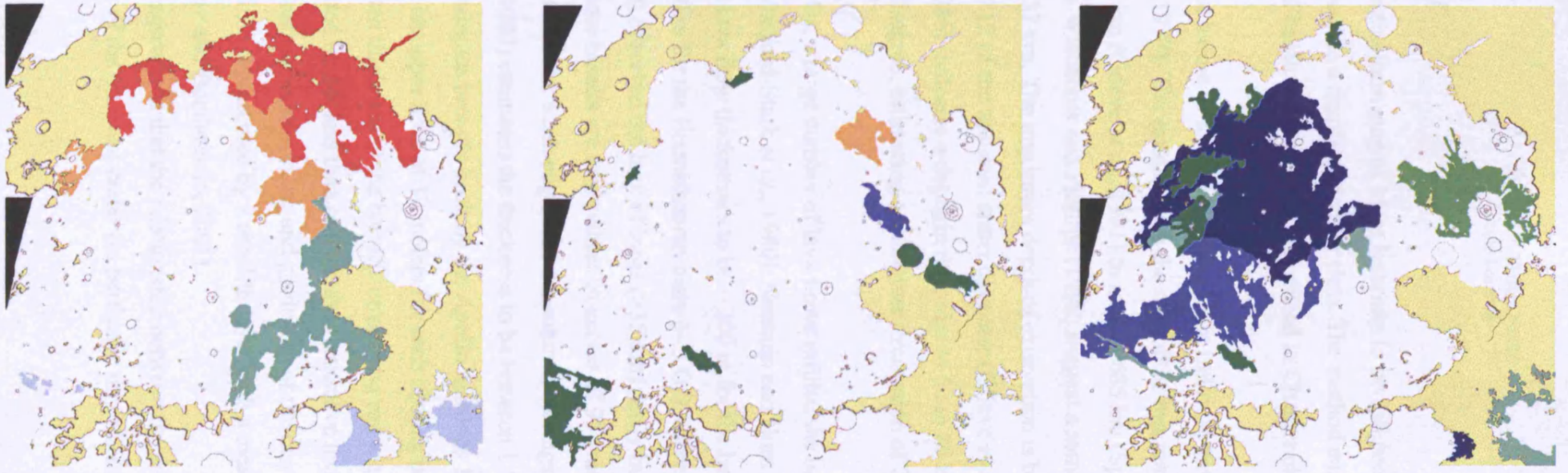

Average chemical composition (%wt)

Iron	15.2	16.3	16.5	15.2	17.3	17.5	18.0	18.8
Titanium	1.4	1.5	2.5	2.8	4.1	6.1	7.2	9.0
Group	2f	2g	3g	3f	5h	7h	8i	9i

CHAPTER 23 BASALT THICKNESS
MARE IMBRIUM

23.1 Background

I used the Clementine iron map of Mare Imbrium to investigate the nature of dark ejecta blankets outside a number of crater rims. The method employed to obtain estimates of local basalt thickness was introduced in Chapter eleven of this work.

Scientists propose a time of formation of the Mare Imbrium basin at around 3.9 Ga (e.g. Turner, 1977). The estimates on the size of the transient crater vary from around 667 ± 87 km (Grieve *et al.*, 1981) to around 685 km (Spudis, 1986). Recent studies from Wieczorek and Phillips (1999) suggest a somewhat larger diameter of 744 ± 37 km. The maximum depth of excavation is believed to lie between 0.09 and 0.12 of the transient crater diameter (Grieve *et al.*, 1981). Accordingly, Spudis (1986) indicates a depth in the order of 62 to 85 km. Wieczorek and Phillips (1999) disagree, estimating a shallower excavation of 29.6 ± 3.4 km.

For the next 1.5 Ga, a large number of lava flows infilled the basin with basaltic materials (e.g. Whitford-Stark *et al.*, 1980). Neukum and Horn (1976) estimated the average total lava flow thicknesses to be ~ 200 m for the Imbrian mare (at ~3.6 Ga) and ~60 m for the Eratosthenian mare (~ 3 Ga). More recently, Whitford-Stark (1980) observed the lack of large (>35 km) partly buried craters as an indication that mare basalts are everywhere in excess of 950 meters minimum thickness, except near the basin edges and the submerged rings. In a different study, De Hon (1980) estimated the thickness to be between 1.5 and 2.5 km. By analysing lunar samples brought back by the Apollo missions 11, 12, and 15, Brett (1975) proposed an upper limit of 10 meters for each cooling unit. Consequently, given the estimated thickness of the basaltic cover, one can argue that the present mare was generated by not less than one hundred extensive lava flows.
Because of the continuous reworking and gardening of the maria, the surface of the Imbrium basin is represented by a regolith layer with a mean thickness of 5.9 meters (Shkuratov and Bondarenko, 2001).
There is general agreement that the relationship between the depth of excavation and the diameter of the transient crater (in particular for craters ≤14 km on the

Moon, Pike 1974) is approximately 1/10 (e.g. Melosh, 1989). If we take the average and minimum maria thickness in the basin to be in excess of one km, we should only expect excavations of ≥ 10 km in diameter to have penetrated down to the crustal base.

Other factors, such as the proximity of the impact to areas contaminated by ejecta from younger craters and highland materials, in addition to the degree of gardening of the ejecta apron itself, dictate the probability of discerning contrasting compositional signature outside the crater rim [against the surrounding mare].

23.2 Results

A number of large impacts are known to have penetrated the mare basalt fill. Whitford-Startk (1980) lists Autolycus, Archimedes, Lambert, and Timocharis as possible sub-surface probes in view of their ejecta enriched in KREEP highland basalts material. On an even larger scale, both Plato and Iridum display anomalously red rims, again, interpreted as material of a different composition excavated from depth (Head *et al.,* 1993).

As predicted, by looking at the iron map (Fig. 18.2), only a few craters actually feature dark material (i.e.. low(er)-Fe material, typical of the potential underlying highland minerals) surrounding their rims; furthermore, they all appear to be located outside the original Imbrian transient crater circumference (one of the proposed inner rings, 670 km in diameter, Fig. 17.2).

Table 23.1 lists the eight crater ejecta blankets that I sampled within the Imbrian basin and one (10) within Sinus Aestuum, and Figure 23.1 shows their geographical location.

Table 23.1. List of craters used to determine minimum depth of penetration

Sample Point	Name of crater	Crater Diameter (km)	Minimum depth of penetration (m)
1	-	2	75
2	-	3	70
3	-	1	65
4	-	2	115
6	Bessarion	10	900
7	Euler	27	970
8	Pytheas	20	960
9	Timocharis	33	1,000
10	-	7	170

Craters 1, 2, and 3 are located on the farthermost northern reaches of Mare Imbrium, very close to the mare/highland contact. The estimated mare cover in this region is 70 ± 5 meters, a relatively thin stratum in good agreement with estimates obtained from other various modelling techniques (e.g. Kiefer, 1977) that are assuming the basaltic thickness decreases linearly with distance from the centre of the basin.

Crater 4, a two km depression south of Cassini, shows much darker ejecta outside its rim. My measurements suggest a minimum of ~115 km mare depth.

The asymmetric ejecta of Bessarion (6), Euler (7), and Pytheas suggest a mare of ~930 ± 30 meters depth not far from the southern margins of the basin, outside Montes Carpatus. These findings agree in broad terms with the estimated values by De Hon (1980), whom recognised a potential 'bench' of basaltic material some 500 meters thicker than the neighbouring isopach, located between the inner (670 km) and outer ring (1160 km, Fig. 17.2).

Timocharis' material, both outside and inside its rim borders, shows a similar composition to that of the nearby Montes Archimedes. We would have expected an impact of this size to penetrate the mare, and indeed my formula suggests a mare depth of around one kilometre at this location.

23.3 Conclusions

Nine sample points scattered across the largest mare basin on the Moon are far too few to construct a reliable isopach map of the region. Nevertheless, we can use larger craters that have not penetrated the maria towards the centre of the basin to estimate a minimum basaltic cover in these areas. Helicon (40.4 N 23.1 W, 24 km) and Le Verrier (40.3 N 20.6 E, 20 km), conveniently located near the proposed centre of Mare Imbrium, do not appear to have excavated material from the underlying basin crust. Therefore, for the purpose of this crude estimate of mare thickness, we can assume a basaltic thickness towards the centre of the basin in excess of 2.5 km.

Figure 23.2 is a simple representation of the modelled mare thicknesses within Mare Imbrium.

Figure 23.2

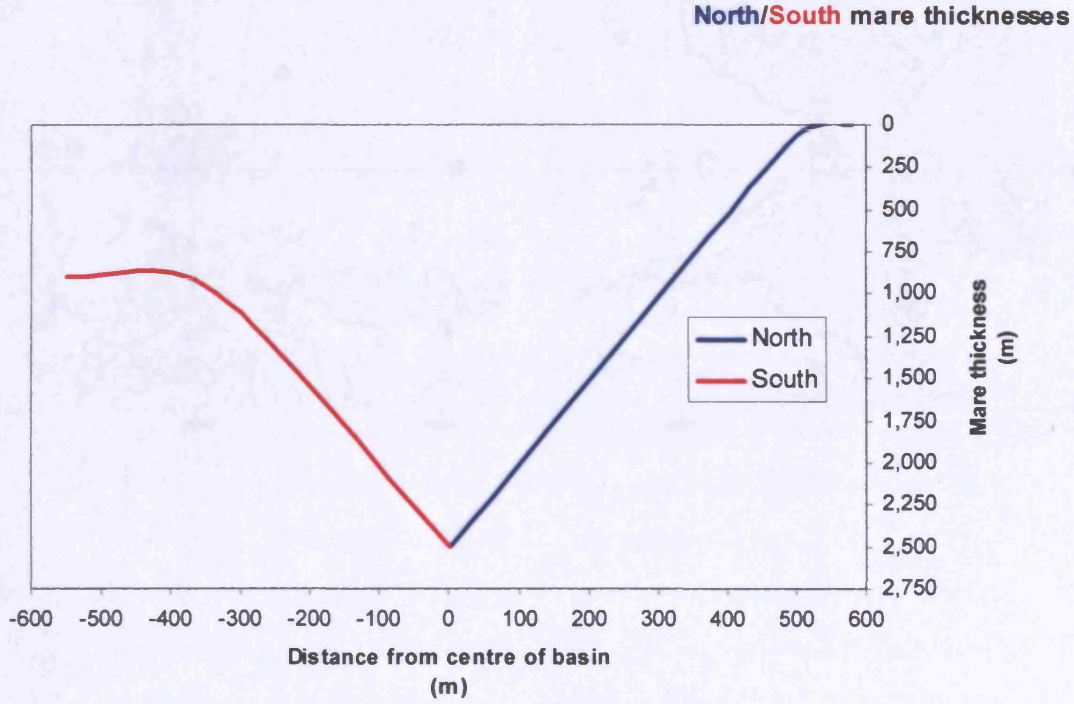

Figure 23.1. Mare penetration sample points

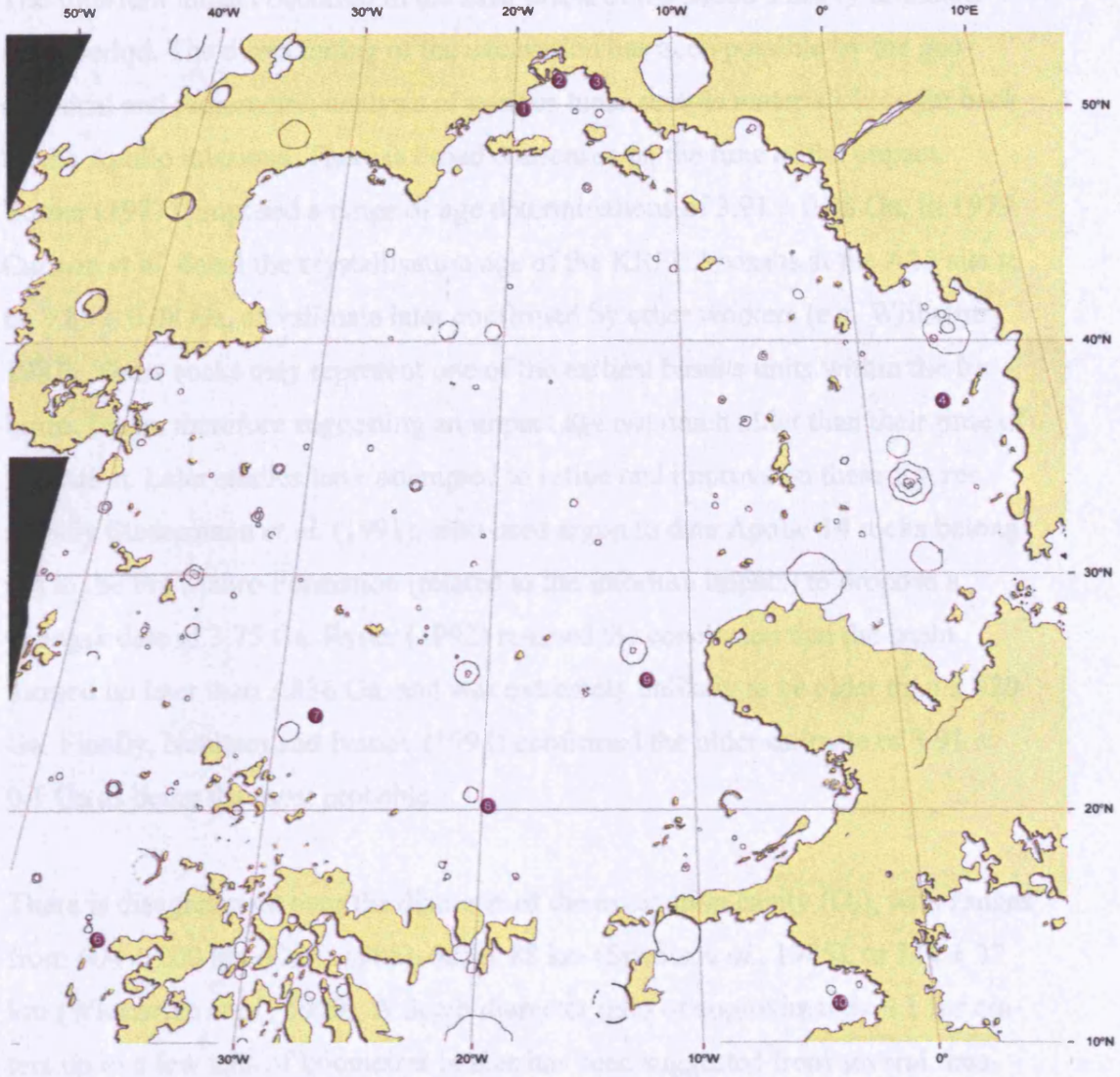

24.1 Basin formation

The Imbrium impact occurred in the final phase of the Moon's heavy bombardment period. The direct dating of the excavation has been possible by the geochemical and radiometric analysis of various lunar sample materials brought back by the Apollo missions. There is broad consensus on the time of the impact. Turner (1977) proposed a range of age determinations of 3.91 ± 0.08 Ga. In 1979 Carlson *et al.* dated the crystallisation age of the KREEP basalts at the A15 site to be 3.85 ± 0.08 Ga, an estimate later confirmed by other workers (e.g. Wilhelms, 1987). These rocks may represent one of the earliest basalts units within the Imbrium Basin, therefore suggesting an impact age not much older than their time of formation. Later studies have attempted to refine and improve on these figures, notably Stadermann *et al.* (1991), who used argon to date Apollo 14 rocks belonging to the Fra Mauro Formation (related to the Imbrium impact) to propose a younger date of 3.75 Ga. Ryder (1992) reached the conclusion that the basin formed no later than 3.836 Ga, and was extremely unlikely to be older than 3.870 Ga. Finally, Neukum and Ivanov (1994) confirmed the older estimate of 3.91 ± 0.1 Ga as being the most probable.

There is disagreement over the diameter of the excavation cavity (D_e), with ranges from 604 ± 200 km (Croft 1985), 685 ± 88 km (Spudis *et al.*, 1985), to 744 ± 37 km (Wieczorec *et al.*, 1999). A depth/diameter ratio of approximately 0.1 for craters up to a few tens of kilometres in size has been suggested from several theoretical and empirical models, computer simulations, and explosion cratering experiments (e.g. Croft, 1980, Melosh, 1989, O'Keefe and Ahrens, 1993). Some workers (e.g. Grieve, 1981, Spudis, 1993) have assumed that proportional scaling of the excavation cavity is also applicable to the largest impact basins. This estimates for D_e would give us a maximum depth of excavation (d_e) for the Imbrium basin on the order of 55 to 82 km.

Other researchers, notably Schultz (1988), proposed a non-proportional scaling theory which indicated that above a critical excavation cavity diameter the

depth/diameter ratio should decrease with increasing crater size. Based on present day measurements, Wieczorek and Phillips (1999) indeed proposed a d_e of only ~30 km, but they consequently conceded that it is likely that the proportional scaling law would have still applied to the Imbrium basin at the time of impact. Soon after, post impact modification effects (i.e. higher temperatures of the target region effecting the viscous relaxation of the basin structure, e.g. Haskin, 1998) would have considerably altered the apparent depth of excavation.

The Imbrium impact generated the second largest multiring system basin on the Moon (second to the South Pole Aitken Basin) and the second youngest (predating the Orientale Basin). There has been some controversy on the location and geometry of the expected ring structures. My interpretation of the Apennine ring as the main topographic rim (1160 km diameter) is in agreement with other workers (see chapter 17), but I failed to locate the two internal rings (550 and 790 km) as described by Spudis (1993). Nevertheless, 'my' inner ring of 670 km, encompassing various isolated massifs such as Montes Teneriffe and Mons La Hire, represents the average middle point circumference of the these rings (Fig. 17.2 and 23.2). There is a possibility that we are both observing related geomorphological expressions.

The energy and ejecta material produced by the cataclysm affected nearly the whole surface of the Moon. Based on the varying estimates on the transient crater dimensions, estimates on the volume of ejecta are in the region of 1.1 to 3.2×10^7 km^3 (Haskin 1998), enough to cover the entire lunar surface with a layer of material 280 to 850 m thick.
Specific nomenclature has been created for the different types of Imbrium deposits based on distinctive morphological characteristics and geographical distribution. The Imbrium Group (Spudis, 1986) includes Apenninus material, the Alpes Formation, Fra Mauro Formation, and the Cayley Formation (see Spudis, 1986 for a full description and map).

Another consequence of the excavation process was an uplifting of the crust-mantle boundary (Moho) and thinning of the crust beneath the multiring basin (e.g. Wise and Yates, 1970, Bratt *et al.*, 1985). Neumann *et al.* (1996) found the

Imbrium basin elevation to be –2740 meters (relative to the reference spheroid) and the present thickness of the crust, corrected for mare fill, 36.3 km (against a nearside average of ~50 km).

The Imbrium basin has been described as a lunar mascon basin due to its positive gravity profile (e.g. Muller & Sjogren 1968). The excess mass could be explained by taking into account the mare load infill (e.g. Conel & Holstrom, 1968) or could be due to a super-isostatic relief at the Moho (e.g. Phillips *et al.*, 1972; Neumann *et al.*, 1996). Kiefer 1997 found that the basalt thickness required by the uncompensated basin fill could be accommodated by present estimates of mare material (e.g. Spudis and Adkins, 1996; Williams and Zuber, 1996). Indeed, Wieczorek and Phillips (1999) found that the Imbrium basin was close to achieving isostasy before being infilled with mare basalt. The relatively rapid return of the crust towards a state of isostatic equilibrium could be explained by a 'hotter' than average target due to its high thorium and KREEP material content (Evenson *et al.*, 1974; Metzger *et al.*, 1974; Tera *et al.*, 1974). The higher degree of viscous relaxation would also explain the apparent shallow excavation depth of Mare Imbrium (Wieczorek and Phillips, 1999)

24.2 Lower Imbrian

The Imbrium basin has been the theatre of a complex and prolonged history of igneous activity and mare infill. Very little evidence of the early bombardment regime has survived to this day. Cassini (40.2 N 4.6 E) is perhaps the largest surviving crater. Its 56 km rim is still protruding from the mare (by 2450 m) but the internal crater floor has been extensively flooded by mare material bearing the same chemical signature as the surrounding basalts. Cassini's interior is also the only large crater in the basin to show evidence of a considerable bombardment regime that probably continued sometime after the Imbrian impact. Among many others, two sizable craters (Cassini A, 18 km, and Cassini B, 9 km) inhabit the crater floor. When viewed in the FC image (Fig. 18.4) Cassini is virtually indistinguishable from the neighbouring highland region, except for an eroded and deformed circular blue 'line' that delineates the crater summit.

The ghostly outline of Lambert R (south of Lambert, 25.0 N 21.0 W) is one of the few craters <50 km in diameter from this period that can be still detected over the surface of the mare. Most of the others were either submerged by igneous flows and/or eroded to oblivion.

24.3 Upper Imbrian impacts

The northwesterly part of the Imbrium basin is characterised by the remnants of the 236 km impact that formed Sinus Iridum (Montes Jura). Promontories Heraclides and Laplace are the only surviving southern part of the original crater rim. Wagner *et al.* (2002) estimated that the crater was excavated about 3.7-3.8 Ga ago. The relatively close temporal proximity with the formation of the Imbrium basin may explain the absence of prominent morphologic features within Imbrium and the common history of mare infill. Montes Jura are also characterised by the lowest relative radar reflectivity of any uplands on the nearside of the Moon, probably due to the rocks' different chemical composition from those (Thompson *et al.*, 1978).

The 101 km crater Plato is located in the highlands north of the Imbrium basin (Fig. 24.1). Albeit not strictly belonging to the objects of study in this work, Plato is worth examining for two main reasons: the mare infill of the crater basin appears very similar and related to the maria south of the highland and the presence of spectral anomalies corresponding to the proximal ejecta deposits (Hawke *et al.*, 2003). I will discuss the chemical significance of the 'red' rim in relation to the stratigraphy of the Mare Imbrium, and its potential significance in the satellite-wide study of the Lunar Red Spots in the following chapters. I speculate that Plato's impact 'deformed' the pre-existing topography of the Imbrium basin north of Montes Teneriffe (see figure 16.1) following the formation of its uplifted rim within Mare Imbrium.

Figure 24.1. Crater Plato, Clementine FC image.

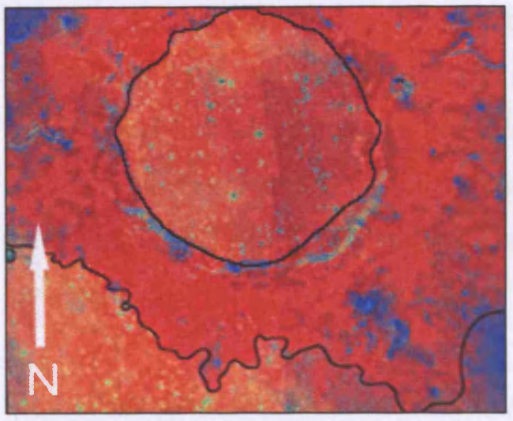

Figure 24.2 shows another large Lower Imbrian Series crater: Archimedes.

Figure 24.2. Crater Archimedes (Orbiter IV and Clementine FC composite)

Archimedes (83 km) is an old terraced crater that displays an unusual compositional asymmetry as regards the lunar red material. More intriguingly, the southern red spot (along with more spectrally neutral ejecta) appears to have 'invaded' the Apennine Bench, an elevated terrain part of Montes Archimedes. It appears that the impact occurred after the emplacement of the plain material but before the onset of the major phase of mare flooding. A more detailed discussion of the stratigraphy of the area will follow in the next chapter.

Figure 24.3 was derived from the False Colour data map (Fig. 18.4). It focuses on the (greatly) exaggerated colour characteristics of the ejecta of the major craters in the Imbrian basin. Both craters Cassini and Archimedes are portrayed with blank crater floors indicating a similar composition to that of the surrounding maria. The present topographic equalisation of these floors with the outside terrain may reflect a regime of basaltic flows breaching through the rim boundaries resulting in the flooding of the crater interior.

24.4 Copernican and Eratosthenian Systems

1.1 Ga is the commonly accepted Eratosthenian-Copernican boundary date (Wilhelms, 1987). More recently, Ryder (1992) among others workers, has proposed an alternative starting time for the Copernican System at 2.1 Ga, based on the study of crater Autolycus. This conclusion has been disputed by Hawke *et al.* (2004) who offered an alternative estimated rate of ray optical maturity degradation that would push forward the proposed onset of the Copernican Period once again into the region of one billion years ago.
Until this aspect of lunar convention is generally agreed, I will base my classification of crater impacts on the geological map of Wilhelms and McCauley (1971) who used Autolycus as the oldest Copernican crater in the region.

24.5 Eratosthenian impacts

Crater Eratosthenes (58 km, 14.5 N 11.3 W) is fundamental in helping to understand the geological history of the Moon by virtue of its location and morphological setting. It sits on clearly Imbrian terrain (across Montes Apenninus) and it appears to be younger than other comparable craters in the area (e.g. Archimedes), but it was geologically and structurally affected by the nearby Copernicus impact.

Figure 24.4. Clementine FC, Orbiter IV, and Apollo 15 mosaic image.

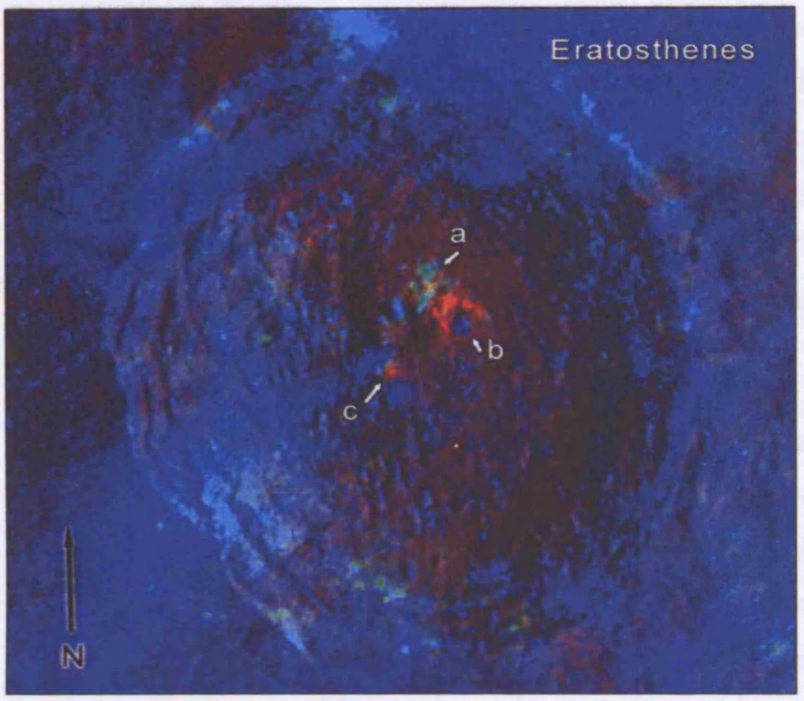

The range of colours in the FC image (Fig. 24.4) reflects the spectral variations characteristic of distinctive lithologies. Spectrally, we can see that materials originating from the Copernicus impact in the west (appearing blue, i.e. fresher) have reached and invaded the eastern flank of the excavation. The energy of the surging materials might have caused removal of weathered cover from the crater flank, exposing more crystalline rocks (light-blue, greenish flank benches). The same ray ejecta might have 'jumped' the low terrain and carried on its journey on the other side of the rim. As evidence, we notice the 'scorched' upper rim perimeter in the northeast. In the titanium map (Fig. 18.3), only the eastern half of the excavation shows a distinctive composition (lower Ti content) from the surrounding mare (corresponding to the hummocky crater floor). The relatively unaffected mixed red/blue materials of the crater floor are typical of soils of intermediate maturity (reflected by the age of impact). There is evidence that the central peak might contain materials excavated from the deep base of the mare (e.g. Pieters *et al.*, 1994).'b' can be interpreted as a relatively fresh impact crater which excavated the red material visible in the northwest of the impact, probably an example of the glass-bearing impact melt filling most of the Eratosthenian cavity. 'c' points to an intense 'blue' patch of terrain encircling a 'red spot'. The spectral resolution of the Clementine image is too coarse to ascertain the crater's precise

nature, but I speculate that the spot might represent the remnants of a relatively pristine impact melt, being sheltered from contamination by the two positive relief formations to the west. These appear to have taken the brunt of the incoming Copernicus ejecta, hence their very shallow near-IR continuum slope. Materials located within the central peaks of large lunar craters that display strong absorption near 1 μm are recognised as olivine bearing rocks. Formation 'a' is an example of such lithology and it may indicate that the crust in this region is not homogeneous with depth (Pieters and Wilhelms, 1985).

Several other large craters are attributed to this period of formation. Lambert (30 km, 25.8 N 21.0 W) stands out from the surrounding mare by virtue of its high iron content (Fig. 18.2). Figure 22.7 shows Eratosthenian basaltic flows nearly encircling the crater edifice. Did the igneous material flow around the crater's topographic high or did the impact occur after the mare emplacement? There is evidence that Lambert modified the general morphology of the region and in particular, it 'interrupted' the otherwise continuous ridges in the area (Dorsi Zirkel and Hicazy). On the other hand, it appears that fresh basaltic material has locally embayed the 'red' traces of the crater's ejecta. I conclude that the impact occurred sometime before the latest emplacement of maria material.

The otherwise inconspicuous craters Delisle (25 km, 29.9 N 34.6 W) and Diophantus (17 km, 27.6 N 34.3 W) are brought into the foreground in the FC image by the fresh ejecta of a small impact that occurred in the last few million of years nearby. In particular, Diophantus' excavation appears bright green and very fresh in comparison to most other craters. The next section will further discuss the geologic interpretation of this region.

Other craters from this period include Heis (14 km, 32.4 N 31.9 W) and C. Herschel (13 km, 34.5 W 31.2 N).

Helicon (24 km, 40.4 N 23.1 W) has been classified by Wilhelms and McCauley (1971) as belonging to the Undivided Crater Material. By looking at the Clementine images I would be inclined to include this crater in the Eratosthenian System, judging by the partial preservation of its ejecta mantle, 'freshness' of the rim top material, and comparable morphology to some Eratosthenian impacts.

Nevertheless, it is apparent that the impact preceded the later flooding phase in the region, consequently suggesting a time of formation in the Early Eratosthenian System.

It would be tempting to interpret the red patch of terrain around Le Verrier (20 km, 40.3 N 20.6 W) as ejecta material. By looking at the FC it becomes clear that the crater edifice represents a topographic high that was unaffected by the latest mare flows. Indeed the elevated rim appears of a different hue of red than the surrounding terrain. I speculate that the area close to Le Verrier belongs to the older basaltic units found in the east of the basin and, unlike Helicon in the west, it was not completely cut off by the Eratosthenian flows.

24.6 Copernican impacts

Aristillus (55 km, 33.9 N 1.2 E) has been the centre of extensive research (e.g. Smrekar and Pieters, 1985; Spudis *et al., 1986;* Le Mouleic *et al.,* 1999; Blewett and Hawke, 2001; Grier and McEwen, 2001; Grier *et al.*, 2001b) because of its apparent young age and the characteristic spectral signatures of its rays, terraced walls, and prominent central peak complex (Fig. 24.5). Clementine images (Figs. 18.1 to 18.4) show a system of rays on a scale comparable to the larger Copernicus in the South. Also similar is the extent of the ejecta blanket extending 4-5 radii from the centre of the craters. The crater count for the mare in the neighbourhood of Aristillus suggests an age of impact ~2.4 Ga. I believe that this age estimate to be exaggerated due to the expected large statistical contribution from secondary impacts. Indeed, Aristillus' spectrographic signature points to a similar age as to that of Copernicus (~1 Ga). Wilhelms (1987) proposed an absolute age for Aristillus of 1.3 Ga, a figure later confirmed by Ryder (1992), and in broad agreement with my revised estimate.

Figure 24.5. Orbiter IV, Consolidated Atlas, and Clementine FC mosaic.

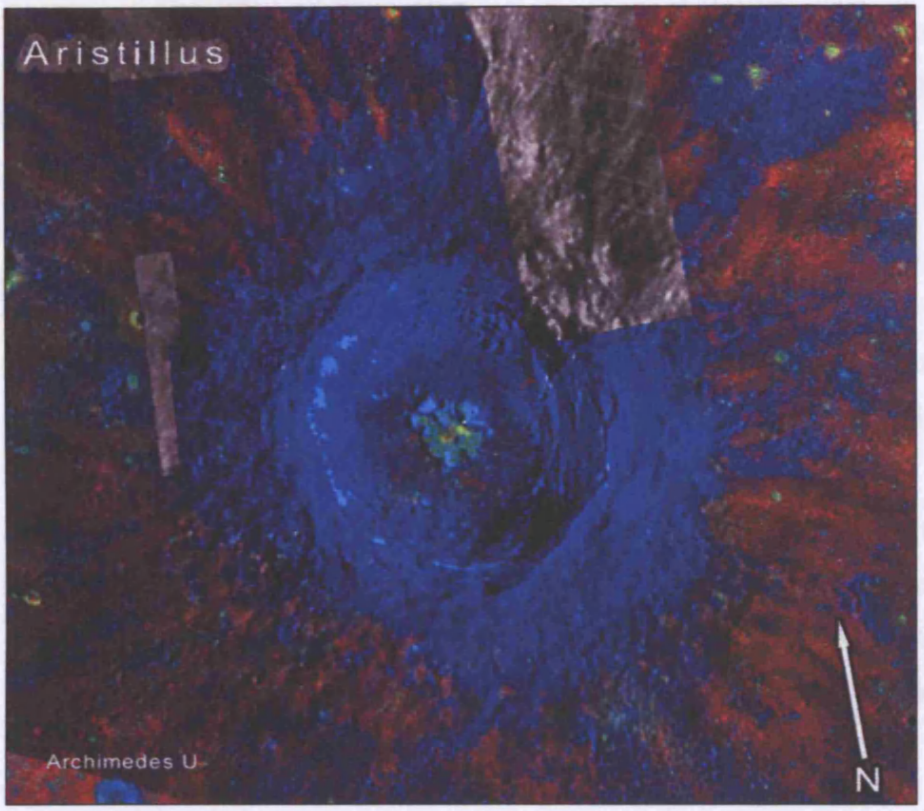

The geological spectral signature of the impact bears strong a resemblance to that of Eratosthenes. This similarity might only be superficial: the hi-Ti material covering most of the crater's walls and rim reflects the actual composition of the ejecta (unlike those of Eratosthenes which hailed from Copernicus). The rays are still clearly visible against the surrounding mare because of their contrasting composition and maturity (albeit Lucey *et al.,* 2000b found the rays to have reached an optical maturity similar to that of the substrate). We also expect that the ejecta rays will eventually 'fade away' through regolith churning due to weathering, and the materials outside the crater will mature (i.e. redden) and mimic the optical maturity of the local maria. The steep, terraced, inner walls will probably retain longer the 'blueness of youth' thanks to continuous exposure of crystalline substrata through gravitational slumping.

Aristillus' central peak stands out from the crater floor because of its shallower near-IR continuum slope of its constituent minerals. Figure 24.5 shows a rough north-south compositional divide, with a bluer northern portion and greener southern. A more detailed study of the crater by Le Mouélic *et al.* (1999) con-

cluded that the 'blue' rocks are dominated by high-Ca pyroxene, while the 'green' ones contain a higher fraction of orthopyroxene. Thus, the bulk composition of the central peak is dominated by norite or anorthositic norite (Blewett and Hawke, 2001).

Aristillus's ejecta have covered the somewhat older Autolycus (34 km) crater in the south and degraded its optical appearance (Hackman, 1966; Hawke *et al.*, 2004). Ryder (1992) estimated the time of impact 2.1 Ga ago. Palus Putredinis probably represents what is left of the Imbrian mare predating the two impacts.

Another prominent Copernican crater can be found 26.7 N 13.1 W in the southern Mare Imbrium: Timocharis (33 km). Its 'blue' ejecta have locally obliterated the 'red' material that can still be detected within the southern outer ring of the Imbrium basin (where it has not been either reworked or covered by the products of Copernicus' impact).

Pytheas (20 km, 20.5 N 20.6 W) is another pre-Copernican impact crater. When viewed through the Clementine composites and true colour images, it appears to possess a highly asymmetrical distribution of the hummocky ejecta deposits just outside its rim (of a delta-like shape, pointing south). Photographic evidence reveals nothing atypical in its rim morphology. Its noticeably peculiar shape results from ray material from Copernicus being intercepted and deviated by the elevated rim of Pytheas (the 'bare' northern side being shielded from the blast effects).

Crater Euler (27 km, 23.3 N 29.2 W) seems to challenge the explanation offered for the peculiar appearance of Pytheas. This time the compositional asymmetry is geographically reversed. I speculate that the impactor that formed Euler landed on a border area between two distinct basaltic flows of contrasting ages and compositions. The 'blue' ejecta in the northern portion belong to an underlying Eratosthenian unit and the 'red' southern to an Imbrian flow. Alternatively, Euler may actually predate one of the last Erothestinian basaltic flows travelling towards the centre of the basin, which flooded and surrounded the crater edifice. Higher-resolution multispectral images could help identify the most probable stratigraphy of the area.

Figure 24.3 shows many more craters of which ejecta material is still detectable through spectrographic analysis. Their colour reflects the age of impact, the depth of penetration, and the nature of the excavated material. Larger craters on the outskirts of the basin have probably reached down to the basement of the mare. Aristillus' ejecta show for instance intermediate titanium content between that of the basalts typical of the upper eastern side of the basin and the higher-Ti type of the west. The complex chemical signature of the ejecta may be the result of the admixing between the relatively high titanium surface basalts and crustal material from beneath the mare.

Soil maturity is the major factor affecting the albedo differences between crater interiors (e.g. Timocharis and Lambert). Nevertheless, Lambert's floor, when viewed on the iron map, appears as the brightest in the basin (i.e. highest Fe content). Only the central peak suggests the presence of low-Fe material. In this case, the impact must have barely reached the basin's crustal floor. Indeed, Lambert's crater walls display a composition that is very similar to that of the uncontaminated maria found further north (with relatively high-Ti). Figure 24.3 depicts these craters' interiors and ejecta as 'blue' because they are both relatively young (i.e. these is a higher crystalline component in the regolith). Interestingly, crater Delisle, of comparable age and size to Lambert, also shows similarities with the composition of the maria that it excavated, in this case low-Fe basalts. Judging by the apparent maturity of the crater's ejecta, it would appear that Delisle preceded the Lambert impact by some time.

The two craters Helicon and Le Verrier have virtually no material around their edifices that could be described as spectrally 'fresh' or of a high crystalline content. Therefore, they might represent the largest full impact structures to survive from the time of the major basin infill phase (except of course for the rim remnants of Cassini and Archimedes at the margin of the Mare Imbrium).

24.7 Smaller and fresher craters

Figure 24.3 shows differences in craters' and associated ejecta colours produced by greatly enhancing their subtle optical variations (FC images, Chapter 4). The green/yellow hues in the false colour images reflect both concentration of iron-bearing minerals (thus providing information concerning the relative abundance of pyroxene and olivine) and soil maturity (Chapters 4 and 18). In order to emphasize the near-IR continuum slope (near 1 μm) I further altered and photographically manipulated the 'green filter' maps of the Imbrium basin (Figs. 18.7 and 18.8) to produce Figure 24.6, focusing on the distribution of fresher iron-bearing mafic minerals. The resulting map offers an alternative view of the maria in the basin. A number of small craters are now the most prominent features of the region and the distribution of their ejecta in some case greatly overemphasise the often modest size of the impact. The most obvious example is represented by a small crater west of Cassini (~ 0 W 40 N). Its apparent crater diameter is around 5 km with a barely detectable ejecta mantle outside its rim (i.e. slightly higher albedo than the surrounding mare). When viewed on the optical maturity parameter image we see a prominent 30 km ring of 'green' material encircling the crater. On closer inspection, it is possible to detect evidence of this material as far as 80 km away from the impact site.

A small 1.5 km crater less than 20 km south from the impact shows a comparable ejecta pattern, with a main ejecta ring 10 km in diameter (both six times larger than the size of the excavation). We can speculate that these two craters may be contemporaneous and representing a double impact from coupled interplanetary bodies. There is a possibility that the major impactor might have excavated sub-mare material, given its geographical proximity to the terra (and consequent thin mare layer). Nevertheless, its small companion almost certainly did not, and the similarity of composition of their ejecta points to soil maturity as the main parameter dictating their spectroscopic characteristics.

Craters Delisle (25 km) and Diophantus (17 km) dominate the topography south of Montes Delisle (Fig. 24.7). When the same area is viewed on the 1 μm map, the

ejecta from a little crater less than 2 km in diameter 16 km north of Diophantus appear as the most prominent geochemical feature.

Figure 24.7. Craters Delisle and Diophantus region

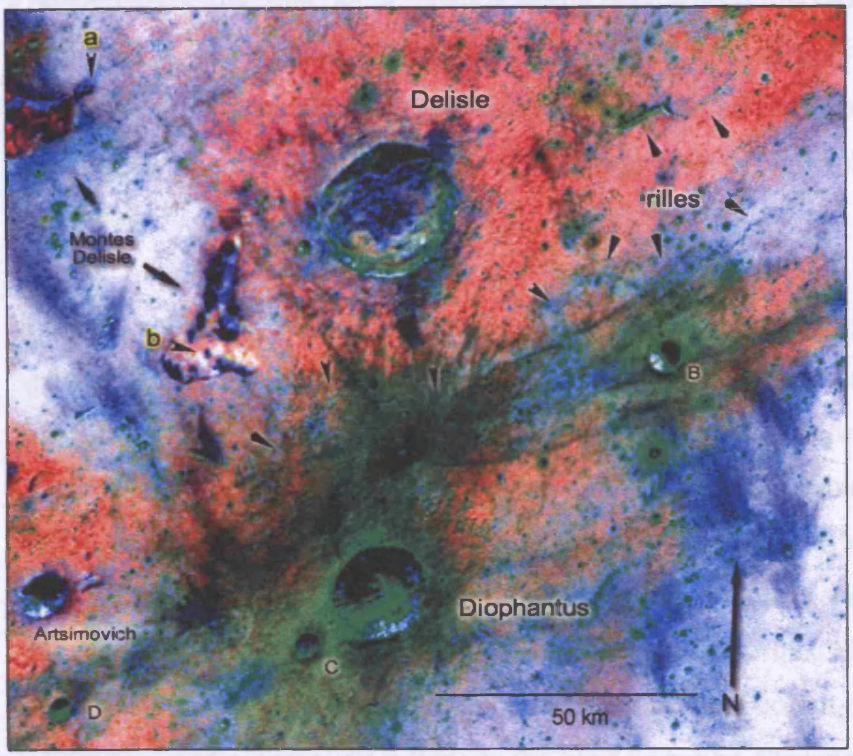

The crater's ejecta are distributed in an inclined axis, channelled along the lower topography between the two major impacts. Ejecta rays can still be detected some 70 km northeast from the crater. If we assume a comparable age for Delisle and Diophantus (e.g. Wilhelms and McCauley, 1971), we need to explain the asymmetrical geometric distribution of the impact materials. The closer proximity to the southern crater would have triggered a higher degree of gravitational slumping of material across Diophantus' steeper terraced walls, thus exposing fresher (more crystalline) material in the process. Geological features such as the rille running along the southern border of Delisle would have contained some of the low-energy surface surges spreading north and southwesterly from the new impact. Other intriguing features are the trail of dark material stretching diagonally between the major craters, the straight ray squeezed between the northern tip of Montes Delisle (b) and Delisle, and the 'bent fork' shaped rays (four major arms) stretching towards Delisle B. There is little doubt that local morphology affected

the geometry of the rays. For instance, the northernmost arm of the Delisle 'fork' appears to be deviated by the intersection with a deep rille running north-south. My crude interpretation of the ejecta distribution involves the relatively recent multiple impact of a celestial body that broke up just before impact. Travelling in a northeasterly direction the first debris would have landed just east of Diophantus D, with the main two sections of the meteor (comet?) impacting several kilometres further north. The interaction of ejecta material scattered at varying low angles could have produced the intricate distribution of fresh materials that we witness today.

Using the soil maturity information provided by the FC image (Figure 24.7) and figure 24.4 we can attempt to reconstruct a model for the impact chronological sequence of the area with Delisle appearing as the oldest of the complex craters in the area characterised by mature ejecta material (red, Figs. 24.3 and 24.7). Nevertheless, the freshly exposed walls and relatively immature crater floor (higher albedo and well-preserved central uplift) places the age of impact within the Early Eratosthenian Period. The rille south of Delisle probably formed after the impact but it is difficult to establish if its sinuous morphology is a consequence of ground deformation and compaction following the blast or can be attributed to larger tectonic forces affecting the wider western Imbrium basin. Diophantus is smaller and it represents a simple impact structure, with steeper crater walls (260 m its highest point) and a rather more modest central peak. It is more difficult to estimate the period of formation because of 'contamination' from the nearby fresh crater. Moreover, there is some evidence that a small impact hit its crater floor contributing to the apparent immaturity of the excavation. A section of the northeasterly flank of the Diophantus ejecta curtain may represent an unaffected and pristine example of material maturity. In this case, the crater would be of comparable age to Delisle.

Given a similar time of formation, the smaller the excavation diameter the less steep is the continuum slope in the multispectral images. Craters smaller than 10 km appear as equalised bright 1 μm sources. Impact structures of this size retain their transient crater depths (Melosh, 1989) including a distinctive circular outline, a bowl-like shape and uplifted rim, and hummocky deposits of ejecta around the

rim (French, 1998). Following the modification stage, fresh material becomes constantly exposed on crater walls due to downslope movement. As the simple impact structures age and fill up with crater debris, the whole edifice stabilises and the slumping of material becomes confined to the edge of the uplifted rim; eventually gravity pull loses against the decreasing slope gradient and the rim material is allowed to age. Therefore, we can expect four types of 'green/yellow' craters in the basin (also see Chapter 12): (1) youngest small craters with extended ray patterns, (2) craters with clearly-defined ejecta apron, (3) craters with 'bright', uniform interiors, and (4) craters with annular brightness. I discussed the most prominent cases of craters with well-defined ray system above. A couple of type (2) examples can be found northwest of Montes Spitzbergen (35.0 N 5.0 W): their extended ray systems have almost disappeared (matured) and they are only visible within the ejecta around the rim. Type (3) is the most common; a good representative of this group is crater Landsteiner (6 km, 31.3 N 14.8 W). Carlini (10 km, 33.7 N 31.2 W) shows a matured ejecta pattern, except for a narrow ring of material around the rim. The crater walls feature exposed crystalline mare material and only the infilled centre of the cavity floor appears mature and similar in optical reflectance to the rim. Type (4) craters are concentrated in the western side of the Mare Imbrium: C. Herschel (13 km, 34.5 N 31.2 W), Heis (14km, 32.4 N 31.9 W), and Gruithuisen (15 km, 32.9 N 39.7 W) are very good examples of Early Eratosthenian impacts with partially exposed, eroded steep walls.

Figure 24.6 highlights the distribution of immature/Fe-poor basalts regolith in Mare Imbrium. Four areas (A to D) appear largely devoid of this material; 'A' and 'D' are within the radius of fallout ejecta of the major Copernican impacts (Copernicus, Aristillus, and Autolycus). Copious mantling by excavated lunar material has concealed most of the pre-existing Eratosthenian impacts.
The paucity of evidence of recent impacts in area 'B' can be understood by taking into account the distribution of the most recent lava flows (Fig. 22.7, Chapter 22), covering a similar geographical region. The last unit flow of fluid basalts would 'reset' the optical maturity clock for the territory it invades. 'B' might therefore represent the extension of the most recent Late Eratosthenian lava flows in the basin.

The explanation for the low fresh-crater count in area 'C' is not as obvious as the other regions. It encompasses flow units of varying crater densities (Fig. 22.1) but similar chemical compositions (Fig. 21.3). One characteristic of area 'C' is its distance from all major recent impacts within the Imbrium region. This would explain a shortage of fresh secondary craters, which are otherwise systematically scattered across the basin.

The upper part of the area encompasses some of the least mafic regolith of the entire basin (and consequently with higher albedo). Titanium poor ejecta from fresh craters would more easily and quickly be masked by a background of low-Ti basalts. This could also partly explain the apparent low statistical count of young impacts in the area.

24.8 Ejecta rays

The Imbrian region is criss-crossed by the optical remnants of numerous ejecta rays. Copernicus is the main source of these optically bright filaments and they can still be observed as far as 35° N (~800 km from the crater). Lunar crater rays are visible because of their contrasting composition with the underlying mare or terra, or/and because of the presence of immature material (Hawke *et al.*, 2004). When Copernicus rays are observed in the DBA image (Fig. 18.1) and Fe maps (Fig. 18.2), they appear prominent and stretching out over large geographical distances. They nevertheless almost disappear when observed in FC and titanium map. My interpretation is that the rays are mostly visible because of the presence of immature mare debris and not because of compositional differences with the surrounding mare. Closer inspection of a number of prominent rays suggests that their appearance may be the result of the presence of bright, immature primary ejecta and fresh interior walls of secondary impact craters. Their 'blending' into the background of distinctive unit flows, when their albedo maturity is not taken into consideration (FC and Ti maps), could be explained by the similar composition of the ejecta material to that of the surrounding soils. We also notice higher titanium content in the rays west of Copernicus reflecting the distinctive east-west compositional dichotomy in the materials of the crater floor and rim.

Aristillus' ray system is still clearly visible, albeit with a relatively more modest geographical distribution than that of Copernicus is, and in a rather less 'filamented' way. There is little doubt that both craters' rays might contain a fraction of highland-rich primary ejecta, contributing to their high albedo characteristic, but evidence suggests that immaturity plays a prominent role in the optical characteristics of the Imbrian rays.

With increasing age, combination rays (rays of both compositional and maturity origin) will become fainter as their surfaces mature (Hawke *et al.*, 2004). Eventually they will evolve into compositional rays. Their optical survival will depend on the proportion of highland material contained in the ejecta debris (and, of course, the absence of fresh lunar flows).

Figure 24.3

Crater ejecta colours in FC sketch map

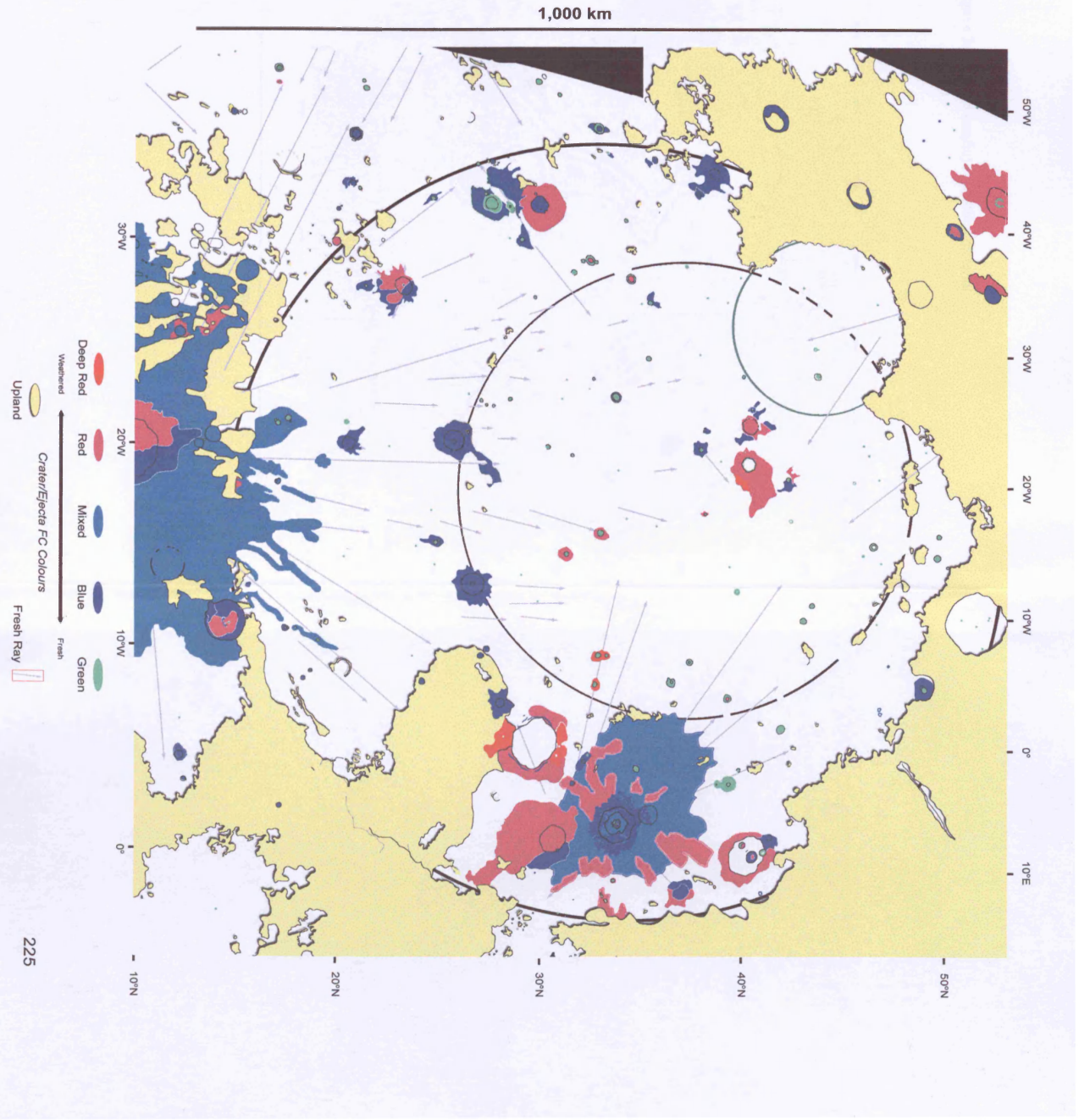

Figure 24.6. Fresh (mafic) crystalline material

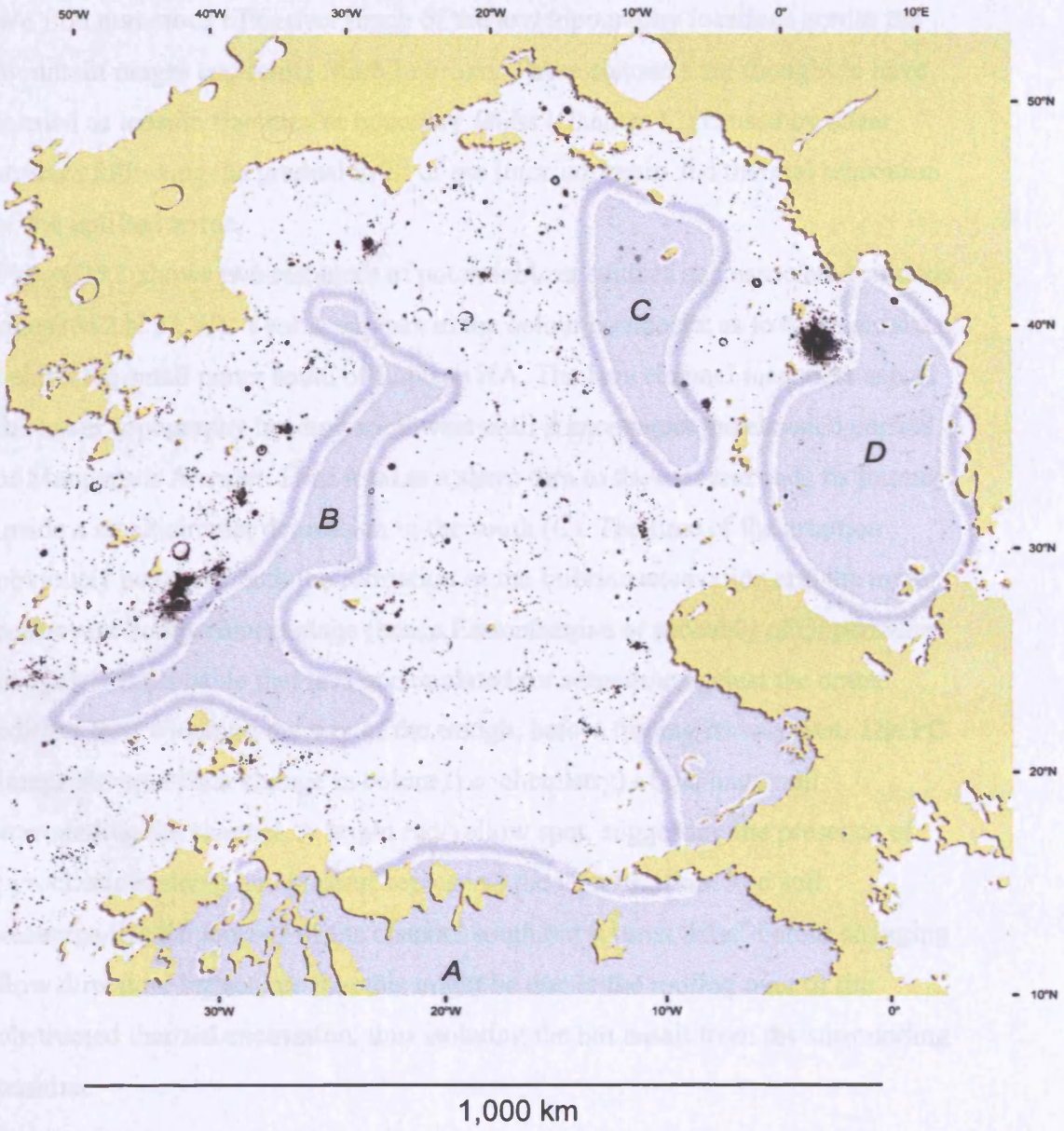

CHAPTER 25 GEOLOGY AND GEOMORPHOLOGY (PART I)

MARE IMBRIUM

25.1 Rilles

We find numerous rilles over much of the low topography locations across the mountain ranges encircling Mare Imbrium. These channels are thought to have formed as tension fractures or boundary faults (Chapter 13) caused by shear stresses following the gradual infill of the Imbrium basin and thermal relaxation of the uplifted terrae.

Figure 25.1 shows two instances of potential lava sources and associated sinuous rilles (~52 N 22 W). Vent A appears in the colour composite as to originate from behind the small crater south of Laplace HA. The lava channel meanders across the lower topography heading southwest until it encounters the elevated edifice of Maupertuis A crater. Here it takes a sharp turn to the east and ends its journey inside a small circular depression in the south (C). The time of the eruption obviously postdates both the formation of the Imbrian excavation and the major post-event bombardment stage (hence Eratosthenian or probably of Copernican in age). It is probable that lava accumulated for sometime against the crater edifice, thus widening the size of the trough, before finding its way east. The FC image shows a clear change in colour (i.e. chemistry) of the lunar soil surrounding the channel. A bright red/yellow spot, suggesting the presence of pyroclastic material and glasses, represents the vent location. Red soil accompanies the journey of the channel south but it turns 'blue' before changing flow direction. I speculate that this might be due to the roofing over of the obstructed thermal excavation, thus isolating the hot basalt from the surrounding terrains.

Figure 25.1. Mosaic of Iron map, Orbiter IV, and FC image.

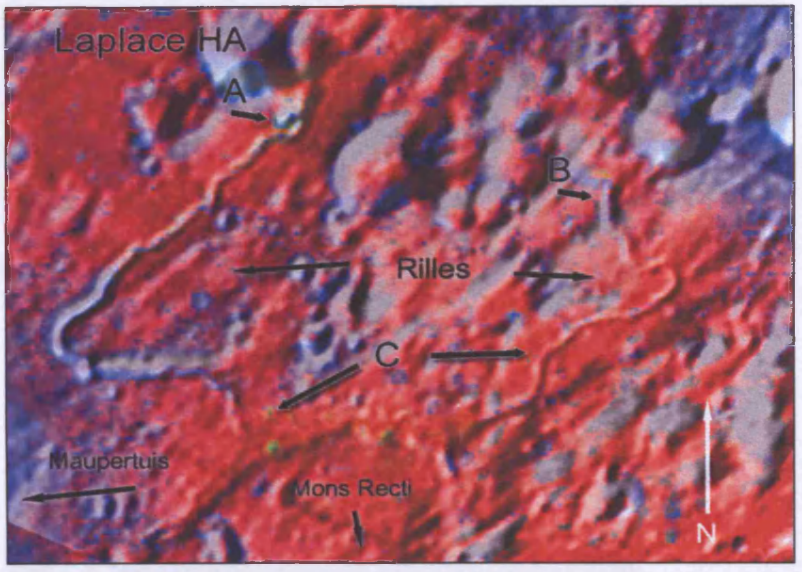

The smaller sinuous rille east of 'A' also seems to originate from the north of the region. The 'head' of the rille, 'B', does not appear to be characterised by an unusual chemistry. Nevertheless, I found evidence that this flow might have been 'reactivated' later in time some five kilometres southeast of the flow, albeit, judging by the width of the channel, with a substantially different effusive regime (either shorter, faster, or less voluminous rate of effusion). Eventually both channels become shallower and terminate within a moat-like depression a few kilometres of distance from Mare Imbrium.

One of the best known rilles in the region crosses the whole length of the Vallis Alpes (figure 25.2, ~18-50 N 0-6 E). This 166 km long depression appears to connect Mare Frigoris in the north with Mare Imbrium in the south, giving the (incorrect) impression of a terrestrial equivalent of a rift valley. Given the acknowledged thermal history of the Moon, it is obvious that the origin of this structure is not tectonic but it might be connected with crustal expansion and stretching following the Imbrian impact.

Figure 25.2. Vallis Alpes, southern section of rille (mosaic OIV and Clementine FC).

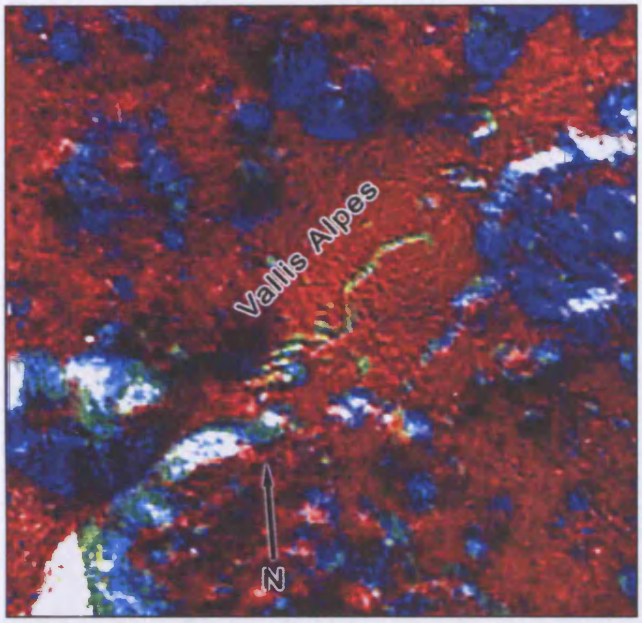

The lower topography floor of the graben was later infilled with basaltic materials of a comparable composition to that of the northeasterly Imbrian mare. Figure 25.2 highlights the southernmost section of the valley, where it connects to the Imbrium basin along a narrow fiord-like inlet. The yellow-green colour of this segment of the rille points to a fresher (more crystalline) composition of the exposed materials. Moreover, when viewed in isolation, this structure appears as a 'typical' example of a lunar sinuous rille, characterised by a well-defined 'head' crater, a potential extrusive locus (in the north end) surrounded by 'red' material, and a sinuous planimetry, which terminates along a progressively shallower channel. The tail end of the channel appears staggered, in an en échelon-like morphology suggesting either a post-formation deformation of the rille, lava infill of pre-existing terrain topography, or an expression of a complex collapse of the original lava tube.

There are a number of rilles within Mare Imbrium but they are mostly located near the base of the scarps (e.g. south of Promontorium Laplace and northern section of Montes Apenninus) or in association with isolated complexes of positive-relief features (e.g. Mons Vinogradov).

The astronauts saw distinct layers of rock on the far wall, witnessing a geological record spanning millions of years of lava flow strata. These are represented by the bright yellow-green colours on the FC composite, suggesting a relatively recent denudation of the rille's flanks and, possibly placing the time of excavation itself in a relatively recent geological time.
We also notice nonsinuous rilles, probably of extensional origin, crossing Locus Mozart and disappearing on the shore of Palus Putredinis. This feature consequently predates both basaltic floodings, but, given that the rille contours are still clearly detectable in photographic imagery (e.g. Apollo 15 AS15-M3-1136) crossing Locus Mozart, it constrains the maximum depth of basaltic material in this location to a few tens of meters.

25.2 Ridges

While most rilles within Mare Imbrium are either restricted to the periphery of the basin or occupy the low topography of the surrounding mountains and uplands, we find wrinkle ridges almost everywhere. Nevertheless, they appear to belong to a small number of morphological groups which origin can be extrapolated to plausible geological settings. As explained in Chapter 17, if one draws a line encompassing the massifs within the Imbrium basin one obtains a circle that I suggested might represent what is left of the original 670 km inner impact rim. This proposition is reinforced by the presence of a system of concentric mare ridges nearly joining into a hexagon with vertices inside this hypothetical ring. Additionally, a ridge runs from the eastern side of Montes Recti to the proposed centre of the basin. These are clues that point to a compressional origin of these formations due to the subsidence of the mare, either from subsurface removal of magma and/or isostatic compensation of the basin interior.

Most mare ridges stand out because of their shallow near-IR continuum slope that is indicative of less mature materials than the surrounding basalts, (e.g. Dorsum Grabau shown in Figure 25.5).

(red terrain: TiO_2 ~ 4.1 wt%; blue terrain ~ 7.1 wt%). The age of the unit to the east also postdates the red terrain by ~ 300 Ma. Ejecta excavated by crater Spitzbergensis A confirms that materials from the west underlie the later Ti-richer basalts found in the east. It is also important to note the high sinuosity of the ridge and its complex braided characteristic. Gathering the evidence, I speculate that the wrinkle ridge formed either prior to the emplacement of the red terrain or soon after. This would partially explain the highly irregular shape of the formation, suggesting a considerable level of crustal plasticity probably uncoupled from underlying structure and topography. The 'blue' section appears more shallow and regular, making it consistent with a scenario where the newer flow had mantled the ridge. 'a' points to a section where the rille becomes nearly indistinguishable from the surrounding mare probably because of the lower topography it once occupied.

As mentioned above, not all ridge systems are concentric to the basin topography. Outside the proposed inner ring, most ridges display a north-south geographical trend. In particular, the southern region enclosed between the inner and main Imbrian crater ring (see Fig. 17.2) is crossed by a swarm of near-parallel basaltic corrugations. This geological arrangement could be partly explained by the general morphology of the basin, including the asymmetrical distribution of the concentric mountain ranges (almost entirely hidden or obliterated in the west), the contribution of major post-Imbrian impacts (Eratosthenes, Copernicus, etc.), the early volcanic episodes within the basin (formation of the Apennine Bench, e.g. Hackman, 1966), and the thickness of the maria (Fig. 23.1). A combination of the above would have contributed to a second phase of crustal compression this time not concentric to the circumference of the excavation, but through an ideal north-south rectilinear line crossing the centre of the basin.

Some wrinkle ridges maybe related to a particular impact phenomenon. Figure 25.7 shows crater Brayley (20.9 N 36.9 W, 14 km) to be the centre of a complex ridge system. The ridges appear to radiate in all four directions with the fulcrum located within the crater itself.

geology of the area can be reconstruct by recognising the low-Ti materials as the exposed examples of early Imbrian flows; the ridge must have formed either during this emplacement period or not longer afterwards (Late Imbrian?); hi-Ti basalts from the south reached the area during the Eratosthenian period. Laplace A, one of the freshest looking craters in the area (Figs. 24.3 and 24.6), was excavated during the late Eratosthenian, splattering the northern flank of the rille with fresh ejecta ('green' material) and, by 'exploiting' a low relief section of the rille, the 'blue' unit with ejecta rays.

CHAPTER 26 GEOLOGY AND GEOMORPHOLOGY (PART II)

MARE IMBRIUM

26.1 Domes

Mare domes are scattered across many marginal basin areas in the nearside of the Moon. Head and Gifford (1980) classified more than 200 of these morphologies and grouped them broadly into two distinct modes of occurrence: one representing primary volcanic structures analogous to small terrestrial shield volcanoes, and the other the result of secondary volcanic products such as draping of lavas and kipukas. The recognised mare domes within the Imbrium basin are found adjacent to highland regions; most domes are located within two relatively narrow geographical districts: one in the south, west of Copernicus (~13-14 N 30-32 W) and the other in the bay south of the Apennine Bench. I tried to locate these constructions using the Clementine data but I could detect no obvious localised compositional anomalies. This is due to the geomorphology of these domes, characterised by relatively low slopes (generally less than 5°), diameters not exceeding 30 km (Head and Gifford, 1980), and heights no more than a few hundred meters. These characteristics would prevent gravitational slumping of lunar material and exposure of unweathered soils; furthermore, the geological nature of these domes, as eruptive centres, would make them by definition spectrally indistinguishable from the related mare materials surrounding them (i.e. same age and composition).

One marginal region of the Imbrium basin has been the centre of extensive geological studies (e.g. Schultz, 1974; Head and McCord, 1978; Chevrel *et al.*, 1995; Hawke *et al.*, 2003): the Gruithuisen Domes region. Figure 26.1 shows the Clementine colour composite image of the region superimposed to the Orbiter IV medium resolution photograph.

infill of the crater. Plato's morphology is rather complex: lava domes can be found just outside the crater (i.e. southeast of Plato L and west of Plato M); large post-impact sinuous rilles meander down the edifice's eastern and western flanks (a-b); pyroclastic material scattered over most of the rim's and flanks' diameter; and finally, possible source(s) of the basaltic materials covering the crater floor.

Rille 'a' has actually two distinctive sources with the smaller one (in the north) flowing into the larger one in the south. Interestingly, lava from the northern eruptive centre appears to postdate the southern one having carved a smaller flow channel inside the main conduit. The rille's course can be followed well within northern Mare Imbrium were it probably contributed basalt to the infill of the basin. Rille 'b' was carved by extrusions from the eastern flank of Plato. The oblong morphology of the head crater points to a fissure eruption style. It is easy to imagine how Plato could have been mistaken for an endogenetic caldera for a long time!

Thompson *et al.* (1978) proposed that Plato B is probably a young impact crater that has exhumed a large area of fresh bare rocks. There is little doubt that the above conclusion is correct. Nevertheless, my Clementine data indicate Plato M to be the most recent impact in the area and responsible for most of the (blue) fresh ejecta mantling over the whole area. The 'green', immature material characterising the inside of the excavation confirms its young age.

Sinus Iridum and Plato represent two major impact craters that formed astride what is most likely to be the northern side of Mare Imbrium transient crater rim crest. Similarly to Plato, the surviving elevated sections of the excavation (Montes Jura) are characterised by red soils coverage. Figure 26.3 shows the southern rim section culminating with Promontorium Heraclides.

spectral presence despite their assumed old age). There is also the intriguing possibility that at least some of this volcanic activity might be relative recent: red soils 'spilling' inside Archimedes crater, infilled by Eratosthenian mare (Fig. 24.2); similar materials invading the maria off Promontorium Heraclides (Fig. 26.3); the smooth, unweathered appearance of the Gruithuisen domes (Fig. 26.1); and finally the presence of these orange glasses scattered far from La Hire into some of the freshest mare in the Imbrium Basin (Fig. 26.4).

This evidence invites one to consider the possibility that we might be witnessing examples of a much later lunar volcanism phase than first thought.

27.1 Background – Vents and basalt flows

Strom (1965) was the first to map the Eratosthenian flows in Mare Imbrium based on telescopic observations from Earth. In the following years, photographs obtained from the Lunar Orbiter, Apollo metric, Hasselblad, and various Earth-based programmes helped locate the potential lava flow fronts and correlate them with spectral studies of the maria (e.g. Fielder and Fielder, 1968; Schaber *et al.,* 1975; Gifford and El-Baz, 1981). Only a very small fraction of the proposed distinct lava flows on the Moon show clear termini. The elusive nature of these features is due mainly to their modest topographical elevation, with measured heights of the flow scarps ranging between 1 and 96 meters, with more than half of these less than 15 m thick (Gifford and El-Baz, 1981). The task of matching spectrally divergent flow boundaries with clear morphologic horizons is further complicated by the nature of the distinctive flows overlapping each other, which tend to share a common point of origin and small variations (if any) in composition.

Mare Imbrium hosts some of the best known and extensively studied flow units' edges on the Moon, helped by their unusually elevated scarp heights averaging 30-35 m with a range from 10-63 m (Schaber, 1973a, b). High-resolution photographs of the lunar surface (Lunar Orbiter and Apollo missions) showed a series of highly lobate termini, including associated blocky outcrops, subdued shallow troughs, and encroached craters (e.g. Schultz, 1974; Orbiter photos V-159 to 161-M). Apollo orbital photography was used by Schaber (1973) to map relatively young lava flows in Mare Imbrium in the following years, he succeeded in correlating his data with their 70 cm radar backscatter variations and characteristics (Schaber, 1975).

Schaber *et al.*'s (1975) proposed distribution map of Eratosthenian lava flows across the western half of the Imbrium basin is superimposed over Figure 22.7 (a combined chemical/age map) and over my geomorphology map to produce

drew their first map according to colorimetric data. The boundaries of earliest flow are mostly the same as those suggested by this research in the east and in the north. Indeed, Eratosthenian materials of average composition TiO_2 ~8.1 wt% and FeO ~18.4 wt% are clearly different from the Imbrian flows they invaded (TiO_2 ~1.5 wt% and FeO ~15.8 wt%). The lack of clear flow flanks in the northern boundaries might be due to the thinning of the magma flows (i.e. less than a few meters high), making them much more difficult to detect. Even wrinkle ridges of modest height, such a those shown in Figures 25.8 and 27.2, marking the border with Sinus Iridum, would suffice to halt and redirect the incoming flow. Schultz *et al.* (1976) concluded that the sparseness of mare flow features is the result the eruptive style and lava composition rather than the effects of weathering.

The major disagreement between the Clementine derived compositional data and the flow chart relates to a large area surrounding Carlini. The False Colour, titanium, and iron maps clearly fail to differentiate between the proposed three flows and a large mare area encircled by them (Figs. 27.1 and 18.2-18.4). Furthermore, this work found the iron values for the area covered by the Eratosthenian mare to be rather homogeneous (including the 'Carlini' region), around 18 to 20 wt%, but with the mafic materials being slightly enriched in titanium (from ~7-8 to 8-9 wt%, see Figure 21.2) north of ~30 N. The metal's variations could be the result of contamination from low-Ti ejecta from Copernicus. Gifford and El-Baz (1981), in a private communication with Whitaker, concluded that most of the scarps are difficult to locate accurately at the resolution of the available colour composite photographs available at the time (i.e. Whitaker 1972a). Sadly, much higher resolution Clementine images still fail to differentiate among the proposed lava flows (also Friedman *et al.*, 1996), suggesting that the late Mare Imbrium volcanic activity, punctuated by at least three major eruptive phases that affected the western basin, extruded basaltic materials with an extremely similar composition over a relatively long geological time (0.5 Ga, Schaber, 1973).

Copernicus ejecta). Its titanium content is nearly half the value for the fresher unit (~4 wt%). Lambert's is clearly older that the similarly sized Timocharis in the east, predating the hi-Ti flow but much younger than the nearly obliterated 60 km Lambert R crater in its immediate south. Gravitational slumping of materials along the terraced internal walls has exposed fresher, crystalline 'green' soil.

The overall geomorphology of this area is highly complex. The 193 km long Dorsum Zirkel cuts through the basin from the northwest, it disappears just north of Lambert, and then re-emerges as a raised section of the surviving eastern rim of Lambert R to continue its journey to the southeast. Further to the east, we see the start of the elevated section belonging to Dorsum Higazy (60 km), which eventually joins into the larger, and nearly circular, Dorsum Grabau (121 km). A few tens of km east of Lambert we encounter an island of massif material 730 m higher than the surrounding terrain; this upland stands out from the maria because of its high albedo, extremely low iron content, low-Ti but of an intense blue hue. This uncommon spectral signature might reflect the immaturity of the exposed surface, which is probably due to gravitational removal of weathered regolith instead of a peculiar compositional characteristic. If we look back at figures 17.1 and 17.2, the morphologic complexity of the area begins to clarify: both Timocharis and Lambert probably sit over the proposed inner 670 km ring of the Imbrian basin. It is likely that the earliest mare basalts erupted near the basin centre and have since being covered by kilometres of additional flow materials (Whitford-Stark, 1980). The concentric ridges north of the craters might represent the surface expression of the post-emplacement shrinking and sagging of the basaltic load confined within the inner ring and uncoupled to the basin crustal floor.

The Clementine colour composite mosaic shows a remarkable contact sharpness between the Ti-rich flow and the red basalts. Additionally, the image (Fig. 18.4) suggests an uninterrupted flow of material into the lower topography of Lambert R, with a few patches of elevated terrain dotting the interior of the infilled excavation. Intriguingly, Figure 27.6 suggests that the Eratosthenian flow 'climbed' over the ghost crater's rim, barely deviated from its original course. A

number of scenarios could explain the observed features: the 'blue' flow a) crossed the rim's crater when it was much lower in topography; b) the point of origin is somewhere west of the ridge barrier, but inside the crater walls; c) it is part of the hi-Ti material flowing from the west. To complicate matters even further, the composition of the ridge is the same as the mare flow! I believe the answer lies on the timing of the Lambert impact and the morphological stress it inflicted to the surrounding area. The relative high elevation of the eastern limb of the ghost crater's rim might have developed after, and as a result of, the impact. The 'blue' flow would have being able to cross a much more subdued (or possibly unexpressed) topography. Indeed, the presence of crater ejecta over the recent flow reinforces the plausibility of this scenario.

28.1 Overview

I used sources and techniques as described in Chapter 17 to produce a map of geographical boundaries of the mare features within the region under investigation, centred on Mare Imbrium. Mare structures such as flow fronts, sinuous rilles, mare domes, cones, and mare ridges were noted and mapped, including the proposed multiring outlines (Fig. 17.2). Clementine data images were used to define potential compositional boundaries of flow units (Fig. 19.2). The resulting 102 areas were thus plotted and numbered (Fig. 19.3). ISIS software was employed to investigate the compositional make up of each unit in regard of its iron and titanium content (Chapter 20). Table 20.1 lists all the values obtained and shows the allocated 'family' code number based on composition (out of 81 potential commutations).

A possible abundance correlation between titanium and iron content in the regolith was found and shown as figure 20.7.

Figures 21.1 and 21.2 are geographical representations (b-i) of the distribution of five iron compositional groups and eight titanium units (2-9) across the Imbrium basin. Comparison and assimilation of potential unit flows with similar Fe and Ti concentrations produced Figure 21.3 (based on data from Table 21.2), showing eight major compositional groups and their geographical distribution. Highlands, uplands, craters and the associated mare regions altered by their ejecta, were not included in the map.

Using statistical techniques developed for this work (Chapter 10), I was able to obtain crater density data for 80% of the mapped unit flows. In aid of convenience and clarity, the gamut of obtained values was grouped into nine density families and displayed as Figure 22.1. When the crater density data of each unit, and their assumed corresponding absolute age estimates, were plotted against composition, the result was a potential clustering of data points around three distinct eruptive

phases (Table 22.5). These findings are illustrated in Figure 22.7, comprising eight unit flow groups with similar chemical composition (Ti and Fe) classified according to their comparative ages.

Chapter 23 describes the difficulties in obtaining reliable data points to estimate depths of excavation and the paucity of suitable sample material. Nevertheless, nine depths values were obtained and, combined with data from published research, used to offer a representation of the modelled mare thickness within Mare Imbrium (Figure 23.2).

The chronology of cratering processes within the Imbrium basin region was documented in Chapter 24, including in-depth analysis of five major impact structures. Figure 24.3 is a representation of the larger craters and fresher ejecta in the region according to their spectral signature in the Clementine FC image. Data derived from the same image was used to produce Figure 24.6: a map of the freshest, mafic, crystalline material scattered around the region. Four areas were found to be particularly devoid of chemical traces (weak 1μm absorption).

The geology and geomorphology of the region was investigated making use of the new Clementine data and compared with published research. In particular, this work focused on a number of geological features that demanded closer scientific scrutiny.

28.2 Titanium

My results show that more than a third (37%, Figure 20.4) of the exposed mare surface has a titanium content between 1-3 wt%, a fraction described by Pieters and McCord (1975) as low to medium. The next major group of basalts have values TiO_2 in the range of 3-5 wt% (23%), and most of the remaining regolith contains titanium in the region of 7-9 wt% (27%).

28.3 Iron

The dominant fraction of FeO in the sampled maria (55%, Figure 20.3) ranges between 16 to 18 wt%. The rest is shared between the larger iron-rich group (FeO 18-20 wt%, 27%) and the smallest (FeO 14-16 wt%, 18%).

28.4 Ages

Three quarters of the sampled mare shows a crater density population between 3.5-5.5 $\times 10^{-2}$N km^{-2}, which translates into an estimated age of ~2.5 to 3.3 Ga. If we average the results for the whole region, we obtain a crater density of 4.7 $\times 10^{-2}$N km^{-2}, or ~3.1 Ga.

28.5 Mare Thickness

No major craters within the inner ring of Mare Imbrium have apparently excavated the mare down to the crustal basement level. The minimum level of basalt thickness at the centre of the basin is given by crater Helicon, which ejecta represents materials excavated from a depth of nearly 2.5 km and does not show crustal material in its composition. As we move away from the thickest mare to the margin of the basin, we encounter craters that have indeed penetrated the whole depth of the basaltic infill. At latitude between 20-30° N, the ejecta composition of a number of larger craters indicate that the mare at these points maybe around one kilometre thick.

29.1 Pre-Imbrian geological setting

The Imbrium impact was dated with some precision to a time between 3.836 Ga and 3.870 Ga by Ryder (1992). Stadermann *et al.* (1991) put forward the case for a younger excavation, based on new dating of Apollo 14 rocks, of 3.75 Ga.

There is evidence that the Imbrium basin was formed within a region with a relatively thin crust, previously altered and modified by older impacts (very little ferroan anorthosite has been identified among the presumed ejecta). Much research shows that the Imbrium excavation did not penetrate down to the mantle, as various studies have failed to find petrological clues pointing to non-crustal materials. Indeed, the ejecta have revealed a complex admixture of rock types at the site of impact: lower crust samples of low-K Fra Mauro basalt (LKFM, e.g. Ryder and Wood, 1977; Lucey and Taylor, 1995) and mafic cumulates of the Mg-suite were found in the nearby Apennines, and, further away, upper crust and surface multi-generational examples of KREEP (K-potassium, Rare Earth Elements, and P-phosphorous) and mare basalts (e.g. Spudis, 1993).

By mapping data of lunar thorium distribution (from Apollo orbiting γ ray spectrometers) Haskin (1998) hypothesized that the Imbrium impactor struck the northwest section of a unique, mafic, trace-element-rich geochemical province (extending over ~5% of the Moon's surface) baptised 'high-Th Oval Region' (also Evenson *et al.*, 1974; Metzger *et al.*, 1974; Tera *et al.*, 1974). Gillis *et al.* (1999, 2000) also proposed a convecting mechanism peculiar to this lunar region (named Procellarum KREEP Terrane) involving transport of K-U-Th to depth as accessory elements of the sinking ilmenite cumulates. This localised high concentration of heat producing elements in the lithosphere would have caused relatively high crustal temperatures in the Imbrium target area with consequent overturn of the cumulate pile in the PKT region. This would have triggered intensified igneous activity in the province (both plutonic and extrusive), eventually affecting the geomorphology of the post-impact area. Furthermore, there is a strong possibility

that the Imbrium impact event most likely excavated into a partially molten KREEP basalt magma chamber (Wieczorek and Phillips, 2000), which resulted into an amplified proportion of melt fraction in the Imbrian ejecta.

Structural modifications of the basin following the excavation phase were both widespread and profound. Spudis (1993) remarked that structural modification of the basin occurred outside its transient cavity (e.g. prominent tangential structures in the Montes Caucasus and Carpatus), continued well after the time of impact, and were not restricted to the massif ranges tangential to the basin rim. Crucially, pressurised melted materials present at depth exploited radial structures and associated areas of crustal weaknesses to escape from their sub-crustal confinement.

29.2 Post-Imbrian stratigraphy

The near-circular morphology of the Imbrium basin is intruded by a modestly elevated limb of pitted plain material anchored to the Montes Apenninus to the east and protruding towards the centre of the crater. Wilhelms and McCauley (1971) described the Apennine Bench as volcanic in origin, brighter than the typical Imbrian mare but darker than the circumbasin and other terra materials. Indeed, albedo differences between the Apennine Bench and Montes are rather difficult to discern (e.g. Clementine DBA image, Figure 16.1); furthermore, optical similarities are mirrored in the iron, titanium, and FC component images (suggesting similar compositions). Apollo gamma-ray data (Davis, 1980; Spudis and Hawke, 1986; and Blewett and Hawke, 2001), all agree on an average composition for the bench's regolith of ~12 wt% FeO, ~1-2 wt% TiO_2, and 8.5-10.5 ppm Th, values consistent and comparable with the figures for the Apollo 15 KREEP basalts with an isotopic age of 3.85 ± 0.05 Ga (Bussey *et al.*, 1998).

Blewett and Hawke (2001) interpreted the composition of Aristillus' central peak, crater walls, and both close and distal ejecta as stratigraphically sorted examples of the 5 km deep composition of the eastern Mare Imbrium. The deepest samples, represented in the central peak, have a similar composition to that of the Apenninus materials, with noritic or anorthositic norite geochemistry. Above this stratrum, they found evidence of Th-rich KREEP plutonics in the interior and ex-

terior deposits. The deepest (i.e. earliest) extrusive basalts are KREEPy in character and similar to the Apennine Bench formation surface exposures. These results would go towards validating Spudis' (1978) hypothesis that KREEP volcanism was a moonwide phenomenon early in the lunar history and that the Apennine Bench represents exposed patches of non-mare basalts.

Whitford-Stark and Head (1980), by collecting spectral data over a larger lunar area including Oceanus Procellarum, found some evidence of (very) low titanium basaltic flows originating from the Aristarchus Plateau which might have supplied the Imbrium basin with the earliest mare infill. The same authors also speculated on the existence of nearly contemporaneous (3.5 ± 0.25 Ga) high-Ti basalts layer hidden by younger flows, erupted near the basin centre.

There is general consensus among lunar researchers that the onset of maria volcanism did not commence soon after the excavation phase. The delay between impact and magmatic extrusion might be due to the time needed for the volatile-rich magma to cool and crystallise, producing overpressures that drove the basalts upward to the surface (Werner and Loper, 2002).

As discussed in detail in Chapter 22, assigning an age estimate to the chemically distinct lava flows has proven rather difficult due to the amount of secondary cratering scattered across the basin by relatively recent major impacts. The copernican Aristillus, Autoclycys, Timocharis, Pytheas, Euler, and obviously Copernicus itself, all large impacts (20-107 km diameter) and all younger than the surrounding mare, have contributed in making the collection of reliable crater density statistics of the neighbouring regions very difficult and uncertain. This is reflected in Figure 24.6, which shows large areas void of data, mostly confined to the south-south-eastern regions.

This work interpreted the gathered geological results as pointing to a three-phase stage of principal mare emplacement (Table 22.5). These findings do not preclude less widespread extrusive periods within Mare Imbrium; indeed, there is an almost uninterrupted record of exposed lava flows spanning 1.4 billion years within the basin.

This work has identified the earliest exposed lava flows mostly in the east and the north of Mare Imbrium (Mid Imbrian, Phase I, 3.3 ± 0.1 Ga). All of these units can be classified as Very Low TiO_2 (1.0-4.5 wt %, Giguere *et al.*, 2000) and within the lower range FeO of typical mare basalts (~15-17%). Nevertheless, a north-south dichotomy is apparent, with the southern flows displaying compositions belonging to the upper scale of the range. It appears that the basalts originating from the southern half of the basin are generally Ti- and Fe-richer than those from the north. This could be due to compositionally heterogeneous magma sources, chronologically distinct eruptions (within a ~200 Ma time window), different regimes of magma transport and crystallisation, or a combination of any of these factors.

It is worth noting that the flows classified in Figure 22.7 as 2g might represent the same unit types as 2f, appearing slightly enriched in iron content due to their relatively remoteness from highland contamination. There is a strong possibility that these types of basalts might underlie most of the basin's younger flows. I was unable to locate well-defined vents, suggesting that the volcanic eruptions occurred through fissures or fissure complexes (e.g. Guest and Murray, 1976). Nevertheless, there is a strong possibility that the resulting flows, and in particular the northern units, might have been fed by vents located near or just within Montes Alpes, as suggested by the similarities in composition of the basalts within Plato and Vallis Alpes, their neighbouring maria, and a system of rilles and lava channels crossing the region.

A further chrono-geological clustering of unit flows was identified (Period II, Late Imbrian, 3.0 ± 0.2 Ga, Figure 22.7). The range of composition of these flows is only marginally skewed towards higher metal values than previous Period I; titanium content varies from ~2.5 to 7.1 wt%, placing these basalts within the "Intermediate" family. The geographical distribution of these terrains is much more limited than the previous and following ones. Figures 22.3-22.6 show a strong polarisation between two compositional types in this age group: most of the samples cluster around relatively low Ti and Fe values (~2.4 wt% TiO_2, ~16.1 wt% FeO) within a narrow time of emplacement (~2.95 ± 0.1 Ba). Unit 13 (Fig. 19.3) has a

strong chemical affinity with the older surrounding mare (VLT, ~1.2 wt%) but with a noticeably lower crater count (suggesting a younger age). The main difference between '2f' and '2g' groups (Fig. 22.7) is the lower iron content of the units bordering with highlands. There is the possibility that contamination from Fe-poor materials originating from the mountain ranges might have caused this. This leaves unit 18, which stands out for its high Ti and Fe average values (7.1 and 17.9 wt% respectively). Figure 21.3 shows the chemical affinity of the area with the Eratosthenian basalts to the west of the basin. Its higher crater population could be the result of its proximity to the nearby copernican impacts (Aristillus and Autolycus) and their dissemination of secondary craters in their neighbouring region.

We have seen that the most of the last erupted basalts originated in the southwestern region of Mare Imbrium and spread north towards the centre of the basin. These Early Eratosthenian flows (~2.3 ± 0.5 Ga) display a wide range of compositions, with distinct units showing high titanium values close to 10 wt% (High to Very High-Ti basalts, e.g. flow 100). Most of the basalts in this Period III have High-Ti and High-Fe compositions except for a few marginal areas: unit 20 represents the distal ejecta apron of crater Aristillus, as evidenced by the ray-like northern margins of the unit flow. It is obvious that in this instance we are not observing pristine mare material. Figure 18.3 shows a radial distribution of intermediate composition regolith around the crater: the impact might have excavated materials with different geochemistry (see previous chapter) and with higher Fe and Ti content than the original target area of Imbrian age, but lower than the Eratosthenes high-Ti basalts. Furthermore, the impact would have 'reset' the age of the area by obliterating a large percentage of the pre-existing crater population, hence the inferred young age of the surrounding mare.

Figure 22.7 suggests that the earliest Eratosthenian flows were low-Ti (~2.5 wt%) and with an iron average of ~17 wt%. They spread over much of the western Mare Imbrium including the low topography of Sinus Iridum. Their point of origin has not being identified and might not necessarily coincide with the later igneous centres. Within a relatively short geological time, basalts with much higher Ti and Fe content (~7.0 and 18.1 wt% respectively) invaded most of the western basin, leav-

ing isolated patches of maria (e.g. units 88 to 91) as the only exposed evidence of older flows. Sinus Iridum also features samples of the LT Eratosthenian basalts, presumably because the later flows could not overcome the newly formed elevated morphology (mare ridges), acting as a barrier to the newer, thinner flows. We find the highest titanium basalts in the northern half of the western flows, with an average higher Ti around ~1 wt%. The 2,500 km^2 of mare represented by unit 100 features the highest titanium and iron regolith of the entire basin (9.8 and 18.8 wt% respectively). This patch of mare may represent: a pristine and unweathered example of Ti-rich basaltic flow belonging to the main extrusive event; the remnant of a larger flow event buried by younger maria; on the most recent, and possibly latest example, of widespread mare volcanism.

CHAPTER 30 CONCLUSIONS

30.1 Mare Imbrium

Figure 30.1 is a geological map of Mare Imbrium showing: the distribution of the exposed flow units, classified according to their inferred age and composition; the crater and ejecta colours derived from the Clementine FC image reflecting the composition of the exposed and excavated materials, and their weathering stage (i.e. relative ages); detectable ray patterns from young craters; and main geological features and morphologies (rilles, ridges, etc.). Blank (white) areas represent regions where compositional data were collected (Ti and Fe), but for which crater density data was deemed too unreliable to be included in this work (e.g. small geographical areas, high proportion of secondary craters etc.).

The Imbrium basin has been the setting of extensive lunar basalt flooding starting soon after the time of impact (3.91 ± 0.075 Ga, Turner, 1977). I identified numerous exposed lava flows, which may be the products of igneous activity relating to the last two major phases of mare infill. Their mode of distribution can be broadly classified along an east-west compositional and chronological divide, centred around 15°W: eastern maria, generally Ti-poor and dating from the Middle to late Imbrian Period (3.0-3.5 Ga), and a system of western flows characterised by higher titanium and iron content of early Eratosthenian age.

There are numerous areas within the basin showing examples of red soils; some are associated with crater rims morphologies (e.g. Plato, Archimedes, etc.), some with lunar domes (e.g. Gruithuisen, Prom Heraclides, etc), others with Massif materials (e.g. Mons La Hire), and some with a sizable region of lunar upland (Apennine Bench). Their age could not be deduced or interpreted through the Clementine data, but there is evidence that some form of pyroclastic volcanism (often associated with red soil materials) occurred after the emplacement of the Eratosthenian basalts.

results are combined, for ease of comparison, in Figure 30.5. Here one can clearly see a common slight increase in iron content in the basalts with time, but also their distinct compositions (as noted above). The average higher Fe content in the Nubium regolith could be partially explained by the age difference between the basins and their exposed mare flows, given that the maturity of the soil affects the iron spectrographical signature (see Chapter 4).
Iron and titanium trends within Mare Nubium appear decoupled and not following similar variations within each distinct unit (Figure 30.4). The proposed unit flows for Mare Imbrium instead show a strong correlation between the metals' concentrations in the regolith (Figure 30.3).

30.3 Petrological discussion - background

Various models for mare basalt source regions have been developed in the last forty years to try and explain the mineralogy of the lunar surface. The cumulate model (Taylor and Jakeš, 1974; Taylor, 1975) is based on the assumption of the existence of an early, planet-wide magma ocean that gave rise to an extensive differentiation of the Moon to depths of 500 km (Taylor, 1978). Bottom-up fractional crystallisation would have occurred leading to the formation of a 60 km thick cumulate crust mainly comprising plagioclase along with Mg- and Cr-rich components, and enriched in Eu, Sr and Al. Coincidently, mafic minerals would have settled to form early magnesian cumulates mainly comprising of olivine and orthopyroxene phases, a layer characterised by negative europium anomalies. In time, more ferriferous and titaniferous ultramafic cumulates would have settled, with pyroxene and ilmenite as the main phases. According to this model, the last liquids to crystallise (KREEP basalts) deep in the crust were enriched in heat producing elements (K-U-Th); consequent re-melting of this layer, potentially coupled with the gravitational instability resulting from the upward decrease of *mg*-number in the ultramafic materials (Delano and Taylor, 1980), could have led to a late production of picritic and ultramafic liquids at 130-480 km depth. Most researchers (with due exceptions, e.g. O'Hara, 2000) recognise these magmas as the bulk source of most of the maria basaltic flows which infilled large low-topography regions of the lunar nearside.

Table 30.2 focuses on the titanium abundances as found in this study and classified according to Giguere *et al.* (2000). As we can see, low-Ti basalts (<5%) are the most common in both basins and in particular, Mare Nubium. This is consistent with the experimental compositions of basalts produced by partial melting of olivine and low-Ca pyroxene cumulates with low abundances of TiO_2 (Longhi, 1992), by far the most common cumulates produced during the crystallisation of the lunar magma ocean (>70%, e.g. Taylor and Jakeš, 1974). More than 90% of the exposed basalts within the Mare Nubium and Mare Cognitum basins exhibit titanium content between 3.0 and 4.5% (Chapter 8).

The basalts within the Imbrium basin display a much wider range of titanium concentrations: low-Ti basalts represent 54% of the sampled regolith, intermediate-Ti 21%, and high-Ti 25%. Formation of mare basalts with >5 TiO_2 wt% have been predicted by many workers (e.g. Dowty, 1975; Herbert, 1980; Ryder, 1991; Hess and Parmentier, 1995) and involves, as described in the previous chapter, sinking and concentration at depths of heat producing elements along with late-stage cumulates (rich in clinopyroxene and ilmenite). Eventually, this would have triggered melting of these materials and mobilisation of partial-melt diapirs. Ilmenite-bearing cumulates (linked to the production of hi-Ti basalts) would have not reached saturation until 90% of the magma ocean had solidified (Giguere *et al.*, 2000) and concentrated in the mantle at depths of 400 km or more (Beck and Hess, 2001). This would explain the presence and time of formation of the late Eratosthenian Ti-rich basalts that flooded parts of Mare Imbrium and Oceanus Procellarum (e.g. Hiesinger *et al.*, 2001; this work). Thus, the geographical distribution of basalt types in the Nubium region, classified according to their titanium abundances, is consistent with the presently accepted models of crystallisation of the inferred lunar magma ocean (Ryder, 1991).

Mare Imbrium shows a more complex suite of mare compositions and time of emplacements: one finds examples of low-Ti basalts throughout one billion years of basin infill. Nevertheless, if we refer back to the actual size distribution of these lavas (e.g. Fig. 22.8, Table 22.4), we see that the large majority of the exposed regolith for each of the three major eruptive periods (Table 22.6) have titanium

concentrations which follow the general petrological trend described earlier (Table 30.3):

Table 30.3. Area percentage distribution of basalt type within each period

Period	Range of compositions TiO_2 wt%	Area distribution of basalt type (%)
I	<1.5	71
II	<2.5	80
III	>4	81

This data confirm that a model of general enrichment in titanium dioxide with time of the erupted basalts may be broadly applied to the exposed mare of the Imbrium basin too. The production of melts of compositions outside this general trend, albeit of much reduced size, could be the result of local tapping of unusual source compositions, particular fractionation history, or admixing with Ti-rich materials before eruption. Clearly more data and research is needed to clarify this issue.

So far I have addressed the questions raised by the results of titanium concentration in the basins' mafics. Nevertheless, Figure 30.5 also raises questions about the apparent complementarily of the FeO figures and symbiotic iron and titanium values for Mare Imbrium (as introduced in the previous chapter). There is a noticeable compositional parallel trend between the variations of iron and titanium in the Imbrium basalts (Figures 20.7 and 30.6), but absent in the Nubium ones. Variations in magma compositions are linked mainly with differences in: depth and/or location of the source region; mineralogical composition of the parental rocks; degree of mixing of the cumulate piles; and mineral assimilation during storage and ascent. The closer chemical affinity displayed in the Imbrium basin basalts might be the result of more localised extrusive fonts and related magma sources, producing melts with more comparable fractionation histories. Furthermore, Mare Nubium basalts are on average ~400 Ma older than those within the Imbrium basin, raising the possibility that regolith maturity might influence the spectral signature of the mafic minerals, regardless of the corrections included in the data compositional algorithms.

ity of crater counting methods, and the use of compositional variations in the excavated materials as tools to estimate mare depths.

REFERENCES

Arvidson R. E., Drozd R., Guiness E., Hohenberg C., and Morgan C. *Cosmic ray exposure ages of Apollo 17 samples and the age of* Tycho. Proc. 7th Lunar Sci. Conf. 2817-2832 (1976).

Beck A. R. and P. C. Hess. *The ilmenite saturation surface of high Ti mare basalts.* LPS XXXII, abstract# 1939 (2001).

Blewett D. T. and Hawke B. R. *Remote sensing and geological studies of the Hadley-Apennine region of the Moon.* Meteoritics & Planetary Science 36, 701-730 (2001).

Boyce J.M. *Chronology of flow units in western nearside maria.* Conference on origins of mare basalts and their implications for lunar evolution. Houston, TX. pp 11-13 (1975a).

Boyce J. M and Dial A. L., Jr. *Relative ages of flow units in Mare Imbrium and Sinus Iridum.* Proc. Lunar Sci. Conf. 6th, p. 2585-2595 (1975b).

Boyce J. M. *Ages of flow units in the lunar nearside maria based on Lunar Orbiter IV photographs.* Proc. Lunar Sci. Conf. 7th, p. 2717-2728 (1976).

Bowker D. E. and Hughes J. K., Orbiter Photographic Atlas of the Moon. NASA SP-206, NASA Scientific and Technical Information Office. Washington DC (1975).

Bratt S. R., S. C. Solomon, J. W. Head, and C. H. Thurber. *The deep structure of lunar basins: Implications for basin formation and modification.* J. Geophys. Res. 90, 3049-3064 (1985).

Brett S. R. *Thicknesses of some lunar mare basalt flows and ejecta blankets based on chemical kinetic data.* Geochim. et Cosmochim. Acta 39, p. 1135-1141 (1975).

Budney C. J. and P. G. Lucey. *Basalt thickness in Mare Humorum: The crater excavation method.* J. Geophys. Res. Vol. 103. NO. E7, pp 16,855-16,870 (1998).

Basaltic Volcanism Study Project (BVSP), Basaltic Volcanism on the Terrestrial Planets: New York: Pergamon (1981).

Bussey D. B. J., Spudis P. D., Hawke B. R., Lucey P. G., and Taylor G. J. *Geology and composition of the Apennine Mountains, Lunar Imbrium Basin.* LPS XXIX, 1532 (1998).

Campbell B. A., B. R. Hawke, and T. W. Thompson. *Regolith composition and structure in the lunar maria: Results of long-wavelength radar studies.* J. Geophys. Res. Vol. 102, No. E8, pp 19,307-19,3200 (1997).

Carlson R. W. and Lugmair, G. W. *Sm-Nd constraints on early lunar differentiation and the evolution of KREEP.* EPSL 45, p. 123-132 (1979).

Carr M. H. *The role of lava erosion in the formation of lunar rilles and Martian channels.* Icarus 22, 1-23 (1974).

Charette M. P., McCord T. B., Pieters C., and Adams J. B., *Application of remote spectral reflectance measurements to lunar geology classification and determination of titanium content of lunar soils.* J. Geophys. Res.79, pp. 1605-1613 (1974).

Charette M. P., Adams, J.B., Gaffey, M.J., and McCord, T.B., *Determination of the iron content of lunar soils using remote spectral reflectance measurements. EOS,* 56, p. 1013 (1975).

Conel J. E. and G. B. Holstrom, *Lunar Mascons: a near-surface interpretation.* Science 162, No 3860, 1403-1405 (1968).

Chevrel S. D., Pinet P. C., Head J. W., and Bellagh F. *UV-VIS-NIR Spectral classification in the Gruithuisen Domes region.* Proc. Lunar Planet. Sci. Conf.26th, 241-242 (1995).

Craddock A. R. and Howard A. D. *Simulated degradation of lunar impact craters and a new method for age dating farside mare deposits.* J.Geophs. Res. Vol 105, NO. E8, pp 20,387-20,401 (2000).

Croft, S. K. Cratering flow fields: *Implications for the excavation and transient expansion stages of crater formation.* Proc. Lunar Planet. Sci. Conf. 11th, 2347-2378 (1980).

Croft S. K. *The scaling of complex craters.* J. Geophys. Res, vol. 90-B2, p. C828-C842 (1985).

Cross, C. A. *The size distribution of lunar craters.* Mon. Not. R. Astr. Soc. 134, p. 245-252 (1966).

Davis P. A. *Iron and titanium distribution on the Moon from orbital gamma-ray spectrometry with implications for crustal evolutionary models.* J. Geophys. Res. 85, 3209-3224 (1980).

De Hon René A. *Mare Humorum and Mare Nubium: Basalt thickness and basin-forming history.* Proc. Lunar Sci. Conf., 8th pp 633-641 (1977).

De Hon René A. *The Imbrium basin: a structural model.* (LPI) p. 15-17, (1980).

Delano J. W. and Taylor S. R. *Composition and structure of the deep lunar interior.* In Lunar and Planetary Science XI, pp. 225-227. Lunar and Planetary Institute, Houston (1980).

Desiree E. S., and Howard K. A. *Lunar maria and circular basins – a review.* Icarus 12, 440-456 (1970).

Dowty E. *Shallow origin of mare basalts.* Conf. On Origins of Mare Basalts 234, 35-39 (1975).

Eliason E. M., E. R. Malaret, and G. Woodiward, *Clementine Mission, The Archive of Image Data Products and Data Processing Capabilities.* Lunar and Planetary Science Conference 26th, pp 369-370, (1995).

Eliason E. M. *Production of Digital Image Models Using the ISIS System.* Lunar and Planetary Science Conference 28th, pp331-332 (1997).

Eliason E. M, C. Isbel, E. Lee, T. Becker, and L. Gaddis. *The Clementine UVVIS Global Lunar Mosaic.* US Geological Survey. Astrogeology Team, 2255 North Gemini Drive. Flagstaff, AZ 86001 (1999).

Elphic R. C. et al., Lunar Prospector Neutron Measurements and TiO_2 in Mare Basalt Soils. *American Geophysical Union*, Spring Meeting 2001, abstract #P21A-06 (2001a).

Elphic R. C., Lawrence, D. J., Maurice, S., Feldman, W. C., Barraclough, B. L., Gasnault, O. M., Lucey, P. G., Blewett, D. T., and Binder, A. B. *Lunar Prospector Neutron Measurements and TiO_2 in Mare Basalt Soils.* American Geophysical Union, Spring Meeting 2001, abstract #P21A-06 INVITED (2001b).

Evenson N. M., Murthy V. R., and Coscio M. R.. *Provenance of KREEP and the exotic component: Elemental and isotopic studies of grain size fractions in lunar soils.* Proc. Lunar Sci. Conf., 5th, 1401-1417 (1974).

Fielder G, and Fielder, J. Boeing Scientific Research Laboratories, Doc. No. D1-82-0749 (1968).

Fisher E. M, and Pieters C. M. Remote determination of exposure degree and iron concentration of lunar soils using VIS-NIR spectroscopic methods. *Icarus* 111, 475-488 (1994).

Fisher, E. M., C. M. Pieters, and S. P. Pratt. *Modelling the space weathering-induced optical alteration of lunar soils: first results.* Lunar Planet. Sci. XXV, 371-372 (1994b).

Fisher E. M, and Pieters C. M. Composition and exposure age of the Apollo 16 Cayley and Descartes regions from Clementine data: Normalising the optical effects of space weathering. *J. Geophys. Res.101,* (E1), 2225-2234 (1996).

French B. M. *Traces of Catastrophe: A Handbook of Shock-Metamorphic Effects in Terrestrial Meteorite Impact Structures.* LPI Contribution No. 954, Lunar and Planetary Institute, Houston. 120 pp (1998).

Friedman R. C., D. T. Blewett, G. J. Taylor, and P. G. Lucey. *FeO and TiO_2 variations in Mare Imbrium.* LPS XXVII, 383-384 (1996).

Gifford A. W. and El-Baz F. *Thickness of lunar mare flow fronts.* The Moon and the Planets 24. 391-398 (1981).

Giguere T. A., Taylor, G. J., Hawke, B. R. and Lucey, P. G. *The titanium contents of lunar mare basalts.* Metoritics and Planetary Science 35, 193-200 (2000).

Gillis J. J. and Jolliff B. L. *Lateral and vertical heterogeneity of thorium in the Procellarum KREEP terrane: As reflected in the ejecta deposits of post-Imbrium craters.* In Workshop on New Views of the Moon II, pp. 18-19. LPI Contribution No. 980, Lunar and Planetary Institute, Houston, Texas, USA (1999).

Gillis J. J., Jolliff B. L, Spudis P. D., and Haskin L. A. *The distribution of Mare Source Regions: Evidence using remote sensing data.* LPS XXXI, abstract no. 2089 (2000).

Gault D. E., Hörtz F., Brownlee D. E., and Hartung J. B. *Mixing of the lunar regolith.* Proc. 5th Lunar Sci. Conf. Vol. 3. pp 2365-2386 (1974).

Govindaraju K. *1989 compilation of working values and sample description of 272 geostandards.* Geostandards Newsletter, 13 (Special Issue), 1-113 (1989).

Greeley R. *Lava tubes and channels in the lunar Marius Hills.* The Moon 3, 289-314 (1971).

Greeley R. and Womer, M. B. *Mare basin filling on the Moon: laboratory simulations.* Proceeding of the Lunar and Planetary Science Conference 9, 3333-3349 (1981).

Grier J. A., McEwen A. S., Lucey P. G., Strom R. G., and Milazzo M. *Relative ages of large rayed lunar craters – Implications.* LPSXXX abstract no. 1910 (1999).

Grier J. A., McEwen A. S. *The lunar record of recent impact cratering.* In: Peuckner-Ehrembrink, B., Schmitz, B. (Eds.), Accretion of Extraterrestrial Matter throughout Earth History. Kluewer Academic, Norwell, MA, pp. 403-422 (2001a).

Grier J. A., McEwen A. S., Lucey P. G., Milazzo M., Strom R. G. *Optical maturity of ejects from large rayed lunar craters.* J. Geophys. Res. 106, 32847-32862 (2001b).

Grieve R.A.F., Robertson P. B., Dence M. R. *Constraints on the formation of ring impact structures, based on terrestrial data.* PLPSC12A, p. 37-57 (1981).

Grieve R. A. F. and Pilkington M. *The signature of terrestrial impacts.* AGSO J. Austral. Geol. Geophys. 16, 399-420 (1996).

Guest J. E. and Murray J. B. *Volcanic features of the nearside equatorial lunar maria.* J. Geophys. Res. Vol. 132, pp. 251-258 (1976).

Hackman R. J. *Geologic Map of the Montes Apenninus Region of the Moon.* U.S. Geol. Survey Map I-463, Washington, D.C., USA (1966).

Hackwill T, Guest J. E. and Spudis P.D. *Basalts in Mare Humorum and S.E. Procellarum.* Lunar Planet Sci. XXXV, 1062 (2004).

Hall J. L. and Solomon S. C. *Tectonics of the Irregular Maria.* Lunar Planet. Sci. XVII, 305-30. (1986).

Hall A. *Igneous Petrology – Second Edition.* Longman Group Limited. Harlow, England. pp 295-297 (1996).

Hapke B., Danielson G. E., Klaasen K., and Wilson L. *Photometric observations of Mercury from Mariner 10.* J. Geophys. Res. Vol. 80, (17), 2431-2443 (1975).

Hartmann W. K. and Wood C. A. *Moon: Origin and evolution of multiring basins.* The Moon 3, 3-78 (1971).

Haskin L. A. *The Imbrium impact event and the thorium distribution at the lunar highlands surface.* J. Geophys. Res. 103, 1679-1689 (1998).

Hawke B. R., and Head J. W. *Pre-Imbrian history of the Fra Mauro region and Apollo 14 sample provenance.* Proc. Lunar Sci. 8th , p. 2741-2761 (1977).

Hawke B. R., Blewett D. T., Lucey P. G., Smith G. A., Taylor G. J., Lawrence D. J., and P. Spudis. *Remote sensing studies of selected spectral anomalies on the Moon.* LPS XXXII, 1241 (2001).

Hawke B. R., Lawrence D. J., Gillis J. J., Blewett D. T., Lucey P. G., Peterson C. A., Smith G. A., Spudis P. D., and Taylor G. J. *Spectral anomalies in the Imbrium region of the Moon.* LPS XXXIV, 1545 (2003).

Hawke B. R., Blewett D. T., Lucey P. G., Smith G. A., Bell III J. F., Campbell B. A., and Robinson M. S. *The origin of lunar crater rays.* Icarus 170 1-16 (2004).

Head J. W. *Lunar mare deposits: areas, volumes, sequence, and implication form melting in source areas.* Conference on origins of mare basalts and their implications for lunar evolution. The Lunar Science Institute, Houston, TX. pp 66-67 (1975).

Head J. W. and McCord T. B. *Imbrian-age highland volcanism on the Moon.- The Gruithuisen and Mairan domes.* Science, 199, 1433-1436 (1978).

Head J. W. and Gifford Ann. *Lunar mare domes: Classification and modes of origin.* The Moon and the Planets 22, 235-258 (1980).

Head J. W. *Lava flooding of ancient planetary crusts: Geometry, thickness, and volumes of flooded lunar impact basins.* Moon and Planets, 26, 61-88 (1982).

Head J. W. *et al. Lunar impact basin: data from the nearside northern high latitudes and eastern limb from the second Galileo flyby.* LPSC XXIV, 623-624 (1993).

Herbert F. *Time-dependent lunar density models.* Proc. Lunar Planet. Sci. Conf. 11th, 2015-2030 (1980).

Hess P. and Parmentier M. *A model for the thermal and chemical evolution of the Moon's interior: Implications for the onset of mare volcanism.* Earth Planet. Sci. Lett. 134, 501 (1995).

Hiesinger H., Jaumann R., Neukum G., and Head J. W. III. *Ages of mare basalts on the lunar nearside.* J. Geophs. Res. Vol. 105, NO. E12, pp 29,239-29,275 (2000).

Hiesinger H., Jaumann R., Neukum G., and Head J. W. III. *Ages and Mineralogical Variation of Lunar Mare Basalts.* American Geophysical Union, Spring Meeting. Abstract #P21A-04 (2001).

Hiroi T. C. M. Pieters, and R. V. Morris. *New considerations fro estimating lunar soil maturity from VIS-NIR reflectance spectroscopy.* LPSC XXX, abstract 1812 (1997).

Hodges C. A. *Mare ridges and lava lakes.* Apollo 17 Preliminary Science Report, NASA SP-330, 31-12-31-21 (1973).

Hoerz F. *How thick are lunar mare basalts.* LPSC IX,Vol. 3, p. 3311-3331 (1978).

Hoerz F., R. Greive, G. Heiken, P. Spudis, and A. Binder. *Lunar surface processes.* In Lunar Sourcebook, Cambridge Univ. Press, New York (1991).

Housley, R.M. *Toward a model of grain surface exposure in planetary regoliths.* Proc. Conf, The Ancient Sun: Fossil record in the earth, moon and meteorites. p. 401-410 (1980).

Hulme G. and Fielder G. *Effusion rates and rheology of lunar lavas.* Phil. Trans. Roy. Soc. London A285, no. 1327, p. 227-234 (1977).

Isbel C. E. *et al. Clementine: a multispectral digital image model archive of the Moon* (abstract). Lunar Planet. Sci. 30, #1812, Lunar and Planetary Institute, Houston, Texas USA (CD-ROM) (1999).

Johnson P.E., Smith M. O. and Adams J. B. Quantitative analysis of planetary reflectance spectra with principal component analysis. .*Proc. Lunar Planet. Sci. Conf. 15tj, J. Geophys. Res. 90 (Suppl.),* C805-C810 (1985).

Johnson J. R., S. M. Larson, and R. B. Singer. *Remote sensing of potential lunar resources* 1. *Near-side compositional properties.* J. Geophys, Res., 96, 18,861-18,882 (1991).

Jolliff B. L., Gaddis, L. R., Ryder, G., Neal, C. R., Shearer, C. K., Elphic, R. C., Johnson, J. R., Keller, L. P., Korotev, R. L., Lawrence, D. J., Lucey, P. G., Papike, J. J., Pieters, C. M., Spudis, P. D. & Taylor, L. A. *New views of the Moon: improved understanding through data integration.* EOS Transactions American Geophysical Union 81(349), 354-355 (2000).

Keller L. P, Wentworth S. J., McKay, D. S. *Space weathering: reflectance spectroscopy and TEM analysis of individual lunar soil grains.* LPSC IXXX. Abstract no. 1762 (1998b).

Keller L. P, Wentworth, S. J., Gezo, J, McKay, D. S., Taylor, L. A., Pieters, C, Morris, R. V. *Space weathering alteration of lunar soil grains..* LPSC XXX. Abstract no. 1820 (1999).

Keller L. P., Wentworth S. J., McKay D. S., Taylor L. A., Pieters C., and Morris R. V. *Space weathering in the fine size fraction of lunar soils: mare/highland differences.* Lunar and Planetary Science Conference XXXI, #1655 (2000).

Kiefer W. S. *Gravity models for lunar mascon basins: distribution and thickness of mare basalts and basin ejecta.* LPS XXVIII, 1576 (1997).

Kreslavsky M. A., Yu. G. Shkuratov, Yu. I. Velikodsky, V. G. Kaydash, and D. G. Stankevich. *Photometric properties of the lunar surface derived from Clementine observations.* J. Geophys. Res. 105. NO. E8, pp 20,281-20,295 (2000).

Kuiper G. P., Whitaker, E. A., Strom R. G., Fountain J. W., Larson S. M. Consolidate Lunar Atlas, Lunar and Planetary Laboratory, University of Arizona (1967).

Le Maitre R. W. *The chemical variability of some common igneous rocks.* J. Petr., 17, 589-637 (1976).

Le Mouèlic S., Longevin Y, and Erard S. *A new reduction approach for the Clementine NIR data set: Application to Aristillus, Aristarchus and Kepler.* J.Geophys. Res. 104, NO. E", 3833-3843 (1999).

Longhi J. *Experimental petrology and petrogenesis of mare volcanics.* Geochim. Cosmochi. Acta 56,, 2235-2251 (1992).

Lucey P. G., Hawke B. R., Pieters C. M., Head J. W., and McCord T. B. J. Geophys. Res. Vol. 91. D344 (1986).

Lucey P. G., Taylor G. J., and Malaret E. *Abundance and distribution of iron on the Moon.* Science, 268, 1150-1153 (1995).

Lucey P. G., Blewett D. T., Johnson J.R., Taylor G. J., and Hawke B. R.. *Lunar titanium content from UV-VIS measurements.* Lunar Planet. Sci. XXV, 781-782 (1996).

Lucey P. G., Blewett D. T. and Hawke B. R. *Mapping the FeO and TiO_2 content of the lunar surface with multispectral imagery .J. Geophys. Res.*, Vol. 103, 3679-3699 (1998).

Lucey P. G., Blewett D. T., and Jolliff B. L. *Lunar iron and titanium abundances algorithms based on final processing of Clementine ultraviolet-visible images.* J. Geophys. Res., Vol. 105, No. E8, 20,297-20,305 (2000a).

Lucey P. G., Bewett D. T., Taylor G. J., and Hawke B. R. *Imaging of lunar surface maturity.* J.Geophys. Res. Vol. 105, NO. E8, 20,377-20,386 (2000b).

Malin M. C. *Lunar red spots: possible pre-mare materials.* Earth Planet Sci. Lett. 21, 331-341 (1974).

Mattingly T. K., Farouk El-Baz, and R. A. Laidley. *Observations and Impressions from Lunar Orbit.* Apollo 16, Preliminary Science Report. NASA Manned Spacecraft Center. pp 28-7, 28-8 (1972).

McEwen A. S., Robinson M. S. *Mapping of the Moon by Clementine.* Adv. Space Res. Vol. 19, No. pp. 1523-1533 (1997).

McEwen A. S., Robinson M. S., Eliason E. M., Lucey P. G., Duxbury T. C. and Spudis P. D. *Clementine observations of the Aristarchus region of the Moon.* Science 266. pp 1858-1862 (1994).

McGetchin T. R., M. Settle, and J. W. Head. *Radial thickness variation in impact crater ejecta: Implications for lunar basin deposits.* Earth Planet. Sci. Lett. 20, 226-236 (1973).

McKay D. S., R. M. Fruland, and G. H. Heiken. *Grainsize and evolution of lunar soils.* Proc. Lunar. Sci. Conf. 5th, 887-906 (1974). In Lunar Sourcebook, pp. 285-356, Cambridge Univ. Press. New York (1991).

McKay D. S., G. Heiken, A. Basu, G. Blanford. S. Simon, R. Reedy, and B. M. French. *The lunar regolith.* In Lunar Sourcebook, pp. 285-356, Cambridge Univ. Press. New York (1991).

Melendrez D. E., J. R. Johnson, S. M. Larson, and R. B. Singer. *Remote sensing of potential lunar resource, 2; High spatial resolution mapping of spectral reflectance ratios and implications for nearside mare TiO_2 content.* J. Geophys. Res., 99, 5,601-5,620 (1994).

Melosh H. J., *Impact Cratering: A Geologic Process*, 245 pp., Oxford Univ. Press, New York (1989).

Metzger A. E., Trombka J. I., Reedy R. C., and Arnold J. R. *Element concentrations from lunar orbital gamma ray measurements.* Proc. Lunar Sci. Conf., 5th, 1067-1078 (1974).

Moore H. J., J. M. Boyce, G. G. Schaber, and D. H. Scott. *Lunar remote sensing and measurements.* U.S. Geological Survey Prof. Pap. 1046-B (1980).

Morris E. C. and Wilhelms D. E. *Geologic Map of the Julius Caesar Quadrangle of the Moon.* U.S. Geol. Survey Misc. Geol. Inv. Map I-510 (1967).

Muller, P. M., and Sjogren, W. L. *Mascons – Lunar mass concentrations.* Science 161. 680-684 (1968).

Mustard J. F., C. M. Pieters. *Photometric phase functions of common geologic minerals and applications to quantitative analysis of mineral mixture reflectance spectra.* J. Geophys. Res. Vol. 94. pp. 13,619-13,634 (1989).

Mysen B. O. and I. Kushiro. *Compositional variations of coexisting phases with degree of melting of peridotite in the upper mantle.* Amer. Min, 62, 843-65 (1977).

Neukum G., B. Koenig, and J. Arkani-Hamed. *A study of lunar impact crater size-distributions.* Moon, 12, 201-229 (1975a).

Neukum G. and P. Horn. *Effects of lava flows on lunar crater population.* The Moon 15, 205-222 (1976).

Neukum G. and B. A. Ivanov. *Crater size distributions and impact probabilities on Earth from lunar, terrestrial-planet, and asteroid cratering data.* In Hazard Due to Comets and Asteroids, edited by T. Gehrels, pp. 359-416, Univ. of Ariz. Press, Tucson (1994).

Neumann G. A., M. T. Zuber, D. E. Smith, and Lemoine F. G. *the lunar crust: Global structure and signature of major basins.* J. Geophys. Res., vol 101, NO. E7, Pp. 16,841-16,843 (1996).

Noble S. K., C. M. Pieters, L. A. Taylor, R. V. Morris, C. C. Allen, D. S. McKay, and L. P. Keller. *Optical properties of the finest fractions of lunar soil: implications for space weathering environments.* Lunar and Planetary Science XXXI. 1810 (2000).

Nozette S. *et al.*,. The Clementine Mission to the Moon: Scientific Overview. *Science* Vol. 266 1835-1839 (1994).

Oberbeck V. R., Quaid W. L., Mahan M., and Paulson S. *Monte Carlo calculations of lunar regolith, thickness, and distribution.* Icarus, 19, 87-107 (1973).

O'Hara M. J. *Flood basalts, basalt floods or Topless Bushvelds? Lunar Petrogenesis Revisited.* Journal of Petrology. 41-11, pp 1545-1651 (2000).

O'Keefe J. D., and T. J. Ahrens. *Planetary cratering mechanics.* J. Geophys. Res. 98, 17,011-17,028 (1993).

Papike J., L, Taylor, and S. Simon, *Lunar minerals,* in Lunar Sourcebook, Cambridge Univ. Press, New York (1991).

Phillips R. J., Conel J. E., Abbott E. A., Sjogren W. L., and Morton J. B. *Mascons: Progress toward a Unique Solution for Mass Distribution.* J. Geophys. Res. 77, 7106-7114 (1972).

Pieters C. M. and McCord T. B. *Classification and distribution of lunar mare basalt types.* LPI Conference 234, 125-129 (1975).

Pieters C. M. *Mare basalts on the front side of the moon: A summary of spectral reflectance data.* Proc. 9th Lunar Planet. Sci. Conf., 2825-2849 (1978).

Pieters C. M. and Wilhelms D. E. J. *Origin of olivine at Copernicus.* Geophys Res. B 90, C415-C420 (1985).

Pieters C. M. *Bullialdus: Strengthening the case for lunar plutons.* Geophys. Res. Lett. 18, 2129-2132 (1991).

Pieters C. M. *Compositional diversity and stratigraphy of the lunar crust derived from reflectance spectroscopy.* Remote Geochemical Analysis (eds. C. M. Pieters and P. A. J. Englert), pp. 309-339. Cambridge Univ. Press, Cambridge, UK (1993a).

Pieters C. M, Sunshine, J. M., Fischer, E. M., Murchie, S. L., Belton, M., NcEwen, A., Gaddis, L., Greeley, R. Neukum, G., Jaumann, R., Hoffmann, H. *Crustal diversity of the Moon: Compositional analyses of Galileo SSI data.* J. Geophys. Res. 98, E9, p. 17,127-17148 (1993b).

Pieters C. M, Staid, M. I., Fischer, E. M., Tompkins, S. He, G. A sharper View of Impact Craters from Clementine Data. *Science* Vol. 266, No.5192, p. 1844-1848 (1994).

Pike R. J. *Depth/diameter relations of fresh impact craters: Revision from Spacecraft data.* Geophys. Res. Lett., 1, 291-294 (1974).

Pike R. J. and Spudis P. D. *Basin-ring spacing on the Moon, Mercury, and Mars.* Earth Moon and Planets 39, 129-194 (1987).

Raitala J., Kreslavsky M.A., Shkuratov Yu. G., Starukhina L. V., and Kaydash V. G. *Nonmare volcanism on the Moon: Characteristics from the Clementine data.* LPS XXX, #1457 (1999).

Regeon P. A., Chapman R. J., and Baugh R., Clementine "The Deep Space Program Science Experiment", *Low-Cost Planetary Mission Conference*, International Academy of Astronautics, IAA-L-0501, 13 pp. (1994).

Rhodes, J.M. Philos. *Some Compositional aspects of lunar regolith evolution. Phil.* Trans. Royal Soc. London A285, no. 1327, 293-301 (1977).

Robinson M. S., McEwen A. S., Eliason E., Lee E. M., Malaret E. and Lucey P. G. *Clementine UV-VIS global mosaic: A new tool for understanding the lunar crust* (abstract). Lunar Planet. Sci. 30, #1931, Lunar and Planetary Institute, Houston, Texas, USA (CD-ROM) (1999).

Ryder G. and Wood J. *Serenitatis and Imbrium impact melts – Implications for large-scale layering in the lunar crust.* A. LPSC VIII, Vol. 1, p. 655-668 (1977).

Ryder G. *Lunar Ferroan Anorthosites and Mare Basalt Sources: The Mixed Connection.* J. Geophys. Res. 97,, 2065-2068. (1991).

Ryder G. *Coincidence in time of the Imbrium basin impact and Apollo 15 KREEP volcanic series: impact-induced melting?* Sudbury Conference, LPI Contributions No. 790, 61-63 (1992).

Salimbeni P. G., R. Lena, Mengoli G., Douglass E., Santacana G. *The domes of the Rima Birt Region.* Geological Lunar Research Group (GLR). Submitted to ALPO Journal (2002).

Schaber, G. G. *Lava Flows in Mare Imbrium: Geologic Evaluation from Apollo Orbital Photography.* Geochim. et Comsochim. Acta, Suppl. 4. Proceedings of the Fourth Lunar Science Conference; Vol. I, pp. 73.92 (1973).

Schaber G. G. *Apollo 17 Preliminary Science Report*, NASA SP-330, National Aeronautics and Space Administratin , 30-17 to 30-25 (1973a).

Schaber G. G. Proc. Fourth Lunar Sci. Conf., Geochim. Cosmochim. Acta. Suppl. 4, 73-94 (1973b).

Schaber G. G., Thompson T. W., Zisk S. H. *Lava flows in Mare Imbrium: An evaluation of anomalously low Earth-based radar reflectivity.* The Moon 13, 395-423 (1975).

Schimerman, L. A., ed, Lunar cartographic dossier: U.S. Defence Mapping Agency Aerospace Centre, St. Louis, Missouri, v. 1, sections 3.1.10 and 3.4.63 (1975).

Schultz P. H. *Moon morphology.* University of Texas Press. Austin and London (1974).

Schultz P. H., Greeley R, and Gault, D. E. *Degradation of small mare surface features.* LPSC VII, Vol. 1, p. 985-1003 (1976).

Schultz P. H. and Spudis P. D. *Beginning and end of lunar mare volcanism.* Nature Vol. 302, No 5905. pp 233-236 (1983).

Schultz P. H. *Cratering on Mercury: A relook.* In *Mercury* (F. Vilas, C. R. Chapman, and M. S. Matthews, Eds.), pp. 274-335. Univ. of Arizona Press, Tucson. (1988).

Scott D. H. *Apollo 16 Preliminary Science Report.* NASA Manned Spacecraft Centre. NASA SP-315, 29-31 29-33 (1972).

Serge D. C., Pinet P. C., and Head J. W. *Gruithuisen domes region: a candidate for an extended nonmare volcanism unit on the Moon.* J. Geophys. Res. 104. NO. E7, 16515-16529 (1999).

Shoemaker E. M. *Interpretation of lunar craters.* Physics and Astronomy of the Moon. Ed. Z. Kopal, pp. 289-359. New York: Academic Press 453p (1962).

Shkuratov Y. G., Kaydash V. G., and Opanasenko N. V. *Iron and titanium abundance and maturity degree distribution on the lunar nearside.* Icarus 137, 222-234 (1999).

Shkuratov Y. G. and Bondarenko N. V. *Regolith layer thickness mapping of the Moon by radar and optical data.* Icarus 149, 329-338 (2001).

Smith M. O., Johnson P. E. and Adams J. B. *Quantitative determination of mineral types and abundances from reflectance spectra using principal components analysis.* Proc.Lunar Planet. Sci. Conf. 15th, J. Geophys. Res. 90 (Suppl.), C797-C804 (1985).

Solomon S. C. And Head J. W. *Vertical moment in mare basins: relation to mare emplacement, basin tectonics, and lunar thermal history.* J. Geophys. Res. 84, 1667-1682 (1979).

Smrekar, S., and Pieters C. M. *Near-infrared spectroscopy of problem impact melt from three large lunar highland craters.* Icarus 63, 442-452 (1985).

Spudis P. D. *Composition and origin of the Apennine Bench Formation.* Proc. Lunar Planet. Sci. Conf. 9th, 3379-3394 (1978).

Spudis P. D. *Apollo 16 site geology and impact melts – implications for the geologic history of the lunar highlands.* LPSC XV, in J. Geophys. Res., vol. 89, p. C95-C107 (1984).

Spudis P. D. and Davis, P. A. *How much anorthosite in the lunar crust?: Implications for lunar crustal origin.* LPS XVI, p. 807-808 (1985).

Spudis P. D. *The materials and formation of the Imbrium Basin.* Workshop on the geology and petrology of the Apollo 15 landing site, p. 100-104 (1986).

Spudis P. D. and Hawke B. R. *The Apennine Bench formation revised.* In Workshop on the Geology and Petrology of the Apollo 15 Landing Site (eds. P. D. Spudis and G. Ryder), pp. 105-107. LPI Tech. Rept. 86-03, Lunar and Planetary Institute Houston, Texas, USA (1986).

Spudis P. D. *Geology Multi-ring Basins,* 263 pp., Cambridge Univ. Press, New York (1993).

Spudis P. D. and Adkins C. D. *Morphometry of basins on the Moon: new results from Clementine Laser Altimetry.* LPS 27, p. 1253-1254 (1996).

Stadermann F. J., Heusser E. K., Lingner S, and Stöffler D. *The case for a younger Imbrium basin: New ^{40}Ar-^{39} ages of Apollo 14 rocks.* Geochimica et Cosmochimica Acta, 55, p. 2339-2349 (1991).

Stöffler D., E. E. Gault, J. Wedekind, and G. Polkowski. *Experimental hypervelocity impact into quartz sand: Distribution and shock metamorphism of ejecta.* J. Geophys. Res., 80, 4062-4077 (1975).

Strom R. G. *Interpretations of Ranger VII Records.* Jet Prop. Lab. Tech. Report 32, 700, Ch. III (1965).

Stuart-Alexandra D. E. and Howard K. A. *Lunar Maria and Circular Basins – A review.* Icarus 12, 440-456 (1970).

Taylor S. R. and Jakeš P. *The geochemical evolution of the Moon.* Proc. Lunar Sci. Conf. 5th, pp. 1287-1305 (1974).

Taylor S. R. *Geochemical constraints on melting and differentiation of the Moon.* Proc. Lunar Sci. Conf. 9th, pp. 15-23 (1978).

Taylor S. R. *Lunar Science: A Post Apollo View.* New York: Pergamon (1975).

Tera F., Papanastassiou D. A., and Wasserburg G. J. *Isotopic evidence for a terminal lunar cataclysm.* Earth Planet. Sci. Lett., 22, 1-21 (1974).

Thompson T. W., Johnson T. V., Shorthill R. W., Zisk S. H., Moore H. J., and Schaber G. G. *Unusual remote sensing signatures of Montes Jura and crater Plato.* Proc. Lunar Sci. Conf. XXVI, 1164-1165 (1978).

Thomson B. J., Spudis P.D., and Bussey D. B. *Impact craters as probes of the lunar crust.* Lunar and Planet. Sci. XXIX, 1820.pdf (1998).

Tompkins S. T., J. F. Mustard, C. M. Pieters, and D. W. Forsyth. *Objective determination of image end-members in spectral mixture analysis.* Lunar Planetary Science XXIV, pp. 1433-1434 (1993).

Tompkins S. T., Pieters C. M., Mustard J. F, Pinet P., and Chevrel D. *Distribution of materials excavated by the lunar crater Bullialdus and implications for the geologic history of the Nubium Region.* Icarus 110, 261-274 (1994).

Torson J. M. and K. J. Becker, ISIS – A Software Architecture for Processing Planetary Images. *Lunar and Planetary Science Conference 28th*, pp. 1443-1444 (1977).

Turner, G. *Potassium-argon chronology of the moon.* Phys. Chem. Earth, Vol. 10, no. 3, p. 145-195 (1977).

Wagner R. J., Head III J. W., Wolf U., and Neukum G. *Stratigraphic sequence and ages of volcanic units in the Gruithuisen region of the Moon.* J. Geophys. Res. 107(E11), 5104 (2002).

Walker D., Longhi, J., Stolper, E.M., Grove. T.L., and Hays, J. F. *Origin of titaniferous lunar basalts* Geochi. Cosmochim. Acta, 39, p. 1219-1235 (1975).

Werner C. L., and Loper D. E. *On lunar asymmetries 2. Origin and distribution of mare basalts and mascons.* J. Geophys Res., 107(E6), 5045 (2002).

Whitaker E. A. *Lunar colour boundaries and their relationship to topographic features: A preliminary survey,* Moon 4, 348-355 (1972a).

Whitaker E. A. Apollo 15 Preliminary Science Report, NASA SP-289, pp. 25-83 to 25-84 (1972b).

Whitaker E. A. *Colour contrasts in Mare Nubium and the Southern Oceanus Procellarum.* Apollo 16 Preliminary Science Report, NASA Manned Spacecraft Centre. pp. 104-105 (1972c).

Whitaker E. A. The Lunar Procellarum basin. In Multiring Basins (P. H. Shultz and R. B. Merrill Eds). Proc. Lunar Planet. Sci. 12A, 105-111 (1981).

Whitford-Stark J. L. *The craters of Mare Imbrium.* LPI 11.1242W, 1242-1244 (1980).

Whitford-Stark J. L. and Head J. W. *The stratigraphy of Mare Imbrium.* LPI, 11.1245W. 1245-1247 (1980).

Wieczorek M. A. and Phillips R. J. *Lunar multiring basins and the cratering process.* Icarus 139, 246-259 (1999).

Wieczorek M. A. and Phillips R. J. *The "Procellarum KREEP Terrane": Implications for mare volcanism and lunar evolution".* J. Geophys. Res. Vol. 105, NO E8, pp 20,417-20,430 (2000).

Wilhelms D. E. and Davis D. E. *Two former faces of the Moon.* Icarus 15, 368-372 (1971).

Wilhelms D. E. and McCauley J. F. *Geological Map of the Nearside of the Moon.* U.S. Geol. Surv. Misc. Inv. Ser., Map I-703, Washington, D.C., USA (1971).

Wilhelms D. E. in Geology of the Terrestrial Planets, NASA SP-469 (NASA, Washington, DC), p 107 (1984).

Wilhelms D. E. *The geologic history of the Moon.* U.S. Geol. Surv. Prof. Pap. 1348, p. 302 (1987).

Williams K. K. and Zuber M. T. *Re-evaluation of mare thicknesses bases on lunar crater depth-diameter relationships.* LPSC 27, p. 1441-1442 (1996).

Wilshire H. G. and Jackson E. D. *Petrology and stratigraphy of the Fra Mauro Formation at the Apollo 14 site.* U.S. Geol. Survey Prof. Paper 785. 26 pp. (1972).

Wilson G. *Wrench movements in the Aristarchus region of the Moon.* Proc. Geolo. Ass. Lond. 81, 595-608 (1970).

Wise D. U. and Yates M. T. *Mascons as structural relief on a lunar 'Moho'.* J. Geophys. Res. 75, 261-268 (1970).

Wood C. A. and Head J. W. *Geologic setting and provenance of spectrally distinct pre-mare material of possible volcanic origin.* . (LPI), p. 189 (1975).

Yoder, H. S. *The great basaltic 'floods'.* S. Afr. J. Geol., 91, 139-56 (1988).